Realizing Efficient Energy Harvesting from Organic Photovoltaic Cells

A Thesis
SUBMITTED TO THE FACULTY OF
UNIVERSITY OF MINNESOTA
BY

Yunlong Zou

IN PARTIAL FULFILLMENT OF THE REQUIREMENTS
FOR THE DEGREE OF
DOCTOR OF PHILOSOPHY

Russell J. Holmes, Advisor

Jan 2016

Acknowledgements

The five years I spent in Minnesota have been fun and meaningful. I gained not only knowledge but also dear friends. The work presented in this thesis could not have been completed without their help and support.

I would first like to thank my academic advisor Russell Holmes for his professional guidance on my research. He helps me find directions and also allows me freedom to explore new research topics. I would not have learned so much about organic electronics without him.

I would like to thank my friends for keeping me company during the last five years. I would like to thank Tuoqi Li for making my life more colorful despite the bitterly cold winter. I would also like to thank Ankit Mahajan for keeping me company during afterhours and share my ups and downs in both work and life. They became my new family here in Minnesota. I never felt alone even though I am seven thousand miles away from hometown.

I would also like to thank the entire Holmes group, Wade, Grant, Kai, Richa, Nick, Matt, Tyler, Nathan, Yi, Tom, Ian, Gang, Kyle, Abbey, Tao and Deepesh, for their help and thoughtful discussion in lab and office. They made working and studying a lot easier.

I would like to thank my collaborators, Dr. James Holst at Sigma-Aldrich and Prof. Ken-Tsung Wong at National Taiwan University. Their hard work on synthesizing high quality materials made it possible for me to carry on with my study.

Finally, I would like to thank my parents and my wife, their patience and unconditional support made this achievement possible. Thank you!

Dedication

This dissertation is dedicated to my parents and my wife.

Abstract

Organic photovoltaic cells (OPVs) are emerging field of research in renewable energy. The development of OPVs in recent years has made this technology viable for many niche applications. In order to realize widespread application however, the power conversion efficiency (η_P) requires further improvement.

The η_P of an OPV depends on the short-circuit current density (J_{SC}), open-circuit voltage (V_{OC}) and fill factor (FF). For state-of-the-art devices, J_{SC} is mostly optimized with the application of novel low-bandgap materials and a bulk heterojunction device architecture (internal quantum efficiency approaching 100%). The remaining limiting factors are the low V_{OC} and FF. This work focuses on overcoming these bottlenecks for improved η_P.

Temperature dependent measurements of device performance are used to examine both charge transfer and exciton ionization process in OPVs. The results permit an improved understanding of the intrinsic limit for V_{OC} in various device architectures and provide insight on device operation. Efforts have also been directed at engineering device architecture for optimized FF, realizing a very high η_P of 8% for vapor deposited small molecule OPVs. With collaborators, new molecules with tailored desired energy levels are being designed for further improvements in η_P. A new type of hybrid organic-inorganic perovskite material is also included in this study. By addressing processing issues and anomalous hysteresis effects, a very high η_P of 19.1% is achieved. Moving forward, topics including engineering film crystallinity, exploring tandem architectures and understanding degradation mechanisms will further push OPVs toward broad commercialization.

Table of Contents

List of Tables

List of Figures

List of Abbreviations

BHJ ..... Bulk Heterojunction
CT state ..... Charge Transfer State
D-A ..... Donor-Acceptor
FF ..... Fill Factor
HOMO ..... Highest Occupied Molecular Orbital
ITO ..... Indium-Tin-Oxide
J_{SC} ..... Short-Circuit Current Density
L_D ..... Exciton Diffusion Length
LUMO ..... Lowest Unoccupied Molecular Orbital
η_{EQE} ..... External Quantum Efficiency
η_P ..... Power Conversion Efficiency
OLED ..... Organic Light-Emitting Device
OPV ..... Organic Photovoltaic Cell
PHJ ..... Planar Heterojunction
PL ..... Photoluminescence
PMHJ ..... Planar Mixed Heterojunction
SubPc ..... Boron Subphthalocyanine Chloride
V_{OC} ..... Open-Circuit Voltage

1. Introduction to Photovoltaic Cells

The intrinsically limited supply of fossil fuels poses a potential threat to economic growth and regional stability. Consequently, it is essential to broaden the portfolio of energy sources to include additional emphasis on renewable energy.

Mainstream renewable energy technologies include: wind power, hydropower, biomass, geo-thermal and photovoltaic. Aside from geo-thermal, all other mentioned technologies directly or indirectly harvest energy from the sun. The sun provides 89 petawatts of power to the Earth's surface every day, capturing 0.02% of it would be sufficient to provide energy for the entire world.[1]

The most direct way of harvesting solar energy is to convert sunlight into electricity, the most convenient form of energy, using the photovoltaic effect. Currently, crystalline Si photovoltaic cells are the most widely adopted first-generation photovoltaic technology, with a power conversion efficiency (η_P) of ~20%.[2] Unfortunately, this technology is limited in its application due to high costs of fabrication and deployment.

There has been a continuous effort to improve over the conventional crystalline-Si photovoltaic cell since its first discovery in 1954.[3] One approach is to develop multi-junction photovoltaic cells and solar concentrators to enhance η_P.[4-5] According to the Shockley-Queisser limit, the maximum efficiency achievable for a single junction photovoltaic cell with an ideal band gap energy (1.34 eV) is 34 %. By using a multi-junction architecture, the efficiency limit can be increased to 84 % under highly concentrated sunlight.[6-7] In practice, the record efficiency for a multi-junction photovoltaic

cell with concentrator is 46 %, much improved over the conventional crystalline Si based photovoltaic cells.[2] However, the cost of these highly efficient multi-junction photovoltaic cells can be significantly higher than conventional crystalline Si based technology and the application is much limited to aerospace.

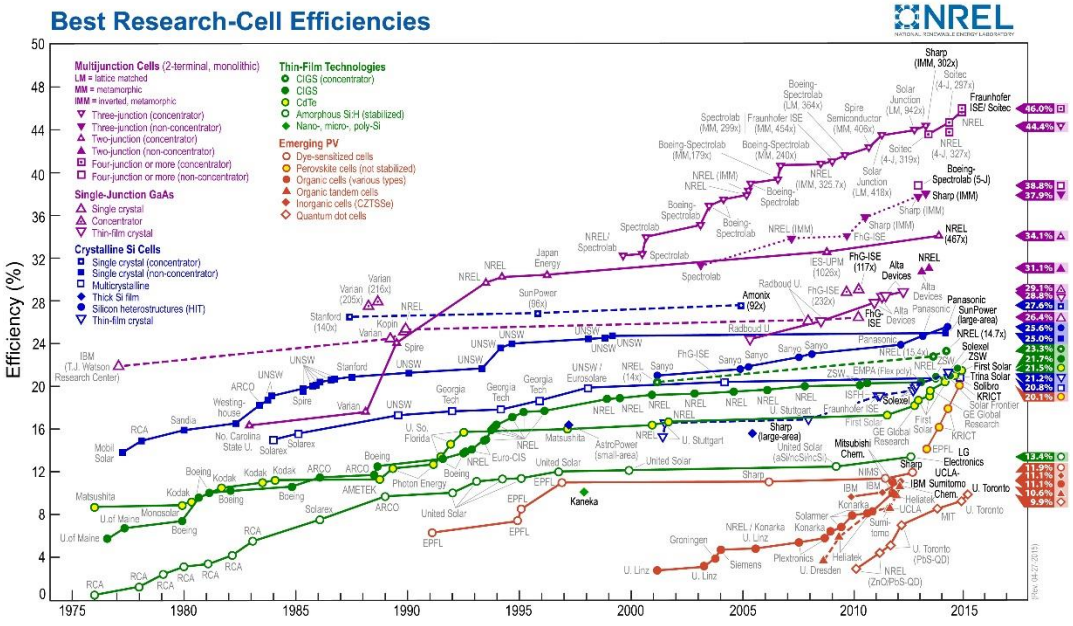

Figure 1.1 Best research-cell efficiencies over the last 40 years. Data compiled by the National Renewable Energy Laboratory.[2]

The other approach is to focus on lowering the manufacturing and deployment cost of photovoltaic cells by adopting second-generation *thin-film* photovoltaic technologies. These new technologies employ improved light-absorbers like cadmium telluride (CdTe), copper indium gallium diselenide (CIGS) and amorphous silicon.[8-11] One of the advantages of thin-film photovoltaic technology is that the cell thickness can vary from tens of nanometers to a few micrometers, much thinner than the conventional crystalline Si photovoltaic cells. This allows the thin-film photovoltaic cells to be made lower in weight

and on flexible substrates. More interestingly, thin-film photovoltaic cells can also be manufactured into different form factors and used as semi-transparent films that can be integrated with windows.[8, 11]

However, the toxicity, stability and use of rare elements limits the market share of second-generation thin-film photovoltaic cells.[10-11] Both academia and industry have been investing heavily in ongoing research of third-generation photovoltaic cells including small molecule or polymer based organic semiconductors, copper zinc tin sulfide, quantum dots and hybrid organic-inorganic organometal-halide perovskite materials to further reduce the cost of manufacturing and enhance the power conversion efficiency in order to compete with conventional crystalline Si photovoltaic cells.[7, 12-13]

Among third-generation photovoltaic technologies, organic photovoltaic cells (OPVs) are compatible with high-throughput roll-to-roll manufacturing and are most cost-effective for photovoltaic applications.[14-17] Beyond this, the tunable optical properties of organic molecules (by changing functional group or molecular weight) offers great versatility for niche applications where only light within a selective wavelength range need be absorbed.[18-21]

1.1 Progress to date

While photoconversion in organic semiconductors has been a topic of study for more than 50 years, the η_P has long been below 1 % in prototype OPVs using a metal-semiconductor-metal configuration.[22-23] It was not until pioneering work by Tang on thin film, planar heterojunction (PHJ) OPVs that efficient photoconversion became possible.[24] A PHJ OPV consists of a bilayer between electron donating and accepting materials, where an energy-level offset at the donor-acceptor (D-A) interface provides the driving force for exciton dissociation by charge transfer. In such a structure, performance is limited by the area of dissociating D-A interface.[25-26] Consequently, large improvements in device performance were realized with the advent of bulk heterojunction (BHJ) OPVs where the D-A materials are blended to increase the area of the dissociating interface.[27-28] To further improve the power conversion efficiency, effort has been made on engineering the vertical composition gradient, phase separation and crystallinity of the active layer, and energy level alignment at electrode-active layer.[17, 29-32] State of the art single-junction OPVs have now achieved η_P of 9~10 % using a variety of materials systems.[33-38] Another focus to further improve η_P is to develop tandem or multi-junction device architectures, where two sub-cells with compensating absorption in the solar spectrum are stacked and connected in series.[39-50] Recently, researchers reported a 12.1 % power conversion efficiency in a small molecule triple-junction OPV.[51] In industry, Heliatek has also demonstrated a similar device performance and the commercialization of OPV technology is ongoing.[52]

1.2 Overview of this thesis

The primary focus of this thesis is to understand various efficiency limiting factors in OPVs and apply theoretical understanding to guide new materials design and device optimization. The most significant remaining bottleneck to further improve device efficiency is the low open-circuit voltage (V_{OC}) compared to the exciton energy upon photoexcitation. The loss of exciton energy is >50% even in most efficient devices while the loss mechanism is not well understood.[53-56] This work approaches the bottleneck by carefully examining the intrinsic limit of maximum V_{OC} for different type of photoconversion process. A deeper understanding of device operation helps guide device architecture engineering without sacrificing V_{OC}.

This thesis also explores newly designed molecules with desired properties and experiments with a new type of hybrid organic-inorganic perovskite material, in order to improve the η_P even further.

2. Organic Semiconductors

2.1 Introduction

Chapter 1 introduced the concept of OPVs as a promising third-generation thin-film photovoltaic technology. This chapter will investigate the physics, characterization and processing of organic semiconductors, which are the building blocks for OPVs.

Organic semiconductors are conjugated small molecules or polymers that comprise of primarily carbon. Due to their structural versatility and unique optical and electronic properties, organic semiconductors are being studied not only for photovoltaic applications, but also for light-emitting devices and transistors.[57-58] The weak intermolecular bonding of organic semiconductors permits thin films to be compatible with flexible substrates that enable high throughput processing. To date, there have already been various successful demonstrations of functional devices fabricated with organic semiconductors on flexible substrates as shown in Figure 2.1.

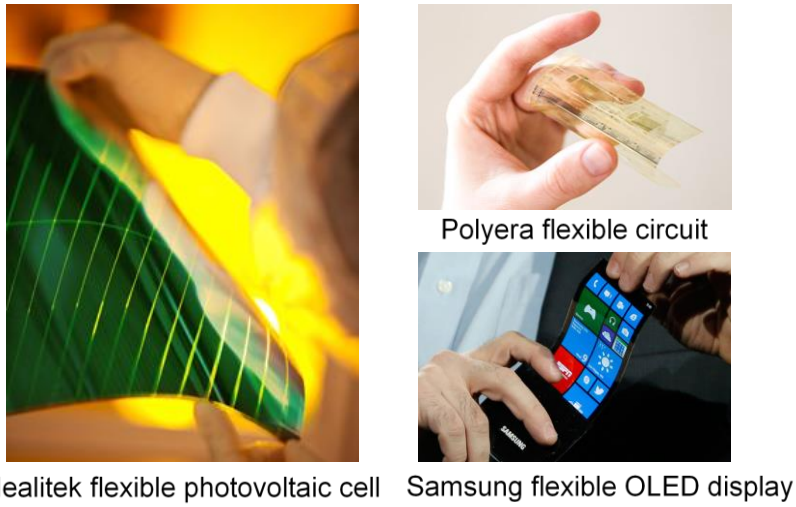

Figure 2.1 Examples of electronic devices employing organic semiconductors.

2.2 Electronic States in Organic Semiconductors

The atoms in organic molecules are held together by covalent bonds. Take carbon for example, its ground state electronic configuration is $1s^2 2s^2 2p^2$. There are two paired s electrons and two unpaired p electrons in the outer electronic level. When forming bonds with other atoms, one possible electronic configuration for the carbon atom can be realized by mixing the 2s orbital and three 2p orbitals to form a hybridized sp^3 orbital, which has a set of four degenerated orbitals. The four orbitals form a tetrahedral with the core at the center.[59] One example of sp^3 hybridization is methane (CH_4) as shown in Figure 2.2a.

The s, p_x and p_z orbitals can also be combined and form triply degenerate sp^2 orbitals. The sp^2 orbitals take on a planar trigonal geometry and adjacent orbitals are separated by 120 º. The remaining p_z orbital is perpendicular to the hybridization plane of the sp^2 orbital. One example is ethylene ($H_2C=CH_2$) as shown in Figure 2.2b. The remaining p_z orbitals from each of the carbon atom will overlap and form the π-bond. The π-bond creates delocalized electron density above and below the sp^2 hybridization plane.[59] By connecting three CH=CH segments to form a ring, the molecular structure of benzene is realized. The benzene molecule is a good demonstration of highly delocalized π bonding formed by a ring of six carbon atoms, with highly localized sp^2 orbitals between carbon and hydrogen atoms residing in the plane, as shown in Figure 2.2c and d. For some organic molecules, there exists a certain degree of intermolecular π orbital overlap that allows electrons to transfer from one molecule to the other. These organic molecules are termed organic semiconductors.

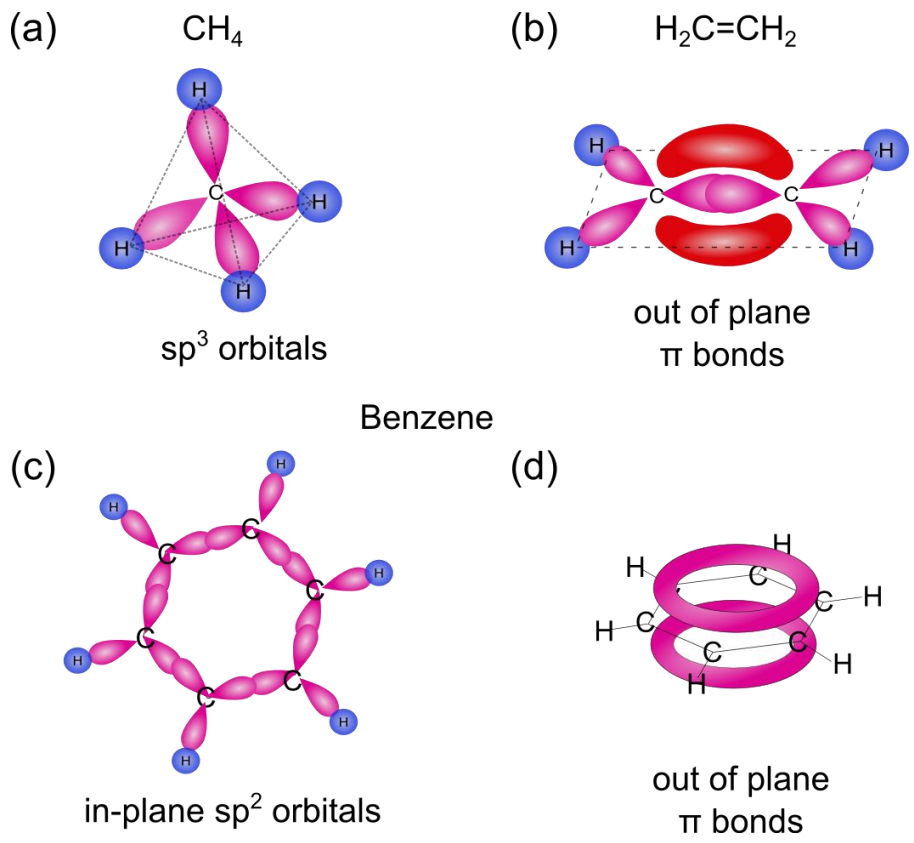

Figure 2.2 Orbital hybridization for methane, ethylene and benzene molecules.

2.2.1 Molecular Orbital Theory

As we have discussed, there will be a variety of atomic orbitals formed in an organic molecule. Typically, the superposition of all atomic orbitals is approximated as the molecular orbital. The ground state can be generated by adding electron pairs to only the lowest energy molecular orbitals and the excited state can be generated by adding electrons to the unoccupied molecular orbitals.[59] The highest occupied molecular orbital (HOMO) is analogous to the valence band and the lowest unoccupied molecular orbital (LUMO) is analogous to the conduction band in inorganic semiconductors.

2.2.2 Formation of Excited States

Upon photoexcitation or electrical excitation, electrons in the HOMO energy level can be promoted to the LUMO energy level and form an excited state. The principles of quantum mechanics dictate that the excited state can be categorized either as a singlet state and triplet state. The difference between them is lies in their degeneracy and the value of the spin angular momentum S. All four possible combinations of spin for two unpaired electrons numbered 1 and 2 are plotted in Figure 2.3, with α and β representing the spin vector for each electron. For the singlet state, two unpaired electrons are exactly out of phase and S equals zero. For the triplet state, two unpaired electrons are in phase, and S equals one.[60]

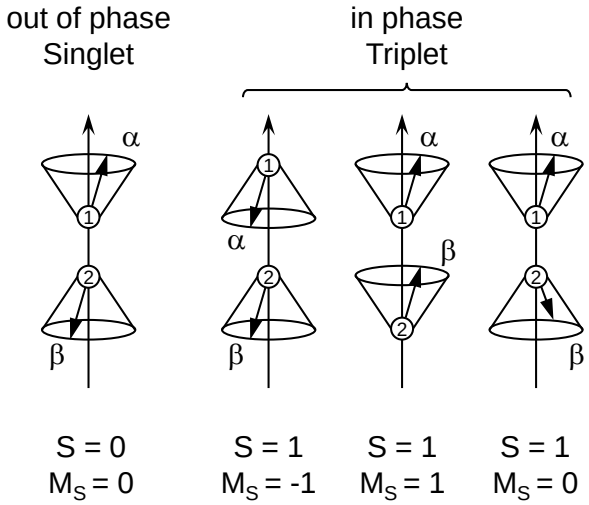

Figure 2.3 Electron spin angular momentum configuration for unpaired electrons in the excited state.

The singlet state has a degeneracy of one as there is only one combination that leads to a total exciton spin of 0. The triplet state has a degeneracy of three as the spin projection quantum number (M_s) can take on a value of -1, 0 or 1. For practical purposes, the ground

state will always be singlet as the relaxation of electronic structure configuration requires the outer shell orbital be filled, excluding unpaired electrons. The singlet and triplet state have different spin angular momentum and cannot interconvert spontaneously, as all photophysics processes require conservation of electron spin momentum. This is especially important in the operation of organic optoelectronic devices. For most organic semiconductors, photoexcitation leads exclusively to the creation of singlet states as the photon cannot supply momentum to flip the spin of an electron. However, under electrical excitation, both singlet and triplet excited states are formed as the electrons do not originate from a previously paired ground state. According to the rules of quantum mechanics, the electrically excited state has a 25% probability of being singlet and 75% probability of being triplet.[59-61] For a triplet state, it is quantum mechanically forbidden to relax back to the ground state as the ground state is a singlet and would require a change in the spin angular momentum. This selection rule has a significant impact on the design of light-emitting devices, where 75% of the excitons formed are triplet in nature and cannot radiatively relax to ground state and emit light, limiting device efficiency. As discussed previously, all interconversion processes between electronic states require the conservation of momentum. In the case of heavy atoms (large atomic number Z), the orbital angular momentum is significant and can interact with the spin angular momentum. This phenomenon is termed spin-orbit coupling. In this case, the intersystem crossing between single state and triplet state and the radiative decay of triplet state can be allowed.[59-60]

2.2.3 Energy Levels and Interconversion of Electronic States

Previously, we have discussed the ground and excited state of organic semiconductors and identified the nature of singlet and triplet excited states. Here, we describe the energy landscape and interconversion between these states.

The Jablonski diagram shown in Figure 2.4 is a convenient way to visualize the various photophysical processes in organic semiconductors. The diagram comprises the ground state (S_0), excited singlet (S_1, S_2) and triplet (T_1, T_2) states. The vibronic states are represented by the lines spaced closely to each other and is related to the quantum harmonic oscillators of the nuclei motion. Note that the triplet energy is lower than the singlet energy as the Pauli exclusion principle will instruct electrons with parallel spin to avoid each other and minimize electron-electron repulsions, thus lowering the energy of triplet state relative to singlet state.[60]

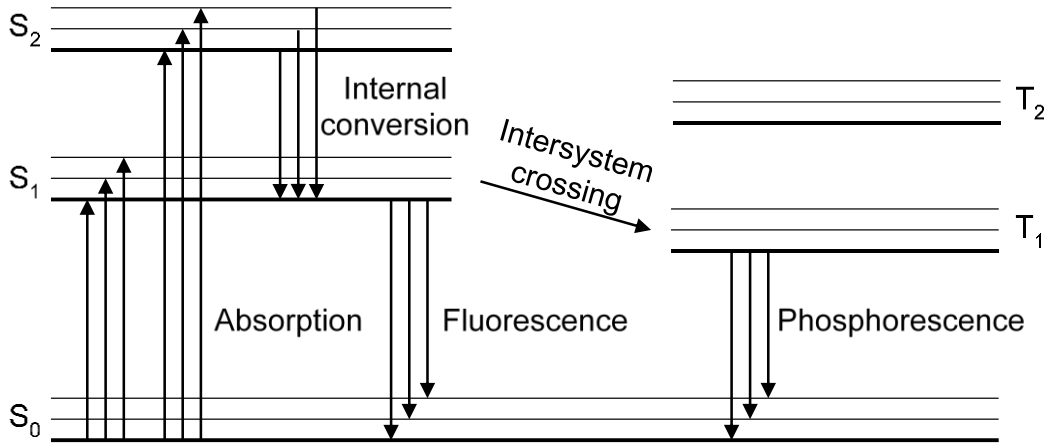

Figure 2.4 Example Jablonski diagram depicting the interconversion between electronic states in organic semiconductors.

Franck-Condon Principle

The possible interconversion processes include: 1. Absorption. Electrons in the lowest vibronic state of S_0 is promoted to S_1 or S_2 via photoexcitation and create excitons. The excitons created in organic semiconductors are localized on one molecule and have a binding energy between 0.1~1 eV.[25] 2. Internal conversion: electrons relax from S_2 to the lowest vibronic state of S_1. 3. Fluorescence: electrons radiatively relax from the lowest vibronic state of S_1 to S_0. 4. Intersystem crossing: electrons convert form excited singlet states to triplet states. 5. Phosphorescence: electrons relax from the lowest vibronic state of T_1 to S_0.

The absorption and fluorescence processes are commonly studied for organic compounds. Due to the existence of vibronic states, the absorption and fluorescence spectra will have many vibronic features. Note that fluorescence originates from the lowest energy vibronic state, as the internal conversion process is much faster compared to competing processes. This is known as Kasha's rule. The relative intensity of each vibronic feature will follow the Franck-Condon principle.[60]

Figure 2.5 demonstrates a visualization of the Franck-Condon principle for radiative transitions (absorption and fluorescence) between the ground and excited states in a diatomic molecule. The potential curves for the nuclear motion in the ground and excited states are labeled as Ψ^0 and Ψ^* respectively and each vibronic state is numbered. Electronic transitions are much faster than the vibronic motion of the nuclei, so that only vertical transitions are permitted between Ψ^0 and Ψ^*, as described by the Franck-Condon principle.

For the example shown in Figure 2.5, the equilibrium nuclear distance is longer in the excited state than in the ground state. As such, the 0-2 and 2-0 transitions will be intense while other transitions will be relatively weak, dictated by the magnitude of positive overlap between the vibrational wavefunctions of the two vibronic states. The absorption and photoluminescence spectra for the diatomic molecule are shown in Figure 2.5. The energy shift between the absorption and photoluminescence transitions is termed the Franck-Condon shift. Commonly, the photoluminescence spectrum is a mirrored image of the absorption spectrum at lower photon energy.

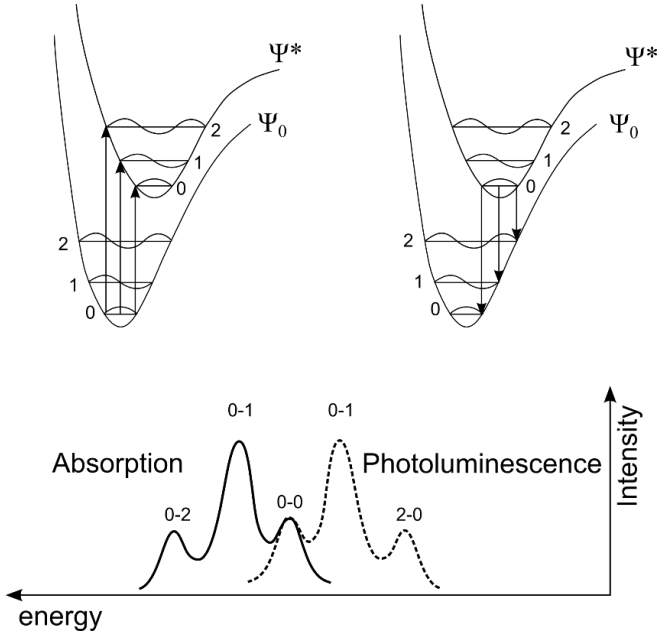

Figure 2.5 Molecular energy diagram for a diatomic molecule undergoing electronic state interconversion between S_0 and S_1. The Franck-Condon principle determines the intensity of these transitions.

In a more realistic scenario, the 0-0 transition of photoexcitation and relaxation will be offset by the Stokes energy shift. The Stokes shift is due to the relaxation of the excited state when the molecule undergoes an internal conformational change. Part of the exciton energy is emitted as heat.[59, 62]

2.2.4 Characterization of Electronic States

The ground state HOMO energy level and excited state LUMO energy level dictate the optical and electrical properties of organic semiconductors. It is thus critical to measure these energy levels with great accuracy. The most widely adopted approach to probe molecular orbital energy levels is photoemission spectroscopy.

Photoemission Spectroscopy

The HOMO energy level can be measured using photoemission spectroscopy (PES). For this technique, ultra-violet light is used to excite the electrons in the HOMO energy level to an energy above the vacuum level (E_{vac}), with the kinetic energy of the excited electron being recorded. The initial energy of the electron relative to E_{vac} can be calculated by subtracting the kinetic energy of the electron from the incident photon energy. One benefit of PES is that the Fermi-energy of an organic semiconductor thin film can be determined simultaneously from the secondary cut-off of the PES spectrum.[29, 63-64] This information can help illustrate the energy level alignment at hetero-interfaces which are common in organic electronics.[65]

In order to characterize the LUMO energy level, inverse photoemission spectroscopy (IPES) is commonly used. A group of electrons with known kinetic energy populates the LUMO energy level of the material of interest and the emitted photon energy is recorded. By subtracting the kinetic energy from the photon energy, the relative energy of electron in the LUMO energy level can be obtained.[66]

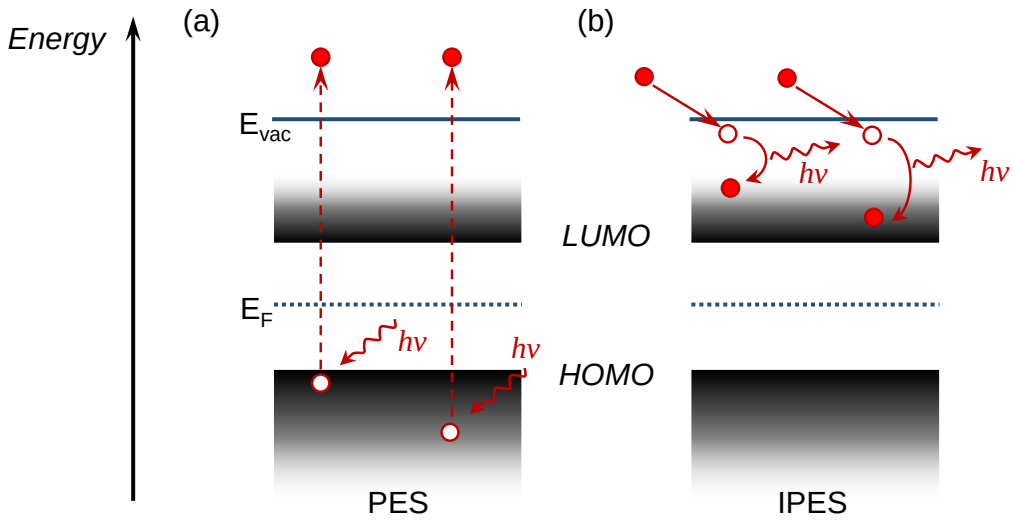

Figure 2.6 Working principle of (a) photoemission sepctroscopy (PES) and (b) inverse photoemission spectroscopy (IPES).

The resolution of PES is typically ~0.2 eV and the resolution for IPES is ~0.4 eV.[66] The IPES measurement has especially low resolution particularly due to the low cross sections of the inverse photoemission process. To improve resolution, alternative methods are used to determine the LUMO energy level. One approach is to correlate the HOMO energy level and the LUMO energy level through the bandgap energy. The bandgap energy can be determined form the shake-up satellite features of the soft X-ray photoemission spectroscopy.[67-68] In this technique, core electrons instead of valence electrons are excited. The shake-up satellite features are associated with the kinetic energy loss due to simultaneously excited HOMO-LUMO transitions. Commonly, the separation in energy between the shake-up satellite feature and the main line corresponds to the energy difference between HOMO and LUMO energy levels. In conjunction with the HOMO energy determined via PES technique, the absolute value of the LUMO energy level can be calculated.

Another drawback of photoemission spectroscopy is the requirement on high-vacuum environment and advanced equipment for analyzing the photon and electron energy, thus limiting its availability. A much more convenient method is to extract optical band gap energy ($E_{g,opt}$) from the low-energy onset of the absorption spectrum. The LUMO energy level can then be approximated as the HOMO energy level (E_{HOMO}) with the addition of $E_{g,opt}$ and exciton binding energy (E_b) as shown in equation 2.1. For this approach, the uncertainty mainly arises from the exciton binding energy.

$$E_{LUMO} = E_{HOMO} + E_{g,opt} + E_b \qquad \text{Equation 2.1}$$

Cyclic Voltammetry

As stated, photoemission has limited availability and resolution. Alternatively, cyclic voltammetry (CV) can also be used to characterize the HOMO-LUMO energy levels. CV is a type of potentiodynamic electrochemical measurement, during which a cyclic bias is applied to the working electrode and the current passing through the working electrode is recorded. A peak in the current indicates an oxidation or reduction event which is due to removing one electron from the HOMO energy level or adding one electron to the LUMO energy level.[66, 69] Typically, a standard material (e.g. ferrocene) with known HOMO and LUMO energy levels is mixed together with the sample material during testing in order to extract the exact values of the HOMO and LUMO energy levels. However, CV measurements requires all materials to be dissolved in solution. The measured values of energy levels will correspond to isolated or solvated molecules and cannot accurately reflect the impact of aggregation in the form of solid-state-thin-film that most organic

electronics are. Despite the limitations, CV measurements provide a fast and convenient way to help predict and compare HOMO and LUMO energy levels in organic semiconductors.

2.2.5 Excitonic Transfer in Organic Semiconductors

As described previously, the photoexcitation process in organic semiconductors will create tightly bound electron-hole pairs termed excitons. The exciton is able to migrate from one molecule via one of three mechanisms, namely, cascade energy transfer, Förster energy transfer and Dexter transfer.[59-60]

Cascade Energy Transfer

Cascade energy transfer, or trivial energy transfer is a radiative process that includes the emission and reabsorption of a photon. The excited state on one molecule will relax to the ground state and the emitted photon will be absorbed by an adjacent another molecule that is in its ground state. This is a long range (10~100 nm) energy transfer process between two molecules and requires good overlap between the photoluminescence spectrum of the excited molecule and the absorption spectrum of the ground state molecule.[59] The photoluminescence efficiency of the excited molecule can also impact the efficiency of cascade energy transfer process as it requires the emission of a real photon.

Förster Energy Transfer

The Förster energy transfer process is similar to the cascade energy transfer process as it also requires overlap between the photoluminescence spectrum of the excited molecule and the absorption spectrum of the ground state molecule, and a high photoluminescence efficiency for the excited state. However, no real photon is emitted and the Förster energy

transfer process is categorized as non-radiative. The interaction between the excited state molecule and the ground state molecule is not through light, but through the electric field perturbation caused by the dipole oscillation of the excited molecule.[59-60] Figure 2.7 demonstrates the scenario where an exciton is formed on molecule A and treated as an oscillating dipole. The oscillation of the dipole will create a perturbation in the electric field that surrounds it. A ground-state molecule B senses the perturbation in electric field and the Förster energy transfer is accomplished by the relaxation of molecule A back to ground state and the excitation of molecule B to excited state. There is no physical exchange of electrons during the process as electron 1 and 2 still reside on the same molecule after the energy transfer event. The rate of Förster energy transfer can be described by the equation below:[70]

$$k_F(d) = \frac{1}{\tau}\left(\frac{R_0}{d}\right)^6 \qquad \text{Equation 2.2}$$

where k_F is rate of Förster energy transfer, d is the distance between the excited molecule and the ground state molecule, τ is the exciton lifetime and R_0 is the characteristic Förster radius for given pair of excited and ground states. R_0 can be expressed as:[70]

$$R_0^{\,6} = \frac{9\eta_{PL}\kappa^2}{128\,\pi^5 n^4}\int \lambda^4 F_A(\lambda)\,\sigma_B(\lambda)\,d\lambda \qquad \text{Equation 2.3}$$

where η_{PL} is the photoluminescence efficiency of the excited state, κ is the dipole orientation factor, λ is the wavelength, n is the refractive index, F_A is the normalized fluorescence spectrum of the excited state molecule A and σ_B is the absorption cross-section of the ground state molecule B. Even though Förster energy transfer is a non-

radiative process, it is still dependent on the η_{PL} of the excited state and the spectra overlap between the excited state and the ground state. This is due to the requirement of a resonant density of states and the ability to emit light ($\eta_{PL} \neq 0$) for efficient coupling between excited and ground state. The length scale of Förster energy transfer is 1~10 nm, much shorter than that of cascade energy transfer.[26, 59]

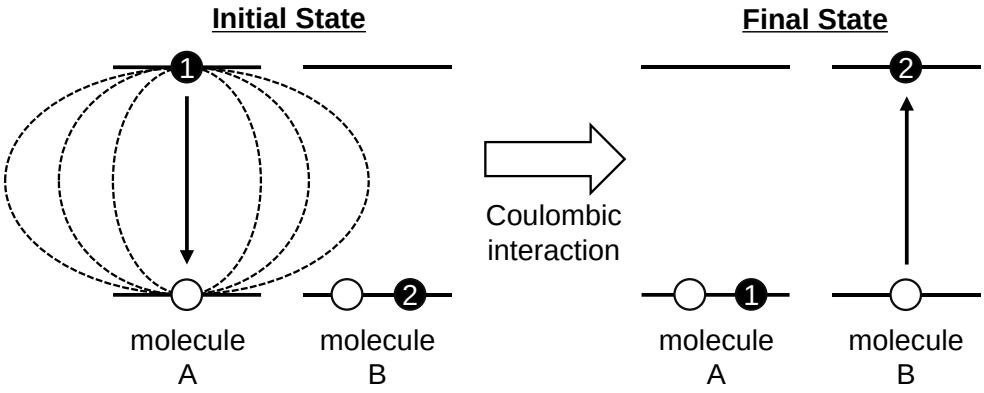

Figure 2.7 Demosntration of the Förster energy transfer process between two molecules. The coupling between two molecules is through the electric field and no physical exchange of electrons occurs during the process.

Dexter Energy Transfer

Dexter energy transfer is a process which involves the physical transfer of electrons between adjacent molecules, as depicted in Figure 2.8. The Dexter energy transfer requires an overlap between the electronic orbitals of the donor molecule and the acceptor molecule and is thus limited between nearest neighbors. The rate of Dexter energy transfer can be written as:[59]

$$k_D = \frac{4\pi^2}{h}\left|\beta_{DA}\right|^2 \int E_D(E)E_A(E)dE \qquad \text{Equation 2.4}$$

k_D is the rate of Dexter energy transfer, h is the Planck constant β_{DA} is the exchange energy

interaction between two molecules, E_D is the normalized photoluminescence spectrum of the excited molecule and E_A is the normalized absorption spectrum of the ground state molecule. β_{DA} is related to the overlap of electronic orbitals between two molecules and will thus fall exponentially with molecular spacing d. With this, the expression for Dexter energy transfer can be re-written as:[60]

$$k_D = K\frac{4\pi^2}{h}\exp(-2d/L)\int E_D(E)E_A(E)dE \qquad \text{Equation 2.5}$$

where K is a prefactor related to the specific orbital interaction between the molecules of interest, d is the spacing between two molecules and L is a characteristic length scale at which the energy transfer rate equals to other energy loss processes. The Dexter energy transfer process does not require the excited molecule be capable of light emission, it is thus most prominent for triplet excited states.

Even though the Dexter energy transfer process does not require the emission of a "real"

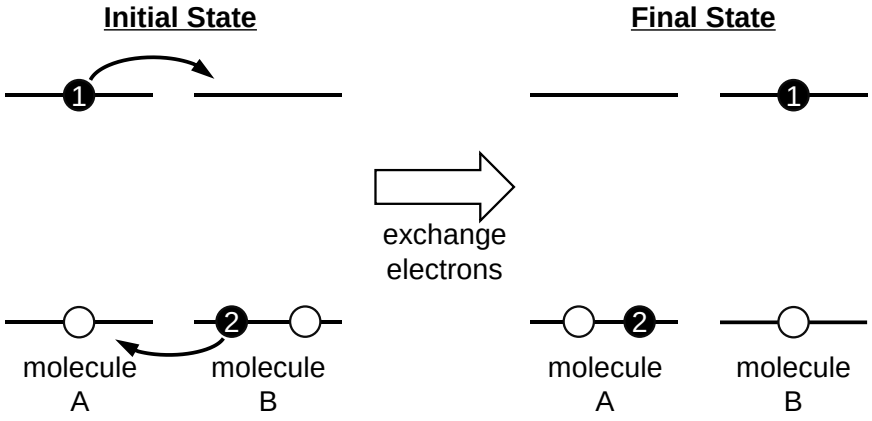

Figure 2.8 Demonstration of Dexter energy transfer between two molecules. Physical exchange of electrons is required in this process.

or "imaginary" photon, k_D still depends on the overlap between the absorption and emission spectra of the molecules of interest. This is due to the transfer of electrons between HOMO and LUMO level requires a resonance of density of states in energy.

2.2.6 Exciton Diffusion

Exciton diffusion is critical for the operation of organic photovoltaic cells as it help determine the fraction of excitons that can be converted into charge carriers. The exciton diffusion process can be thought of as multiple energy transfer events with the detailed mechanism depending on the nature of the exciton (singlet vs. triplet). From the perspective of device optimization, a longer exciton diffusion length is beneficial for improving η_P in OPVs. A more detailed discussion on the role exciton diffusion length in photoconversion is provided in Chapter 3.

2.3 Charge Transport in Organic Semiconductors

In order for charge transport to occur, overlap of electron wavefunctions between the two sites is required. There are two extreme types of charge transport phenomenon: band-like transport and hopping transport, depending on the degree of wavefunction overlap.

2.3.1 Band-like Transport

Band-like transport is first developed to describe the charge transport phenomenon in crystalline inorganic semiconductors. Inorganic semiconductors commonly have a well-defined crystal structure and periodic electronic potential. This leads to a broad energy band in which carriers have small effective mass. In this scenario, charge carriers travel as a highly delocalized plane wave in a broad carrier band with a mean free path expanding over several times the molecular separation. Band-like transport can also be observed in a few crystalline organic semiconductors like acenes.[71-72]

2.3.2 Hopping Transport

Most organic semiconductors have weak Van der Waals type intermolecular interactions and are amorphous or polycrystalline in nature, complicating the observation of band-like transport. The charge transport mechanism in disordered organic semiconductors is described by a hopping mechanism. The probability of hopping from site *i* to site *j* can be described by the Mott's variable range hopping model:[73]

$$\nu_{ij} = \begin{cases} \nu_0 \exp\left(-2\alpha R_{ij} - \dfrac{E_{ij}}{2k_B T}\right), & E_{ij} > 0 \\ \nu_0 \exp\left(-2\alpha R_{ij}\right), & E_{ij} < 0 \end{cases} \qquad \text{Equation 2.6}$$

where α is a measure of the effective wavefunction overlap between two sites, R_{ij} is the hopping distance, k_B is the Boltzmann constant, T is the temperature and E_{ij} is the energy difference between two sites.

As shown in Equation 2.6, the hopping probability strongly depends on the hopping distance and wavefunction overlap. Most organic semiconductor molecules are highly anisotropic in structure, thus carrier hopping from one molecule to the next will be strongly impacted by the relative orientation and alignment of the two molecules. Specifically, the overlap between charge transport relevant HOMO and LUMO energy levels (π and π^* orbitals) needs to be optimized for enhanced charge carrier mobility. There have been a number of approaches to evaluate the π orbital overlap in literature and one effective approach is to evaluate the transfer integrals between two molecules using density functional theory. Experimentally, direct control of the π orbital overlap can be achieved by engineering the steric effect of functional group on the molecular back-bone. For example, tetracene single crystals have a hole mobility of <1 $cm^2V^{-1}s^{-1}$ while rubrene is a remarkable improvement from tetracene, achieving mobility of 20 $cm^2V^{-1}s^{-1}$.[74-77] Even though the pendant phenyl groups in rubrene do not contribute to π-conjugation, they help the tetracene backbone to stack in a way to maximize the transfer integral.

Note that the hopping probability also depends on the energy difference between two sites. This is another limiting factor of carrier mobility in organic semiconductors. The amorphous nature of organic semiconductor thin films leads to a large degree of electronic disorder.[78] As shown in Figure 2.9, a large degree of disorder will lead to a broadened

density of states (DOS) profile. Mott's variable range hopping model suggests that hopping towards a close lower-energy-state will be favored over hopping to a distant higher-energy-state. As a result, the charge carriers will typically hop between available lower energy states as depicted in Figure 2.9. Disordered materials thus have a lower mobility compared to crystalline materials due to a higher probability of trapping charge carriers in the lower energy tail states of the DOS. In some cases, the disorder in electronic structure can be aggravated by the dipole moment within the molecule, as it further disrupts the electronic environment, creating more trap states that impair charge transport.[78-79]

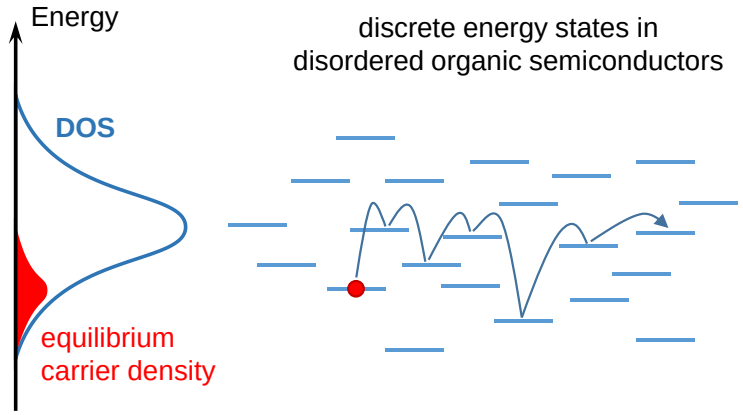

Figure 2.9 Electrons hopping through a series of dicrete energy states in disordered organic semiconductors.

Efforts towards enhancing the charge carrier mobility in organic semiconductors are twofold: engineering thin film crystallinity to reduce disorder and aligning the π-π stacking direction with the flow of charge carriers. Experimentally, they can be realized through solvent or thermal annealing of the organic thin film and engineering molecular sterics.

2.4 Processing of Organic Semiconductors

Organic electronic devices typically exists as a stack of thin films with thicknesses in the range of ~10-1000 nm. The ability to form uniform and pinhole-free thin films with well-defined interfaces is critical to realizing high performance devices via high-throughput roll-to-roll manufacturing. Depending on the molecular weight of the chosen active materials, different processing techniques are required for optimized film formation. Generally, the processing techniques of organic semiconductors can be divided into two categories: solution processing and vapor processing.

2.4.1 Solution Processing

Solution processing is a very desirable processing technique for organic semiconductors. Many existing techniques like doctor blade coating and slot die coating may also be applied for the roll-to-roll fabrication of organic electronic devices. Currently, spin-coating is the most widely adopted solution processing technique on lab scale. Compared to other printing techniques, spin-coating requires very little active material to create a uniform thin film across the substrate. This is beneficial on lab scale as the synthesis of organic semiconductors are typically in small quantities. During spin-coating, a small amount of solution is dispensed on a static or rotating substrate. The substrate rotates at a speed of 500-6000 rpm until the liquid film is set.[80] Films with mixed composition can also be obtained by premixing the solution containing different molecules.

Commonly, polymeric organic semiconductors are more suitable for the spin-coating technique compared to most small molecule organic semiconductors due to higher viscosity.

In order to overcome this bottleneck, alky chains are commonly added to the end group of small molecule organic semiconductors to help increase the viscosity of solution for better film formation.[38] Aside from the viscosity of solution, spin speed, ventilation of the film during spin-coating, wettability of the substrate and the choice of solvent will also impact the film quality greatly.[80] The major limitation of spin-coating technique is the challenge of selecting orthogonal solvents to avoid intermixing of sequentially deposited layers.

2.4.2 Vapor Deposition

Another widely used processing technique for organic semiconductors is vapor deposition. During the vapor deposition process, organic materials are heated (~150 ℃ for lighter molecules and up to 400 ℃ for molecules with larger molecular weight) in a vacuum chamber with a pressure $<10^{-6}$ Torr as shown in Figure 2.10. Most small molecule organic semiconductor will undergo solid-vapor phase transition and sublime under these conditions. The necessity of high vacuum is twofold: first of all, a high vacuum environment can help reduce the degradation of organic semiconductor materials at the deposition temperature. Secondly, a high vacuum environment increases the mean free path of organic molecules in vapor phase. This technique is only viable for small molecule organic semiconductors as the cohesive energy of polymers is typically larger than the covalent bond energy. Polymers will decompose into oligomers before sublimation.

The most significant advantage of the vapor deposition process is the capability of controlling compositional profile throughout the film thickness. For a common vapor deposition chamber, multiple sources with different materials can be operated at the same time. The instantaneous film composition can be tuned by monitoring and controlling the

sublimation rate of each component individually, with the help of multiple quartz crystal microbalances (QCMs).

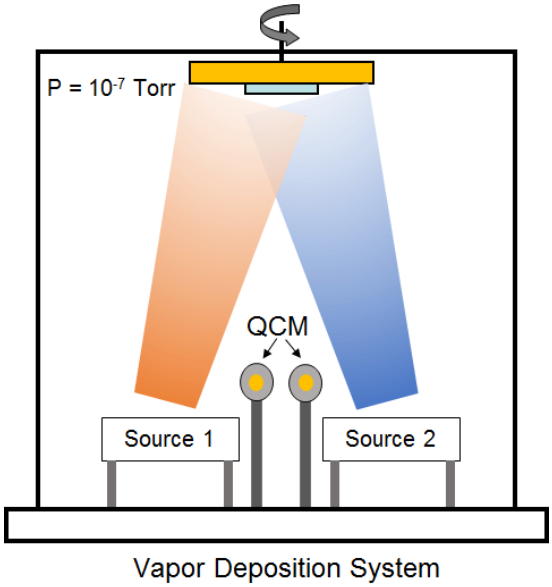

Figure 2.10 Vapor deposition process in a large vacuum chamber with two sources operating simultaneously.

2.4.3 Purification of Organic Semiconductors

Organic semiconductor materials used for research purposes are typically purchased from chemical suppliers or synthesized by individual chemists. Multi-step chemical reaction is commonly required to synthesize the target molecule. The yield of target product may be low and the desired species is often mixed with a number of impurities. These impurities include unreacted starting material, molecules formed by side reaction or decomposition and solvents used in the process. The purity of synthesized organic semiconductor material is often <95% and there is significant amount of impurities mixed with the desired molecule.[81] The existence of impurities can cause degradation or decomposition of the desired molecule during storage and shorten the lifetime of the

fabricated device.[81] More importantly, impurities can quench excitons or trap charges even at very low concentration, which will significantly impact the photoconversion process and charge transport behavior in organic electronic devices.[82-83] It is thus necessary to purify the materials before use. Typical purification methods include liquid-phase chromatography and vapor-phase sublimation. For polymer materials, only liquid-phase chromatography is viable as polymers will decompose before sublimation. Small molecules, on the other hand, are more convenient to purify as they are compatible with both techniques.

Liquid-phase Chromatography

In the simplest incarnation of liquid-phase chromatography, a mixture of materials (i.e. the synthesized products from a multi-step low-yield reaction) are dissolved in solvent and passed through a column filled with absorbent material. Based on the relative polarity difference between the absorbent material and each of the component in the mixture, separation between different components can be realized as the mixture flows through the column. As each component is eluted at different time, target molecules can be collected separately from the impurities. To purify polymers, a special type of column packed with porous absorbent is used to separate products by molecular weight.

Vapor-phase Sublimation

Another method for purifying small molecule organic semiconductors is vapor phase sublimation. The most widely used technique of vapor-phase sublimation is called temperature gradient train sublimation.[84]

In a train sublimation, a boat filled with unpurified material is loaded into the closed

end of a tube as shown in Figure 2.11. The other end of the tube is connected to a vacuum pump. When the pressure reaches $<10^{-6}$ Torr, a temperature gradient is applied along the tube. Typically, the temperature is ~300 ℃ (high enough to allow sublimation of target molecule) at the location of the unpurified material and gradually decreases along the tube, with the other end of the tube at room temperature. Based on the molecular weight, different components will deposit at different positions along the tube where the temperatures are different. Thus, a geometrical separation of target molecule from impurities can be realized. Heavy impurities will deposit closer to or remain in the boat while light impurities will deposit further down the tube. The middle section is where the desired molecule will deposit as shown in Figure 2.11.

A better separation between desired molecule and impurities can be achieved by carefully tuning the temperature gradient applied to the purification tube. To achieve a desirable purity, multiple train sublimation process can be used sequentially.[85]

In practice, liquid-phase chromatography is applied as the first purification step and vapor-phase sublimation is applied consecutively to further improve the purity of organic semiconductors as it can help eliminate solvent residues.

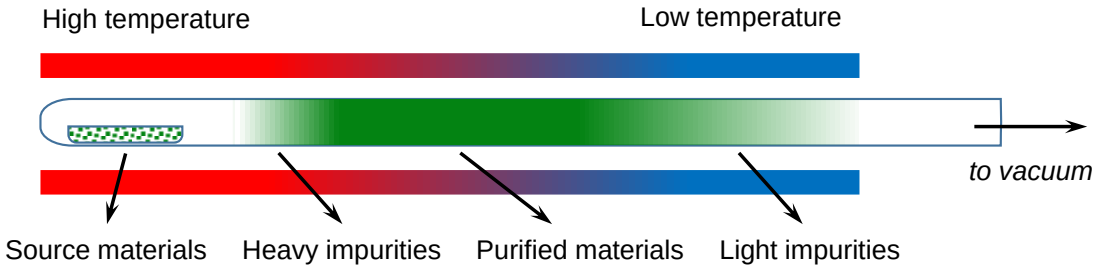

Figure 2.11 Schematic of a temperature gradient train sublimation system in operation.

3. Working Principles of Organic Photovoltaic Cells

3.1 Introduction

In its simplest incarnation, OPVs comprise an active layer of organic semiconductor sandwiched between two electrodes. The organic active layer absorbs light and the electrodes collect photogenerated charge carriers. For optimized absorption of sunlight, organic semiconductors of choice typically have a bandgap energy of 1~2 eV. More detailed photoconversion process will be discussed based on device architectures.

3.2 Schottky Junction Cells

The photovoltaic effect was first demonstrated in many organic dyes in the 1960s. The first device architecture used for OPV comprised of a single layer of organic active material sandwiched between two electrodes as shown in Figure 3.1. However, the η_P for this type of architecture was <<1%. The major limiting factor of efficiency is the inability to dissociate tightly bind excitons with built-in electric field. Recently, Zhang et al. demonstrated that by using C_{60} as the active material and employing a high work function

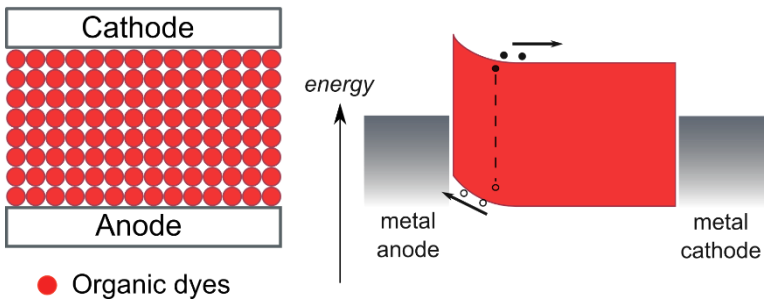

Figure 3.1 Schematic of a Shottcky OPV comprising an organic active layer sandwiched between two electrodes. The generation of photocurrent is driven by the built-in electic field.

anode, the efficiency of Schottky OPVs can be increased up to ~0.5%. However, the oversimplified Schottky OPV remains an inefficient route to harvest solar energy.

3.3 Heterojunction Cells

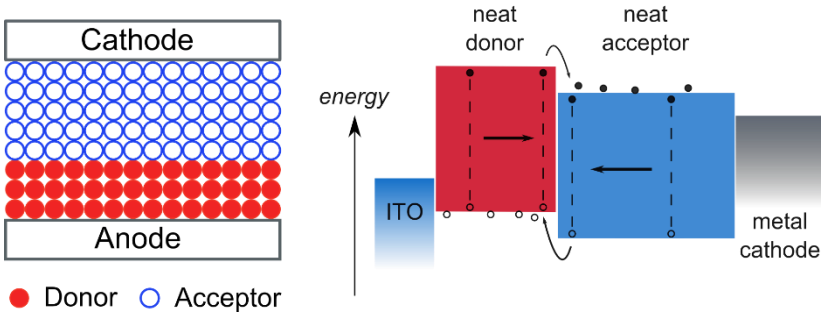

Figure 3.2 Schematic of a planar heterojunction OPV with a bilayer structure of donor and acceptor. The dissociation of excitons is facilitated by the energy level offset at the donor-acceptor interface.

In 1986, Tang introduced a bilayer device architecture which consisted of a heterojunction between two materials referred to as the electron donor and electron acceptor. This architecture is known as a planar heterojunction (PHJ) OPV (Figure 3.2). The electron donor has shallower HOMO and LUMO energy levels compared to those of the acceptor. Due to this favorable energy offset at the donor-acceptor (D-A) interface, the dissociation of excitons now becomes exothermic and more efficient.[25, 86]

The choice of electrode is also important for improving device performance. Indium-tin-oxide (ITO) is the most widely used anode material for its high electrical conductivity, good transparency in the solar spectrum and ideal work function for hole collection (4.8~5 eV).[87] However, due to the growing scarcity of indium, there has been effort to replace ITO with materials like aluminum-zinc-oxide (AZO), F:SnO_2 (FTO) or silver nanowires that

have comparable transparency and conductivity.[20-21, 88-89] The cathode typically consists of metals like Al and Ag. In situations where a lower work function cathode is desired, a thin layer of Ca or Mg is deposited first on the organic layer and then capped with Al or Ag.[90]

3.4 Device Operation

When light is incident on a PHJ OPV, molecular excited states known as excitons are created in donor or acceptor layer. The exciton is essentially a tightly bound electron-hole pair which diffuses towards the D-A interface. At this D-A interface, the energy offset is larger than the exciton binding energy, allowing the exciton to be dissociated by a charge transfer process, forming a charge transfer state with a hole in the donor material and an electron in the acceptor material. The charge transfer state is dissociated by the built-in electric field, and the now separated charge carriers are collected at their respective electrodes. Typically, the choice of acceptor is limited to several fullerene (C_{60}, C_{70}) or perylene derivatives. For the donor materials, molecules like phthalocyanine derivatives, thiophene oligomers, merocyanines and acenes have been widely studied. As shown in

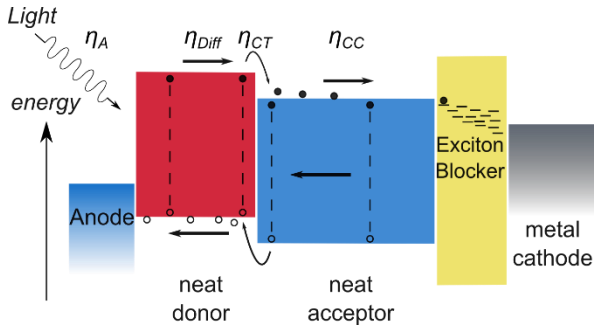

Figure 3.3 The four steps of photoconversion in an OPV: 1. Light absorption (η_A), 2. exciton diffusion (η_{Diff}), 3. charge trasfer (η_{CT}) and 4. charge collection (η_{CC}).

Figure 3.3, A wide-bandgap exciton blocking layer is often inserted between the organic active material and the metal cathode to prevent damage to the organic material during metal deposition and exciton quenching at the metal-organic interface.[91]

3.5 Advanced Device Architectures

As previously discussed, excitons must diffuse towards the D-A interface in order to be efficiently dissociated into charge carriers. However, the diffusion length of exciton (L_D) in OPVs is ~10 nm, much shorter than the optical absorption length (~100 nm).[25-26] Thus, the bottleneck of photoconversion in a PHJ OPV is the exciton diffusion process. Advanced device architectures are being developed to help address the exciton diffusion bottleneck.

Bulk Heterojunction Cells

Instead of adopting the PHJ architecture, the organic active layer can also be fabricated by co-depositing the donor and acceptor material or casting a solution of premixed donor and acceptor material. This is known as a bulk heterojunction (BHJ) architecture where the D-A interface area is significantly increased.[27-28, 92-93] With the use of this architecture, ~100% of the excitons generated can be dissociated into charge carriers and contribute to photocurrent.[94] In most cases, a certain degree of phase separation is required to maintain a continuous pathway for charge carriers to reach their respective electrodes as shown in Figure 3.4a, which can be achieved by using a thermal or solvent annealing process.[95-96] The BHJ is currently the most widely adopted OPV device architecture.

Planar-mixed Heterojunction Cells

By moving from a PHJ architecture to a BHJ architecture, there no longer exists an energy barrier to prevent electron leakage to the anode or hole leakage to the cathode when device is under forward bias. The lack of rectification will cause a reduction in device operating voltage.[163, 208] To address this problem, planar layers can be added to form a planar-mixed heterojunction (PMHJ) architecture where neat layers of donor and acceptor material are placed at the two sides of the mixed layer, as shown in Figure 3.4b. The existence of additional planar layers can help improve the rectification, contribute to photocurrent and collect charges from the mixed active layer.[97]

Ordered Bulk Heterojunction Cells

Ideally, to balance the need for large D-A interface area and continuous charge carrier pathway, an ordered bi-continuous interpenetrating morphology is preferred. The desired features will have a width of ~10 nm to facilitate exciton diffusion and a height of ~100 nm to absorbed most of the light, as shown in Figure 3.4c. The ordered bulk heterojunction architecture can be realized by engineering the spontaneous phase separation of block copolymers or by growing ordered structure of the donor material and infiltrating with the acceptor material.[98-100]

Tandem Cells

The Shockley-Queisser limit dictates that multi-junction tandem architectures can achieve higher η_P than single-junction architectures due to a more efficient harvesting of photon energy.[6] Tandem OPVs are fabricated by stacking sub-cells that contain material with different bandgap energy. This helps realizing compensating absorption of the solar

spectrum as shown in Figure 3.4d.

The facile formation of interfaces via vapor-deposition allows the tandem architecture to be fabricated conveniently using small molecule materials. Electrically, the sub-cells can either be connected in series or in parallel.[89, 101-102] When the sub-cells are connected in series, the photocurrent flow through each of the cell needs to be matched or additional recombination loss of photogenerated charge carriers will occur. It is thus necessary to engineer the light field intensity in each of the sub-cell for balanced photocurrent. When the sub-cells are connected in parallel, the current matching criterion need not be satisfied. However, the tandem OPV will operate at an intermediate voltage between that of each individual sub-cell. Thus, there will be additional loss of photon energy if the sub-cells have drastically different output voltage.

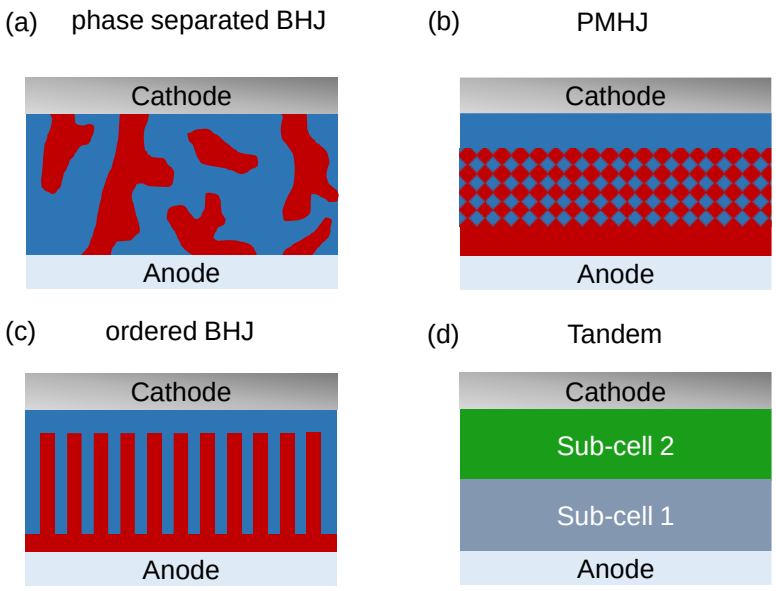

Figure 3.4 Device architectures for (a) phase separated BHJ OPVs, (b) planar mixed heterojunction OPVs, (c) ordered BHJ OPVs and (d) tandem OPVs.

3.6 Device Characterization

3.6.1 Power Conversion Efficiency (η_P)

The most important figure of merit for OPVs is the η_P. Typically, OPVs are tested under AM 1.5G simulated solar illumination (100 mW/cm^2) in ambient environment. Figure 3.5 demonstrates typical current density-voltage characteristics of an OPV under illumination. The η_P depends on short-circuit current (J_{SC}), open-circuit voltage (V_{OC}) and fill factor (FF) as shown in Equation 3.1. The FF is defined as the ratio between the maximum power obtained from the cell and the theoretical maximum power attainable ($J_{SC} \times V_{OC}$) by Equation 3.2. The FF reflects the loss of charge carriers during the charge collection process in an OPV. Improved charge collection leads to higher FF and vice versa.

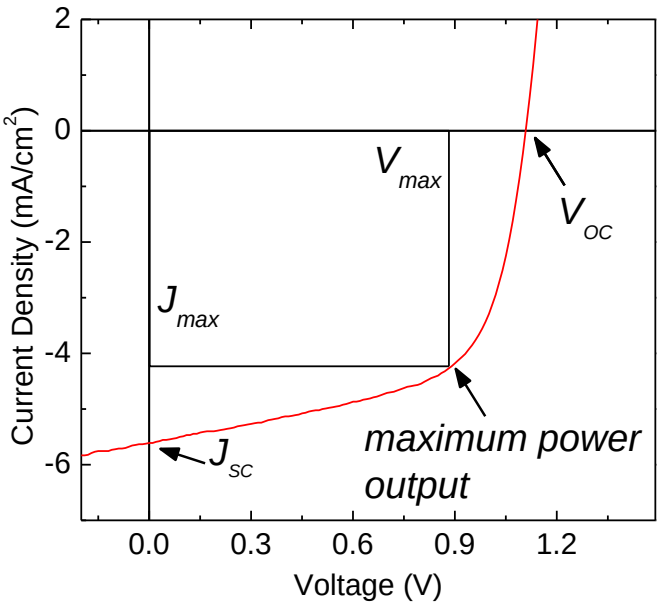

Figure 3.5 An example current density-voltage characteristics plot for an OPV under illumination. Critical parameters are denoted in the plot.

$$\eta_p = \frac{J_{SC} V_{OC} FF}{P_{optical}} \times 100\% \qquad \text{Equation 3.1}$$

$$FF = \frac{(JV)_{\max}}{J_{sc} V_{oc}} \qquad \text{Equation 3.2}$$

For state of the art single-junction OPVs, J_{SC} typically takes a value of 12~16 mA/cm^2, V_{OC} ranges between 0.8~1 V and FF is typically >0.65. To date, η_P >9% has been demonstrated using multiple platforms.[33, 39, 41-42, 47-48, 51]

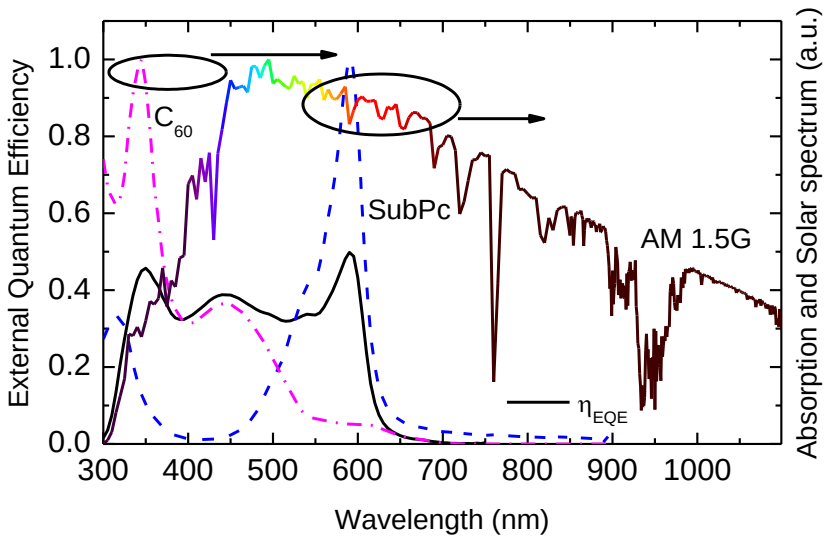

Figure 3.6 Plot of the AM 1.5G solar spectrum. Also shown are the absorption spectra of C_{60} and boron subphthalocyanine chloride (SubPc) together with an example η_{EQE} spectrum for an OPV fabricated with SubPc and C_{60}.

3.6.2 External Quantum Efficiency (η_{EQE})

The generation of charge carriers involves four steps, each with its own efficiency η, absorption of incident light to create an exciton (η_A), exciton diffusion to D-A interface (η_{Diff}), charge transfer at D-A interface (η_{CT}), and subsequently charge collection at the

respective electrode (η_{CC}). The η_{EQE} is given by:

$$\eta_{EQE} = \eta_A \eta_{Diff} \eta_{CT} \eta_{CC} \qquad \text{Equation 3.3}$$

The η_{EQE} is a measurement of the OPV spectral response and is defined as the percentage of incident photons converted into charge carriers collected at the electrodes as shown in Figure 3.6. Experimentally, the device is illuminated with monochromatic light and the output photocurrent is measured using a lock-in technique to reject the interference from the dark current. The η_{EQE} is calculated by normalizing the photocurrent to the incident optical power at each wavelength. It can also be integrated with the solar spectrum to calculate J_{SC}:

$$J_{SC} = \frac{q}{hc} \int \frac{\eta_{EQE} P_\lambda}{1/\lambda} d\lambda \qquad \text{Equation 3.4}$$

where λ is the wavelength, h is the Planck's constant, c is the speed of light, q is the elementary charge and P_λ is the solar spectrum.

3.6.3 Charge Collection Efficiency

The charge collection efficiency (η_{CC}) is used to characterize the loss of charges during transport. It is defined as the ratio between charge carriers collected at the electrode and the total number of photogenerated charge carriers in the device. By rearranging Equation 3.3, η_{CC} is given by:

$$\eta_{CC} = \frac{\eta_{EQE}}{\eta_A \eta_{Diff} \eta_{CT}} \qquad \text{Equation 3.5}$$

In BHJ OPVs, both η_{Diff} and η_{CT} can be approximated as unity, thus η_{CC} can be

approximated as:

$$\eta_{CC} = \frac{\eta_{EQE}}{\eta_A} \qquad \text{Equation 3.6}$$

The η_{CC} is strongly dependent on the bias voltage. When the device is biased with a large negative voltage, photogenerated charge carriers will be quickly extracted out of the organic active layer before recombination and the η_{CC} will approach unity. This will lead to a saturation of η_{EQE} at reverse bias, and the saturation value can be approximated as the η_A. This allows η_{CC} to be solved using Equation 3.6 at given bias.[103-104] Experimentally, the η_{CC} is <0.7 at the maximum power output point even in most efficient devices and is thus a major efficiency limiting factor.[103] The limited η_{CC} is due to both geminate and non-geminate recombination losses of charge carriers, and the detailed mechanism will be discussed later in Section 3.7.3.[105]

3.6.4 Impedance Spectroscopy

Impedance spectroscopy is another useful technique used to characterize not only the dynamic charge generation-recombination process but also equilibrium electrostatic interaction in OPVs.[106-111] For a typical impedance spectroscopy measurement, a small magnitude of AC voltage signal (~ 20 mV) is applied to the OPV on top of a constant DC bias voltage and the phase and magnitude of the resulting current is recorded to calculate the complex impedance. By sweeping the frequency of the applied AC voltage signal, the dependence of complex impedance on frequency can be obtained. Commonly, a detailed equivalent circuit model consisting of multiple capacitors and resistors is needed to analyze

the impedance spectroscopy data. The capacitance extracted from the model can be used to estimate the built-in potential of the Schottky junction by using the Mott-Schottky analysis given by:

$$C^{-2}=(2/q\varepsilon N)(V_{bi}-V), \quad \text{Equation 3.7}$$

where C is the capacitance, q is the elementary charge, ε is the permittivity of the organic layer, N is the effective doping density, V_{bi} is the built-in potential and V is the applied voltage. The impedance spectroscopy can also shed light on charge carrier transport and recombination rate constant by extracting RC products from the equivalent circuit model. This technique has proven its usefulness in understanding the charge extraction mechanism in OPVs.[107]

3.7 Modeling Device Photocurrent

3.7.1 Optical Modeling

OPVs commonly utilize a reflective metal electrode and a semitransparent oxide electrode. When light is incident through the transparent oxide electrode side, the reflected light will interfere with incident light and create a standing wave with nodes and anti-nodes. The spacing between nodes and anti-nodes is typically 100~200 nm, comparable to the active layer thickness of OPVs.[25, 112] It is thus important to model the light field in OPVs and carefully position the absorptive material in the light field to maximize photon absorption.

The most widely used method for modeling the light field is the transfer matrix model developed by Pettersson et al.[112] For a stack of isotropic and homogenous thin films with

parallel plane interfaces, its interaction with light can be described using a series of 2×2 matrices termed the system transfer matrix (S). The system transfer matrix is built upon the refractive index and extinction coefficient of each layer in the stratified structure to account for both the reflection at the interface and transmission within each layer. The incident light and the transmission light at the two boundaries of the stratified structure is then given by:

$$\begin{bmatrix} E_0^+ \\ E_0^- \end{bmatrix} = S \begin{bmatrix} E_{m+1}^+ \\ E_{m+1}^- \end{bmatrix} \qquad \text{Equation 3.8}$$

The superscript denotes the propagation direction of the light and the subscript denotes the index of the layer. With the input of proper boundary conditions, the light intensity profile at given position in the stratified structure can be solved by adjusting the system transfer matrix. By multiplying the light field intensity with the solar spectrum and the extinction coefficient of the organic active layer, the exciton generation profile and eventually the J_{SC} can be calculated with great accuracy.

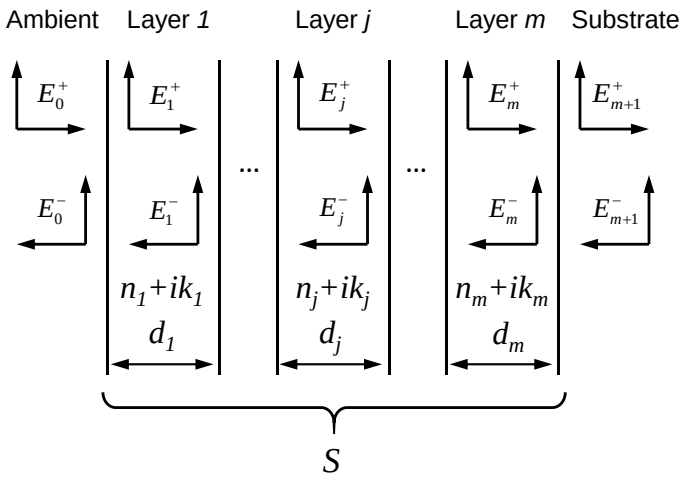

Figure 3.7 A general multi-layer structure containing *m* layers between semi-infinite ambient and substrate. Each layer has a thickness *d* and a complex index of refraction (*n*+*ik*). The optical electric field in layer *j* is characterized by two components, E_j^+ and E_j^-, propagating in opposite directions.

3.7.2 Electrical Modeling

Shockley Equation

The Shockley equation was initially developed to model the current density-voltage characteristics in inorganic homojunction diodes and has now become a widely adopted approach to model the device operation of OPV. The equation is given by: [113]

$$J = \frac{R_P}{R_S + R_P}\left\{ J_S[\exp\left(\frac{q(V - JR_S)}{nk_BT}\right) - 1] + \frac{V}{R_P} - J_{ph} \right\} \qquad \text{Equation 3.9}$$

where R_s and R_p are the series and shunt resistance respectively, n is the ideality factor, J is the total current density, J_s is the reverse saturation current density and J_{ph} is the photocurrent density. By rearranging Equation 3.9, V_{OC} can be approximated as:

$$V_{OC} \approx \frac{nk_BT}{q}\ln(\frac{J_{ph}(V_{OC})}{J_S}) \qquad \text{Equation 3.10}$$

J_s is thermally activated and obeys Equation 3.11:[114]

$$J_S \approx J_0 \exp(\frac{-E_{eff}}{k_BT}) \qquad \text{Equation 3.11}$$

In this model, J_s is related to the generation of electron hole pairs at D-A interface with an activation energy equals to the effective bandgap (E_{eff}). J_0 is a temperature independent prefactor. Combining Equation 3.10 and 3.11, the expression of V_{OC} can be re-written as:

$$V_{OC} \approx E_{eff} - \frac{nk_BT}{q}\ln(\frac{J_0}{J_{ph}(V_{OC})}) \qquad \text{Equation 3.12}$$

As shown in Equation 3.12, the magnitude of V_{OC} depends on both temperature and illumination intensity. In order to compare V_{OC} across different material systems, a

common reference point is needed. This common reference point is often taken as the E_{eff} in Equation 3.12 and can be extracted from the temperature dependence of V_{OC}.[115-117] An in-depth discussion of the physical meaning of E_{eff} will be provided in Chapter 4.

Geminate and Non-geminate recombination

The charge carriers generated by exciton dissociation will either be collected at the electrode or recombine in the organic active layer. The ratio between charge carriers collected and the total number of generated charge carriers is termed η_{CC}, as described in Section 3.6.3. There are two possible mechanisms describing the recombination process of photogenerated charge carriers: geminate recombination (charges generated from the same exciton dissociation event) and non-geminate recombination (charges generated by different exciton dissociation events).[105, 118-119]

When the OPV is under reverse bias, the charge extraction is fast so that charge carriers generated by exciton dissociation have a low probability of recombining. Instead, charges generated by the same exciton dissociation event will be in close proximity and Coulombically bind to form a charge transfer (CT) state. In this scenario, the geminate recombination process is dominant.[86, 120-122] The geminate recombination mechanism can be described by Onsager-Braun theory where the dissociation rate of the charge transfer state is given as:[123]

$$k_{diss}(T,F) = \frac{3e\langle\mu\rangle}{4\pi a^3\langle\varepsilon\rangle} e^{-E_B/k_BT} J_1(2\sqrt{-2b})/\sqrt{-2b} \quad \text{with} \quad b = \frac{q^3F}{8\pi\varepsilon k_B^2T^2}. \qquad \text{Equation 3.13}$$

where the parameter k_{diss} is the polaron dissociation rate constant, $<\mu>$ and $<\varepsilon>$ are the effective mobility and dielectric constant across the D-A interface respectively, E_B is the

CT state binding energy, J_1 is the first order Bessel function, F is the electric field, a is the initial separation of the polaron-pair.

Under positive bias, the extraction of charge carriers is less efficient, leading to a build-up of charge carriers and increased non-geminate recombination.[124-128] The rate of non-geminate recombination is usually described as a Langevin type process given by:[59, 78]

$$R = \frac{q\mu}{\varepsilon} np \qquad \text{Equation 3.14}$$

where R is the rate of recombination, q is the elementary charge, μ is the mobility, ε is the dielectric constant and n, p are the electron and hole concentration respectively. An accurate model of non-geminate recombination also requires in-depth knowledge of active layer morphology and charge transport pathways.[119]

3.8 Outline of Thesis

The photon-to-electron conversion process in OPVs can be made very efficient to maximize the current output of the cell. However, η_P also depends on the V_{OC}. V_{OC} is a key figure of merit that is ultimately proportional to the overall power conversion efficiency. However, the theoretical limit and loss mechanism of V_{OC} are not well understood. These unsolved puzzles hold the key to a more thorough understanding of V_{OC} in OPVs and will help eliminate the final bottleneck for high efficiency in order to enable widespread application of this technology. Chapters 4 and 5 will discuss the upper limit of V_{OC} and its relationship to the charge transfer state energy and the work function of anode interlayer. Chapter 6 will describe the impact of a high work function anode on the photoconversion process in fullerene-rich bulk heterojunction OPVs. With a deeper understanding of device

operation, efforts on simplifying device architecture for improved charge collection without impairing V_{OC} will be described in Chapter 7. In order to further improve η_P, new molecules with engineered energy levels and a novel hybrid organic-inorganic perovskite based absorber have also been included in this thesis. These results are discussed in Chapter 8 and 9. Finally, Chapter 10 discusses the conclusions of this thesis and future research directions to realize more efficient energy harvesting from organic photovoltaic cells.

4. D-A Interfaces and Open-circuit Voltage

4.1 Background

Organic photovoltaic cells (OPVs) frequently adopt an electron donor-acceptor (D-A) heterojunction architecture to facilitate efficient exciton dissociation.[24-25] The performance of conventional planar heterojunction (PHJ) OPVs is ultimately limited by the ability of the exciton to migrate to the dissociating D-A interface as shown in Figure 4.1a. By mixing the donor and acceptor materials to create a mixed cell termed bulk heterojunction (BHJ) OPV, ~100% of the excitons can be dissociated into charge carriers as shown in Figure 4.1b.

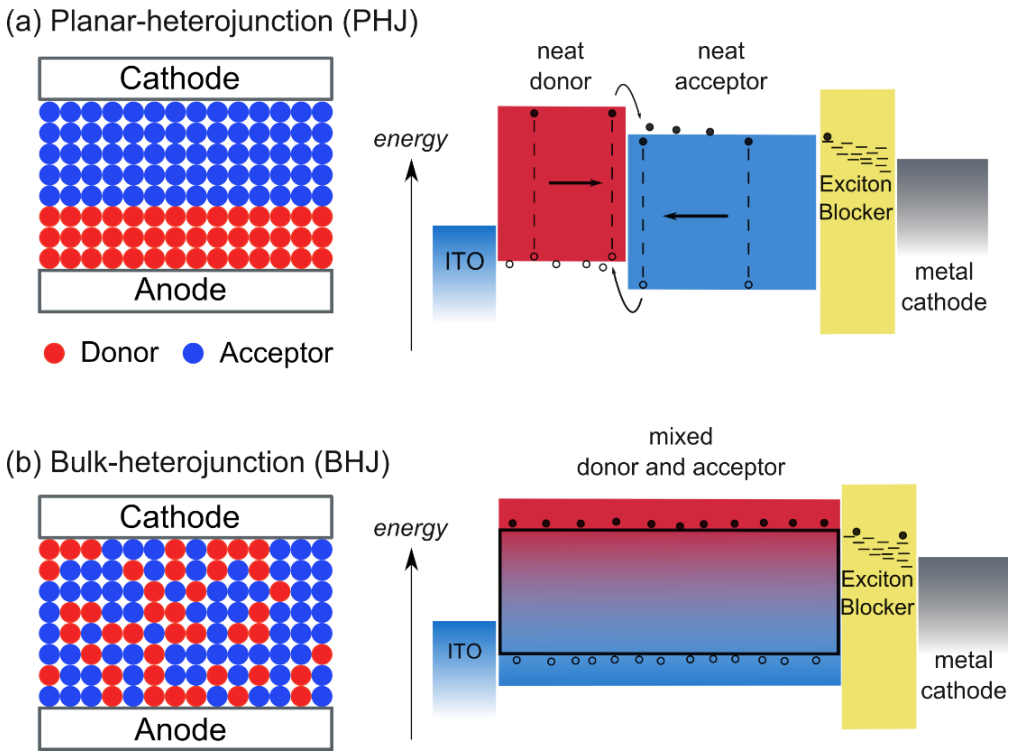

Figure 4.1 Device architectures and photoconversion processes in (a) PHJ and (b) BHJ.

In others words, the photon-to-charge conversion process can be made very efficient to maximize the current output of the cell.[94, 129-132] However, the power conversion efficiency (η_P) also depends on the voltage supplied by the cell, much like the behavior of a conventional battery. The open-circuit voltage (V_{OC}) is a key figure of merit that is ultimately proportional to the overall η_P. Currently, V_{OC} is the major source of inefficiency in converting optical power to electrical power using OPVs. A typical photon has an effective voltage of 2 V, while the OPV generally outputs only a maximum voltage of 1 V upon conversion. This inefficiency in energy harvesting is the last remaining bottleneck to high efficiency in OPVs, and remains an area of intense research, both in understanding the relevant loss mechanisms and in engineering materials and device architectures to maximize V_{OC}.

4.2 Energetic Landscape at the D-A interface

While driving exciton dissociation by charge transfer, the required energy offset at the D-A interface leads to an inherent energy loss during photoconversion. For the electron transfer process between a donor molecule and an acceptor molecule, the energy level diagram of the initial and the final state can be described by Figure 4.2. The magnitude of this energy offset directly impact the charge transfer rate as described by the Marcus theory:[133]

$$k_{CT} = \left(\frac{4\pi^3}{h^2 \lambda k_B T}\right)^{1/2} \mathbf{H}^2 \exp\left(-\frac{(\Delta G + \lambda)^2}{4\lambda k_B T}\right) \qquad \text{Equation 4.1}$$

k_{CT} is the charge transfer rate, h is the Planck's constant, k_B is the Boltzmann constant, T

is the temperature, λ is the molecular reorganization energy, **H** is the electronic coupling matrix element and ΔG is the Gibbs free energy change after charge transfer. The ΔG at a D-A interface is essentially the highest occupied molecular orbital (HOMO) or lowest unoccupied molecular orbital (LUMO) energy offset (ΔHOMO or ΔLUMO) between the donor and acceptor molecules. The lifetime of singlet excitons in most organic semiconductors is on the order of 10^{-9} s, which would require a k_{CT} of $>10^{10}$ s^{-1} for efficient exciton dissociation. Thus, a ΔHOMO or ΔLUMO of > 0.4 eV is necessary.[117]

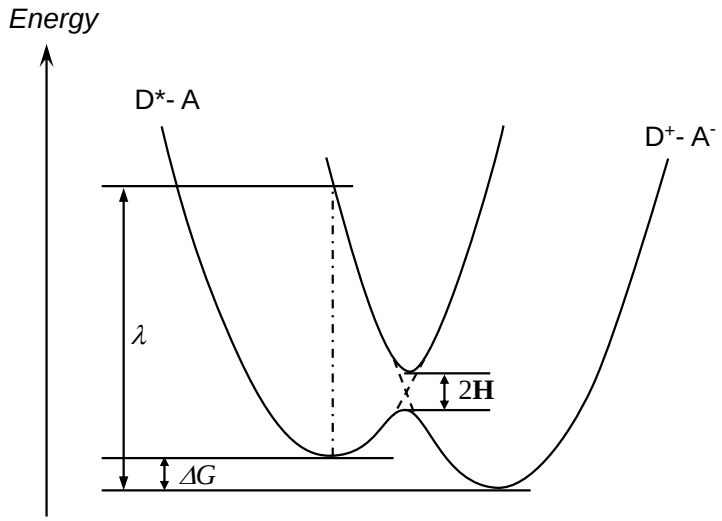

Figure 4.2 Energy diagram for an electron transfer process with the reorganization energy λ, change in Gibbs free energy ΔG and the electronic coupling matrix **H** labeled. The x-axis indicates the motion of all atomic nuclei (nuclear coordinate).

As a consequence, the D-A heterojunction architecture typically operates with a lower V_{OC} than devices that instead rely on bulk exciton ionization, as is the case in Schottky OPVs.[134-138] It is thus critical to better understand the theoretical maximum achievable V_{OC} for a particular D-A junction, and develop techniques to drive the observed V_{OC} closer to this ideal value. Previous research has demonstrated that the maximum achievable V_{OC} in

a D-A heterojunction OPV can be determined at low temperature and is related to the difference between the HOMO and LUMO energy levels of the donor and acceptor materials, respectively, termed the interface energy level offset (E_{DA}).[115-117] While these quantities are related, the observed maximum V_{OC} is smaller than E_{DA} and an exact correlation requires the inclusion of an empirical energy offset term.[117]

One possible source for this additional energy loss is the need to overcome the binding energy of the charge transfer (CT) state that forms after exciton dissociation.[139] The Coulombic attraction between the oppositely charged carriers serves as a barrier for further charge separation and reduces the CT state energy (E_{CT}) relative to E_{DA}. Recently, it has been demonstrated that in polymer-fullerene based OPVs, a direct correlation can be made between E_{CT}, as determined by fitting the sub-bandgap feature in η_{EQE} spectra, and the extrapolated V_{OC} at 0 K, termed V_0.[115]

In this chapter, small molecule based OPVs are examined as model systems to establish a relationship between CT state emission energy as measured from electroluminescence and the extracted maximum achievable V_{OC} (or V_0) for multiple D-A pairings. The CT state emission energy is chosen over the absorption energy from η_{EQE} for two reasons. First, the thermalization of the CT state is rapid so that the V_{OC} is likely impacted by the relaxed CT state.[131] Second, the broad CT state absorption feature will partially overlap with fullerene absorption features for D-A pairings with a large E_{DA}. This makes it difficult to separate the measurement of E_{CT} from photocurrent generated by the fullerene in the η_{EQE} spectra. In addition to correlating E_{CT} and V_0, we also demonstrate that the E_{CT} for a given D-A pairing can be tuned using dielectric spacer layers.

Figure 4.3 shows the energy landscape that excitons experience at the D-A interface prior to dissociation into separated charge carriers. The first step is charge transfer, during which the electron (hole) is transferred to the acceptor (donor), sacrificing part of the original exciton energy. The partially separated exciton now forms an intermediate state, namely the CT state. The CT state experiences rapid thermalization, leading to an additional loss of energy. The relaxed CT state is Coulombically bound, frustrating further separation.[140] The final dissociation of the CT state into separated charge carriers is based on an electric-field-assisted process that is well-described by the Onsager-Braun theory.[123] Within the entire photoconversion process, the CT state is the lowest energy state and thus should determine the theoretical maximum achievable V_{OC} of the OPV.

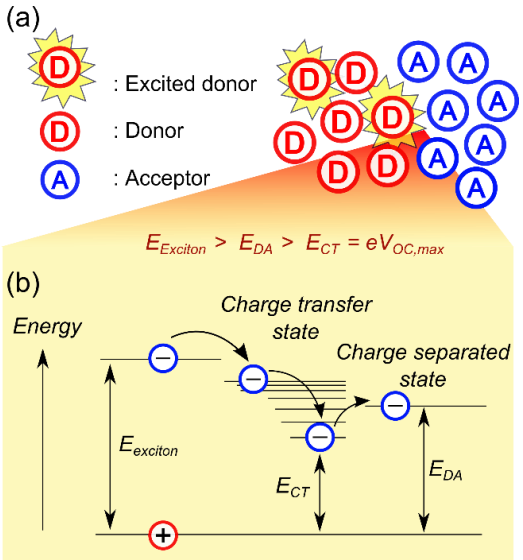

Figure 4.3 (a) The conversion of an exciton into separated charge carriers at a D-A interface. (b) Energy landscape for the process depicted in (a).

Experimentally, the theoretical maximum achievable V_{OC} is typically estimated from the temperature dependence of V_{OC}, which can be described by equation 3.12.[53, 117] In the

case of a D-A heterojunction, E_{eff} equals the CT state energy.[115] In reality, the V_{OC} is also limited by the quasi-Fermi level offset at a finite illumination intensity, and the observed V_{OC} will often deviate from the dependence of Equation 4.2 and plateau at low temperature. [53, 117, 141] Thus, the extrapolated V_{OC} at 0 K, i.e. V_0, is often chosen to approximate the theoretical maximum achievable V_{OC} and E_{eff}.[53, 115, 142]

4.3 Experimental Methods

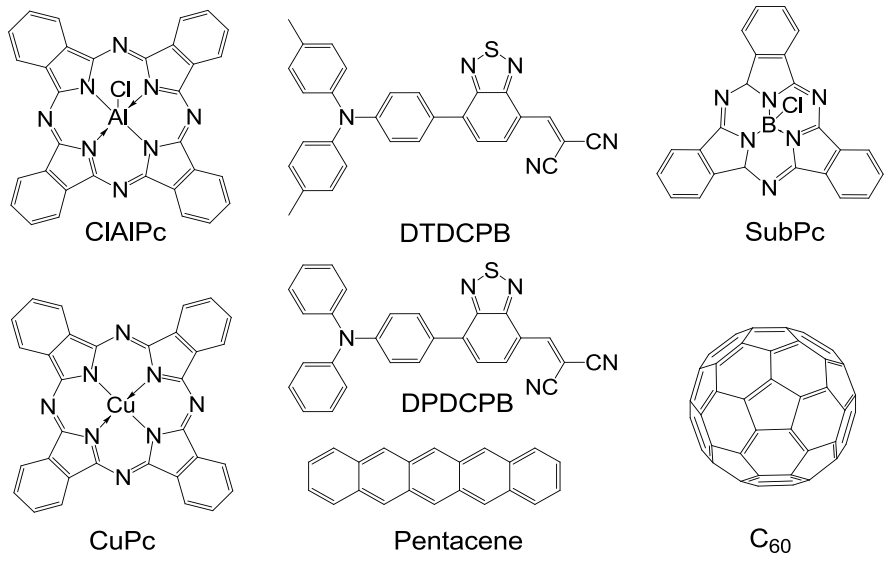

Figure 4.4 Molecular structures of materials used in this study.

A variety of different donor materials including copper phthalocyanine (CuPc), 2-[7-(4-N,N-diphenylaminophenylen-1-yl)-2,1,3-benzothiadiazol-4-yl]methylene malononitrile (DPDCPB), chloroaluminum phthalocyanine (ClAlPc), pentacene, 2-[7-(4-N,N-ditolylaminophenylen-1-yl)-2,1,3-benzothiadiazol-4-yl]methylene malononitrile (DTDCPB) and boron subphthalocyanine chloride (SubPc) with various HOMO energy levels are included in the study. C_{60} is chosen as the common acceptor material. Their molecular structures are shown in Figure 4.4.

BHJ OPVs having the structure: ITO/MoO_x 10 nm/mixed active layer 60 nm/BCP 10 nm/Al 100 nm were fabricated on pre-patterned indium-tin-oxide (ITO)-coated glass substrates having a sheet resistance of ~8-12 Ω/□, using the materials mentioned above. Substrates were cleaned in tergitol solution and in organic solvents and treated in UV-ozone ambient for 10 minutes prior to thin film deposition. All layers were deposited by high vacuum thermal evaporation at a base pressure of $<8\times10^{-7}$ Torr. For all devices, a 10-nm-thick interlayer of MoO_x was deposited at 0.05 nm/s on the ITO anode.[137] In bulk BHJ devices, mixed organic active layers were prepared via co-deposition at a total rate of 0.2 nm/s at room temperature. The inclusion of an interlayer of MoO_x ensures that the V_{OC} is not limited by the energy levels of the electrodes.[97, 104, 137, 143] A detailed discussion on the impact of MoO_x layer to the OPV operation will be provided in Chapter 5. A uniformly mixed active layer with a D:A volume ratio of 1:1 is chosen to maximize the D-A interface area and minimize the impact of exciton bulk-ionization as described in previous literature.[138, 144] All OPVs were capped with a 10-nm-thick exciton blocking layer of bathocuproine (BCP).[91] Device active areas are defined by the overlap between a 100-nm-thick Al cathode layer and a pre-patterned ITO anode, giving a device active area of 9 mm^2.

4.4 Correlating Open-circuit Voltage to D-A Interface Energetics

4.4.1 Temperature Dependence of Open-circuit Voltage and Interface Energy Offset

All temperature dependent device parameters were measured under AM1.5G simulated solar illumination (100 mW/cm^2) using an Oriel Xe solar simulator in a Janis cryogenic probe station with liquid nitrogen cooling. Device temperature was monitored

using a Si thermometer. Current density-voltage characteristics were measured using a Keithley 2400 source meter. All devices exhibit a monotonic increase in V_{OC} with decreasing temperature, as shown in Figure 4.5. The temperature dependence of V_{OC} for the D-A pairing of pentacene-C_{60} is re-plotted from Ref. 117.[117] The value of V_0 for each D-A pairing is obtained by linearly extrapolating the temperature dependence of V_{OC} to 0 K. Literature values of the energy levels for materials used in this study are listed in Table 4.1 for the calculation of E_{DA}. The literature values for the various HOMO energy levels are determined via photoelectron emission spectroscopy and the literature values for the various LUMO energy levels are determined via soft X-ray spectroscopy, inverse photoelectron emission spectroscopy or cyclic voltammetry.[66-67, 97]

A comparison between V_0 and E_{DA} for each D-A pairing is shown in Figure 4.6 and a linear relationship is found between the two parameters. However, similar to previous

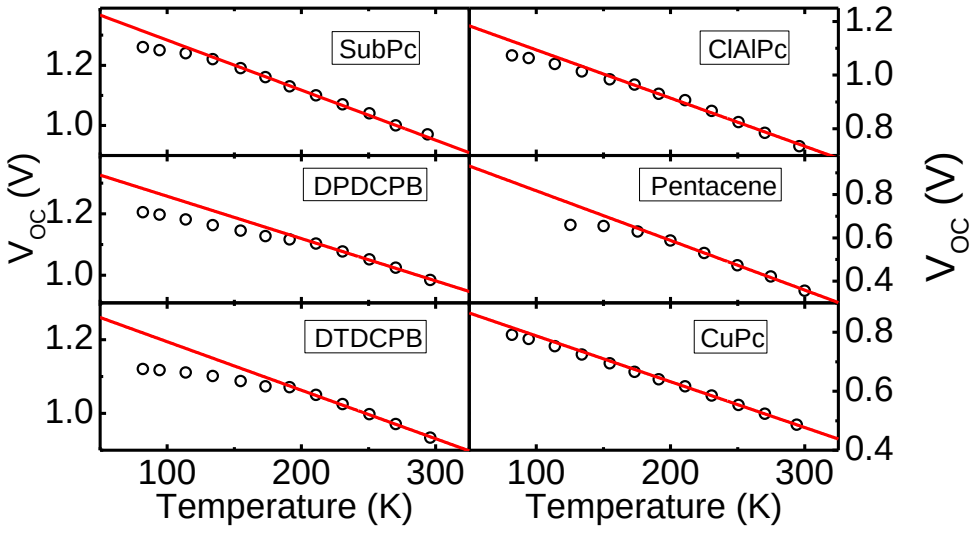

Figure 4.5 Temperature dependence of V_{OC} for BHJ OPVs (D:A ratio=1:1) based on different donor materials and C_{60}. The temperature dependence of V_{OC} for the D-A pairing of pentacene-C_{60} is re-plotted from Ref. 117.

studies, the observed linear relationship does not pass through the origin.[53, 117]

Table 4.1 Energy levels of materials studied

Material	HOMO (eV)	LUMO (eV)	E_{DA}* (eV)	Reference
SubPc	5.6	3.2	1.9	67
DPDCPB	5.5	3.4	1.8	97
DTDCPB	5.4	3.4	1.7	97
ClAlPc	5.3	3.4	1.6	67
Pentacene	5.2	3	1.5	66
CuPc	5.0	3.3	1.3	67-68
C_{60}	6.2	3.7	-	66

*Energy level offset between the HOMO level of donor material and the LUMO level of C_{60}.

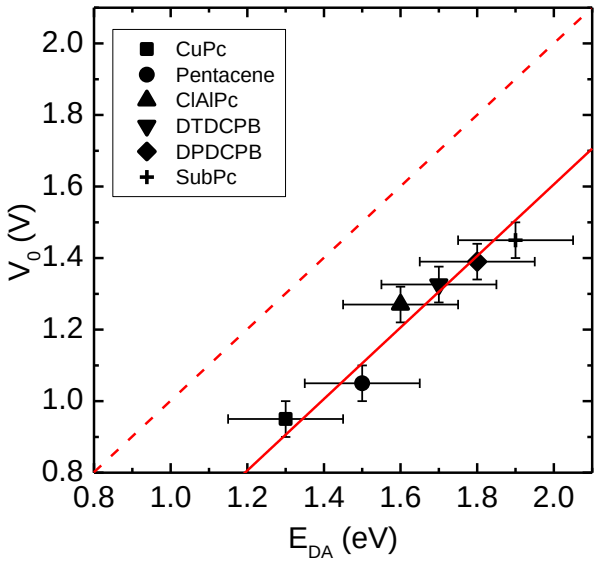

Figure 4.6 The correlation between the linearly extrapolated V_{OC} at 0 K (V_0) and E_{DA}. The solid line is fit to the data and the dash line represents perfect correlation.

4.4.2 Charge Transfer State Energy

This lack of agreement highlights the fact that E_{DA} does not simply equal E_{CT}, due chiefly to the binding energy of the CT state. In order to better correlate the theoretical maximum achievable V_{OC} and D-A interface energetics, a direct measurement of E_{CT} is necessary. Here, we use CT state electroluminescence spectroscopy to determine E_{CT}.[145-148] Under electrical excitation, CT states are formed across the D-A interface and may recombine radiatively as shown in Figure 4.7a. Electroluminescence spectra were

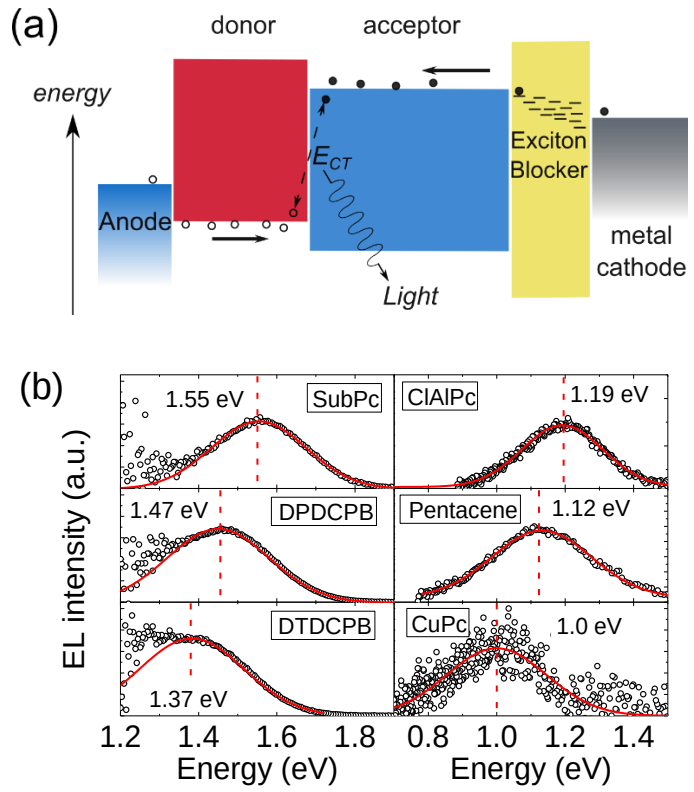

Figure 4.7 (a) The mechanism of electroluminescence from an OPV under forward bias. (b) Electroluminescence (EL) spectra for BHJs based on six different donor materials paired with an acceptor layer of C_{60} measured under a current density of ~80 mA/cm^2. Each spectrum is fit with a single Gaussian function, with the peak energy taken as the charge-transfer state energy (E_{CT}).

measured using an Ocean Optics USB4000 fiber-coupled spectrometer and a Photon Technology International Quantum Master 4 Fluorometer. In most cases, for current injection levels (~80 mA/cm^2) slightly higher than J_{SC}, only CT state electroluminescence is observed, avoiding direct exciton decay on either the donor or acceptor material. The observed CT state electroluminescence spectra are broad and located in the near-infrared region of the spectrum with a typical full-width half-maximum (FWHM) of ~0.2 eV, as shown in Figure 4.7b. Electroluminescence spectra are fit using a single Gaussian function, with the peak position taken as the value of E_{CT}.

A comparison between the extrapolated V_0 and E_{CT} for each D-A pairing is plotted in Figure 4.8, with a clear linear relationship being preserved. More importantly, the linear relationship between E_{CT} and V_0 has almost zero intercept, confirming that a stronger correlation can be made between E_{CT} and V_0, over E_{DA} and V_0.

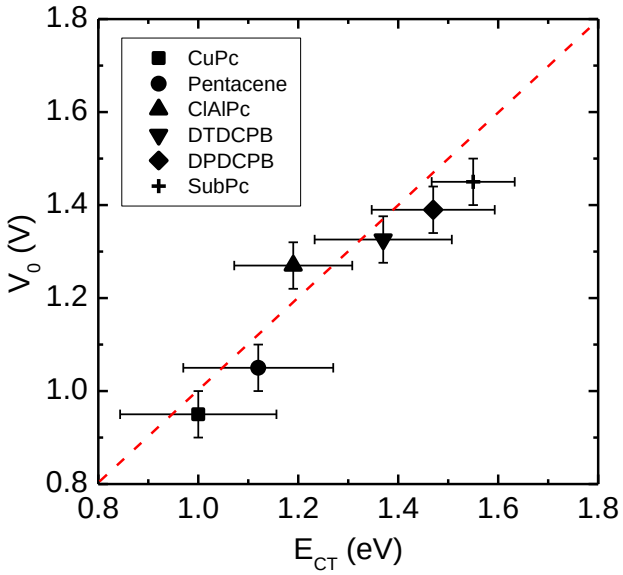

Figure 4.8 The correlation between the linearly extracted maximum achievable V_{OC}, V_0, and E_{CT}. The dash line represents perfect correlation.

4.4.3 Dielectric Engineering at the D-A Interface

In comparing the measured values for E_{DA} and E_{CT}, a fairly constant offset of ~0.36 eV is observed. In previous work, this energy shift has been ascribed to the binding energy of the CT state.[149] As a result, the V_{OC} can be improved if the binding energy of the CT state can be reduced. Previously, Campbell et al. have demonstrated that the exciton dissociation and CT recombination rates in a tetracene-C_{60} planar heterojunction (PHJ) can be tuned by inserting a wide-energy-gap spacer layer between the donor and acceptor.[150] Both the J_{SC} and η_P are enhanced with the incorporation of a 1-nm-thick spacer layer. Liu et al. have carried out a theoretical analysis for this device architecture to model the dependence of V_{OC} on the spacer layer thickness. The model calculates V_{OC} from the CT state density at the D-A interface and predicts that the V_{OC} will follow the trend of J_{SC}.[151]

Here, the focus is instead on how the presence of a spacer layer impacts the initial size of the CT state, and hence, V_{OC}. A thin spacer layer of UGH2 is inserted at the D-A interface in PHJ OPVs. UGH2 is a wide energy gap host material used in the construction of blue organic light-emitting devices, and is characterized by a deep HOMO level (7.2 eV) and a shallow LUMO level (2.8 eV).[152] Insertion of the UGH2 layer enables spatial separation between holes residing on the HOMO level of the donor material and electrons residing on the LUMO level of the acceptor material.

Planar devices based on donor layers of CuPc and ClAlPc were constructed with a spacer layer of UGH2 included at the D-A interface in order to vary the initial separation of the CT state as shown in Figure 4.9. Here, the spacer layer is found to have a deleterious effect on the J_{SC} for both devices as shown in Figure 4.10a.

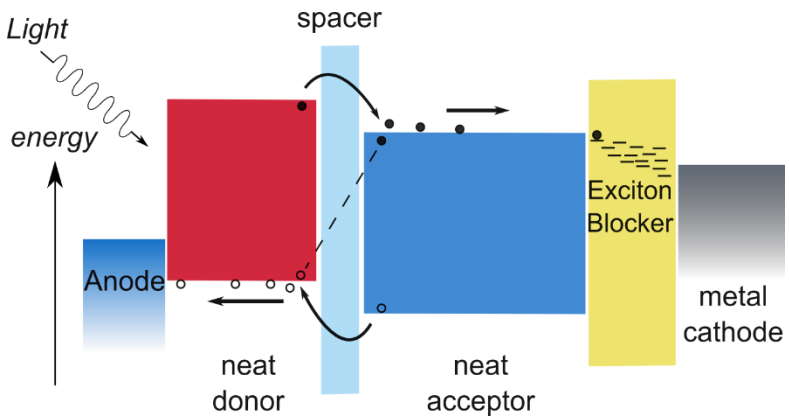

Figure 4.9 Schematic of the spacer effect on the delocalization of charge transfer state.

The incorporation of a spacer layer is also found to impact the temperature dependence of J_{SC}. Previous literatures have observed a decrease in J_{SC} with decreasing temperature.[117, 137] Interestingly, the temperature dependence of J_{SC} changes as the thickness of the spacer layer increases, as depicted in Figure 4.10b. The J_{SC} shows a plateau when cooling from

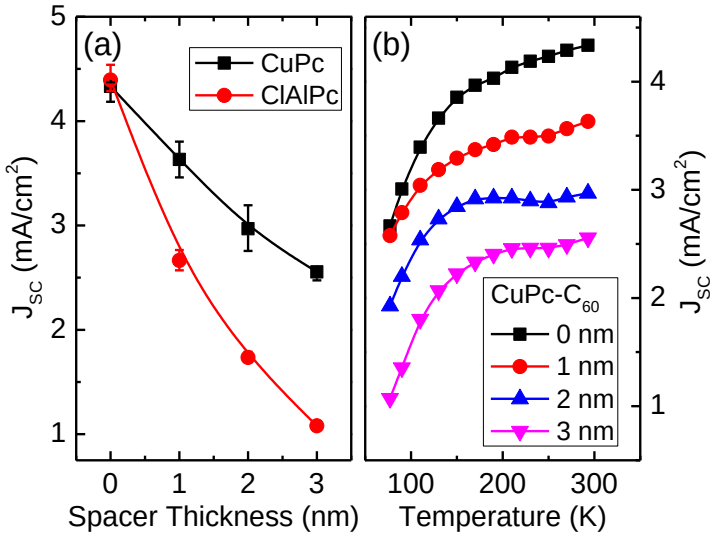

Figure 4.10 (a) Measured values of J_{SC} for planar heterojunction OPVs (ITO/CuPc 20 nm or ClAlPc 15 nm/UGH2 x nm/C_{60} 40 nm/BCP 10 nm/Al 100 nm) as a function of UGH2 spacer layer thickness. (b) Temperature dependence of J_{SC} for the D-A pairing of CuPc-C_{60} with the device architecture in (a) as a function of UGH2 spacer layer thickness.

250 K to 190 K in devices containing a UGH2 spacer layer for the D-A pairing of CuPc-C_{60}. The plateau in J_{SC} may reflect a counterbalance between increasing exciton lifetime and decreasing CT state dissociation yield at low temperature.[25, 150]

The V_{OC} is found to increase monotonically as the thickness of the UGH2 layer increases (Figure 4.11a). This is in contrast to the dependence of V_{OC} on the spacer layer thickness predicted by Liu et al.,[151] which is calculated based on CT state density obtained from a numerical device model and will thus follow the trend of J_{SC}. Experimental results indicate that the spacer layer changes not only the CT state density, but also the CT state energy. As a result, V_{OC} shows no reduction even with a 3-nm-thick spacer layer.

The CT state energy is ultimately the electric potential difference between the HOMO level of the donor material and the LUMO level of the acceptor material (E_{DA}) less the CT state binding energy. In the simplest incarnation, the CT state binding energy is the Coulombic attraction between oppositely charged carriers. This permits the relationship between E_{CT} and the spacer layer thickness to be written using a simple Coulombic attraction as:

$$E_{CT} = E_{DA} - E_b \frac{a_0}{a_0 + \frac{\varepsilon_{spacer}}{\varepsilon_{active}} d} \qquad E_b = \frac{e^2}{4\pi\varepsilon_0 \varepsilon_{active} a_0} \qquad \text{Equation 4.3}$$

where E_b and a_0 are the binding energy and initial separation of the CT state in the absence of a spacer layer, d is the thickness of the spacer layer, ε_0 is the permittivity of vacuum, ε_{active} is the relative permittivity of the active material, and ε_{spacer} is the relative permittivity of the spacer layer. Previously, the relationship has been established between E_{CT}, E_{eff} and

the theoretical maximum achievable V_{OC}. By replacing E_{eff} with the expression of E_{CT}, Equation 4.2 can be re-written as:

$$eV_{OC} = E_{DA} - nkT\ln(\frac{J_0}{J_{ph}(V_{OC})}) - E_b \frac{a_0}{a_0 + \frac{\varepsilon_{spacer}}{\varepsilon_{active}} d} \qquad \text{Equation 4.4}$$

Equation 4.4 permits a direct correlation to be made between V_{OC} and the spacer layer thickness (d), allowing the parameters a_0 and E_b to be extracted by fitting the results of Figure 4.11b. In order to reduce the number of fitting parameters, the ratio between ε_{spacer} and ε_{active} is estimated using the near-infrared refractive indices of UGH2 and the active material mixture (D:A mixing ratio=1:1).

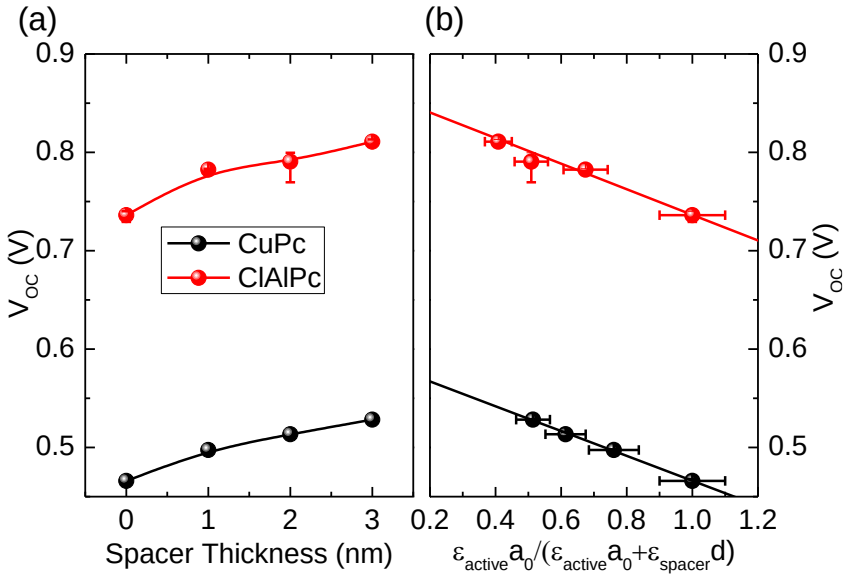

Figure 4.11 (a) Measured values of V_{OC} for planar heterojunction OPVs (ITO/CuPc 20 nm or ClAlPc 15 nm/UGH2 x nm/C_{60} 40 nm/BCP 10 nm/Al 100 nm) as a function of UGH2 spacer layer thickness. (b) Modeling the increase of E_{CT} with the incorporation of a spacer layer by fitting the spacer thickness dependence of V_{OC}.

For the D-A pairing of CuPc-C_{60}, E_b=0.17 eV and a_0=1.6 nm, while for the D-A pairing of ClAlPc-C_{60}, E_b=0.13 eV and a_0=0.96 nm. The value of ε_{active} can be separated calculated from the fitted values of E_b and a_0 using Equation 4.3. A value of ~5 is found for the D-A pairing of CuPc-C_{60} and a value of ~8 is found for ClAlPc-C_{60}. This result is similar to the dielectric constant estimated from the square of refractive index of the active material mixture in the near-infrared wavelength range (~4 for CuPc-C_{60} and ~6 for ClAlPc-C_{60}). The extracted values of a_0 suggest that the CT state is tightly bound, likely spanning two molecules.

In order to further demonstrate that the observed increase in V_{OC} comes from a change in CT state energy and not a reduction in dark-current due to the presence of the wide-gap-spacer layer, its dependence on temperature was examined further. If the variation in V_{OC} with spacer layer thickness came only from changes in the dark current, the values of V_{OC}

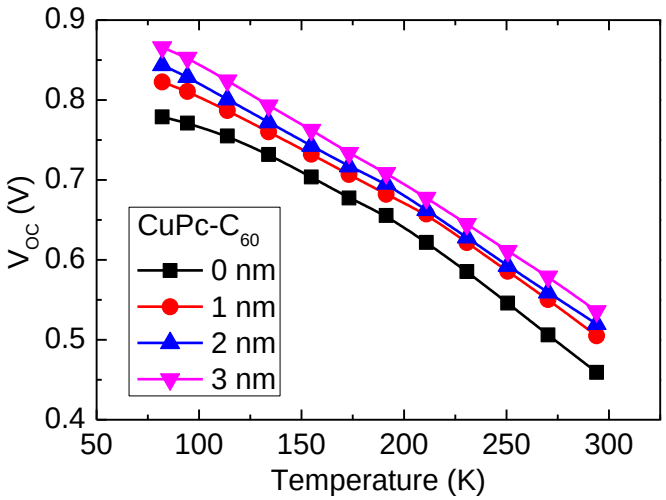

Figure 4.12 Temperature dependence of V_{OC} for the D-A pairing of CuPc-C_{60} with the device architecture in (a) as a function of UGH2 spacer layer thickness.

for the control and spacer layer devices should converge at low temperature. Figure 4.12 shows the measured V_{OC} down to a temperature of 82 K. The values of V_{OC} for devices constructed using various spacer layer thicknesses do not converge at low temperature, supporting a model where the increase in V_{OC} is related to the increase of E_{CT} and not a reduction in the dark current.

4.5 Conclusions and Summary

A direct correlation between the charge-transfer state energy as extracted from electroluminescence and the theoretical maximum achievable V_{OC} in OPVs has been demonstrated for the first time. This is in contrast to much previous work where only a partial correlation is made between E_{DA} and V_{OC}. The discrepancy between E_{CT} and E_{DA} is attributed to the binding energy of the CT state formed at the electron donor-acceptor interface. Here, the CT state binding energy is successfully modeled as a Coulombic electron-hole attraction. A wide energy gap spacer layer is used to effectively tune the size of the CT state, and also the resulting V_{OC}.

As a result, the energy level offset at the D-A interface together with the CT state binding energy are both responsible for the low V_{OC} compared to the exciton energy. In order to increase the upper limit of V_{OC} in OPVs, the energy level offset at the D-A interface need to be minimized while maintaining efficient charge transfer. Strategies to achieve donor molecules with ideal bandgap energy will be discussed with more details in Chapter 8. Another route that has long been ignored is minimizing the binding energy of the CT state which can be achieved by increasing the delocalization of the CT state or by screening

the Coulombic attraction. Previous literatures has demonstrated that the delocalization of the CT state can be increased by enhancing the crystallinity of the fullerene domain.[139, 153] Additionally, effort should also be made to engineer the dielectric constant of the donor materials by incorporating high-dielectric-constant moiety to the molecular structure.

It is also worth noticing that even though the charge transfer state energy at the D-A interface governs the theoretical maximum achievable V_{OC} in OPVs, the apparent V_{OC} is also impacted by many other factors in reality. In the next chapter, the impact of electrode-organic interface on V_{OC} will be examined.

5. Impact of Anode Interlayers on Open-circuit Voltage

5.1 Background

In Chapter 4, it was demonstrated that the maximum achievable value of the open-circuit voltage (V_{OC}) in heterojunction OPVs is strongly determined by the charge transfer state energy at the D-A interface. In reality however, the V_{OC} can also be affected by the work function of the electrode. Most highly efficient OPVs adopt anode or cathode interlayers to optimize the energy level alignment at the electrode interface for improved V_{OC} and η_P.

The impact of the electrode work function on V_{OC} is commonly explained by a metal-insulator-metal (MIM) model as shown in Figure 5.1. OPVs with a large work function difference between anode and cathode ($\Delta\phi$) will have a large built-in potential (V_{bi}). A larger forward bias is then required to reach the flat-band condition and thus the device can output a larger V_{OC}. For $\Delta\phi$ values larger than the bandgap of the organic active material, a V_{OC} plateau will exist due to the Fermi level pinning effect.[11, 40-41]

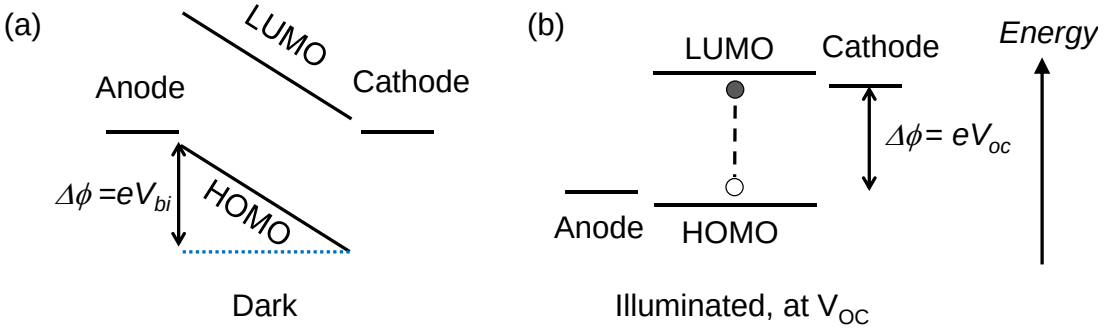

Figure 5.1 Energy level diagram of the metal-insulator-metal (MIM) model (a) in the dark at equillibrium and (b) at open-circuit condition under illumination.

According to Figure 5.1, a large $\Delta\phi$ value is favored so that the V_{OC} is not limited by the work function of the electrodes. Previous work has focused on reducing the work function of the cathode by using low work function metal, self-assembled monolayer or conjugated polyelectrolyte.[40, 154-159] For the anode, UV-ozone treatment is the most common technique for increasing the work function of ITO. UV-ozone treatment will help remove C-containing contaminants and increase the O concentration on ITO surface. Research has shown that the work function of ITO can be increased from 4.8 eV to over 5 eV with 5 minutes of UV-ozone treatment.[160] Aside from the UV-Ozone treatment, anode interlayers like poly (3,4-ethylenedioxythiophene):poly (styrenesulfonate) (PEDOT:PSS) is also widely used. PEDOT:PSS has a relatively deep work function of 5.0 eV and can also help planarize the ITO surface for better film formation of the active layer. However, there are also problems with the use of PEDOT:PSS since it may react with ITO due to its acidic nature and cause degradation of the interface. Recently, transition metal oxides like MoO_x, WO_3 and V_2O_5 have received intense study as alternate anode buffer layer materials in both planar heterojunction (PHJ) OPVs and bulk heterojunction (BHJ) OPVs. The incorporation of a 10-nm-thick layer of MoO_x in an optimized boron subphthalocyanine chloride (SubPc)-C_{60} BHJ OPV can lead to a significant increase in both V_{OC} and η_P as shown in Figure 5.2.[143, 161-166]. Photoemission spectroscopy measurements have shown the energy levels for these transitional metal oxides are much deeper than the work function of ITO. However, the mechanism for the increase in V_{OC} is not well understood and understanding the effect of interlayer on device V_{OC} is important and will serve as a guide to approaching theoretical V_{OC} limit in ambient environment.

5.2 Experimental Methods

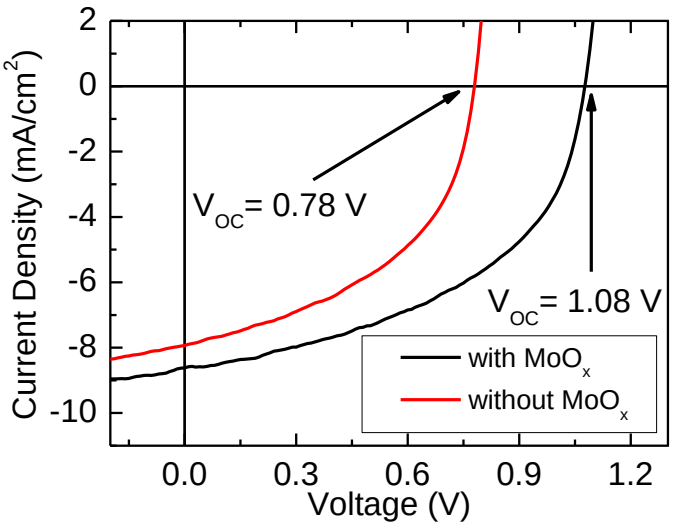

Figure 5.2 Current density-voltage characteristic shift towards higher voltage with the inclusion of a 10-nm-thick MoO_x anode interlayer in a BHJ OPV.

Many previous reports have examined the temperature dependence of V_{OC} in OPVs fabricated on an ITO anode. These studies have shown an increase in V_{OC} with decreasing temperature due to a corresponding reduction in dark current, which is caused by a reduction in electron-hole recombination at the D-A interface.[117, 167]. The increase of V_{OC} with the insertion of MoO_x interlayer is also ascribed to a reduction in dark current while impact of MoO_x interlayer on the photoconversion process has rarely been discussed.[168] Here, the role of a MoO_x interlayer in determining the maximum achievable V_{OC} in planar heterojunction OPVs is examined by characterizing the temperature dependence of V_{OC} for a variety of donor materials. The temperature dependence of V_{OC} is previously described by the modified Shockley equation (Equation 3.12).[53, 117]

The energy E_{eff} equals to the CT state energy as proved in Chapter 4. The insertion of

MoO_x should not affect E_{eff} if the photoconversion process is not influenced. In other words, the V_{OC} should converge at low temperature regardless of the existence of MoO_x interlayer for the same D-A pairing.

To test our hypothesis, OPVs were fabricated on pre-patterned indium-tin-oxide (ITO)-coated glass substrates having a sheet resistance of ~8-12 Ω/□. Substrates were cleaned in tergitol solution and in organic solvents and treated in UV-Ozone ambient for 10 minutes prior to thin film deposition. All layers were deposited by high vacuum thermal evaporation at a pressure of $<8\times10^{-7}$ Torr. Organic active layers were deposited at room temperature at a rate of 0.2 nm/s. Three different devices were examined having the following active layer structures: 13 nm SubPc/35 nm C_{60}, 15 nm chloroaluminum phthalocyanine (ClAlPc)/40 nm C_{60}, and 20 nm copper phthalocyanine (CuPc)/40 nm C_{60}. When included as an interlayer between the ITO anode and the organic active layers, a 10-nm-thick layer of MoO_x was deposited at 0.05 nm/s using a source of MoO_3. The X-ray photoemission spectroscopy was used to identify the oxidation state of Mo in as deposited film and the results are shown in Figure 5.3. The spectrum contains mostly signal from Mo^{6+} oxidation state. A small shoulder is observed in the low energy tail of the 3d 5/2 feature which indicates possible existence of lower oxidation states of Mo. For accuracy, the anode interlayer will be referred to as MoO_x instead of MoO_3. X-ray diffraction measurements showed no obvious signature of crystallinity, consistent with previous reports on films obtained using the same methods.[134, 169-172]

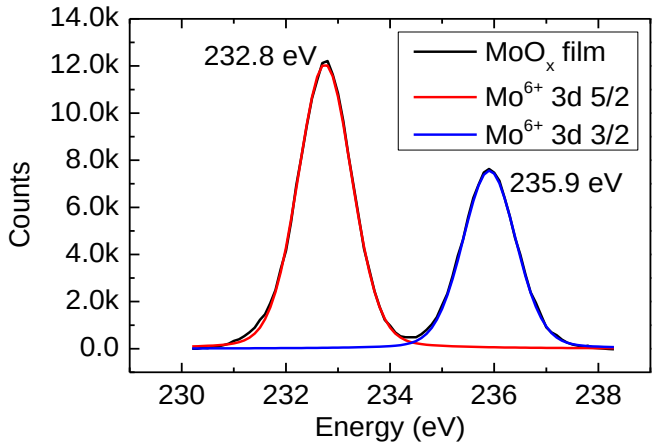

Figure 5.3 The X-ray photoelectron spectroscopy result of as deposited MoO_x thin film composed of mostly Mo^{6+}.

All OPVs were capped with a 10-nm-thick exciton blocking layer of bathocuproine (BCP). Device active areas were defined by the overlap between a 100-nm-thick Al cathode layer and a patterned ITO bottom anode, giving a device active area of 9 mm^2.

As already noted, interlayers of MoO_x have been previously used in BHJ OPVs to reduce device dark current and increase V_{OC}.[164, 166] In the SubPc-C_{60} system, this permits the use of active layers that are acceptor-rich, a configuration that without an MoO_x interlayer would lead to large electron leakage currents and low V_{OC}.[143] Here, the focus is instead on the planar heterojunction architecture where the incorporation of MoO_x is not expected to significantly reduce dark current due to existence of the rectifying D-A interface. In this way, the planar heterojunction offers a simple platform through which to examine the role of the MoO_x-donor interface in determining the maximum observable V_{OC}. The HOMO and LUMO energy levels for the materials used in this study are taken from literature values measured by photoemission spectroscopy and inverse photoelectron

spectroscopy respectively and are shown in Figure 5.4.[66-67, 173-176] The deep lying Fermi level of MoO_x and its alignment with a variety of organic semiconductors has been previously reported to enhance hole injection from the ITO anode.[177-178]

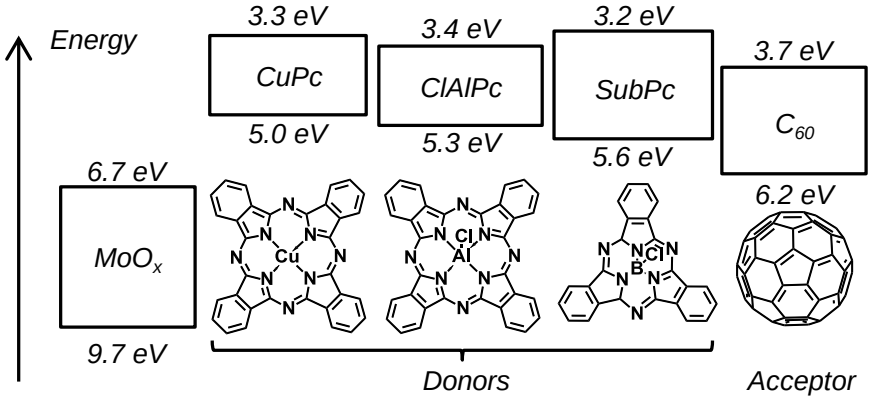

Figure 5.4 Energy levels and molecular structures for the materials used in this study.

5.3 Temperature-dependent Measurements of Device Performance

5.3.1 Temperature-dependent Open-circuit Voltage in PHJ OPVs

The role of MoO_x in determining the maximum achievable V_{OC} was assessed by characterizing planar heterojunction OPVs as a function of temperature. The temperature dependent experiments were carried out in a Janis cryogenic probe station with liquid nitrogen cooling under simulated AM1.5G solar irradiance using a 300 W Oriel solar simulator. Device temperature was monitored using a Si thermometer. Current density-voltage characteristics were measured using a Keithley 2400 source meter. Figures 5.5a and 5.5b show device operation in the dark and under simulated solar illumination (AM 1.5G 100 mW/cm^2) at 294 K and 153 K, respectively. Devices that contain an interlayer of MoO_x show a slight reduction in V_{OC} and the short-circuit current density (J_{SC}) at 294 K

but also exhibit an increased fill factor (FF) and η_P. As temperature decreases, J_{SC} and FF decrease drastically while V_{OC} increases.

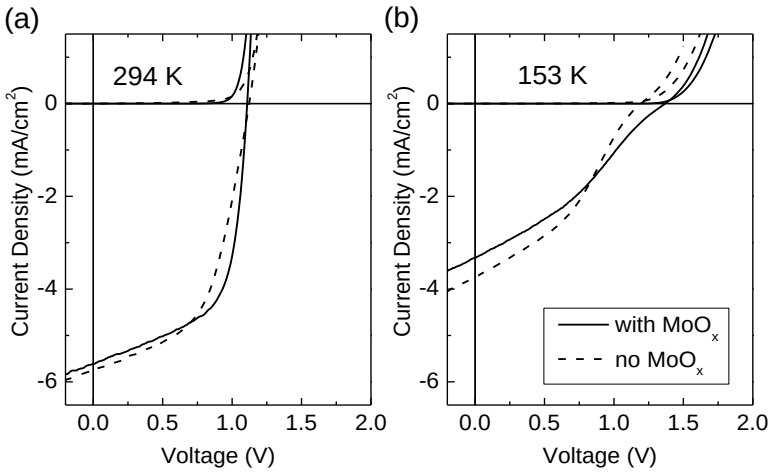

Figure 5.5 Current density-voltage characteristics in the dark and under simulated AM1.5G solar illumination at 100 mW/cm^2 for SubPc-C_{60} OPVs both with and without an anode interlayer of MoO_x at temperatures of (a) 294 K and (b) 153 K.

As shown in Figure 5.6, devices that do not contain an interlayer reach a plateau in V_{OC} with decreasing temperature. A maximum V_{OC} of 1.2 V is realized at 210 K. Devices containing an interlayer show a more pronounced dependence of V_{OC} on temperature, with

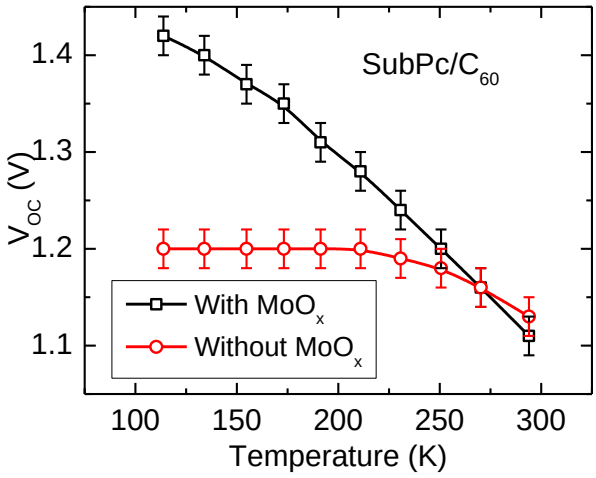

Figure 5.6 Dependence of V_{OC} on temperature for the devices in Figure 5.5.

no clear plateau observed down to a temperature of 113 K. Interestingly, devices with an interlayer show a V_{OC} that is 0.2 V larger at 113 K than those with no interlayer.

5.3.2 MoO_x-SubPc Schottky OPV

In order to directly probe the origin of the additional V_{OC} observed at low temperature, MoO_x-SubPc Schottky cells were fabricated and tested as a function of temperature. The thicknesses of the MoO_x and SubPc layers were 10 nm and 13 nm, respectively. The additional layers of C_{60} and BCP were omitted in order to focus attention on the photovoltaic behavior of the MoO_x-SubPc interface. This Schottky device showed almost no V_{OC} at room temperature (Figure 5.7a). This is likely due to the absence of a D-A interface capable of efficiently dissociating photogenerated excitons. In addition, the presence of a metal cathode directly in contact with the donor could lead to exciton quenching at the metal-organic interface. The V_{OC} in these devices is also limited by a large

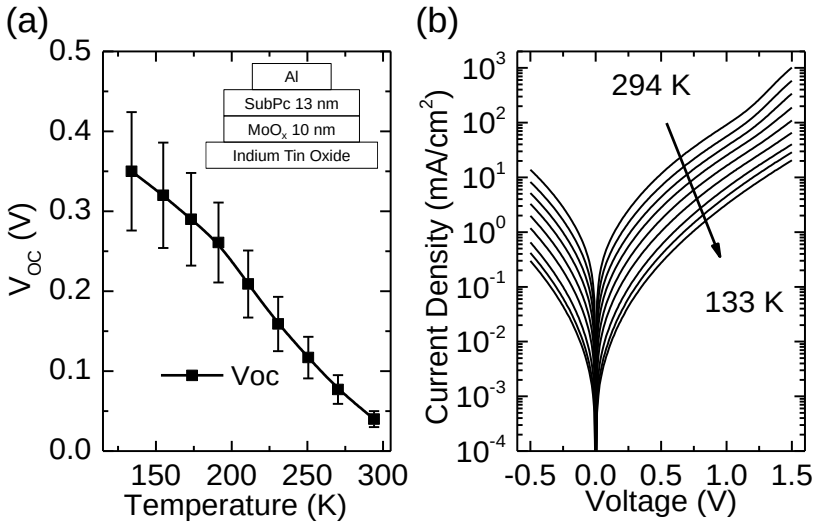

Figure 5.7 (a) Dependence of V_{OC} on temperature for a MoO_x-SubPc Schottky cell. (b) Dark current density-voltage characteristics for a MoO_x-SubPc Schottky cell for temperatures ranging from 294 K to 133 K in ~20 K steps.

dark current that rivals the photocurrent. The V_{OC} was found to increase with decreasing temperature, driven mainly by a corresponding reduction in the magnitude of the dark current (Figure 5.7b), reaching a maximum value of 0.35 V at 133 K.[179]

The same experiment was also carried out on a Schottky cell without the MoO_x layer (i.e. ITO/SubPc/Al). In these devices, no V_{OC} or J_{SC} was observed down to a temperature of 155 K as shown in Figure 5.8.

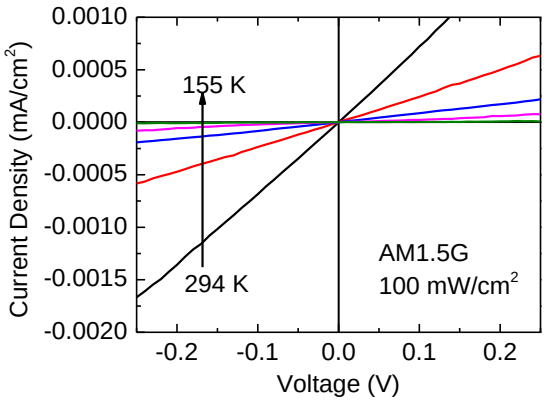

Figure 5.8 Current density-voltage characteristics for devices with the architecture of ITO/SubPc 13 nm/Al 100 nm at various temperatures.

A recent report has shown that MoO_x-C_{60} forms a Schottky junction photovoltaic cell with high V_{OC},[134] suggesting the high work function of MoO_x may permit exciton dissociation via a built-in potential. For the MoO_x-SubPc interface of interest here, it is likely that a similar mechanism is present. The exciton-dissociating ability of the MoO_x-SubPc interface was separately examined by measuring the photoluminescence from a 5-nm-thick layer of SubPc both with and without an adjacent layer of MoO_x. For films adjacent to MoO_x, the photoluminescence is strongly reduced as shown in Figure 5.9.

While the quenching mechanism could be non-radiative exciton quenching or charge

transfer, non-radiative exciton quenching alone will not generate V_{OC}. This indicates the existence of charge transfer at the MoO_x-SubPc interface. Based on the energy levels of MoO_x and SubPc, holes in SubPc are likely transferred to the conduction band of MoO_x while the electrons left in SubPc will be swept out by the built-in field.

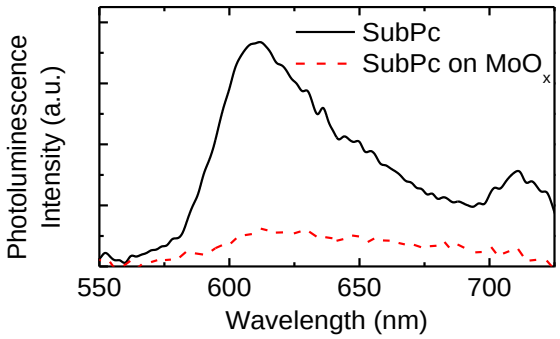

Figure 5.9 Photoluminescence quenching experiment on a 5-nm-thick SubPc thin film. The emission from SubPc is largely quenched in the presence of a 10-nm-thick adjacent MoO_x layer.

Impedance measurements were carried out to confirm the existence of the built-in field using an HP 4192A impedance analyzer with an AC amplitude of 20 mV to ensure the linearity of response. By measuring the frequency dependence of the impedance, the entire Schottky cell can be modeled as a capacitor, a shunt resistance and a series resistance (Figure 5.10a). The shunt resistance and the capacitor describe the impedance of the Schottky junction. Impedance data were collected as a function of bias voltage at 10 kHz and 100 kHz, and then solved for the capacitance. Mott-Schottky theory describes the capacitance-voltage relationship as $C^{-2}=(2/q\varepsilon N)(V_{bi}-V)$.[109, 180] Here, C is the capacitance of the depletion region, q the elementary charge, ε the permittivity of the organic layer, N the effective doping density, V_{bi} the built-in potential and V the applied voltage. Thus, a plot of C^{-2} versus voltage (Figure 5.10b) allows for the determination of the built-in voltage from

the intercept. As shown in Figure 5.10b, a device with a MoO_x interlayer exhibits a built-in voltage of ~1.25 V, while no clear Mott-Schottky characteristics have been observed for devices without MoO_x.

The built-in voltage is the driving force for exciton dissociation in Schottky devices and thus sets an upper limit for V_{OC}. In reality, V_{OC} will be lower than this value due to the existence of dark current and a potentially low photocurrent. The deep Fermi level of MoO_x creates a large built-in field in the active layer that may assist with charge collection. This could account for the increased FF observed in devices that contain an interlayer of MoO_x.

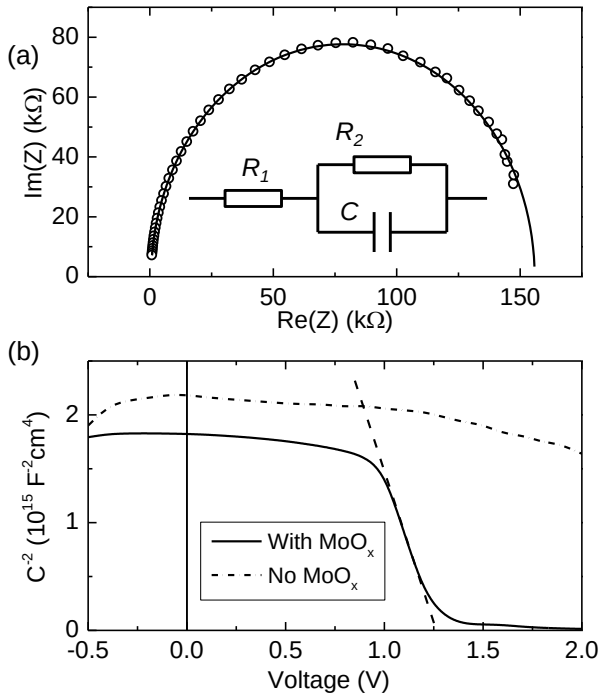

Figure 5.10 (a) Imaginary and real parts of the impedance for a MoO_x-SubPc Schottky cell at various driving frequencies. The inset shows the equivalent circuit (b) Mott-Schottky plot for the Schottky cell. The device containing MoO_x shows clear Mott-Schottky characteristics with a built-in voltage of ~1.25 V. No Mott-Schottky characteristics are observed for the Schottky device that does not contain MoO_x.

5.4 Impact of MoO_x-Donor Schottky Junction on PHJ Operation

With the observation in Figure 5.7a that the MoO_x-SubPc junction is capable of dissociating excitons and exhibiting a V_{OC}, the devices of Figure 5.5 that contain a MoO_x interlayer should be considered as a MoO_x-SubPc Schottky junction in series with a conventional SubPc-C_{60} planar heterojunction (Figure 5.11).

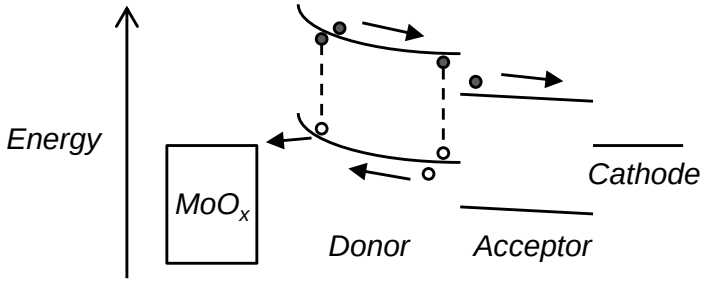

Figure 5.11 Photoconversion process in an OPV with an anode interlayer of MoO_x.

Charge carriers generated at both interfaces can be transported to the respective electrodes without crossing any energy barrier, thus the current matching criterion often discussed in the context of multi-junction OPVs need not be satisfied. The V_{OC} originates from the quasi-Fermi level offset at the D-A interface and the built-in potential in the Schottky-junction. Using this assumption, the total predicted V_{OC} can be thought of as the sum of the individual V_{OC} contributions from the Schottky junction and the SubPc-C_{60} heterojunction. In order to test this model, Figure 5.12 compares the predicted V_{OC} based on simple addition with the experimentally measured V_{OC} for a device containing a MoO_x interlayer. While the predicted V_{OC} and the measured V_{OC} show a similar trend as a function of temperature, this simple addition overestimates the V_{OC}.

This is not unexpected due to the fact that the SubPc layer in the device with MoO_x is shared by both the Schottky junction and the D-A heterojunction. The exciton dissociation

efficiency at the MoO_x-SubPc interface is likely lower than unity and it will compete with the D-A interface for excitons. In addition, the existence of two interfaces for exciton dissociation requires that both electrons and holes be transported through the SubPc layer, which will cause additional recombination loss (Figure 5.11). These possible loss pathways in SubPc may explain the decrease in J_{SC} that is observed in Figure 5.5 upon adding a MoO_x interlayer. Another reason for the overestimate of V_{OC} could result from the fact that the light intensity profile in an actual device will be different from that found in a simple Schottky junction.

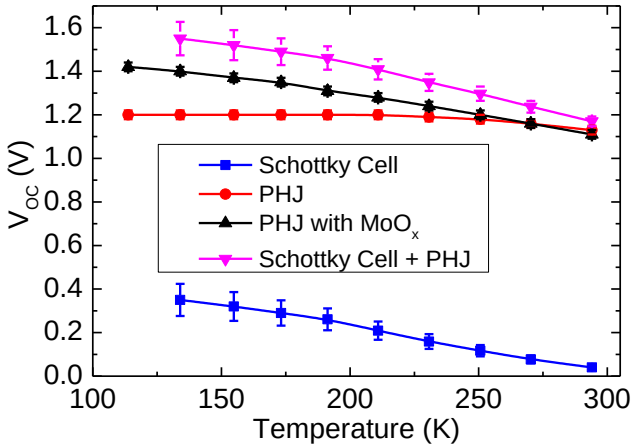

Figure 5.12 The temperature dependence of V_{OC} for SubPc-C_{60} PHJ OPVs both with and without an interlayer of MoO_x and for a Schottky cell OPV based on MoO_x-SubPc. Also shown is the sum (inverse triangle) of the measured V_{OC} of the Schottky cell (square) and the device with no MoO_x interlayer (circle).

The proposed charge transfer mechanism at the MoO_x-donor interface should depend strongly on the position of the donor HOMO level. To examine this dependence, measurements of V_{OC} as a function of temperature were also carried out using the alternative donor materials, CuPc and ClAlPc, both of which have a shallower HOMO level than SubPc as shown Figure 5.13.

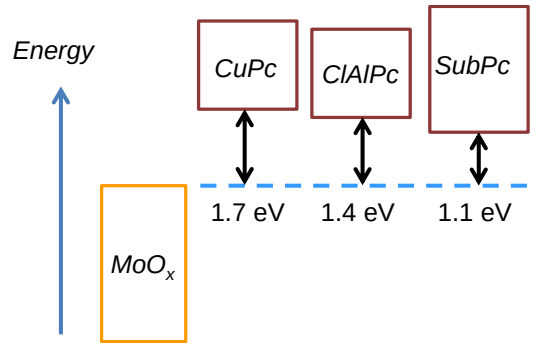

Figure 5.13 Energy level alignment between the HOMO level of donor molecules and the conduction band of MoO_x.

The V_{OC} of devices containing a donor layer of ClAlPc showed a reduced dependence on the presence of an anode interlayer while the V_{OC} for devices containing CuPc showed no dependence on the presence of MoO_x (Figure 5.14). By applying the vacuum level continuity criterion, the donor HOMO level at the MoO_x-donor interface will be pinned above the conduction band of MoO_x. Thus, the charge transfer process at the MoO_x interface favors donor materials with a deep HOMO level since the transfer of the hole from the donor HOMO level to the conduction band of MoO_x is endothermic.

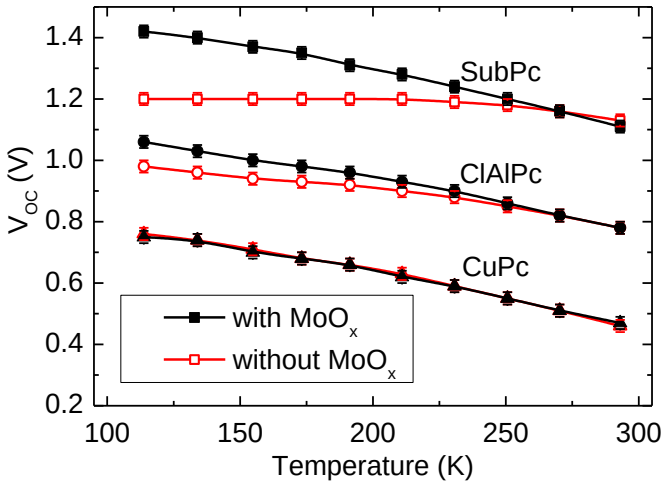

Figure 5.14 Temperature dependence of V_{OC} for devices based on different donor materials. Open symbols represent devices without MoO_x and close symbols represent devices with MoO_x.

5.5 Conclusions and Summary

In summary, the maximum achievable V_{OC} in a planar heterojunction OPV is not solely determined by D-A interface energetics, but also by the anode-organic layer interface. Anode interlayers with deep energy levels can form a Schottky junction with the donor layer and generate additional V_{OC}. The observed additional V_{OC} is most significant for donors with a deep HOMO level, and could result in values of V_{OC} that are larger than the limit set solely by the D-A energy level offset at low temperature.

Additionally, a significant improvement in V_{OC} has also been observed for bulk heterojunction OPVs with the addition of a MoO_x interlayer, even at room temperature. In these structures, the morphology of the mixed layer and the fact that MoO_x interlayer is in contact with both the donor and acceptor materials will complicate the device model. In the next chapter, work will focus on understanding the impact of built-in potential generated by MoO_x in bulk heterojunction OPVs.

6. The Role of Bulk-ionization in Photoconversion

6.1 Background

In order to realize efficient photoconversion in organic semiconductors, photogenerated excitons must be dissociated into their constituent electronic charges. As described in previous chapters, this is most often accomplished using a heterojunction where efficient dissociation is facilitated by a charge transfer process occurring at an electron donor-acceptor (D-A) interface in OPVs. Interestingly, recent work on MoO_x/C_{60} Schottky OPVs has demonstrated that excitons in C_{60} may also undergo efficient bulk-ionization and generate photocurrent as a result of the large built-in field created by the MoO_x/C_{60} interface.

6.2 Bulk-ionization vs. Charge Transfer

Among the most efficient OPVs, many adopt a fullerene-rich bulk heterojunction (BHJ) architecture and utilize a transition-metal-oxide with a deep Fermi level as an anode interlayer.[104, 156, 181-185] In some cases, the composition of the BHJ may consist of more than 90 wt.% fullerene.[161, 186-187] For example, Zheng et al. have reported that an OPV containing 95 wt.% C_{70} with an anode interlayer of MoO_x can achieve a power conversion efficiency (η_P) of ~6%, with an open-circuit voltage (V_{OC}) close to 1 V.[186] The photocurrent in this device arises mainly from absorption by C_{70}, with the donor material acting as a hole-transporting phase to maintain a reasonable fill factor (FF) and contribute to exciton dissociation.

In fullerene-rich BHJs, the use of a high-work-function anode interlayer like MoO_x helps to increase the built-in potential for improved rectification and charge collection. Recent work has shown that the high-work-function anode-fullerene interface forms a Schottky junction that can dissociate excitons and generate V_{OC}.[134, 136] In Schottky OPVs, excitons undergo bulk-ionization and contribute to photocurrent despite the absence of a dissociating donor-acceptor (D-A) interface.[144, 188] Photoconversion via bulk-ionization is advantageous as it avoids the intrinsic energy loss associated with charge transfer at the D-A interface. This in turn increases the upper limit for the maximum achievable V_{OC}. For example, a MoO_x/C_{60} Schottky device exhibits a V_{OC} >1.2 V, even at room temperature.

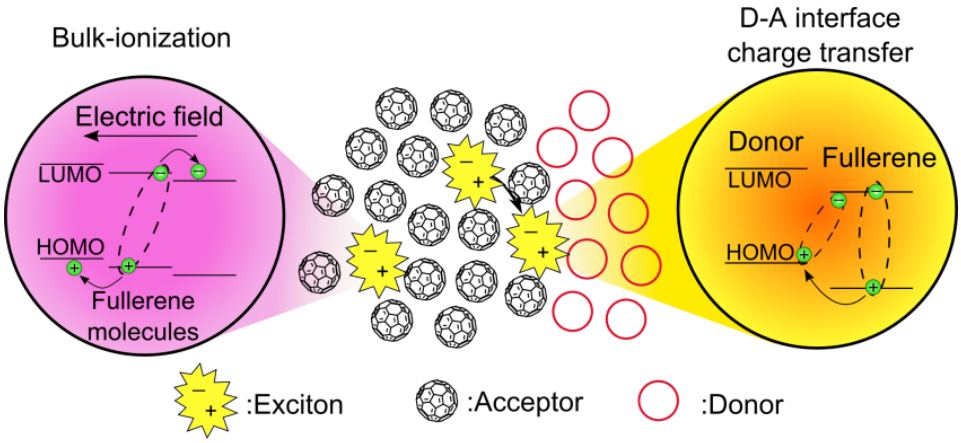

Figure 6.1 The two competing exciton dissociation processes in fullerene-rich BHJ OPVs. Excitons generated close to the D-A interface have a higher probability of undergoing charge transfer. Excitons generated far from the D-A interface in the fullerene are more likely to undergo bulk-ionization.

Chapter 4 has demonstrated that the maximum achievable V_{OC} for a device based on charge transfer at a D-A interface is limited by the associated charge transfer state (CT state) energy, which is the low-energy intermediate state in the exciton dissociation process as shown in Figure 6.1.[115-116, 189-191] In fullerene-rich BHJs, the fullerene makes up most of

the active layer and is very likely to be continuous, forming a direct charge carrier pathway between the anode and the cathode. However, due to the built-in potential generated by the large Fermi energy difference between the MoO_x interlayer and the acceptor, the interface between the MoO_x interlayer and the acceptor becomes a Schottky junction, preventing electron leakage to the anode when forward biased. The large built-in potential also allows excitons generated on fullerene molecules to contribute to photocurrent via bulk-ionization, as also shown in Figure 6.1. For a Schottky junction, the ultimate limit of V_{OC} is the built-in potential. Most previous work has focused on understanding the charge transfer process at the D-A interface in BHJs, the role of bulk-ionization is discussed less frequently.[129, 131, 147, 153, 188, 192-194] In this chapter, both charge transfer processes at the D-A interface and bulk-ionization processes within C_{60} are demonstrated to contribute to photocurrent in fullerene-rich BHJs. In fact, bulk-ionization accounts for ~16% of the total photocurrent in an optimized BHJ OPV (active layer consists of 80 vol. % fullerene) based on the D-A pairing of boron subphthalocyanine chloride (SubPc) and C_{60}. The role of bulk-ionization processes is also discussed in determining the V_{OC} and FF of fullerene-rich BHJ OPVs.

6.3 Experimental Methods

Organic photovoltaic cells were fabricated on pre-patterned indium-tin-oxide (ITO)-coated glass substrates having a sheet resistance of ~8-12 Ω/□. Substrates were cleaned in tergitol solution and in organic solvents and treated in UV-Ozone ambient for 10 minutes prior to thin film deposition. All layers were deposited by high vacuum thermal evaporation at a pressure of $<8\times10^{-7}$ Torr. A 10-nm-thick layer of MoO_x was deposited at 0.05 nm/s as

the anode interlayer. Mixed organic active layers were prepared via co-deposition from two sources at a total rate of 0.2 nm/s at room temperature. All OPVs were capped with a 10-nm-thick exciton blocking layer of bathocuproine (BCP).[91] Device active areas were defined by the overlap between a 100-nm-thick Al cathode layer and a pre-patterned indium tin oxide (ITO) anode, giving a device active area of 9 mm^2.

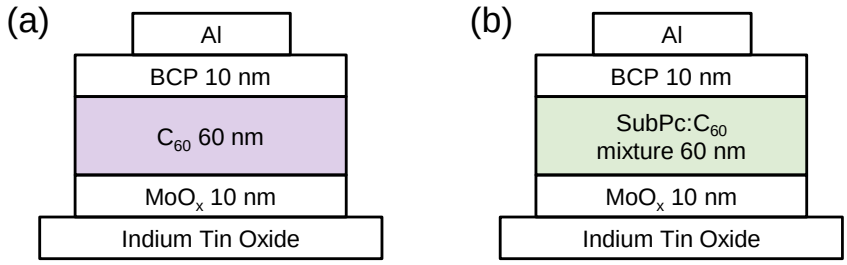

Figure 6.2 Device architectures of (a) a C_{60} Schottky OPV having an active layer thickness of 60 nm and (b) a BHJ OPV consisting of uniform mixture of SubPc:C_{60} (20:80 vol.%) of the same thickness.

6.4 Bulk-ionization in Fullerene-rich Bulk Heterojunctions

As discussed previously, the bulk-ionization of excitons may contribute to photocurrent in BHJs, especially in the case of fullerene-rich BHJs where the D-A interface area is reduced. Here, we compare the device performance of a C_{60} Schottky OPV having an active layer thickness of 60 nm and a BHJ consisting of uniform mixture of SubPc:C_{60} (20:80 vol.%) of the same thickness. The device architectures are shown in Figure 6.2. A 10-nm-thick MoO_x anode interlayer is included in both devices. Current density-voltage characteristics were measured using a Keithley 2400 source meter. The absence of an electron donor material in the Schottky OPV drastically changes the device performance under illumination, as shown in Figure 6.3.

The most noticeable effect is a reduction in J_{SC} for the C_{60} Schottky OPV, which comes mainly from the absence of donor absorption to harvest low energy photons in the solar spectrum, and the lack of a D-A interface to help dissociate photogenerated excitons. The current density-voltage characteristics of the C_{60} Schottky OPV show a nearly linear behavior in the fourth quadrant, which is consistent with the bias dependence of photogenerated charge carriers in the C_{60} layer, as described previously by Jeong et al.[144] Despite poor device performance, the Schottky OPV still produces a photocurrent >1 mA/cm^2 under AM1.5G simulated solar illumination at 100 mW/cm^2, comparable to the photocurrent in a BHJ under the same illumination condition.

Based on this result, it is clearly possible for C_{60} to efficiently generate photocurrent in the absence of a dissociating donor-acceptor interface via bulk-ionization. To further examine the role of bulk-ionization processes in BHJs, current density-voltage characteristics for devices fabricated with variable acceptor concentration, ranging from 50 vol.% to 100 vol.% were recorded under AM1.5G simulated solar illumination (100

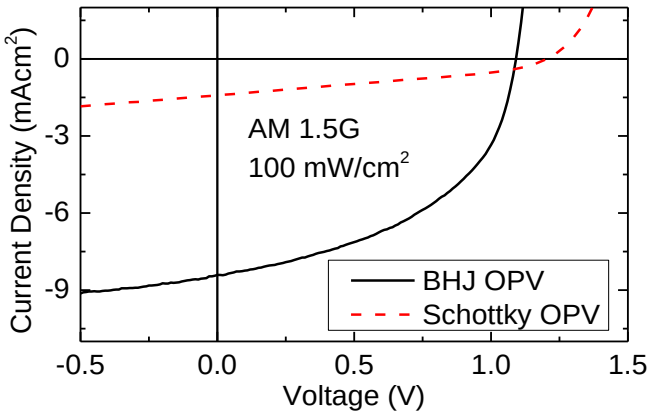

Figure 6.3 Current density-voltage characteristics for devices with the structure shown in Figure 6.2, under AM1.5G simulated solar illumination at 100 mW/cm^2.

mW/cm^2) at various temperatures (Figure 6.4). All temperature dependent experiments were carried out in a Janis cryogenic probe station with liquid nitrogen cooling under AM1.5G simulated solar illumination using a 300 W Oriel Xe solar simulator. Device temperature was monitored using a Si thermometer.

For all devices, V_{OC} is observed to increase as temperature decreases due to a corresponding reduction in the dark current. The J_{SC} is found to decrease with decreasing temperature for all BHJ OPVs, but remain nearly constant for the C_{60} Schottky OPV. The temperature dependence of both J_{SC} and V_{OC} are explored further to reveal the interplay between bulk-ionization and charge transfer in the photoconversion process.

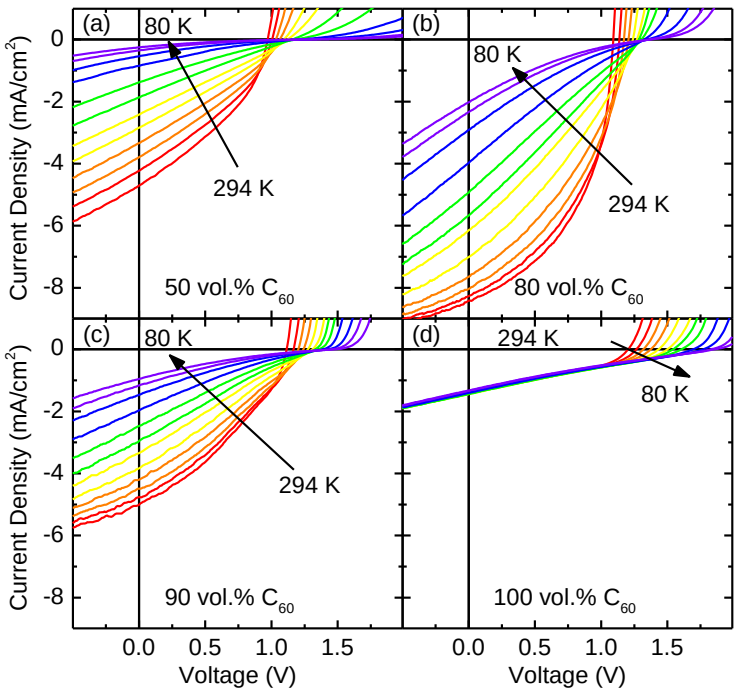

Figure 6.4 Current density-voltage characteristics for SubPc:C_{60} BHJ OPVs containing (a) 50 vol.%, (b) 80 vol.%, (c) 90 vol.%, and (d) 100 vol.% C_{60} measured from 294 K to 80 K at ~20 K intervals under AM1.5G simulated solar illumination at 100 mW/cm^2.

6.4.1 Impact of Bulk-ionization on Short-circuit Current Density

In a BHJ, it is difficult to distinguish between photocurrent generated via charge transfer at the D-A interface and bulk-ionization, since only the total device photocurrent can be measured. However, for excitons undergoing charge transfer, the binding energy of the resulting CT state will add a strong temperature dependence to its dissociation probability. Thus, the temperature dependence of photocurrent generated via charge transfer is expected to be stronger than the bulk-ionization process. This argument is strongly supported by our experimental results. Figure 6.5 shows the J_{SC} extracted from the current-density voltage characteristics shown in Figure 6.4.

The C_{60} Schottky OPV shows almost constant J_{SC} from room temperature to ~80 K, indicating that the exciton dissociation process in C_{60} is nearly temperature independent. Previous work has shown that the photocurrent generation process in pristine C_{60} thin films comes mostly from intermolecular charge transfer states.[195-197] This suggests that the

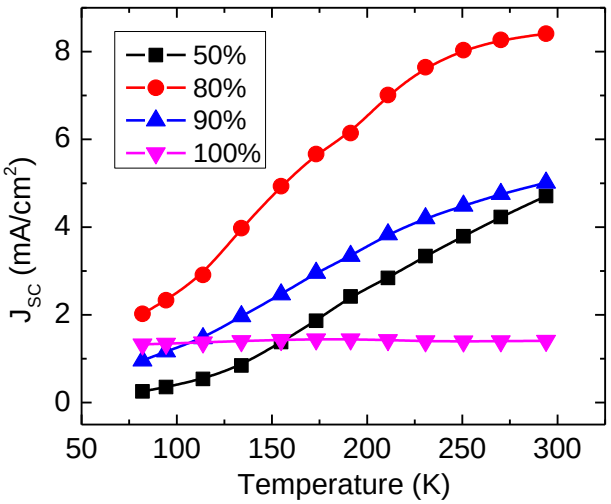

Figure 6.5 Temperature dependence of the short-circuit current density (J_{SC}) for SubPc:C_{60} BHJ OPVs with variable acceptor concentration and for C_{60}-Schottky OPVs.

electron-hole pair binding energy in C_{60} is small, and that charge carriers may be formed shortly after photoexcitation with the assistance of an electric field.

The BHJ containing 80 vol.% C_{60} shows a J_{SC} plateau at low temperature. This non-zero photocurrent at low temperature suggests that a portion of the photocurrent generated in C_{60} originates from bulk-ionization. Recent work has shown that in SubPc:C_{60} BHJs with high fullerene content, C_{60} may still exhibit crystallinity.[198] This crystallinity may reduce the area of the D-A interface, forcing excitons generated in C_{60} to diffuse over longer distances in order to undergo charge transfer. This may increase the likelihood of charge generation via bulk-ionization over charge transfer.

Figure 6.5 shows that the J_{SC} of BHJs containing 50 vol.% C_{60} will approach zero at low temperature, exhibiting limited bulk-ionization characteristics. To quantify the relative dominance of bulk-ionization and charge transfer processes in determining the overall photocurrent, the temperature dependence of J_{SC} for BHJs is modeled using an Onsager-Braun formalism for geminate polaron-pair recombination.[86, 123] The CT state is treated as a polaron-pair in the model, and non-geminate recombination is ignored since the major loss of photocurrent at short-circuit comes via geminate polaron-pair recombination.[105] For SubPc:C_{60} BHJs, the current density-voltage characteristics collected under variable illumination intensity (AM1.5G) collapse onto each other from -0.5 V to 0.5 V when normalized to J_{SC}. The invariability of the photocurrent shape with light intensity suggests a first order recombination mechanism, and confirms that non-geminate polaron-pair recombination is indeed negligible in this system at short-circuit. The Onsager-Braun model describes the dissociation rate constant for polaron-pairs as [123]

$$k_{diss}(T,F) = \frac{3e\langle\mu\rangle}{4\pi a^3\langle\varepsilon\rangle} e^{-E_B/k_BT} J_1(2\sqrt{-2b})/\sqrt{-2b}$$

with $b = \frac{q^3F}{8\pi\varepsilon k_B^2 T^2}$. Equation 6.1

In Equation 6.1, the parameter k_{diss} is the polaron dissociation rate constant, $<\mu>$ and $<\varepsilon>$ are the effective mobility and dielectric constant across the D-A interface respectively, E_B is the CT state binding energy, J_1 is the first order Bessel function, F is the electric field, a is the initial separation of the polaron-pair. In terms of these rates, the polaron-pair dissociation probability (ϕ) can be written as:

$$\phi = \frac{k_{diss}}{k_{diss} + k_{rec}} + \phi_{bulk}$$ Equation 6.2

where k_{rec} is the polaron-pair recombination rate constant and ϕ_{bulk} is a constant probability of bulk-ionization of excitons in C_{60}.

In order to apply Equations 6.1 and 6.2 to experimentally measured values of the current density, J_{SC} is first converted to a charge collection efficiency (η_{CC}) by normalizing its value to the reverse-bias voltage saturation photocurrent (J_S) as previously described in the literature.[103] A large reverse bias (5~10 V) was applied to the device in order to extract all photogenerated charge carriers for an estimation of the reverse-bias saturation photocurrent. Under the assumption of negligible non-geminate recombination at short-circuit; ϕ equals to the η_{CC}. The extracted values of the charge collection efficiency are tabulated as a dissociation probability in Figure 6.6 and are well-fit using Equation 6.2.

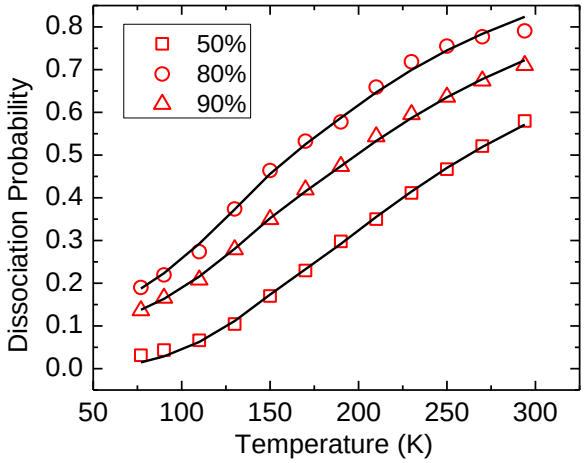

Figure 6.6 CT state dissociation probability vs. temperature for the SubPc:C_{60} BHJ OPVs showed in (a), fit with an Onsager-Braun model. The CT state dissociation probability is approximated by normalizing J_{SC} to the room temperature reverse saturation photocurrent.

The effective mobility, polaron binding energy and polaron recombination rate constant associated with the fits are shown in Table 6.1. Interestingly, values of the polaron-pair (and hence CT state) binding energy and recombination rate are found not to vary substantially with BHJ donor-acceptor ratio. This invariance suggests that the behavior of the CT state is not significantly affected by changes in composition, indicating that the modeled J_{SC} in each case likely originates from the same D-A CT state. It can also

Table 6.1 Parameters extracted by modeling the temperature dependence of the CT state dissociation probability using Onsager-Braun theory for SubPc:C_{60} BHJ OPVs with various compositions. The CT state dissociation probability (ϕ) is calculated by normalizing J_{SC} to the room temperature reverse-bias saturation photocurrent.

C_{60} concentration (vol.%)	ϕ (at 294 K)	Binding energy (eV)	Mobility ($cm^2V^{-1}s^{-1}$)	k_{rec} (s^{-1})
50	0.58	0.28	1.3×10^{-3}	2.5×10^{8}
80	0.79	0.27	1.8×10^{-3}	2.5×10^{8}
90	0.71	0.27	1.4×10^{-3}	2.5×10^{8}

be concluded that the key parameter determining the charge collection efficiency is the effective charge carrier mobility. According to previous work on the D-A pairing of SubPc:C_{60}, the hole mobility peaks at 20 vol.% donor concentration, leading to optimum device performance.[198] The observations of this work support this previous result.

The fraction of excitons that undergo bulk-ionization at room temperature is taken as the ratio between ϕ_{bulk} and ϕ. In a C_{60} Schottky OPV, this fraction would be unity. This fraction is plotted as a function of composition in Figure 6.7, and the fraction of excitons that undergo bulk-ionization in a BHJ shows a steep increase when the C_{60} concentration exceeds 80 vol.%, potentially indicating the formation of a continuous C_{60} agglomeration phase at this concentration. It is important to point out that the optimized device architecture based on the D-A pairing of SubPc:C_{60} derives >10 % of the total photocurrent and >30% of the photocurrent originating from C_{60} from bulk-ionization. Given the

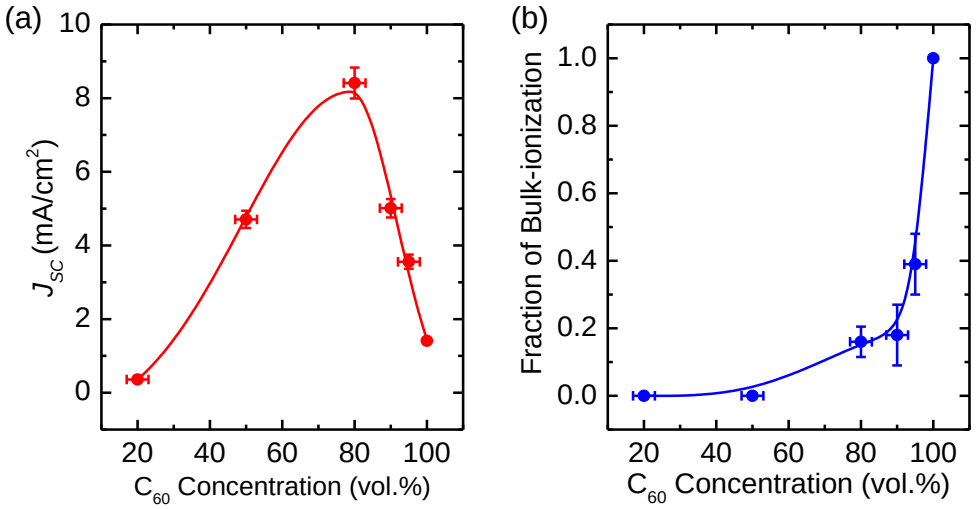

Figure 6.7 (a) The J_{SC} of SubPc:C_{60} BHJ OPVs with variable C_{60} concentration and C_{60} Schottky OPVs at room temperature under AM1.5G simulated solar illumination (100 mW/cm^2). (b) Fraction of excitons which undergo bulk-ionization for BHJ OPVs with variable C_{60} concentration at room temperature. The solid line is a guide to the eye.

common use of fullerene-rich BHJs in highly efficient OPVs, it is reasonable to expect that many of the most promising OPVs may rely in part on the bulk-ionization.

6.4.2 Impact of Bulk-ionization on Open-circuit Voltage

The concentration dependence of V_{OC} in BHJs has been previously ascribed to the delocalization and dielectric screening of CT state at the D-A interface.[153, 190] In these reports, V_{OC} is found to increase with fullerene concentration for fullerene-rich BHJs, due to an increase in the dielectric constant with increasing C_{60} content. This reduces the binding energy of the CT state and increases the CT state energy (E_{CT}). The magnitude of the dielectric constant determines the degree to which the Coulomb interaction between the electron and hole is screened. For the SubPc:C_{60} BHJ architecture discussed in this work, electroluminescence spectra were measured using an Ocean Optics USB4000 spectrometer. E_{CT} was extracted from the peak in electroluminescence (EL) by fitting the spectrum with a Gaussian function as shown in Figure 6.8a-d.[145-147]

For a SubPc:C_{60} BHJ OPV containing 50 vol.% C_{60}, the emission spectrum can be fit with a single Gaussian function centered at 1.55 eV. For devices with a fullerene-rich composition, a second EL feature is observed that originates from C_{60} at 1.67 eV.[199-201] After comparing the low-energy feature across all film compositions, we find that the difference in E_{CT} with varying C_{60} content is <0.03 eV.

To further confirm the similarity in E_{CT}, high-sensitivity measurements of the external quantum efficiency were carried out by measuring the photocurrent under monochromatic light illumination using a 300 W Oriel Xe lamp, a monochromator, an optical chopper wheel and a SR810 lock-in amplifier and used to measure the CT state absorption energy

in SubPc:C_{60} BHJ OPVs containing 50 and 80 vol.% C_{60}. The difference between the CT state absorption energy in these two devices is also <0.03 eV. However, the observed difference in V_{OC} for these devices is ~0.15 V at room temperature as shown in Figure 6.9 and >0.2 V at 110 K. This suggests that the change in CT state energy alone cannot explain the difference in device V_{OC}.

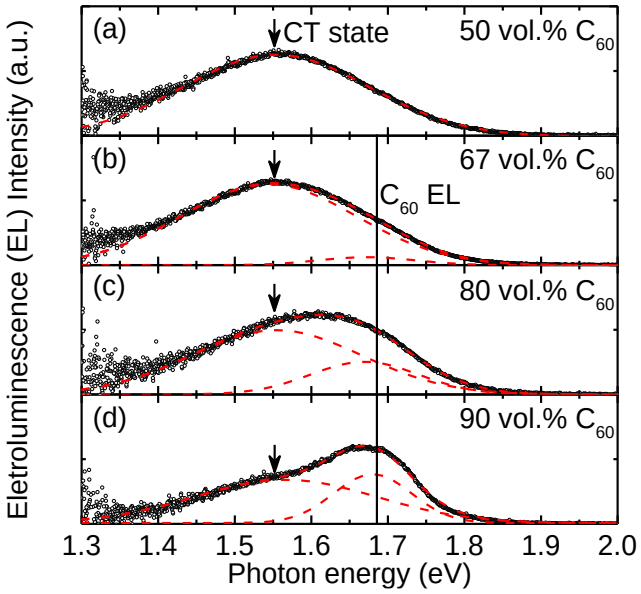

Figure 6.8 (a)-(d) Electroluminescence (EL) spectra measured from BHJ OPVs as a function of C_{60} composition, varying from 50 vol.% to 90 vol.%. A similar CT state energy (~1.5 eV) can be extracted for all compositions by excluding electroluminescence solely from C_{60} (~1.67 eV).

Here, the disagreement between the change in CT state energy and the observed change in V_{OC} is attributed to the role of bulk-ionization processes in C_{60}. The MoO_x/C_{60} Schottky OPV has a larger V_{OC} (>1.2 V) than comparable SubPc:C_{60} BHJs (<1.1 V) at room temperature, and a much stronger temperature dependence as shown in Figure 6.10. The temperature dependence of V_{OC} can be modeled with a modified Shockley equation (Equation 4.2).[117] According to Chapter 4, E_{eff} is directly related to the lowest-energy

intermediate state in the exciton dissociation process. In the case of a D-A heterojunction, E_{eff} equals the CT state energy.[115]

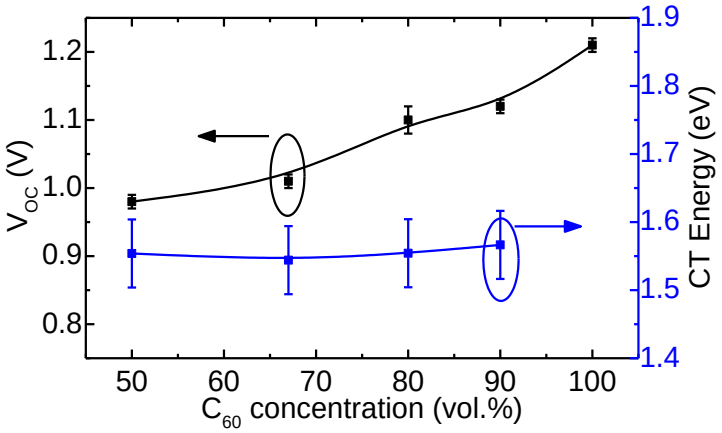

Figure 6.9 Concentration dependence of CT state energy and V_{OC} for BHJ OPVs with variable C_{60} concentration.

The observed V_{OC} will often deviate from the dependence of Equation 6.3 and plateau at low temperature. This is due to the limit of the quasi-Fermi level offset at a given illumination intensity, since not all molecules at the D-A interface are excited.[53, 141, 202] The extrapolated maximum achievable V_{OC} at 0 K (V_0) is chosen to approximate the theoretical maximum achievable V_{OC} and E_{eff} in Equation 6.3 as described previously and shown in Figure 6.10.[117]

The extrapolated V_0 is significantly higher for the Schottky OPV than that of BHJs containing 50 vol.% C_{60}. Here, we propose that the difference in V_0 comes due to differences in the photoconversion mechanisms in these devices. In a BHJ, the majority of the photocurrent is generated by excitons dissociated at the D-A interface, leading to CT state formation. Further dissociation requires the splitting of the quasi-Fermi levels (equal to the V_{OC} multiplied by elementary charge) to be less than the CT state energy. Otherwise

the recombination of charge carriers into CT states will overwhelm the dissociation of CT states into mobile charge carriers.[149]

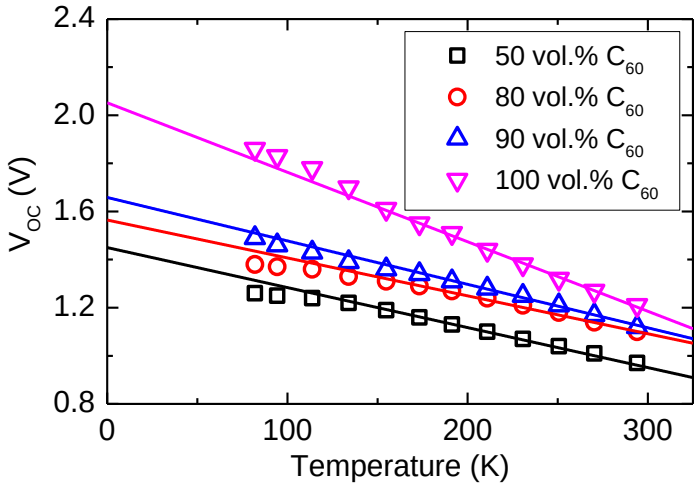

Figure 6.10 Temperature dependence of the open-circuit voltage (V_{OC}) for SubPc:C_{60} BHJ OPVs with variable C_{60} concentration and C_{60} Schottky OPVs.

In a Schottky junction, excitons undergo only the bulk-ionization process. In the case of MoO_x/C_{60} Schottky OPVs, the bottleneck for generating photocurrent now becomes charge carrier collection via the built-in potential. The built-in voltage was estimated by carrying out a Mott-Schottky analysis using a HP 4192A impedance analyzer. The C_{60} Schottky junction shows an extrapolated V_0 of 2.1 V, which matches well with the built-in potential measured by Mott-Schottky analysis as shown in Figure 6.11.[109-110, 180]

In light of the discussion above, the measured V_{OC} in a fullerene-rich BHJ can be treated as an interpolation between the V_{OC} of a Schottky junction and the V_{OC} from the D-A interface. A portion of the excitons will diffuse to the D-A interface and be dissociated, while the rest that do not recombine will go through the bulk-ionization process. For the D-A pairing of SubPc and C_{60}, E_{CT} is much lower than V_{bi}, so that the introduction of D-A interface by mixing the donor and acceptor materials will reduce V_{OC}. The BHJ with 50

vol.% C_{60} has the largest D-A interface area and thus the lowest V_{OC}. The Schottky cells have no D-A interface and thus the highest V_{OC}, as all excitons are forced to dissociate via bulk-ionization.

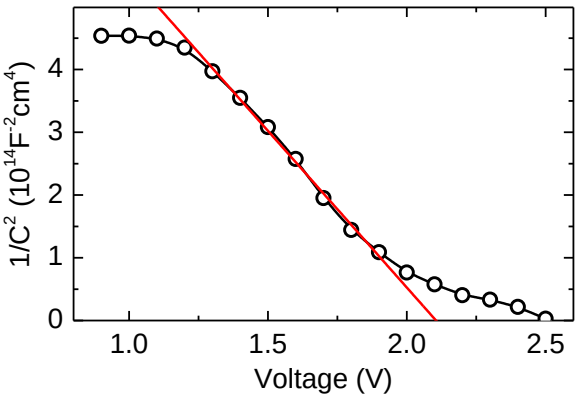

Figure 6.11 Mott-Schottky analysis of a C_{60} Schottky OPV, exhibiting a built-in potential of ~ 2.1 V.

6.4.3 Impact of Bulk-ionization on Fill Factor

With knowledge of how bulk-ionization processes impact J_{SC} and V_{OC}, it is tempting to analyze the FF in a similar manner. Figure 6.12 shows the temperature dependence of FF for devices shown in Figure 6.4. At room temperature, BHJ OPV with 80 vol. % C_{60} has the highest FF (0.48) while the rest of BHJ OPVs and C_{60} Schottky OPV have similar low FFs (~0.35). This supports preiouvs work done in our group that the formation of nanocrystalline domain leads to increased mobility and phase separation in BHJ OPVs at a C_{60} concentration of 80 vol. %.[198] Compared to charge transfer process, bulk-ionization is less efficient at room temperature and is linearly dependent on the electric field as described in previous literature.[144] The C_{60} Schottky OPV has a FF of ~0.34 at room

temperature. Thus, the existence of bulk-ionization will unfavorably affect FF for the optimized BHJ OPVs at room temperature.

A rapid reduction of FF in BHJ OPVs to a value lower than the FF in C_{60} Schottky OPV is observed at low temperature, due to the inability to dissociate bound charge transfer state. The bulk-ionization process in C_{60} is however, nearly temperature independent and the FF is not significantly affected by temperature. Thus, bulk-ionization favorably impacts the FF of BHJ OPVs at low temperature.

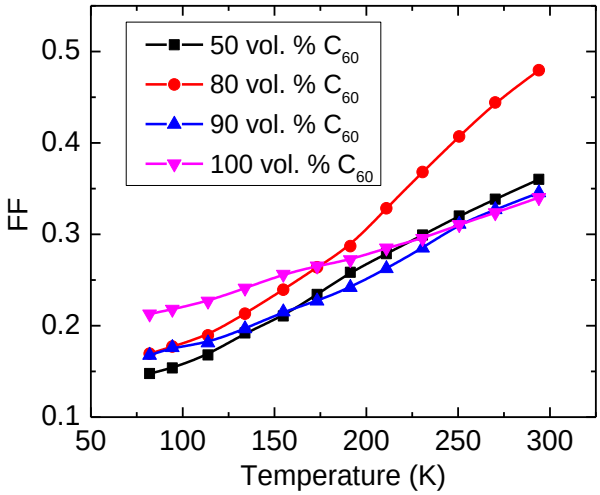

Figure 6.12 Temperature dependence of the fill factor (FF) for SubPc:C_{60} BHJ OPVs with variable C_{60} concentration and C_{60} Schottky OPVs under AM1.5G simulated solar illumination (100 mW/cm^2) at variable temperature.

6.5 Conclusions and Summary

The operation of BHJ and Schottky OPVs fabricated using the D-A pairing of SubPc and C_{60} was carefully examined using temperature dependent current density-voltage measurements. Two competing mechanisms for photocurrent generation were found in fullerene-rich BHJs: charge transfer at the D-A interface and the bulk-ionization of excitons

in C_{60}. The first mechanism can be modeled using a Braun-Onsager theory. The efficiency of charge transfer at a D-A interface is found to be strongly reduced at low temperature, while dissociation via bulk-ionization is almost temperature independent. The weak temperature dependence of the bulk-ionization process is also observed in fullerene-rich BHJs. Interestingly, the CT-state energetics are not affected significantly by the acceptor concentration, and that the bulk-ionization and charge transfer processes compete independently for excitons generated in the acceptor domain, with their impact on J_{SC} being additive.

The bulk-ionization processes was also found to impact V_{OC}. Excitons that undergo a bulk-ionization process can potentially lead to higher V_{OC} compared to those that undergo charge transfer at a D-A interface. Donor-acceptor mixing increases the dissociating interface area in the active layer and the potential for recombination between electrons and holes at the D-A interface. This lowers the theoretical limit of the maximum achievable V_{OC} set by the built-in potential, which causes BHJs to have a lower V_{OC} than Schottky cells. Given that most highly efficient OPVs adopt fullerene-rich compositions, it is likely that bulk-ionization plays a significant role in many BHJ OPVs.

The existence of bulk-ionization in BHJ OPVs also highlights the importance of balancing the D-A interface area and the crystallinity of the fullerene domain for concurrently optimized J_{SC} and V_{OC}. For future device optimization, the impact of bulk-ionization on device operation must be taken into consideration.

7. Rational Design of Mixed Heterojunction Device*

7.1 Background

A challenge sometimes encountered in BHJ OPVs is increased charge carrier leakage due to either donor or acceptor phase continuity between the anode and cathode.[143, 203] Solution processed OPVs typically utilize solvent additives to promote vertical phase separation, thus making the electrode selective for holes or electrons.[204-205] Another approach developed to address this challenge and also offer the potential for increased photocurrent is the incorporation of neat donor and acceptor layers on either side of the mixed D-A layer. This is especially common in small molecule OPVs where vapor-processing permits the facile formation of interfaces between the neat and mixed layers. These devices are often termed planar-mixed heterojunction (PMHJ) OPVs. This architecture was first demonstrated by Hiramoto et al., and has since been used by many groups to realize high efficiency.[30, 50, 92, 182, 206-207] The PMHJ is often chosen for its

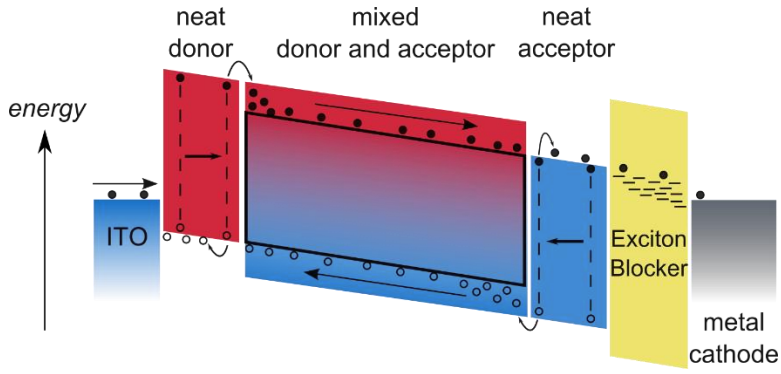

Figure 7.1 The device structure and operation of a PMHJ OPV, where excitons generated in the neat layers may diffuse into the mixture and contribute to photocurrent.

* This work was done in collaboration with Dr. James Holst at Sigma-Aldrich.

potential to improve rectification and enhance photocurrent, as excitons generated in the neat layers may diffuse into the mixture and be dissociated (Figure 7.1).[208-209] However, the existence of additional planar layers may lead to increased resistance for charge collection and adversely impact device efficiency.

More recently, the PMHJ approach has been used with the D-A pairing of 2-[7-(4-N,N-ditolylaminophenylen-1-yl)-2,1,3-benzothiadiazol-4-yl]methylene malononitrile (DTDCPB) and C_{70} to demonstrate a very high single-cell power conversion efficiency of 6.8% as shown in Figure 7.2.[97] However, the fill factor (FF) for this device is still limited, indicating a large internal loss. This internal loss is likely caused by the additional neat layers in the PMHJ architecture.

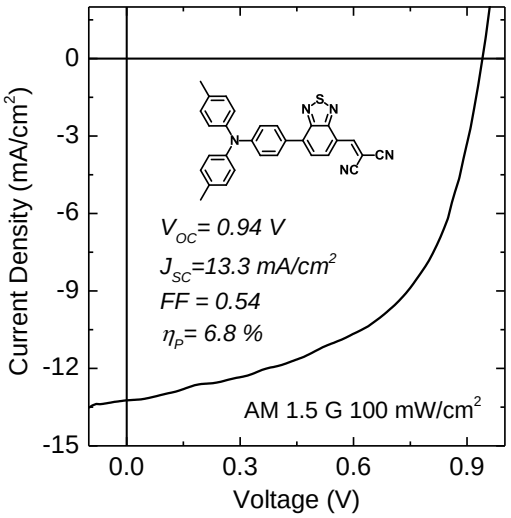

Figure 7.2 Current density-voltage characteristics for the optimized PMHJ OPV with the D-A pairing of DTDCPB-C_{70}.[97] The inset shows the molecular structure of DTDCPB.

By examining the performance of DTDCPB-C_{70} as a function of device architecture, this work shows that in cases where the donor is resistive to hole transport, the neat layers in the PMHJ may actually hurt overall device efficiency. For the DTDCPB-C_{70} system, modifications in device architecture can lead to power conversion efficiencies exceeding 8% in champion devices. This result is among a handful of vapor-deposited small molecule OPVs with such high efficiency.[182, 210]

7.2 Experimental Methods

Organic photovoltaic cells were fabricated on indium-tin-oxide (ITO)-coated glass substrates having a sheet resistance of ~8-12 Ω/□. Substrates were cleaned in tergitol solution and organic solvents and treated in UV-Ozone ambient for 10 minutes prior to thin film deposition. All layers were deposited by high vacuum thermal evaporation at a pressure of $<8\times10^{-7}$ Torr. In all devices, a 10-nm-thick layer of MoO_x was deposited at 0.05 nm/s on the ITO anode as a buffer layer. When included, neat layers of DTDCPB and C_{70} were deposited at room temperature at a rate of 0.2 nm/s. Mixed active layers consisting of a D-A mixture of DTDCPB-C_{70} were prepared via co-deposition from two sources at a total rate of 0.2 nm/s. The overall film composition was varied by separately adjusting the donor and acceptor deposition rates. All devices were capped with a 10-nm-thick exciton blocking layer (EBL) of bathocuproine (BCP) and a 100-nm-thick Al cathode.[91] The active area of the resulting device is 0.785 mm^2, defined by the area of the cathode. Pre-patterned ITO substrates were used to fabricate devices for lifetime testing. In this case, device active area is defined by the overlap between the cathode and the anode to be 9 mm^2. All current

density-voltage (J-V) characteristics were measured with an Agilent 4155C parameter analyzer under simulated AM1.5G illumination using a 150 W Oriel Xe lamp.

7.3 Interlayers and Device Operation

In a BHJ with no electrode interlayer layer, the poor rectification of the homogeneous active layer can lead to increased dark current and reduced V_{OC}.[166, 211] The planar layers in the PMHJ exist to overcome this problem.[212] For example, the relatively shallow lowest unoccupied molecular orbital (LUMO) energy level of the neat donor layer compared to that of the acceptor material can prevent electron leakage to the anode, thus reducing the dark current. In this way, the anode now becomes selective for holes, pinning its Fermi level to the quasi-Fermi level of holes in the mixed layer. A similar argument can be made for charge carriers at the cathode when a neat acceptor layer is included. In the PMHJ architecture, the Fermi levels of the anode and the cathode are pinned to the quasi-Fermi level of holes and electrons in the mixed layer respectively, and the V_{OC} will be the difference between these two Fermi levels. Another benefit of including the planar layers is that they will contribute to the photocurrent.

The use of planar layers is not however without complication due to the often low charge carrier mobility in organic semiconductor materials. The additional planar layer may adversely impact charge collection and increase the non-geminate recombination of electrons and holes. This will cause a reduction in FF and adversely impact efficiency. The remaining question is whether the benefit of generating more excitons in the planar layers outweighs the disadvantage of reduced charge collection efficiency. Of course, while many

inorganic materials with high carrier mobility can be used to replace the organic planar layer, they usually have very weak absorption across the solar spectrum and thus do not contribute to photocurrent. Among them, MoO_x is a highly efficient hole transport material that has been widely used in both organic light-emitting devices and OPVs.[165-166, 174-175, 213-214] Recent research has also pointed out that the MoO_x buffer layer can form a Schottky junction with materials that have a deep highest occupied molecular orbital (HOMO) energy level to prevent electron leakage current to the anode.[134, 137] Aside from not contributing to photocurrent, MoO_x is a good candidate to replace organic planar layers in a PMHJ.

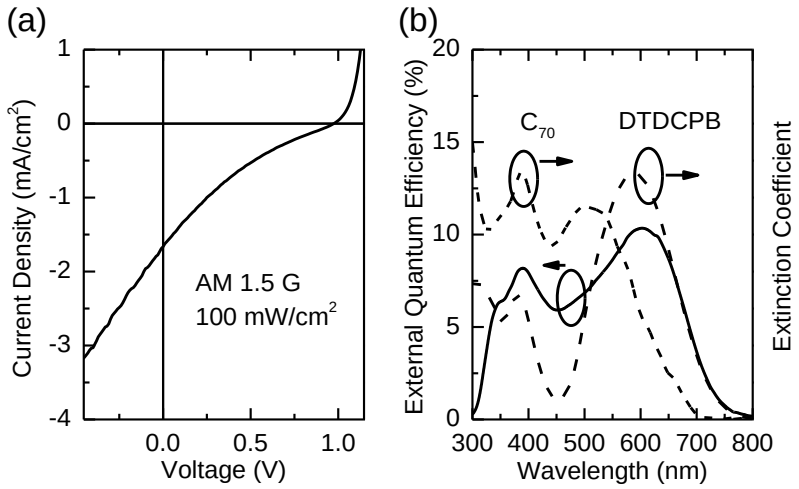

Figure 7.3 (a) Current density-voltage characteristic for a planar heterojunction OPV with the structure: 10 nm MoO_x/15 nm DTDCPB/40 nm C_{70}/10 nm BCP/100 nm Al under simulated AM1.5G illumination at 100 mW/cm^2. (b) External quantum efficiency for the device in (a). Also plotted are the extinction coefficients of DTDCPB and C_{70} measured via spectroscopic ellipsometry.

7.3.1 DTDCPB-C_{70} PHJ OPVs

Prior to investigating the performance of DTDCPB in a PMHJ, the performance of planar heterojunction (PHJ) OPVs consisting of a 15-nm-thick layer of DTDCPB and a 40-

nm-thick layer of C_{70} was examined. As shown in Figure 7.3a, the PHJ device shows low J_{SC} and FF. The current density-voltage characteristics show a severe kink in the fourth quadrant indicating the existence of an imbalance in mobility between electrons and holes and possibly a hole extraction barrier at the anode-DTDCPB interface.[215-218] The external quantum efficiency spectrum (EQE) in Figure 7.3b shows very low response from both DTDCPB and C_{70}.

7.3.2 Exciton Diffusion Length of DTDCPB

The photoluminescence (PL) quenching technique is adopted to measure the exciton diffusion length in neat DTDCPB films. Experiments were carried out using a Photon Technology International Quantum Master 4 Fluorometer.

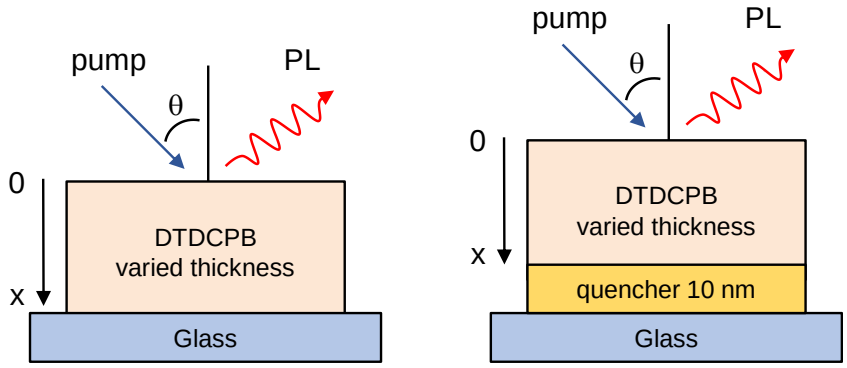

Figure 7.4 Schematic of photoluminescence quenching experiments.

The experimental configuration is shown in Figure 7.4. A planar DTDCPB film is deposited on glass or an exciton quenching layer at various thicknesses. The DTDCPB film is pumped with monochromatic light and the PL intensity is recorded by a detector. The ratio between the PL intensities obtained with and without the presence of the quenching layer (PL ratio) is then calculated at various film thicknesses and excitation wavelengths:

$$\text{PL ratio} = \frac{\text{PL with quencher}}{\text{PL without quencher}} \qquad \text{Equation 7.1}$$

Theoretically, the steady state exciton density profile is modeled by a 1-D diffusion equation:

$$L_D^2 \frac{d^2 n(x)}{dx^2} - n(x) + \tau \frac{Q(x)}{h\nu} = 0 \qquad \text{Equation 7.2}$$

where L_D is the exciton diffusion length, τ is the exciton lifetime, x is the position in the layer, n is the exciton density, h is the Planck constant and ν is the frequency of incident light. Q(x) is the light intensity profile in the film of interest, which is calculated using the transfer matrix model discussed in Section 3.7.1.[112] The x=0 boundary condition is always set to be reflective, where there is no net exciton flux. The other boundary condition is set to be perfectly quenching (n(x)=0) with the presence of quencher or reflective without the presence of quencher. The predicted PL ratio is determined by the ratio between the integrated exciton densities calculated in these two scenarios for given L_D. By matching the predicted PL ratio to the experimentally measured PL ratio, L_D can be fit using the model.

Both thickness dependent and spectrally resolved photoluminescence quenching experiments were carried out on neat films of DTDCPB with C_{60} as a quencher. Results suggest a reasonable exciton diffusion length of ~5 nm as shown in Figure 7.5.[219-220] Thus, the low η_{EQE} may suggest that the neat DTDCPB layer is not efficient in transporting photogenerated carriers away from the D-A interface. This will lead to a buildup of holes at the D-A interface and increase the rate of recombination, reducing the J_{SC} and FF.

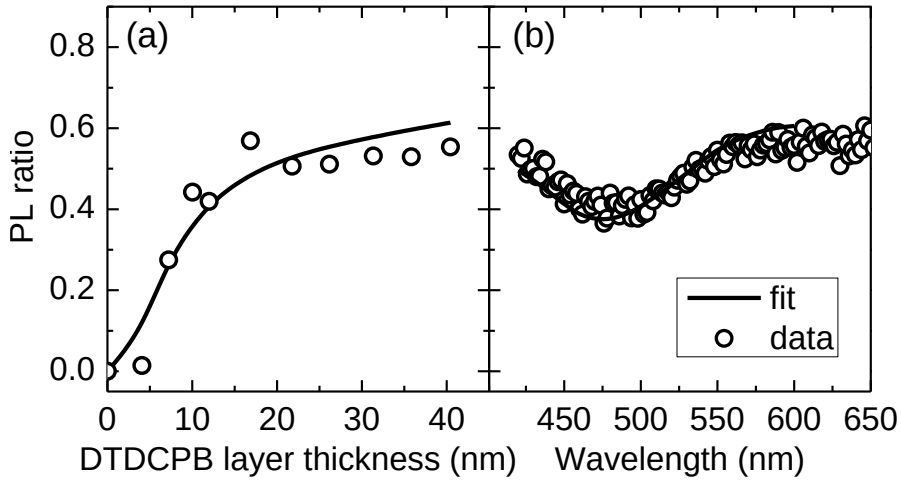

Figure 7.5 (a) PL ratio at various DTDCPB film thicknesses when excited at λ=580 nm. (b) PL ratio of a 40-nm-thick DTDCPB film at various excitation wavelengths.

7.3.3 Planar Layer Thickness and Device Performance

The poor hole transporting behavior of the neat DTDCPB layer is also an obstacle to high efficiency in PMHJ devices. In order to focus on the role of the resistive neat donor layer, the neat C_{70} layer was omitted from the PMHJ architecture. Figure 7.6a shows an overlay of current density-voltage characteristics for OPVs as a function of the neat DTDCPB layer thickness under simulated AM1.5G illumination (100 mW/cm^2). Figure 7.6b shows the associated device operating parameters as a function of the neat DTDCPB layer thickness. The FF shows a monotonic decrease of ~20% as the thickness of the neat DTDCPB layer increases. The J_{SC} increases slightly with a thin DTDCPB layer but is quickly reduced when the DTDCPB thickness reaches 6 nm. Similar devices constructed without a buffer layer of MoO_x show a lower V_{OC} and FF.

In order to estimate the charge collection efficiency (η_{CC}) for the devices in Figure 7.6 as a function of neat DTDCPB layer thickness, device photocurrent was measured under

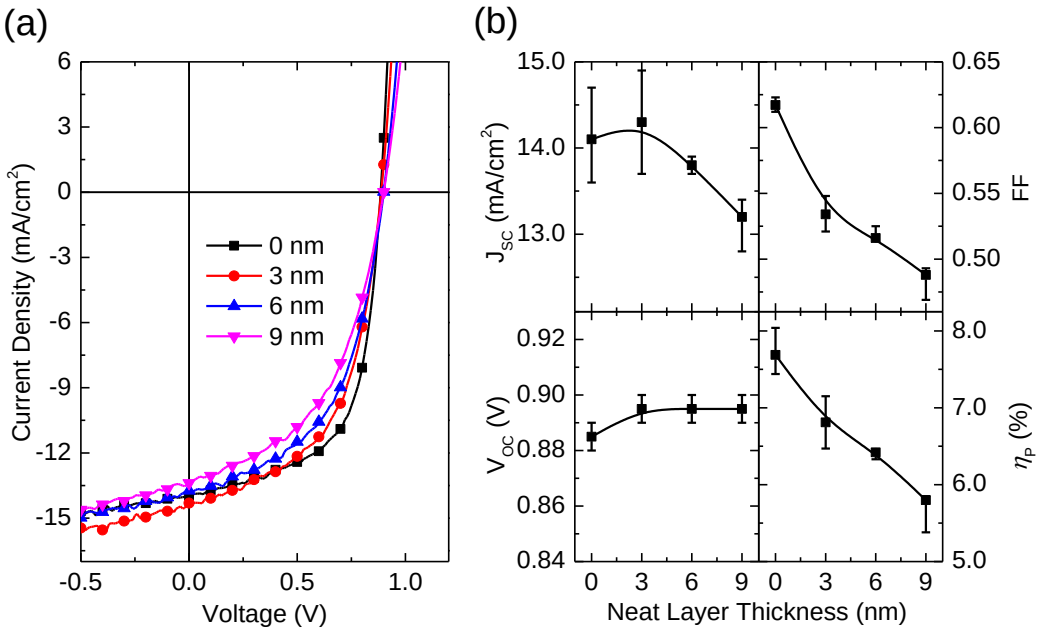

Figure 7.6 (a) Current density-voltage characteristics for PMHJ OPVs with the following device structure: 10 nm MoO_x/x nm DTDCPB/70 nm DTDCPB:C_{70} (1:2)/10 nm BCP/100 nm Al under simulated AM1.5G solar illumination at 100 mW/cm^2. (b) Operating parameters for the devices in (a).

monochromatic illumination as a function of applied bias (+0.8 V to -5 V). Light having a wavelength of λ=462 nm was chosen to excite only C_{70} in the mixture, so that no excitons are generated in the neat DTDCPB layer and their diffusion into the mixture need not be considered. For all devices, the measured photocurrent was found to plateau to the same value under large reverse bias, and at this point, the charge collection efficiency was taken to be 100%.[103] Using this normalization, the charge collection efficiency is plotted as a function of applied bias in Figure 7.7a. The dependence of η_{CC} on bias is very similar for all devices from -5 V to -3 V, where the reverse bias is capable of extracting charge carriers efficiently. In the range of -1 V to 1 V, devices with a neat DTDCPB layer show a reduction in the collection efficiency even at a DTDCPB thickness of 3 nm. The reduction in charge

collection efficiency in the low bias regime may reflect increased geminate and non-geminate recombination in the mixed layer with the insertion of the resistive neat DTDCPB layer.

The dark current density-voltage characteristics for the devices in Figure 7.6 were fit using a generalized Shockley equation and the associated values of the series resistance were extracted and plotted in Figure 7.7b.[117] An ideality factor of ~2 is observed for all devices. The increase in series resistance trends with the reduction in FF as the thickness of the neat DTDCPB layer is increased. As a conclusion, the neat DTDCPB layer is not capable of efficiently extracting photogenerated holes from the mixed layer. Efficient charge carrier extraction is critical for high efficiency, and the resistive neat donor layer may not always lead to optimum performance.

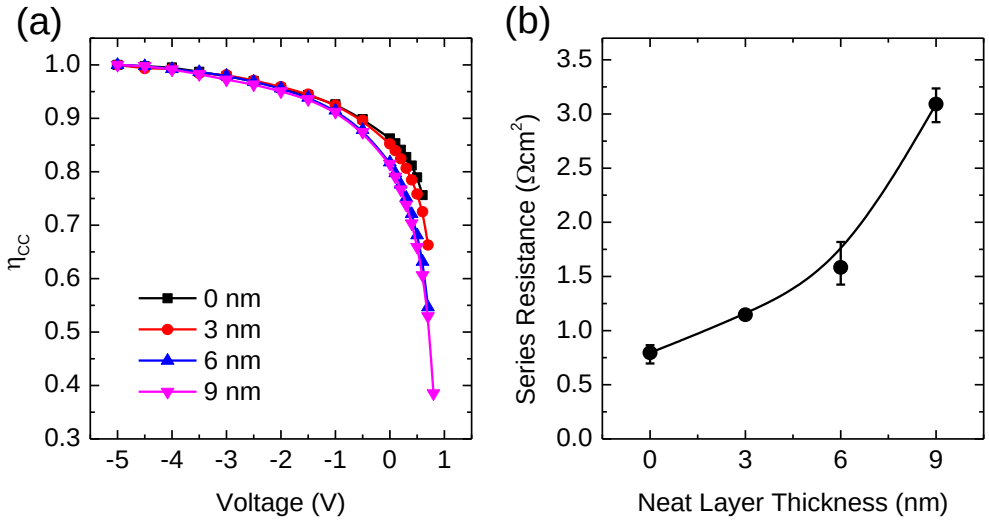

Figure 7.7 (a) Charge collection efficiency (η_{CC}) for PMHJs with the following device structure: 10 nm MoO_x/x nm DTDCPB/70 nm DTDCPB:C_{70} (1:2)/10 nm BCP/100 nm Al under monochromatic illumination (λ=462 nm) as a function of applied bias. (b) Series resistance for the PMHJs in (a), calculated by fitting the dark current using generalized Shockley equation.

7.3.4 Optimization of DTDCPB-C_{70} BHJ OPV

In light of this result, a composition and thickness optimization of the mixed layer was carried out. Figures 7.8a-d show the performance of a BHJ with a 60-nm-thick active layer as a function of composition. Both J_{SC} and FF peak at a D:A ratio of 1:2, suggesting the possible existence of an optimal microstructure at this composition. Previous work on DTDCPB-C_{70} reported an apparent phase separation at a D:A ratio of 1:1.6, very close to the optimal composition observed here.[97] The device performance (DTDCPB:C_{70} = 1:2) is plotted versus active layer thickness in Figures 7.8e-h. The J_{SC} increases with active layer thickness up to 70 nm, with the FF showing only a minimal reduction. An average power

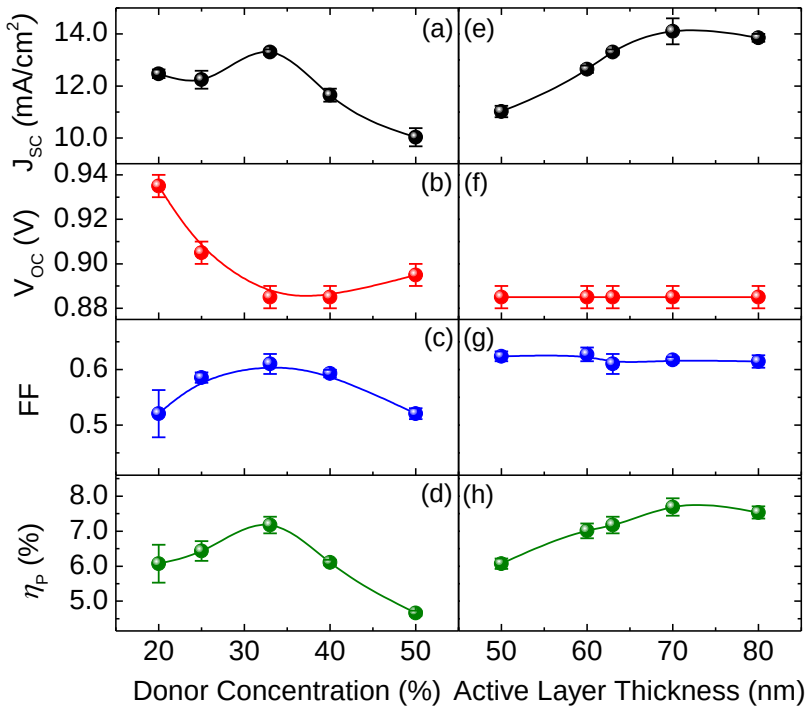

Figure 7.8 (a)-(d): Operating parameters as a function of donor concentration for a DTDCPB-C_{70} BHJ OPV with the active layer being 60-nm-thick. (e)-(h): Device operating parameters as a function of active layer thickness for a DTDCPB-C_{70} BHJ with a donor: acceptor ratio of 1:2. The lines only serve as guides to the eye.

conversion efficiency of (7.7±0.3%) is obtained for devices with a 70-nm-thick active layer at a D:A ratio of 1:2, with the efficiency of champion devices reaching 8%. The fact that FF remains almost constant with increasing active layer thickness is rarely observed for BHJs constructed by vapor processing. In general, the simplified device architecture based on the D-A pairing of DTDCPB-C_{70} appears to be very robust, promising > 6% η_P over a wide range of donor concentration and active layer thickness.

External quantum efficiency of the champion device was determined by measuring the photocurrent under monochromatic light illumination using a 300 W Oriel Xe lamp, a monochromator, an optical chopper wheel and a SR810 lock-in amplifier. A representative plot of the EQE spectrum for the optimized BHJ device architecture is shown in Figure 7.9. > 60% photoconversion efficiency has been realized over a wide spectral range.

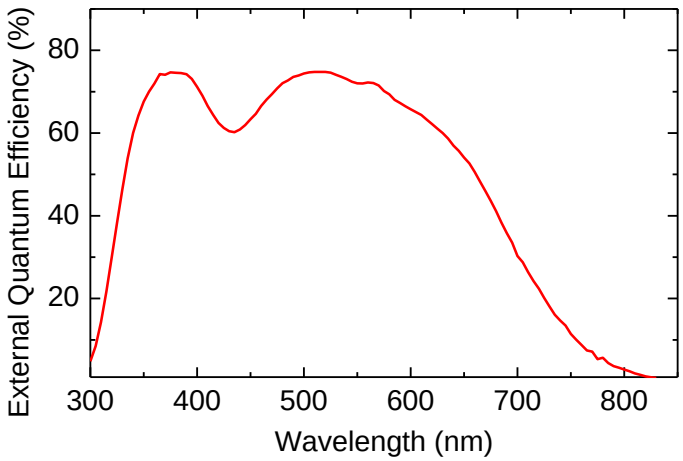

Figure 7.9 External quantum efficiency (η_{EQE}) for a device with the following structure: 10 nm MoO_x/70 nm DTDCPB:C_{70} (1:2)/10 nm BCP/100 nm Al.

7.3.5 Spectral Mismatch and Device Statistics

In order to account for the mismatch between solar spectrum and the spectrum of the lamp used, and more accurately assess the efficiency of the devices shown in Figure 7.8, the spectral mismatch factor (M) was calculated using previously described method as: [221-222]

$$M = \frac{\int R_{ref}(\lambda)E_{solar}(\lambda)d\lambda}{\int R_{ref}(\lambda)E_{Lamp}(\lambda)d\lambda}\frac{\int R_{cell}(\lambda)E_{Lamp}(\lambda)d\lambda}{\int R_{cell}(\lambda)E_{Solar}(\lambda)d\lambda} \qquad \text{Equation 7.3}$$

A comparison between the solar spectrum and the spectrum of lamp used for device characterization is shown in Figure 7.10. The spectral mismatch factor for this work is calculated to be 0.98. After applying the spectral mismatch factor, the average corrected J_{SC} and power conversion efficiency for the optimized device architecture are (14.3±0.5) mA/cm^2 and (7.9±0.3)%, respectively. The champion device exhibits a mismatch-corrected J_{SC} of 14.8 mA/cm^2, a FF of 0.62, a V_{OC} of 0.89 V and a power conversion efficiency of 8.2%.

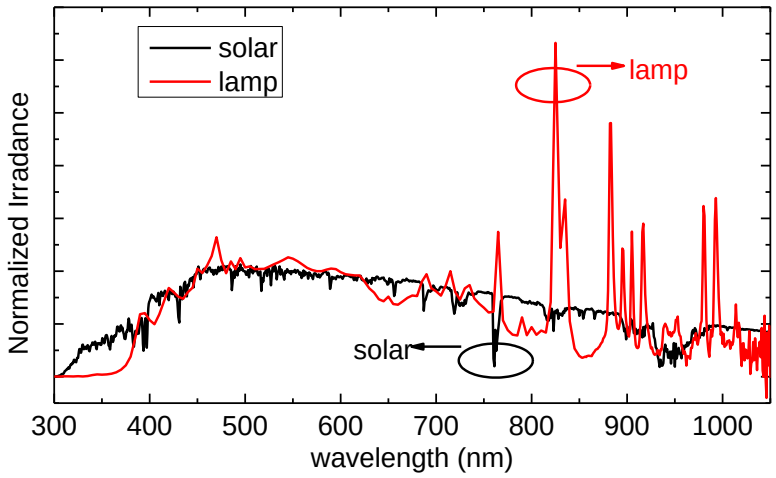

Figure 7.10 A comparison between the AM1.5G solar spectrum and the lamp spectrum used for device characterization.

Two batches of ITO coated glass substrates were used for device fabrication and found to impact the V_{OC}, J_{SC} and FF of the fabricated devices. ITO batch A was used for all the device optimization experiments and ITO batch B was only used for charge extraction efficiency measurements in Figure 7.8. The optimized device structure (70 nm DTDCPB:C_{70} = 1:2) was grown on both batches of ITO. All operating parameters are summarized and plotted in Figure 7.11. Among 33 devices, the ones fabricated on ITO batch B exhibit higher FF, lower J_{SC} and lower V_{OC} than devices on ITO batch A, but the overall efficiency stays roughly the same.

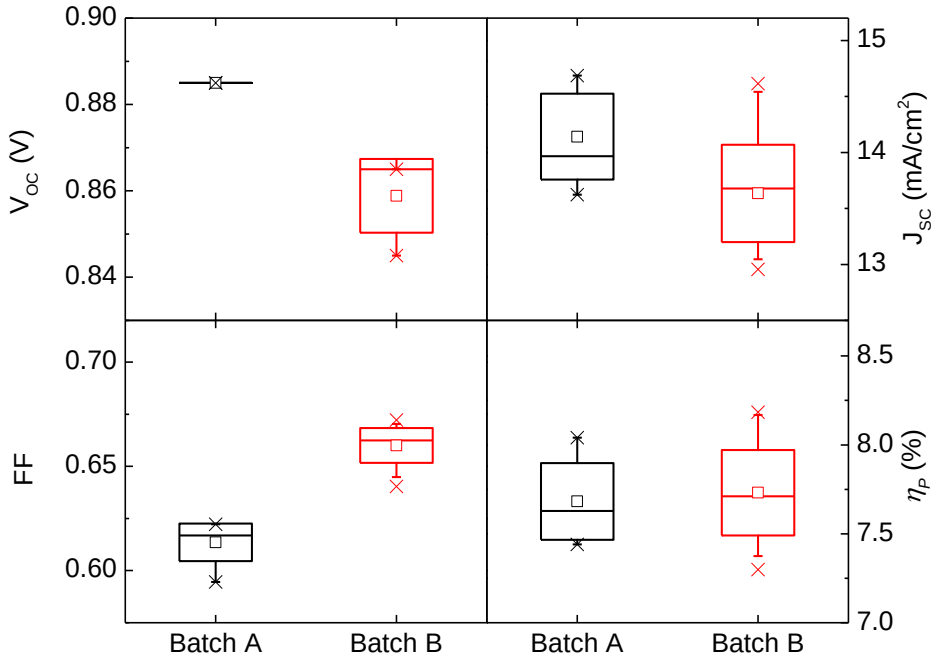

Figure 7.11 Operating parameters for devices fabricated on different batches of ITO, shown as a 5-95 whisker plot and a box plot of standard deviation. The □ indicates the mean value, and the × indicates the maximum or minimum value.

Atomic Force Microscopy (AFM) experiments were carried out on these two batches of ITO substrates and the results are shown in Figure 7.12. Based on a 4 μm^2 image, the

root mean square roughness (R_{ms}) is calculated to be 2.06 nm for batch A and 3.52 nm for batch B. Batch A is smoother than batch B.

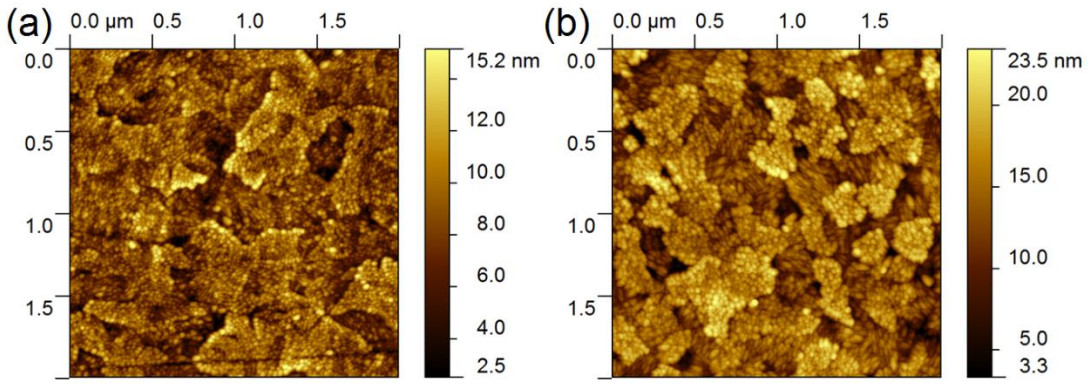

Figure 7.12 Atomic force microscopy images for ITO batch A (a) and B (b).

Previous literature has shown that the sheet resistance of ITO substrate can significantly impact device operation. As a result, low sheet resistance is favored over high transmittance when selecting ITO substrates.[223] For the ITO substrates used in this study, sheet resistance was measured using the four-point probe method and calculated using Equation 7.4.

$$R_{sheet} = \frac{\pi}{\ln 2} \cdot \frac{I}{V} \qquad \text{Equation 7.4}$$

The values are listed in Table 7.1. No significant difference in sheet resistance is observed for these two batches of ITO. The reduction of V_{OC} can be explained by the larger R_{ms} observed in ITO batch B. A rougher ITO substrate may lead to a less uniform organic film grown on top of it, possibly causing local hot spots with high dark current which reduces V_{OC}.

Table 7.1 Morphological and electrical parameters for two batches of ITO substrates

ITO Batch	**R_{ms} (nm)**	**Sheet resistance (Ω/□)**	**Fitted R_s (Ωcm^2)**
A	2.06	9.12±0.53	0.79±0.06
B	3.52	8.99±0.39	0.46±0.03

Series resistance (R_s) of devices grown on different batches of ITOs are calculated by fitting the dark current with generalized Shockley equations and are also listed in Table 7.1.[117] Devices grown on ITO batch B show a >40 % reduction in series resistance when compared to devices grown on ITO batch A, albeit the two batches of ITO show roughly the same sheet resistance according to the four-point probe measurement. ITO morphology may play a role in determining R_s. The difference in R_s will eventually impact FF, with ITO batch B (with lower R_s) showing higher FF.

Both large-area and small-area devices based on the optimized architecture are fabricated to ensure that the testing results are not inflated by errors in defining device active area.[222, 224] Typical current density-voltage characteristics of devices with the following structure: 10 nm MoO_x/70 nm DTDCPB:C_{70} (1:2)/10 nm BCP/100 nm Al, and an active area of 0.785 mm^2 and 9 mm^2 are plotted in Figure 7.13. Device operating parameters extracted from the plot are listed in Table 7.2, containing both the measured and spectral mismatch corrected J_{SC} and η_P. The large-area device shows lower V_{OC} and J_{SC} but a higher FF, overall the η_P stays roughly the same.

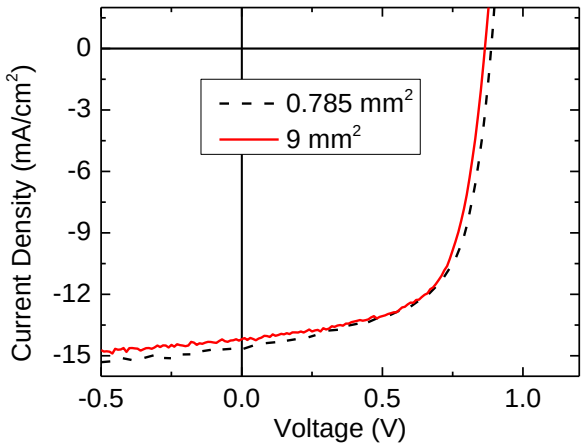

Figure 7.13 Comparison of device performance between large-area device and small-area device under simulated AM 1.5G illumination at 100 mW/cm^2.

Table 7.2 Operating parameters for devices with two different active areas

Device Area (mm^2)	**V_{OC} (V)**	**J_{SC} (mA/cm^2)**	**J_{SC} corrected (mA/cm^2)**	**FF**	**η_P (%)**	**η_P corrected (%)**
0.785	0.89	14.6	14.8	0.62	8.0	8.2
9	0.86	14.2	14.4	0.65	7.9	8.1

7.4 Device Lifetime and Stability

In order to characterize the stability of BHJs constructed from DTDCPB-C_{70}, device lifetime was tested. Devices with an area of 9 mm^2 were hermetically packaged using a microscope cover glass and OG142-112 UV curable epoxy obtained from Epoxy Technology Inc., followed by UV curing (100 mW/cm^2) for 3 minutes. The packaged devices were continuously exposed to simulated AM1.5G solar illumination (100 mW/cm^2) and kept in open-circuit condition in between testing. The device operating parameters are shown in Figure 7.14.

Over a testing period of 90 hours, both J_{SC} and FF reamined constant while V_{OC} showed minor reduction. The overall η_P followed the trend of V_{OC}. The reduction of V_{OC} can be related to the degradation at MoO_x-organic interface or D-A interface and furhter characterization is needed to identify the detailed mechanism. As a result, the projected lifetime (t_{50}) of the encapsulated device exceeds 5000 hrs based on the preliminary results.

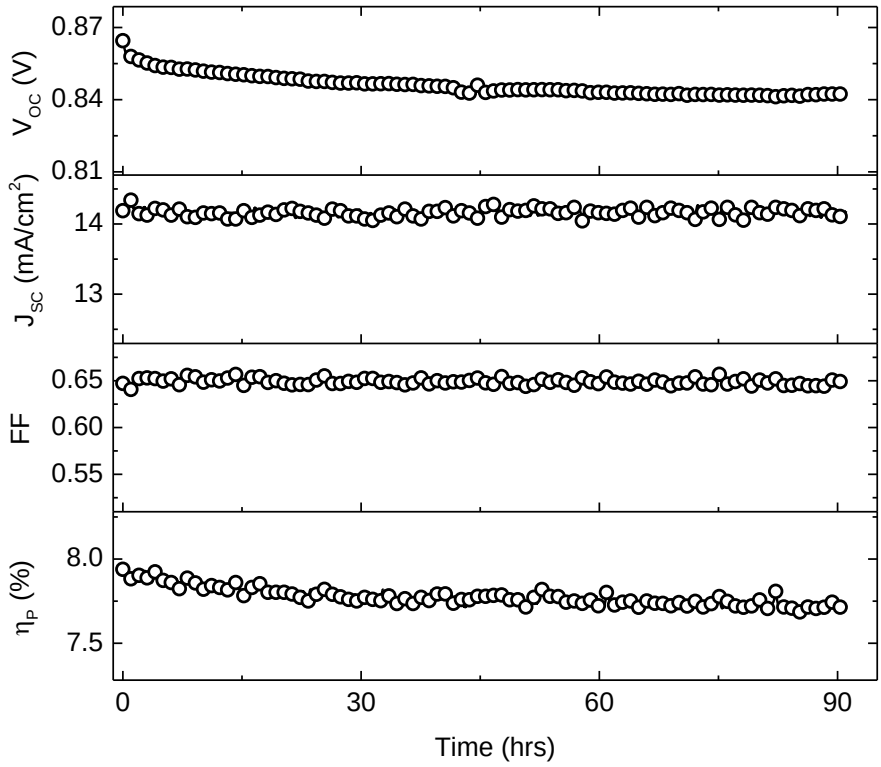

Figure 7.14 Degradation of a hermetically packaged BHJ OPV containing a 1:2 mixture of DTDCPB:C_{70} (70 nm) under continuous exposure to AM1.5G simulated solar illumination at 100 mW/cm^2.

The shelf lifetime of the packaged device is also examined to study the stability of various interfaces in the device architecture. The packaged devices were stored in ambient, and tested periodically under AM1.5G simulated solar illumination (100 mW/cm^2). Figure

7.15 shows the resulting device operating parameters with time. Within one year, the V_{OC} remains almost unchanged, while J_{SC} shows a minor reduction and the FF increases slightly. After one year, both J_{SC} and FF start to decrease drastically, possibly due to the delamination of cathode or the crystallization of exciton blocking layer. Further characterization is needed to identify the failure mechanism. In general, the BHJ OPVs fabricated show not only superb performance but good stability as well.

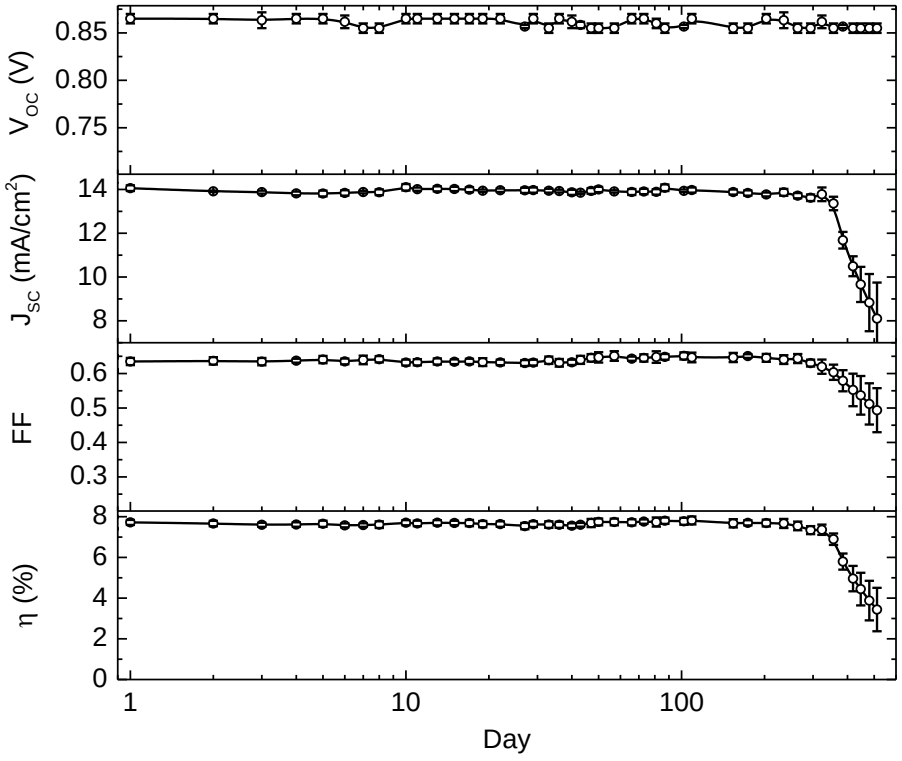

Figure 7.15 Device operating parameters tested intermittently under simulated AM1.5G illumination at 100 mW/cm^2 for a hermetically packaged BHJ OPV containing a 1:2 mixture of DTDCPB:C_{70} (70 nm).

7.5 Conclusions and Summary

The PMHJ architecture is near ubiquitous in the field of vapor-deposited small molecule OPVs. Here however, we demonstrate that the organic planar layers in the PMHJ may not always favorably impact device efficiency. The significance of this result is not limited to the D-A pairing of DTDCPB:C_{70} as most small molecule donor materials have low charge carrier mobilities and tend to limit the overall charge collection efficiency. This work has permitted the realization of high efficiency in a simple BHJ device based on the D-A pairing of DTDCPB-C_{70}. Unlike many BHJ OPVs based on vapor-deposited small molecules, this efficiency does not come at the expense of the FF. In fact, the high FF observed in the optimized DTDCPB-C_{70} device rivals those often observed in the most efficient solution processed BHJ OPVs.[223, 225] An average power conversion efficiency of (7.9±0.3)% is achieved under AM1.5G solar simulated illumination (mismatch-corrected), demonstrating that this simple device architecture can outperform the more commonly applied PMHJ structure.

8. New Donor Materials for Improved Efficiency[†]

8.1 Design Rules for Narrow-bandgap Donor Molecules

From previous discussion, it is clear that donor molecules with narrower bandgaps and deep HOMO levels are needed to further improve η_P. The most widely adopted method to reduce the bandgap of an organic molecule is to adopt a D-A molecular architecture which contains an electron-donating moiety and an electron-withdrawing moiety.[226-227] The electron-donating moiety has shallower HOMO-LUMO energy levels compared to the electron-withdrawing moiety. When the two are bridged to form a new molecule, the hybridization of molecular orbitals will result in an unusually low HOMO-LUMO gap as shown in Figure 8.1.

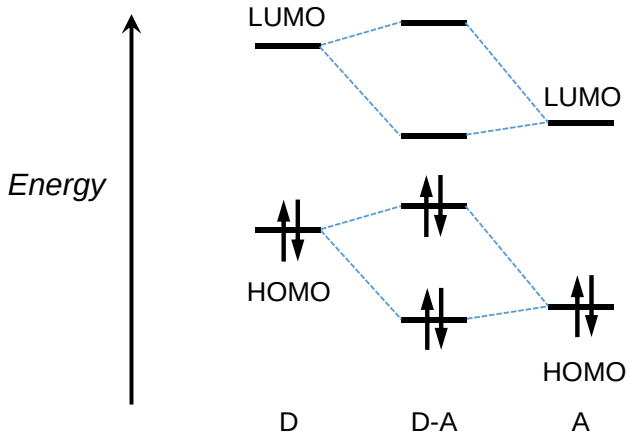

Figure 8.1 Hybridization of energy levels between the electron donating (D) and electron withdrawing (A) moieties. The resulting molecular orbital shows a much reduced HOMO-LUMO energy separation.

[†] The new donor materials were synthesized by Prof. Ken-Tsung Wong's research group in the Department of Chemistry at National Taiwan University.

8.2 Introduction to D-A-A Structures

Chapter 7 showed that by using a D-A-A type donor molecule of DTDCPB, record high device efficiency can be achieved.[104] The D-A-A molecular architecture composed of an electron-donating moiety and two electron-withdrawing moieties. In comparison to the more general D-π-A molecular architecture, the degree of downshift on the LUMO energy level is larger than the upshift on the HOMO energy level in the D-A-A molecular architecture. This leads to a smaller bandgap and deep HOMO level, and eventually synergistic enhancement of both J_{SC} and V_{OC}.[228] In this chapter, we will further explore the property of a series of D-A-A type molecules derived from the structure of DTDCPB and evaluate their performance in OPVs.

8.3 Narrow-bandgap Donor Materials

Recently, the thieno[2,3-b]indole and thieno[3,2-b]indole have been studied as novel building blocks for light sensitizers in dye-sensitized photovoltaic cells.[229-230] Their structures are derived from carbazole, with the second benzene ring replaced by a thiophene ring, which has stronger electron donating ability. Therefore, the inclusion of thieno indole in molecular structure is expected to result in a red-shift of the absorption spectrum and improve the light absorption capability.[229] By replacing the ditolylaminophenyl moiety in the DTDCPB molecule with thieno[3,2-b]indole or thieno[2,3-b]indole, new donor molecules named NTU-1 and NTU-2 can be obtained. Their molecular structures are shown in Figure 8.2.

The absorption coefficients for ~30-nm-thick films of NTU-1 and NTU-2 are

measured and plotted in Figure 8.3. Both new compounds show broader and stronger absorption in the solar spectrum compared to DTDCPB. A narrow optical band gap of 1.65 eV and 1.58 eV can be extracted for NTU-1 and NTU-2 respectively. Both new compounds show more desirable optical properties compared to DTDCPB.

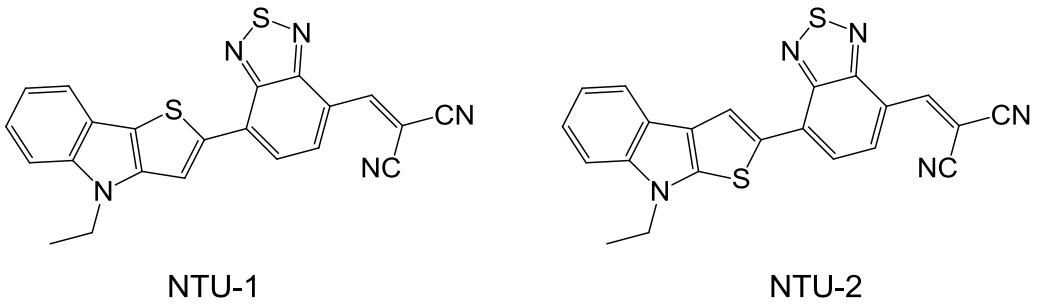

Figure 8.2 Molecular structures for NTU-1 and NTU-2.

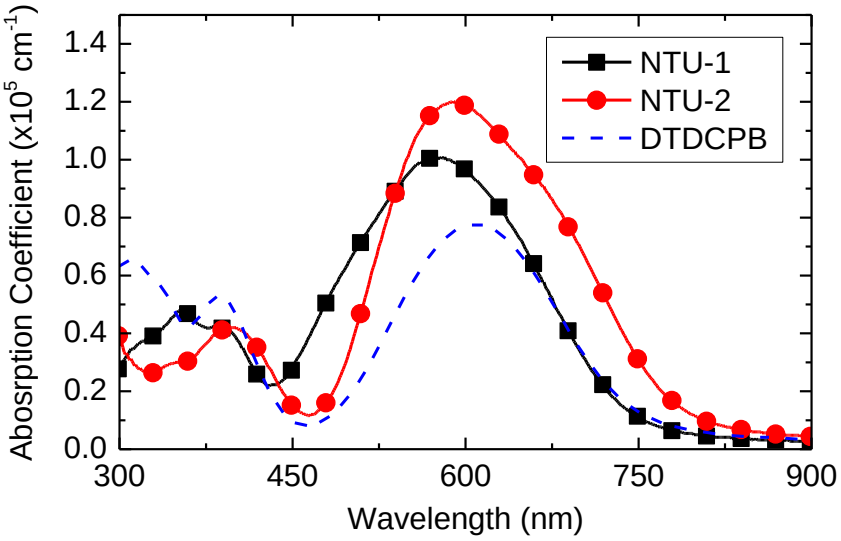

Figure 8.3 Absorption coefficient spectra for NTU-1 and NTU-2 obtained from ~30-nm-thick films on glass substrates. The spectrum for DTDCPB is overlaid for comparison.

Both NTU-1 and NTU-2 are paired with an acceptor material of C_{70} to fabricate PHJ OPVs with the device architecture of ITO/MoO_x 10nm/NTU 13 nm/C_{70} 40 nm/BCP 10

nm/Al 100nm. The current density-voltage characteristics for both devices show a kink in the fourth quadrant as depicted in Figure 8.4, indicating the existence of an imbalance in mobility between electrons and holes and possibly a hole extraction barrier at the anode-donor interface. The broadband reduction in the η_{EQE} further support that the device efficiency is primary limited by the charge transport.

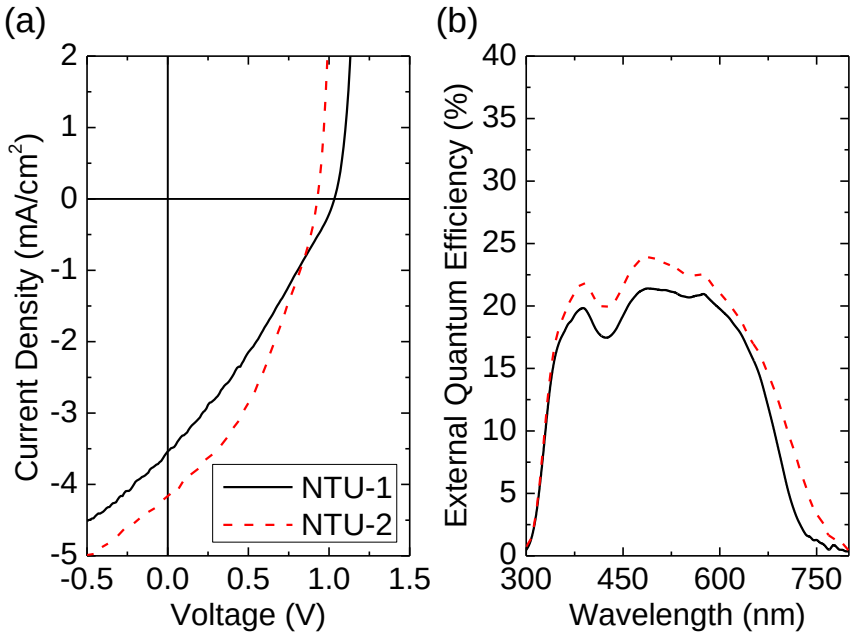

Figure 8.4 (a) Current-density voltage characteristics for PHJ OPVs with the device architecture of ITO/MoO_x 10nm/NTU 13 nm/C_{70} 40 nm/BCP 10 nm/Al 100nm. (b) External quantum efficiency spectra for devices in (a).

BHJ OPVs with the device architecture of ITO/MoO_x 10nm/donor: C_{70} ~55 nm/BCP 10 nm/Al 100 nm were also fabricated and tested. A wide range of donor concentration is explored to optimize light absorption and charge transport in the active layer. The device operating parameters are summarized in Figure 8.5. The donor concentration is optimized at 20% for both NTU-1 and NTU-2, with NTU-2 achieving a η_P of ~5%. The V_{OC} for both

sets of the devices showed improvement over the optimized DTDCPB:C_{70} BHJ OPV, indicating a deeper HOMO energy level of the new compounds. This improvement is consistent with the HOMO energy level estimated from cyclic voltammetry measurements.

However, BHJ OPVs fabricated with newly designed donor materials showed a much lower J_{SC} and FF compared to OPVs fabricated with DTDCPB. The cause for low FF is probably due to the poor hole mobility of the NTU compounds and the lack of phase separation in the uniformly mixed active layer. These two factors will lead to increased geminate and non-geminate recombination between photogenerated charge carriers and result in decreased J_{SC} and FF.

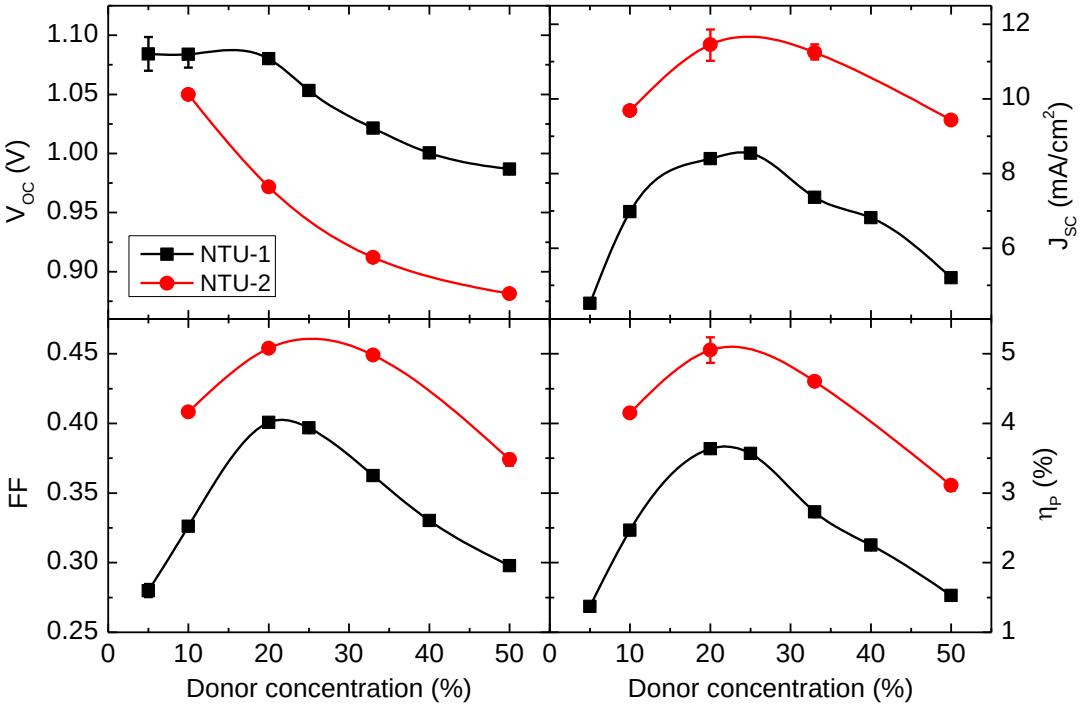

Figure 8.5 Device operating parameters for BHJ OPVs (ITO/MoO_x 10nm/donor:C_{70} ~55 nm/BCP 10 nm/Al 100 nm) fabricated with NTU-1 and NTU-2 at various donor concentrations.

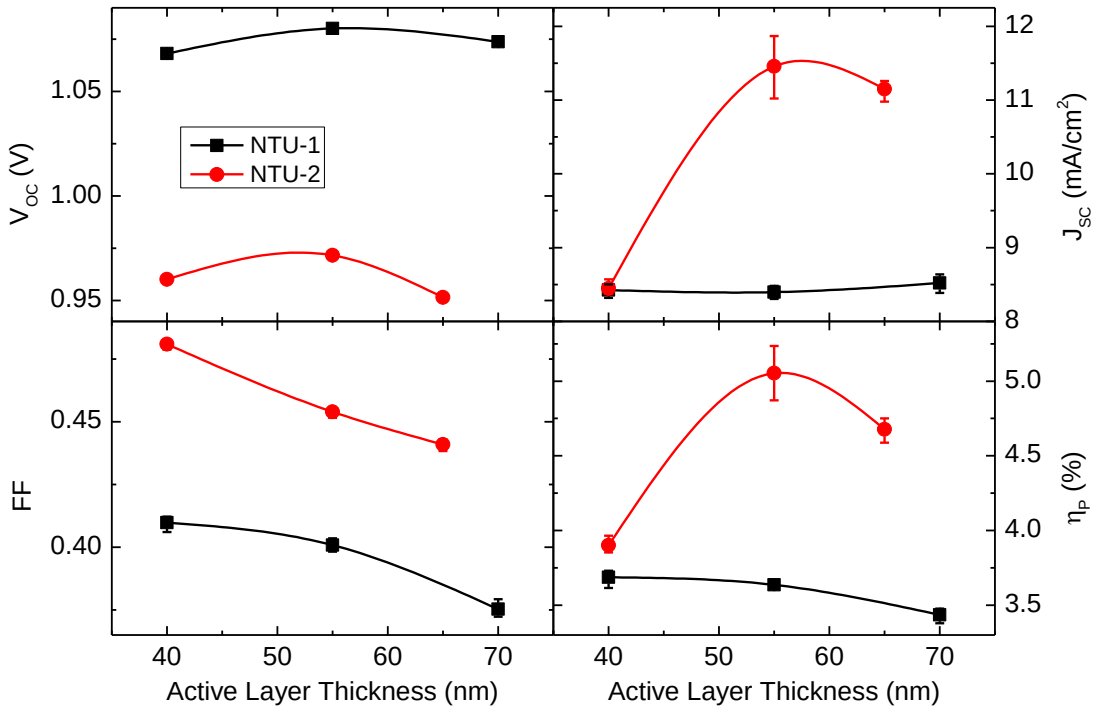

Figure 8.6 Device operating parameters for BHJ OPVs (ITO/MoO_x 10nm/donor: C_{70}=20:80 vol. x nm/BCP 10 nm/Al 100 nm) fabricated with NTU-1 and NTU-2 at various active layer thicknesses.

The dependence of device operating parameters on the active layer thickness is also measured and plotted in Figure 8.6. A drastic decrease of FF with increasing active layer thickness indicates that the favorable phase separation observed in the DTDCPB:C_{70} mixtures likely does not exist in the NTU:C_{70} mixtures.[97] The η_{EQE} spectra for the optimized BHJ OPV fabricated with NTU-1 and NTU-2 are plotted in Figure 8.7. The NTU-2:C_{70} BHJ OPV shows a broader coverage of the solar spectrum as NTU-2 has narrow bandgap compared to NTU-1.

Even though both NTU-1 and NTU-2 have superior optical properties compared to DTDCPB, the operation of OPVs is also strongly impacted the electrical properties of the materials used. In this case, the inferior hole mobility of NTU-1 and NTU-2 compared to that of DTDCPB overweighs the superior light absorption ability, and results in deteriorated η_P. To overcome the bottleneck of low mobility, the effect of thermal annealing on film crystallinity needs to be studied. The device efficiency can also be greatly enhanced if phase separation can be promoted with post-treatment of the organic active layer. More details related to this topic will be discussed in Section 10.2.1.

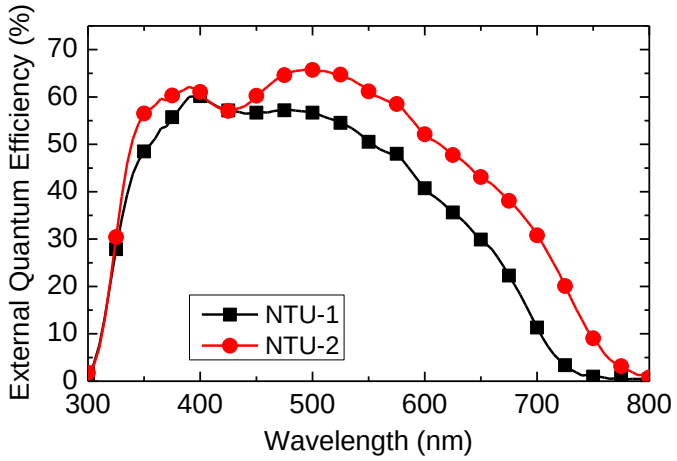

Figure 8.7 The η_{EQE} spectra for the optimized BHJ OPVs in Figure 8.5.

8.4 Fluorinated DTDCPB Compounds

The previously described method of synthesizing D-A-A type molecules with newly designed electron-donating moiety is effective in synergistically improving both light absorption and V_{OC}. However, there is unpredictable impact on the molecular packing and

the charge carrier mobility of the newly designed molecule by making such drastic change to the molecular backbone. An alternative is to introduce subtle chemical modification to an existing efficient molecule like DTDCPB.

In this section, the impact of fluorination on the DTDCPB molecule is studied. Two possible forms of the mono-fluorinated DTDCPB named DTDCPB-F_o and DTDCPB-F_m are shown together with the original DTDCPB molecule in Figure 8.8.

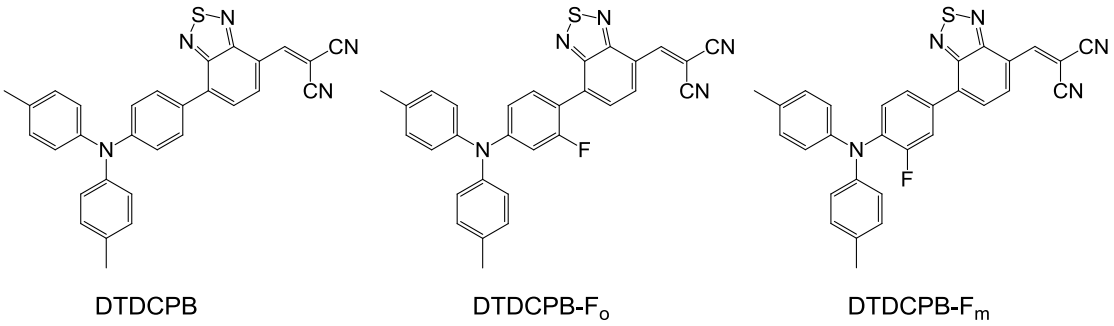

Figure 8.8 Molecular structures for DTDCPB, DTDCPB-F_o and DTDCPB-F_m.

By introducing F as an electron withdrawing group to the backbone of DTDCPB, a deeper HOMO energy level can be achieved. This will lead to an increase in V_{OC} for OPVs fabricated with fluorinated DTDCPB. However the fluorination is not without consequences. The LUMO energy level of the molecule is not significantly affected by the fluorination due to the addition of F on electron-donating moiety rather than the electron accepting moiety. Consequently, the HOMO-LUMO energy gap of the fluorinated compound is increased. This change is reflected in the absorption spectra of the fluorinated DTDCPB as shown in Figure 8.9. Additionally, by withdrawing electrons away

from the donor moiety, the absorption coefficient is also reduced. These features lead to a reduction in J_{SC} for OPVs fabricated with fluorinated DTDCPB.

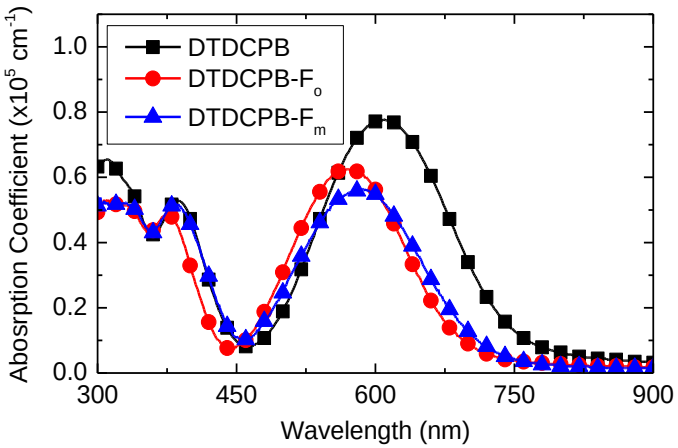

Figure 8.9 Absorption coefficient spectra of DTDCPB, DTDCPB-F_o and DTDCPB-F_m obtained from ~30-nm-thick films on glass substrates.

The question now becomes whether the increase in V_{OC} will compensate for the decrease in J_{SC} and improve η_P. To answer this question, BHJ OPVs with the device architecture of ITO/MoO_x 10nm/donor:C_{70} ~55 nm/BCP 10 nm/Al 100 nm are fabricated by co-depositing the fluorinated DTDCPB and C_{70} at a total rate of 0.2 nm/s. The dependence of device operating parameters on donor concentration is plotted in Figure 8.10. Both fluorinated DTDCPB compounds showed improved V_{OC} together with reduced J_{SC} as predicted. More importantly, the FF of devices fabricated with fluorinated DTDCPB is very similar to that of the devices with regular DTDCPB throughout a wide range of donor concentrations. This suggests that the charge transport property and the morphology of the mixed DTDCPB:C_{70} film is not affected by the fluorination process. Even though devices

containing fluorinated DTDCPB show a lower η_P owing to the low J_{SC}, the fluorination method introduces less disruption to the electrical performance of the original material.

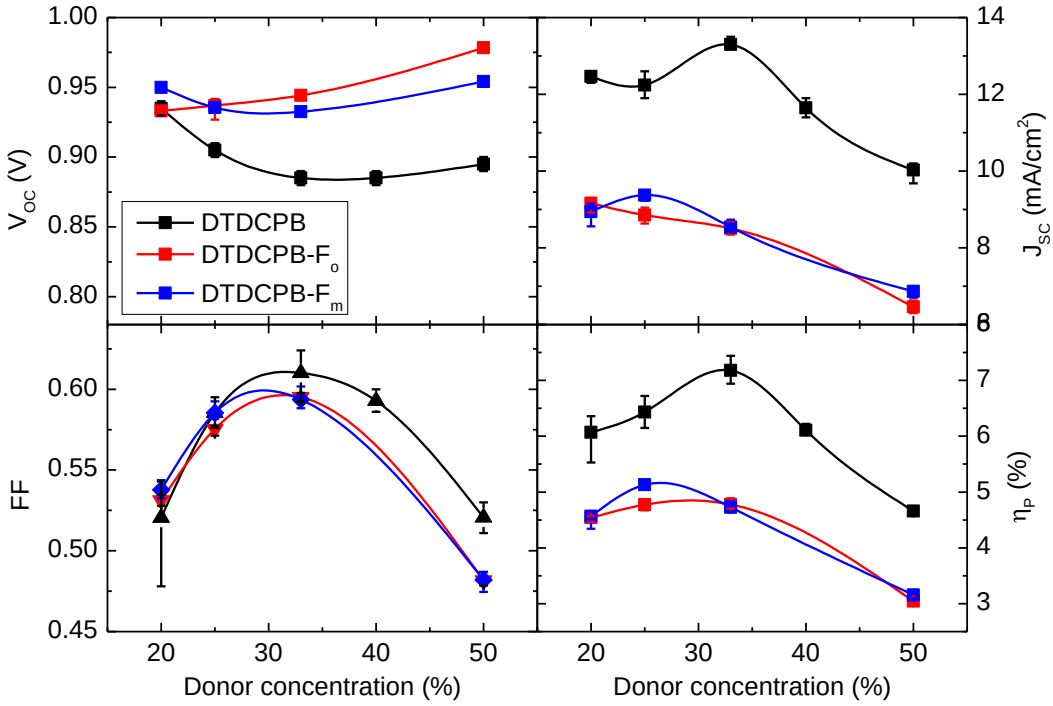

Figure 8.10 Device operating parameters for BHJ OPVs (ITO/MoO_x 10nm/donor: C_{70} ~55 nm/BCP 10 nm/Al 100 nm) fabricated with fluorinated DTDCPB at various donor concentrations.

A direct way to recover the loss in J_{SC} due to reduced absorption coefficient is increasing the active layer thickness. The data is compiled in Figure 8.11. The J_{SC} showed significant improvement by increasing the active layer thickness from 55 nm to 80 nm while the V_{OC} and FF are not significantly affected. The overall η_P follow the trend of J_{SC}. Finally, the fully optimized OPVs based on DTDCPB-F_o and DTDCPB-F_m can both achieve >6% η_P.

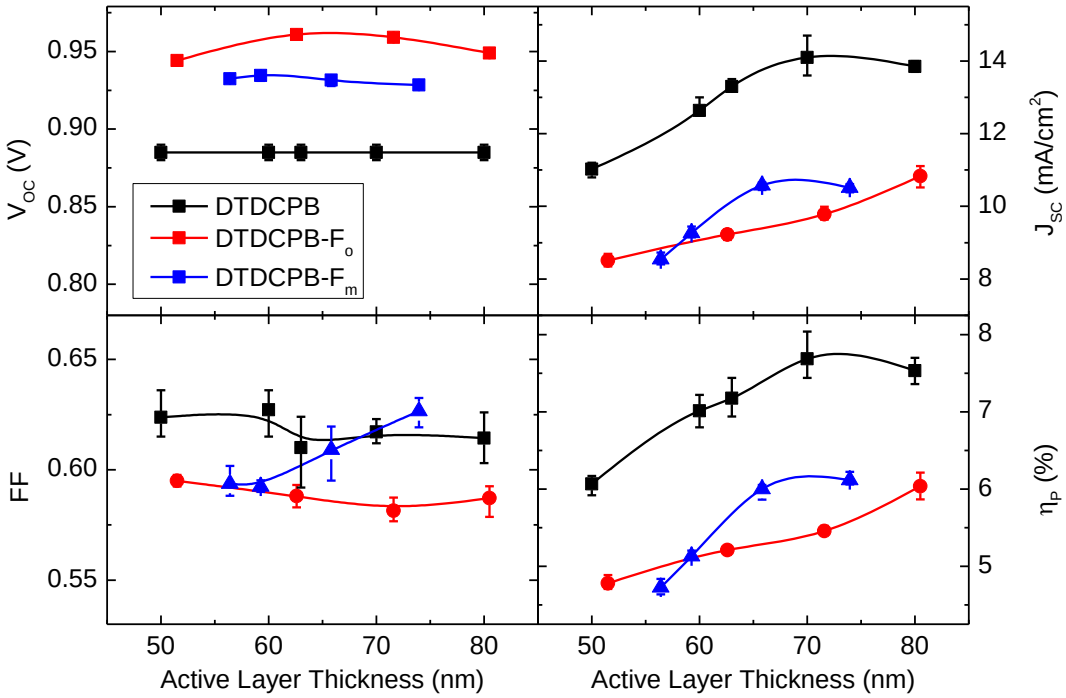

Figure 8.11 Device operating parameters for BHJ OPVs (ITO/MoO_x 10nm/donor: C_{70}=33:67 vol. x nm/BCP 10 nm/Al 100 nm) fabricated with fluorinated DTDCPB at various active layer thicknesses.

The η_{EQE} spectra for the optimized devices are shown in Figure 8.11. The low photoconversion efficiency at λ>700 nm is a major efficiency limiting factor. However, these materials would be beneficial when included in a tandem architecture, where an additional low-bandgap material is used to absorb light at longer wavelength. The independence of FF on the active layer thickness also allows more freedom in engineering the optical field for optimized photocurrent generation. More related details will be discussed later in section 10.2.2.

The V_{OC} can be further increased by introducing a secondary F atom to the backbone. Despite the increase in V_{OC}, secondary fluorination will also lead to further blue-shift of

the absorption spectrum and reduction of the absorption coefficient. As a result, these materials showed reduced η_P compared to mono-fluorinated DTDCPB materials, even though generating a V_{OC} of >1 V. The detailed device operating parameters are included in the Appendix C.

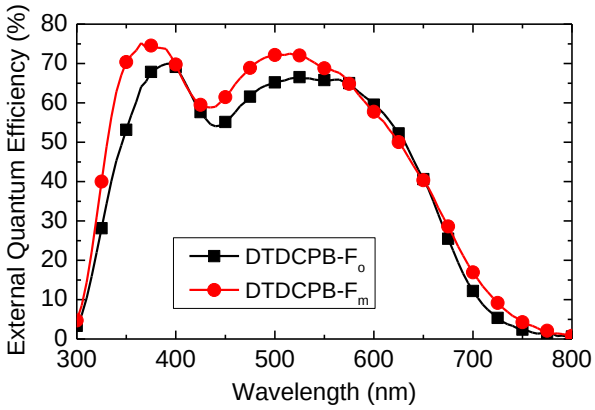

Figure 8.12 The η_{EQE} spectra for the optimized BHJ OPVs in Figure 8.11.

8.5 Conclusions and Summary

A series of new compounds based on the D-A-A molecular structure were synthesized. The NTU compounds adopt a thieno indole unit to replace the ditolylaminophenyl unit in the DTDCPB molecule and achieved more desirable optical property for photovoltaic applications. However, the newly designed NTU compounds lack the ability to transport holes efficiently, leading to increased charge recombination and low FF in both PHJ and BHJ OPVs. The optimized BHJ OPV achieved a η_P of 3% with NTU-1, and 5% with NTU-2 when using C_{70} as the acceptor. Further studies on the impact of thermal annealing on film crystallinity may help improve the η_P.

Work has also been done on developing fluorinated DTDCPB compounds for enhanced V_{OC}. The enhancement in V_{OC} is however at the price of decreased J_{SC} and the overall η_P decreases after the fluorination. Even though current results do not show improved η_P in single junction architecture, the blue-shifted spectra of these fluorinated DTDCPB compounds may prove useful in a tandem architecture.

Strategies for improving the η_P of devices based these new donor materials will be discussed in section 10.2.

9. Novel Hybrid Organic-Inorganic Perovskite Photovoltaic Cells

9.1 Overcoming the Voltage Loss

In previous chapters, the major losses for V_{OC} in OPVs have been identified as the D-A interface energy offset and the CT state binding energy. Both mechanisms originate from the nature of Frenkel excitons in organic semiconductors. For OPVs, these loss pathways can be minimized but not eliminated. Developing new materials with minimal exciton binding energy is the only way to fully overcome the V_{OC} loss.

However, very few materials promise minimal exciton binding energy and low fabrication cost simultaneously. Both academia and industry are searching for a solution processable material that can achieve comparable η_P to that of conventional crystalline Si technology. Recently, the use of organo-metal halide perovskite materials for photovoltaic applications has attracted growing attention. This new type of material has the advantages of strong absorption, high charge carrier mobility, low non-radiative carrier recombination rate and low cost. Together with the ability to build on over 20 years of experience of related dye-sensitized and organic photovoltaic technology, perovskites are ideal candidates for replacing crystalline Si photovoltaic cells. With 6 years of development, the η_P of perovskites cells now exceeds 20%, on par with existing commercialized thin film photovoltaic technologies.[2] The only drawbacks are the toxicity of lead that constitute all highly efficient perovskite photovoltaic cells to date, the rapid degradation when exposed to moisture and ultraviolet radiation and the anomalous hysteresis effect.

9.2 Introduction to Perovskites

9.2.1 Structure of Perovskites

Perovskites are materials with the chemical structure of ABX_3 and have a well-defined crystal structure as shown in Figure 9.1. The two major groups of perovskites are oxide perovskite and halide perovskite, while the latter is of great interest for photovoltaic application. The X in ABX_3 represents halide anions like F^-, Cl^-, Br^- and I^-. The B represents divalent metal cations including Pd^{2+}, Sn^{2+}, Ge^{2+}, Fe^{2+}, Co^{2+}, Ni^{2+} and so on. The A can represent two different types of monovalent cations: alkali metal cations (Li^+, Na^+, K^+, Rb^+ or Cs^+) and organic cations (aliphatic or aromatic ammonium).[231-233]

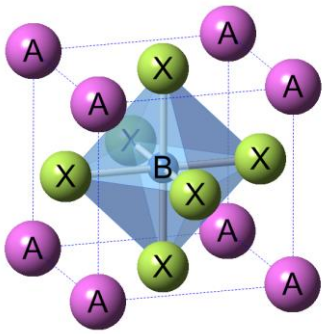

Figure 9.1 Example of the perovskite ABX_3 unit cell with a cubic structure.

Given the relative size of cations and anions in the perovskite structure, the unit cell can take cubic, tetragonal or orthorhombic configurations. The tolerance factor t ($(R_A+R_X)/\sqrt{2}(R_B+R_X)$) and octahedral factor μ (R_B/R_X) are often calculated as constraints for the formation of perovskite structure. Commonly, $0.81 < t < 1.11$ and $0.44 < \mu < 0.90$ is required.[233] Such loose constraints on ion radius adds to the versatility of perovskites.

The size of ions can not only affect crystal structure but also electronic structure.

Generally, the bandgap of perovskite can be reduced with larger ions. For example, the bandgap of $CH_3NH_3SnI_3$ has a 0.3 eV lower than $CH_3NH_3PbI_3$. Additionally, even though the organic ions do not participate in the formation of frontier orbitals, the steric effect induced by the organic ions can also affect the bandgap. Commonly, perovskites with larger organic ions will have smaller bandgap.

The first report on halide perovskite materials for photovoltaic applications dated back to 1980, when Salau et al. discovered that $KPbI_3$ has a direct bandgap of 1.4~2.2 eV, which matches well with the solar spectrum.[234] However, no device was made using this material. Recent studies on halide perovskites are based more on work by Mitzi and coworkers on thin film transistors and light emitting diodes since 1995.[235-236] In 2008, Miyasaka and coworkers showed a $CH_3NH_3PbBr_3$ dye-sensitized cell with an efficiency of 2.2%, which was the first demonstration of halide perovskite for photovoltaic application. By replacing bromine with iodine, the efficiency is further improved to 3.8% in 2009.[237] Subsequently, $CH_3NH_3PbI_3$ has been widely studied to replace conventional N719 dye sensitizers in dye-sensitized solar cells. However, the liquid electrolyte used in DSSCs will dissolve the halide perovskite and cause rapid degradation of performance.[238] This has led to the replacement of electrolytes with a solid-state hole transporting layer. As a result, both efficiency and stability were greatly improved.[239-240] In 2012, two breakthroughs lead to a rapid expansion in the use of perovskite for photoconversion. The first was the use of a mixed-halide $CH_3NH_3PbI_{3-x}Cl_x$ which has been proven to exhibit better stability and charge transport than the pure iodide equivalent.[241] The second is the discovery of ambipolar charge transport in $CH_3NH_3PbI_3$ which can eliminate the use of scaffolding.[242] To date, the

η_P of perovskite photovoltaic cells has exceeded 20%.[2, 243]

9.2.2 Ideal Properties for Applications in Photovoltaics

Among a wide variety of halide perovskites, $CH_3NH_3PbI_3$ is the most widely studied due to its ideal properties for photovoltaic application. This material shows strong absorption in the solar spectrum, comparable to that of a direct bandgap III-V material like GaAs.[231-233, 244-246] Absorption measurements on halide perovskites shows two strong spin-orbit split excitonic absorption threshold. In consequence, a 300-nm-thick film of $CH_3NH_3PbI_3$ is sufficient for light absorption.[247] This would help reduce the device thickness for light absorption and facilitate charge collection. Additional temperature dependent photoluminescence quenching measurements confirm that the excitons generated in $CH_3NH_3PbI_3$ are delocalized with a binding energy of ~19 meV, an order of magnitude smaller than excitons generated in organic semiconductors.[248] About 57% of the excitons generated in $CH_3NH_3PbI_3$ will spontaneously dissociate into free charge carrier at room temperature.

The charge carrier lifetime is another critical parameter for minimizing the loss of V_{OC} compared to the bandgap.[249] Surprisingly, $CH_3NH_3PbI_3$ exhibits a low non-radiative recombination rate given the polycrystalline nature of the film. The grains in $CH_3NH_3PbI_3$ thin films are near micrometer in size and can help reduce intragranular defects and non-radiative recombination.[249] In addition to long lifetime, photogenerated charge carriers need also have high mobility for realizing efficient charge collection at the electrode. Transient photoluminescence quenching experiment estimated >1 μm diffusion lengths for

both hole and electron, exceeding the film thickness required for efficient light absorption.[26, 241, 246]

More interestingly, $CH_3NH_3PbI_3$ shows unusual defect mechanisms. Density functional theory (DFT) calculations concluded that the defects responsible for forming mid-gap trap states have very high formation energies, so that they are not likely to exist.[250-251] These mid-gap trap states could serve as recombination centers for Shockley-Read-Hall recombination mechanism which leads to loss in V_{OC}.

9.2.3 Device Architecture and Fabrication

p-i-n Architecture

Perovskite photovoltaic cells ubiquitously adopt a p-i-n architecture where the perovskite layer is sandwiched between a p-type hole transport layer (HTL) and an n-type electron transport layer (ETL) as shown in Figure 9.2. Due to the long carrier diffusion length, the perovskite layer is typically >300-nm-thick, sufficient for light absorption. The HTL and ETL can also improve the rectification of the junction and enhance V_{OC}. Organic semiconductors like spiro-OMeTAD and conjugated polymers are ideal candidates for

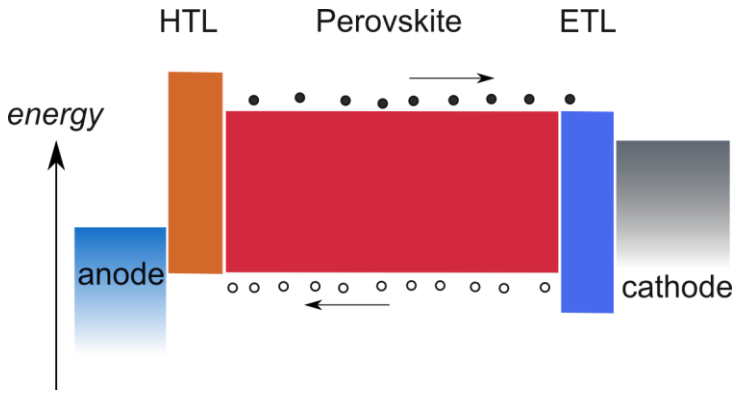

Figure 9.2 Energy level diagram of a perovskite photovoltaic cell.

HTLs, while ZnO, TiO_2, ZrO_2 and PCBM are widely used as ETLs. The processing of HTLs and ETLs are directly borrowed from experiences in dye-sensitized solar cells and organic photovoltaic cells while the fabrication of pinhole-free perovskite layer is most challenging.

Spin-coating

Spin-coating is the most widely adopted method for fabricating perovskite photovoltaic cells due to its simplicity. A single precursor solution is prepared by dissolving stoichiometric quantities of CH_3NH_3I and PbI_2 ($PbCl_2$) in polar solvents like γ-butyrolactone, dimethyformamide or dimethylsulfoxide. The solution is then spun-cast onto TiO_2 coated substrates at optimized concentration and temperature followed by thermal annealing. However, during the drying process, perovskites tend to agglomerate, leading to non-uniformity and voids in the resulting film. The reduced coverage will lead to a loss in light absorption and reduced shunt resistance, which eventually results in deteriorated device efficiency.[252]

In order to obtain a uniform and pinhole-free perovskite thin film, mesoporous scaffold are widely used to facilitate film formation. The mesoporous scaffold is prepared by spin-coating and sintering TiO_2 or Al_2O_3 nanoparticles with sizes of ~20 nm on top of the bottom electrode.[240] The scaffold can effectively confine the perovskite so that agglomeration is not likely to occur. Alternatively, a two-step process can also be applied to achieve uniform perovskite thin film. First, a PbI_2 solution is spun-coat on the TiO_2 coated substrate to form a compact layer of PbI_2. Secondly, the CH_3NH_3I vapor or solution is introduced to react with the PbI_2 film.[253-255] For the CH_3NH_3I solution, orthogonal solvent like isopropyl

alcohol is required to avoid dissolution of the deposited PbI_2 layer. Upon reaction with CH_3NH_3I, the PbI_2 thin film will expand in volume by ~75%. Consequently, pin-hole free perovskite layer can be formed on smooth substrates.

Vapor Deposition

There has also been significant effort on achieving pinhole-free film of $CH_3NH_3PbI_3$ via vapor deposition. Commonly, CH_3NH_3I and PbI_2 precursors are loaded into individual crucibles and heated till sublimation in a vacuum chamber. The deposition rate of each precursor is adjusted to allow stoichiometric deposition of $CH_3NH_3PbI_3$ on the substrate. The mixed film of two precursors is then annealed at elevated temperature to complete the reaction and form perovskite.

9.3 Remaining Challenges

Even though the field of organo-metal halide perovskite photovoltaic cells has seen extraordinary development over the last few years, there still exists several major challenges prior to commercialization. First of all, perovskite is sensitive to moisture and UV irradiation which can cause significant degradation in device performance.[256] Secondly, the toxicity of Pb is a major limiting factor for the widespread application of perovskite photovoltaic cells. The cost for disposal and recycling toxic materials together with increasingly restrictive legislation may marginalize the perovskite technology compare to other safer technologies.[233]

More importantly, the anomalous hysteresis effect observed in perovskite photovoltaic cells hinders reliable energy harvesting.[257-262] This problem is especially severe for

perovskite photovoltaic cells with a planar architecture compared to devices using a mesoporous TiO_2 scaffold.[258-259, 262-263] The variation in η_P can be >50%, depending on the testing condition. Mainstream theories for the anomalous hysteresis effect can be categorized as (i) defect states within or near the surface of the material that can act as traps for charge carriers. The trapping of charge carriers create good contacts at the electrode interface and facilitate charge collection;[264] (ii) the ferroelectricity of perovskite that will lead to the polarization of the material. This polarization could potentially impact the charge collection at the electrodes;[262, 265-266] (iii) ion motion within the perovskite layer under bias. The migration of ions can create doping and screen space charge that can affect charge collection.[250-251, 267]

Unger et al. have previously demonstrated that the performance of perovskite photovoltaic cells can be greatly enhanced by applying a positive bias on the device prior to measurements.[259] This bias poling effect has also been reported by Xiao et al in a later publication and the cause is attributed to ion motion under electric field. The ion motion introduces self-doping effect at the electrode interface and creates band bending.[255] In this work, we explore both temporal and temperature dependence of bias poling effect in $CH_3NH_3PbI_3$ based planar perovskite photovoltaic cells and propose explanations to the anomalous hysteresis effect observed.

9.4 Results and Discussion

9.4.1 Experimental Methods

Perovskite photovoltaic cells were fabricated using indium-tin-oxide (ITO)-coated glass substrates having a sheet resistance of ~8-12 Ω/□. Substrates were cleaned in tergitol solution and in organic solvents and treated in UV-Ozone ambient for 10 minutes prior to thin film deposition. A compact TiO_2 layer with a thickness of ~40 nm was deposited on ITO substrates by spin-coating a mildly acidic titanium-isopropoxide (Sigma-Aldrich 97 %) solution in isopropanol (700 μl titanium-isopropoxide in 10 ml isopropanol with 0.013 M HCl and) at 3000 rpm for 30 seconds followed by sintering at 500 ℃ in air for 30 minutes. PbI_2 (Sigma-Aldrich 99%) was dissolved in dimethyl sulfoxide (DMSO) at a concentration of 1 M and filtered at 100 ℃. Both the TiO_2 coated substrates and the filtered PbI_2 solution were maintained at 100 ℃ prior to spin-coating. A smooth PbI_2 film can be obtained by dynamically spin-coating the PbI_2-DMSO solution while hot at 4000 rpm for 40 seconds.[268] A 40 mg/mL solution of CH_3NH_3I (Lumtec Inc.) in isopropanol was then spun on PbI_2 with the same spin speed and duration. The film stack was then annealed at 100 ℃ for 2 hours to allow the reaction between the two precursors (Figure 9.3a). Afterwards, a 15 mg/mL poly 3-hexylthiophene (Rieke Metals Inc., Regioregularity = 91-94%) solution was spin-coated at 3000 rpm for 45 seconds and dried at 100 ℃ for 30 minutes to form a 40-nm-thick hole transport layer. The structure was capped by sequential deposition of MoO_x (10 nm) and Al (100 nm) through a shadow mask at 0.05 nm/s and 0.3 nm/s respectively to define a device active area of 0.785 mm^2 (Figure 9.3b). All device parameters were

measured under AM1.5G simulated solar illumination (100 mW/cm^2) using an Oriel Xe solar simulator. All temperature dependent experiments were carried out in a Janis cryogenic probe station with liquid nitrogen cooling. Device temperature was monitored using a Si thermometer. Current density-voltage characteristics were measured using an Agilent 4155C parameter analyzer.

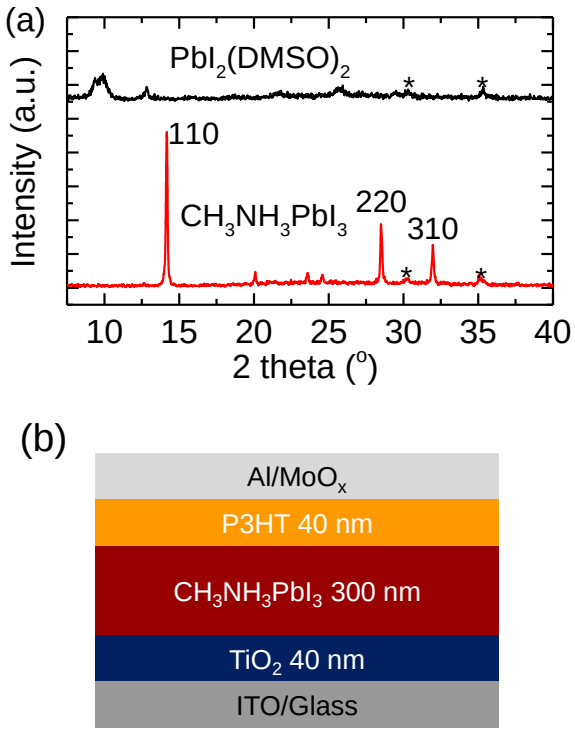

Figure 9.3 (a) The X-ray diffraction pattern of the $PbI_2(DMSO)_2$ precursor and the $CH_3NH_3PbI_3$ synthesized using the interdiffusion method. Peaks labeled with * are from the substrate. (b) Device architecture of the perovskite photovoltaic cell studied.

9.4.2 Observation of Poling Effect

Figure 9.4a shows the time-evolution of device performance at room temperature under simulated AM 1.5G solar irradiation at 100 mW/cm^2 while poling at +2 V. The

current density-voltage characteristics are recorded every 50 s by sweeping the voltage from 1.5 V to -0.5 V at a rate of 0.2 V/s, and the device remains illuminated and poled at +2 V in between scans. A significant improvement in device performance is observed within the first 100 s. Figure 9.4b and 9.4c show the evolution of device operating parameters with poling time. Both open-circuit voltage (V_{OC}) and fill factor (FF) increase significantly while short-circuit current density (J_{SC}) stays almost constant. Overall, the power conversion efficiency follows the trend of V_{OC} and FF, and increases from 4.9 % to 14 %.

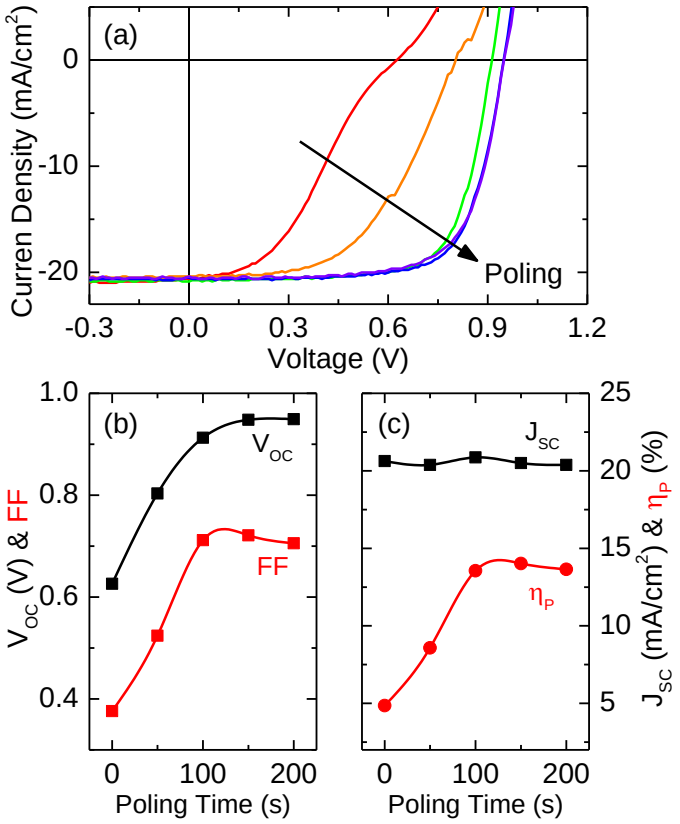

Figure 9.4 (a) The evolution of current density-voltage characteristics for a perovskite photovoltaic cell under +2 V bias poling. Scans were taken at 50 second intervals. (b), (c) Device operating parameters extracted from the current density-voltage characteristics in (a).

9.4.3 Temperature-dependent Measurements

While poling at a relatively large positive bias compared to V_{OC} can significantly improve device performance, the poling effect does not persist at room temperature and the device slowly evolves toward the initial state. We propose that the poling effect is related to the anomalous hysteresis observed in perovskite photovoltaic cells. When measuring the current density-voltage characteristics in the reverse-direction (from positive to negative voltage), the device is inevitably poled at high positive voltage prior to the maximum power output point and will thus show higher efficiency than scanning in the forward direction.

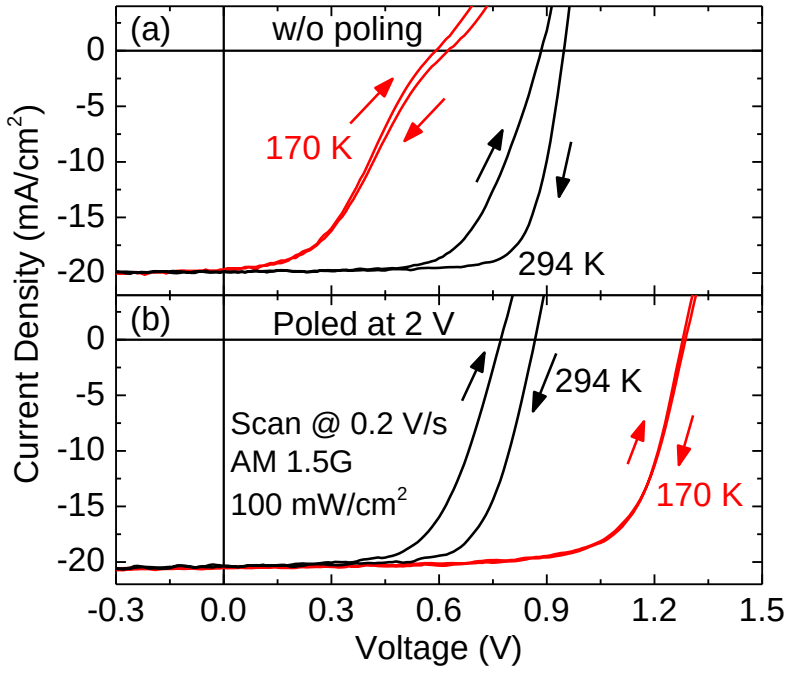

Figure 9.5 Current density-voltage characteristics of perovskite photovoltaic cells measured at 170 K and 294 K. (a) Device was kept in dark and open-circuit condition during cooling. (b) Device was kept in dark and poled at +2 V during cooling.

The temperature dependence of device performance is studied to explore the mechanism of poling.[269] Figures 9.5a and 9.5b show the device performance at room temperature and 170 K for two sets of devices. For the device of Figure 9.5a, no illumination or bias is applied during cooling. The hysteresis is much alleviated even though the device performance is as poor as the unpoled device shown in Figure 9.4a. In comparison, a constant bias voltage of +2 V is applied to the device of Figure 9.5b while cooling in the dark. Interestingly, not only is the hysteresis eliminated, the η_P is also much

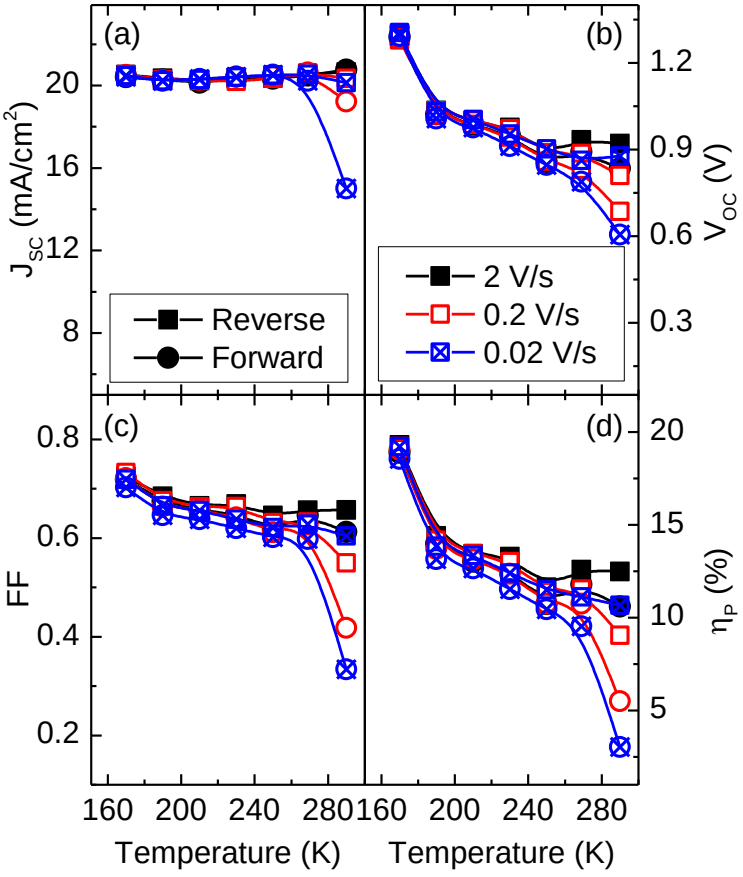

Figure 9.6 Operating parameters for the device mentioned in Figure 9.5b. Data collected by warming the device up from 170 K to 290 K.

improved from 12 % to over 19 %. This improvement of η_P is attributed to an increase in V_{OC} due to reduced charge carrier recombination and device dark current at low temperature. This observation indicates that perovskite photovoltaic cells can be stabilized in one poling state (poled or un-poled) at low temperature.

In order to examine the relaxation of the poled state with temperature, device operating parameters for the perovskite photovoltaic cells of Figure 9.5b are tracked upon warming from 170 K to 290 K. For this measurement, both scan directions and various scan rates are used to reveal the anomalous hysteresis effect. Figures 9.6a-d show the temperature dependence of all four device operating parameters, which can be divided into two phases. In phase I (170 K-250 K), both V_{OC} and FF decrease with increasing temperature while J_{SC} stays almost constant, consistent with the low exciton binding energy (~20-30 meV) in $CH_3NH_3PbI_3$.[270-271] Minimal hysteresis in device performance is observed at various scan rates during phase I. In phase II (250 K to 290 K), V_{OC} and FF continue to decrease with increasing temperature. Device operating parameters extracted from forward scan directions at low scan rates begin to deteriorate quickly. Significant hysteresis is observed and the poled state is no longer stable. Similar measurements on devices containing a poly-TPD hole transporting layer also show that the hysteresis is much reduced at low temperature when poled with a positive bias of 2 V during cooling and that the η_P is improved from 9% to 14.5%. A temperature of 250 K appears to be the critical value for stabilizing the poling effect, which indicates a small activation energy for the relaxation of poling effect.

To further examine the critical temperature, the decay of J_{SC} under illumination for a poled device is tracked upon continuous warming from 170 K to 295 K. Experimentally, the device is biased at +2 V to reach steady state and then quickly switched to short-circuit, allowing the relaxation of poling to be observed. The decay of J_{SC} with increasing temperature and time is shown in Figure 9.7. For T ≤250 K, no decay of J_{SC} is observed over 300 s. As expected, the stability of the bias poling effect is reduced at T >250 K and a clear decay in photocurrent is observed with time.

9.4.4 Proposed Theory for Hysteresis

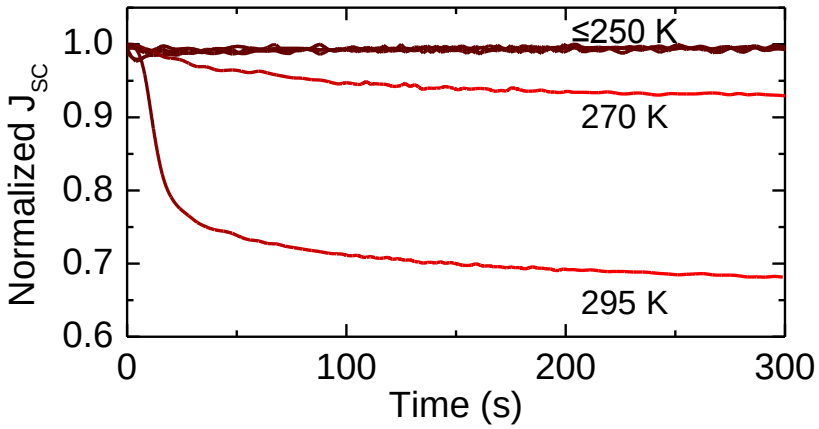

Figure 9.7 The decay of J_{SC} under AM1.5G simulated solar illumination (100 mW/cm^2) for perovskite photovoltaic cells at various temperatures.

Experimental observations show that the anomalous hysteresis effect in organo-metal halide perovskite photovoltaic cells is strongly temperature-dependent. Recently, Xiao et al. reported a giant switchable photovoltaic behavior under bias poling for $CH_3NH_3PbI_3$-based photovoltaic cells.[267] The switchable photovoltaic behavior is ascribed to a self-doping effect due to point defects created by the drift motion of ions in the perovskite thin film. These vacancy and interstitial defects have rather low formation energies and can

create shallow traps to induce self-doping according to previous DFT calculations on $CH_3NH_3PbI_3$.[250-251] The self-doping effect will strongly impact the charge transport in $CH_3NH_3PbI_3$ photovoltaic cells and is a possible cause of the observed temperature dependent hysteresis effect.

Films of $CH_3NH_3PbI_3$ fabricated on a smooth layer of TiO_2 layer likely have interfacial dipoles at the TiO_2-$CH_3NH_3PbI_3$ interface due to the oriented growth of perovskite on TiO_2 layers and defects with low formation energy (MA^+ vacancies).[245, 250, 272-274] This may result in an energy barrier for electron collection, as shown in Figures 9.8a-b. Thus, the interfacial defects cause inferior device performance prior to bias poling. The poling process may cause MA^+ to drift towards the bottom of the film and introduce n-type doping. Eventually, the electron extraction barrier at the TiO_2-$CH_3NH_3PbI_3$ interface is alleviated as shown in Figure 9.8c, thus improving the performance of the device with positive bias poling. At low temperature, the drift and diffusion of MA^+ is frustrated so that the device can be "frozen" in poled or unpoled state, thus leading to stabilized device operation with minimal hysteresis.

The mechanism described above is more plausible than an interfacial charge trapping/de-trapping mechanism as the poling bias is required during cooling to observe high efficiency in the poled state at low temperature. At 170 K, charge carriers remain sufficiently mobile (as indicated by the high J_{SC} and FF shown in Figure 9.6) to find and fill up traps. If only a model of trapping/de-trapping were sufficient to explain the results, devices would show high efficiency without constant poling during cooling, in contradiction of the data in Figure 9.5a.

Interestingly, not all perovskite photovoltaic cells show severe hysteresis or require bias poling to function.[243, 255, 275-276] In fact, the anomalous hysteresis is strongly related to device architecture and fabrication method. For example, devices fabricated on substrates covered by a hole transporting material like poly(3,4-ethylenedioxythiophene) polystyrene sulfonate (PEDOT:PSS) do not show hysteresis, as demonstrated by Xiao et al.[267] This is likely due to the fact that the band bending induced by defects does not impede hole extraction at the PEDOT:PSS-$CH_3NH_3PbI_3$ interface as also shown in Figure 9.8b or the absence of interfacial dipole at the PEDOT:PSS-$CH_3NH_3PbI_3$ interface. Bryant et al. have further demonstrated that for the PEDOT/perovskite/fullerene device architecture, there exists a much faster hysteresis mechanism which may relate to a capacitive charging/discharging current. This faster mechanism appears to be absent in the TiO2/perovskite/HTL device architecture examined here.[277].

For devices fabricated on a mesoporous TiO_2 scaffold, the collection of electrons is not limited to the bottom of the perovskite film, where the energy barrier exists. The TiO_2 scaffold may penetrate into the defect-free region of the perovskite film or disrupt the orientation of the interfacial dipole so that electrons can be collected through the scaffold without experiencing any energy barrier as shown in Figure 9.8c-d. By simply switching the conductive TiO_2 scaffold with an insulating Al_2O_3 scaffold, the same degree of hysteresis observed in planar devices will reappear.[240, 260, 262] This is due to the fact that electrons will again have to overcome the energy barrier at bottom electrode.

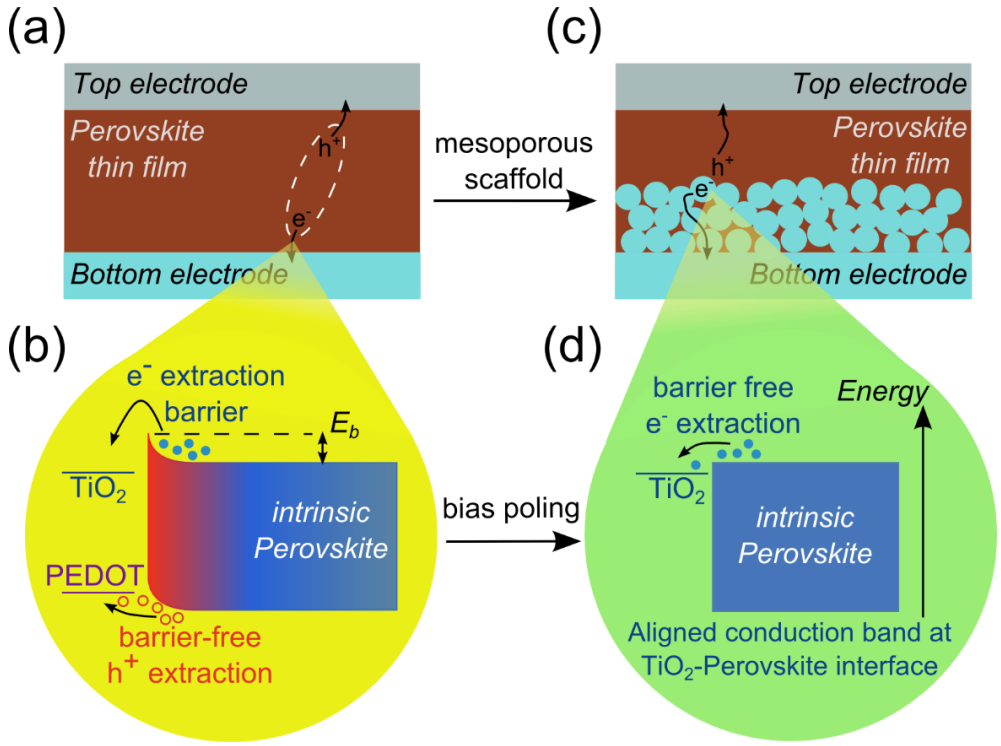

Figure 9.8 (a) Device architecture of a planar perovskite photovoltaic cell and (b) the possible energy level alignment at the bottom electrode-perovskite interface. The band bending at the bottom of the perovskite film will frustrate electron extraction but favor hole extraction. (c) Device architecture of a mesoporous perovskite photovoltaic cell and (d) the energy level alignment at the mesoporous electrode-perovskite interface. The barrier-free TiO_2-perovskite interface can also be achieved in planar perovskite photovoltaic cells after bias poling.

9.5 Conclusions and Summary

Organo-metal halide perovskites have been intensively studied for photovoltaic applications due to their superb optical and electrical properties. Even though the η_P of perovskite photovoltaic cells exceeds 20%, there still remain many challenges to the commercialization of this technology. One of the major obstacles is the observed hysteresis in device performance that could hinder stable device operation. We propose that the anomalous hysteresis is related to the observed bias poling effect on the current density-

voltage characteristics. The relaxation of poled state is observed to be fast at room temperature but can be significantly reduced at low temperature. By applying a positive poling bias during cooling, the poled state can be frozen at low temperature. Thus, the anomalous hysteresis in planar perovskite photovoltaic cells is eliminated and the device efficiency can be enhanced up to 19 % at 170 K. We also propose that the bias poling effect is due to the ion motion under applied electric field, which can reduce the electron extraction barrier near the TiO_2-$CH_3NH_3PbI_3$ interface.

However, the poling effect does not persist at room temperature and the device operating parameters will slowly decay to their initial values when the poling bias is removed. We propose that the poling effect is likely the cause of hysteresis effect in perovskite photovoltaic cells. When measuring the current density-voltage characteristics in reverse-direction (from positive to negative voltage), the device is inevitably poled at high positive voltage prior to the maximum power output point and will thus show higher efficiency than scanning in the forward direction.

Further research on this topic will require characterization of the compositional depth profile and local electric potential measurements to optimize the energy level alignment at various interfaces.

10. Conclusions and Future Research Directions

Previous chapters have described work exploring the impact of the D-A interface and anode interlayer on the operation of OPVs. A better understanding of the limit and loss mechanisms for V_{OC} in OPVs helped guide device engineering and new material synthesis for improved η_P. This chapter will highlight some of the important conclusions that have been arrived at and propose future research direction to help realize efficient energy harvesting from OPVs.

10.1 Conclusions

The majority of this work has focused on understanding the intrinsic limit and loss mechanisms of V_{OC} in OPVs. Chapter 4 established the method of combining temperature dependent measurements and electroluminescence technique to identify the theoretical maximum achievable $V_{OC.}$ The charge transfer state energy has been determined as the effective bandgap energy and also the theoretical maximum achievable V_{OC} in OPVs. The low V_{OC} is partially due to the Coulombic binding energy of the CT state. By engineering the local dielectric environment at the D-A interface to screen the Columbic attraction between oppositely charged carriers, the V_{OC} can be effectively improved.

Chapter 5 focused on other factors that may affect V_{OC} in OPVs. It has been observed that by incorporating a high-work-function MoO_x anode interlayer, a Schottky junction will be formed at the MoO_x-organic interface. The existence of this Schottky junction does not strongly impact the V_{OC} of a PHJ OPV at room temperature, but can significantly increase the upper limit for the maximum achievable V_{OC} at low temperature. Chapter 6 built on the

results of Chapter 5 and investigated the impact of the MoO_x-organic interface in fullerene-rich BHJ OPVs. A unique, temperature independent photoconversion process termed bulk-ionization was discovered in fullerenes and found to be responsible for ~16% of the total photocurrent and >30% of the photocurrent originating from C_{60} in an optimized SubPc-C_{60} BHJ OPV. Nonetheless, the V_{OC} of fullerene-rich BHJ OPV is governed by both charge transfer at the D-A interface and bulk-ionization in fullerene.

With a better understanding of device operation, Chapter 7 focused on simplifying device architecture for improved η_P. The D-A pairing of DTDCPB-C_{70} has previously been demonstrated to generate a record high efficiency of 6.8% in 2013, adopting a PMHJ architecture. However, by carefully examining the electrical and optical properties of DTDCPB, the existence of a DTDCPB planar layer was found to negatively impact device performance. The η_P was improved to > 8%, by simplifying the device architecture to a single bulk heterojunction. The superb robustness and stability of the simplified device architecture was also found to be ideal for manufacturing.

Based on the high-efficiency result achieved in Chapter 7, a collaborative effort was initiated with chemists from National Taiwan University to develop new donor materials with further optimized energy levels. Approaches including alternating the electron donating moiety and introducing fluorination have been explored. The newly designed molecules showed promising properties for realizing efficient energy harvesting from OPVs, yet further effort on optimizing film crystallinity and developing tandem device architecture is required.

Chapter 9 took a new approach at enhancing η_P by investigating a new type of hybrid organic-inorganic perovskite material as the light absorber. The minimal exciton binding energy in perovskites eliminates the loss of exciton energy at the D-A interface, yet the challenge remaining is overcoming the anomalous hysteresis effect. We found that the device operation can be stabilized at low temperature, realizing a reliable η_P of 19.1%.

10.2 Future Research Directions

Previous chapters have examined the efficiency limiting factors in OPVs and applied theoretical understanding to guide device optimization. However, the η_P of OPVs needs to be further improved for widespread application. Additionally, the stability of OPVs is another field that has not been fully explored yet vital to the commercialization of this technology. Future research will focus on addressing these issues.

10.2.1 Engineering Active Layer Crystallinity

In Chapter 8, newly designed NTU compounds were found to show improved optical absorption across the solar spectrum. However the η_P of BHJ OPVs consisting of NTU-C_{70} mixtures is limited by the low FF. The cause of low FF is commonly ascribed to the low charge carrier mobility and the lack of phase separation in the uniformly mixed active layer to form continuous charge carrier pathways. In order to improve FF, future work should focus on improving the charge carrier mobility and promoting phase separation between the donor and acceptor.

The mobility of amorphous material can be enhanced by increasing the π-orbital overlap between molecules and reducing local disorder in electronic structure through

crystallization.[59] Previously, there have been many successful demonstrations where thermal annealing is used to enhance the crystallinity of the organic active layer for improved η_P.[27, 30, 95, 278] During vapor deposition, the crystallinity of the resulting film is determined by the ability of the condensed molecule to find a similar molecule. By heating the substrate during deposition, molecules will be able to sample the substrate for a longer time before sticking. This can help increase the chance of finding a similar molecule and eventually improve the film crystallinity. For example, the PHJ OPV fabricated with the D-A pairing of SubPc-C_{60} shows an increase in external quantum efficiency across a wide range of wavelength (Figure 10.1) when deposited at elevated temperature, indicating improved charge transport property of the SubPc film.

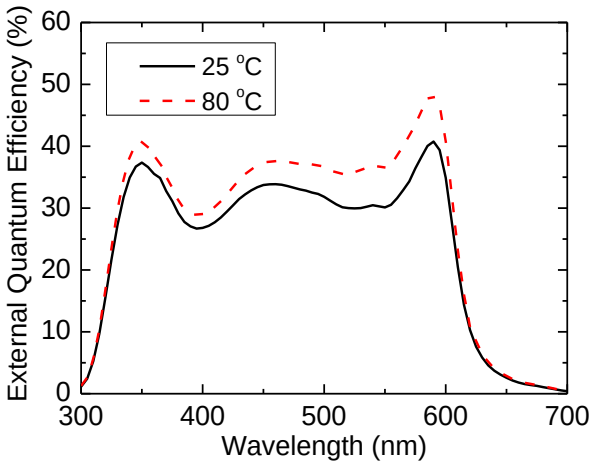

Figure 10.1 Broad spectrum improvement of η_{EQE} for a SubPc/C_{60} PHJ OPV (ITO/MoO_x 10 nm/SubPc 13 nm/C_{60} 35 nm/BCP 10 nm/Al 100 nm) when deposited at elevated temperature.

The same technique can also be applied to the NTU-C_{70} system to allow rearrangement of molecules for crystallization. Additional characterization techniques like dynamic

scanning calorimetry (DSC) and thermogravimetric analysis (TGA) should be applied to determine the glass transition temperature and the decomposition temperature of the NTU compounds and better inform the selection of annealing conditions. Variable annealing temperature and duration can be used to help understand the crystallization kinetics of NTU compounds. Polarized light microscopy, X-ray diffraction and spectroscopic ellipsometry can be applied to examine the crystallinity and anisotropy of the annealed film. Alternatively, substrate pretreatment techniques like self-assembled monolayer and epitaxial templating can also be applied in combination with thermal annealing to improve crystallinity.[29, 279]

10.2.2 Tandem OPVs with Fluorinated DTDCPB

As previously described, the spectrum loss (sub-bandgap photons and excess photon energy compared to the bandgap of the active materials) is one of the major efficiency limiting factors in single-junction photovoltaic cells as shown in Figure 10.2a. The shaded area indicates the theoretical maximum power output without V_{OC} loss in a single-junction photovoltaic cell. By adopting the tandem device architecture, the shaded area can be increased, leading to enhanced η_P as shown in Figure 10.2b. The same principle also applies to the field of OPVs where the highest efficiency records are currently held by devices with tandem architecture.[51]

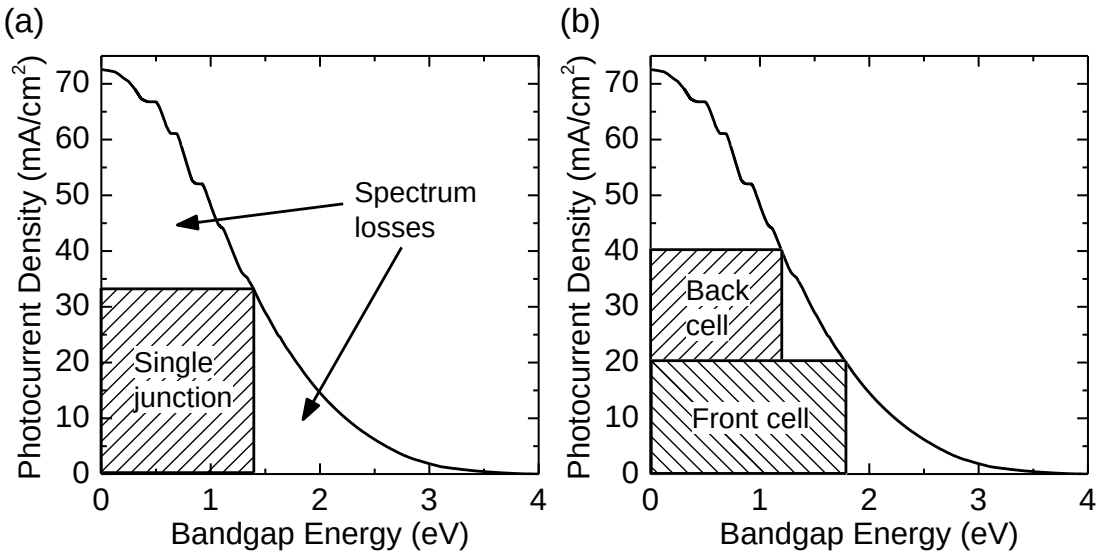

Figure 10.2 (a) Theoretical efficiency limit (shaded area) for a single-junction photovoltaic cell with no V_{OC} loss. (b) Improved efficiency with a double-junction tandem architecture.

The fluorinated DTDCPB compounds described in Chapter 8 are ideal candidates for the application in tandem OPVs. The absorption spectral of fluorinated DTDCPB compounds are blue-shifted compared to regular DTDCPB, and does not overlap much with common red absorber like 2-[7-(5-N,N-Ditolylaminothiophen-2-yl) -2,1,3-benzothiadiazol-4-yl] methylene malononitrile (DTDCTB) in the tandem architecture. This is beneficial for tandem OPVs as it leads to balanced photocurrent generation from each sub-cell. A comparison of absorption spectra for DTDCPB-F_o and DTDCTB are shown in Figure 10.3a.

More importantly, devices fabricated with the D-A pairing of fluorinated DTDCPB-C_{70} do not show roll off in η_P at high active layer thickness. This allows more freedom in optimizing the light intensity profile in the tandem architecture by engineering the sub-cell thickness. The simulated device photocurrent output for a tandem OPV fabricated with

these two materials are predicted using transfer matrix model and the projected efficiencies are plotted in Figure 10.3b. With optimized sub-cell thicknesses, a η_P of ~10% can be achieved.

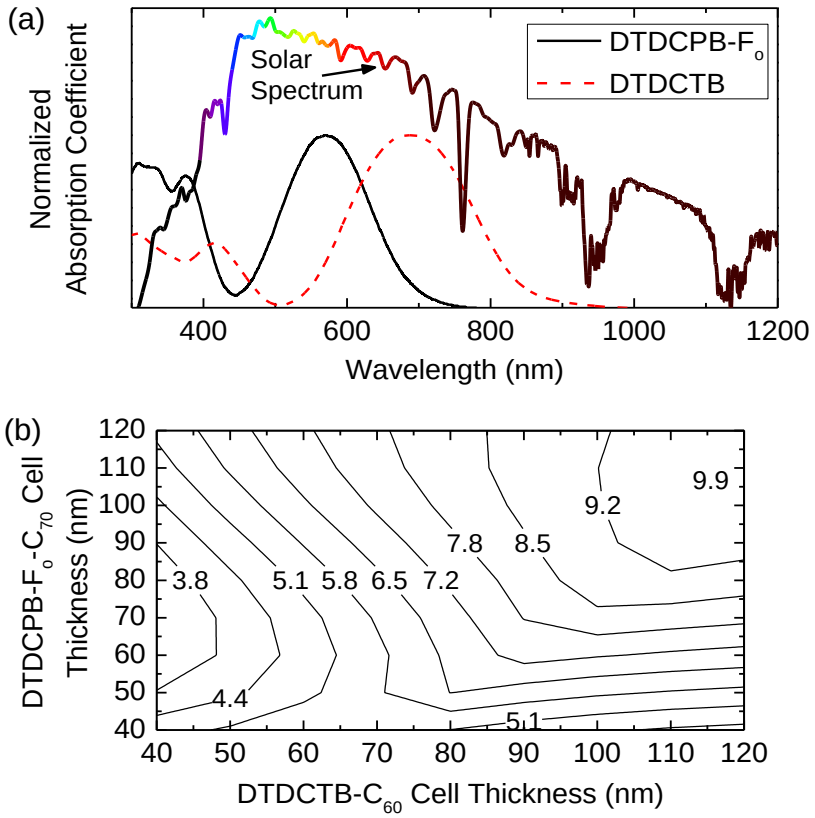

Figure 10.3 (a) Overlay of the donor absorption spectra with the AM 1.5G solar spectrum. (b) Predicted η_P for a tandem OPV as a function of the sub-cell thicknesses.

10.2.3 Understanding Degradation Mechanisms

In order to realize the commercialization of OPVs, good lifetime and stability are also important requirements. There are many characterization techniques that are available for studying the degradation mechanism of OPVs. For example, steady state or transient PL measurements can provide information on the formation of exciton quenching sites while

electrical measurements like impedance spectroscopy and charge extraction measurement can shed light on the generation of charge carrier traps during degradation processes. Understanding the degradation mechanisms would provide useful information for the future commercialization of OPVs.

In Chapter 7, preliminary lifetime and stability testing has been carried out on DTDCPB:C_{70} BHJ OPVs and the results are very promising. Based our preliminary measurements, the reduction of V_{OC} is limiting device lifetime under continuous illumination. However, the V_{OC} stayed almost constant during storage in the dark. It is thus important to investigate the photochemical degradation mechanism at various interfaces (MoO_x-active layer interface or D-A interface) that may lead to the reduction of V_{OC}. The robustness of interfaces and encapsulation is another area awaiting investigation. Based on our observation, the encapsulated DTDCPB:C_{70} device start to fail after storage in ambient environment for one year, which is likely the result of cathode delamination, crystallization of the exciton blocking layer or the failure of encapsulation.

Aside from the degradation mechanisms mentioned above, other factors like material purity can also play an important role in determining device lifetime. Impurities can activate photochemical reactions in active materials that lead to exciton quenching sites and charge traps, resulting in rapid degradation of the OPV.[280-282] It is thus important to identify the impurities that can inferiorly impact device lifetime and effectively eliminate them from the device architecture.

10.3 Afterword

Emerging photovoltaic technologies like OPVs and hybrid organic-inorganic perovskite photovoltaic cells undergo significant development in the last few years, with η_P viable for commercial application. Further improvements to the technology require collaborative effort from chemists, physicists and engineers. The fundamental understanding on device operation contributed by this work will help guide new material synthesis and device optimization. It is in the belief of this author that the realization of low-cost yet highly efficient photovoltaic technology is not far in the future.

11. Bibliography

1. Goyal, K. K., *Renewable Energy*. Mahaveer & Sons: 2009.

2. *National Renewable Energy Laboratory (NREL) 'Best Research Cell Efficiencies' reference chart. Rev. Mar 19 2015*.

3. Chapin, D. M.; Fuller, C. S.; Pearson, G. L., A New Silicon P-N Junction Photocell for Converting Solar Radiation into Electrical Power. *J. Appl. Phys.* **1954,** *25*, 676.

4. Dimroth, F.; Kurtz, S., High-Efficiency Multijunction Solar Cells. *MRS Bull.* **2007,** *32*, 230.

5. Law, D. C.; King, R. R.; Yoon, H.; Archer, M. J.; Boca, A.; Fetzer, C. M.; Mesropian, S.; Isshiki, T.; Haddad, M.; Edmondson, K. M.; Bhusari, D.; Yen, J.; Sherif, R. A.; Atwater, H. A.; Karam, N. H., Future Technology Pathways of Terrestrial III–V Multijunction Solar Cells for Concentrator Photovoltaic Systems. *Sol. Energ. Mater. Sol. C.* **2010,** *94*, 1314.

6. Shockley, W.; Queisser, H. J., Detailed Balance Limit of Efficiency of P-N Junction Solar Cells. *J. Appl. Phys.* **1961,** *32*, 510.

7. Green, M., *Third Generation Photovoltaics: Advanced Solar Energy Conversion*. Springer-Verlag Berlin Heidelberg: 2013; p 160.

8. Hamakawa, Y., *Thin-Film Solar Cells: Next Generation Photovoltaics and Its Applications*. Springer: 2004.

9. Cahen, D.; Barnea, L. In *Assessing Possibilities & Limits for Thin Film Solar Cells*, Photovoltaic Specialists Conference (PVSC), 2010 35th IEEE, 20-25 June 2010; 2010; pp 000323.

10. Fthenakis, V., Sustainability Metrics for Extending Thin-Film Photovoltaics to Terawatt Levels. *MRS Bull.* **2012,** *37*, 425.

11. Shah, A.; Torres, P.; Tscharner, R.; Wyrsch, N.; Keppner, H., Photovoltaic Technology: The Case for Thin-Film Solar Cells. *Science* **1999,** *285*, 692.

12. Mart ́ı A.; Luque, A., *Next Generation Photovoltaics: High Efficiency through Full Spectrum Utilization*. CRC Press: 2003.

13. Green, M. A., Third Generation Photovoltaics: Ultra-High Conversion Efficiency at Low Cost. *Progress in Photovoltaics: Research and Applications* **2001,** *9*, 123.

14. Shaheen, S. E.; Ginley, D. S.; Jabbour, G. E., Organic-Based Photovoltaics: Toward

Low-Cost Power Generation. *MRS Bull.* **2005,** *30*, 10.

15. Forrest, S. R., The Path to Ubiquitous and Low-Cost Organic Electronic Appliances on Plastic. *Nature* **2004,** *428*, 911.

16. Gaudiana, R.; Brabec, C., Organic Materials - Fantastic Plastic. *Nat. Photonics* **2008,** *2*, 287.

17. Darling, S. B.; You, F., The Case for Organic Photovoltaics. *RSC Advances* **2013,** *3*, 17633.

18. Chen, Y. H.; Chen, C. W.; Huang, Z. Y.; Lin, W. C.; Lin, L. Y.; Lin, F.; Wong, K. T.; Lin, H. W., Microcavity-Embedded, Colour-Tuneable, Transparent Organic Solar Cells. *Adv. Mater.* **2014,** *26*, 1129.

19. Chang, C. Y.; Zuo, L.; Yip, H. L.; Li, C. Z.; Li, Y.; Hsu, C. S.; Cheng, Y. J.; Chen, H.; Jen, A. K. Y., Highly Efficient Polymer Tandem Cells and Semitransparent Cells for Solar Energy. *Adv. Energy. Mater.* **2013**, 1301645.

20. Ameri, T.; Dennler, G.; Waldauf, C.; Azimi, H.; Seemann, A.; Forberich, K.; Hauch, J.; Scharber, M.; Hingerl, K.; Brabec, C. J., Fabrication, Optical Modeling, and Color Characterization of Semitransparent Bulk-Heterojunction Organic Solar Cells in an Inverted Structure. *Adv. Funct. Mater.* **2010,** *20*, 1592.

21. Bailey-Salzman, R. F.; Rand, B. P.; Forrest, S. R., Semitransparent Organic Photovoltaic Cells. *Appl. Phys. Lett.* **2006,** *88*, 233502.

22. Kearns, D.; Calvin, M., Photovoltaic Effect and Photoconductivity in Laminated Organic Systems. *J. Chem. Phys.* **1958,** *29*, 950.

23. Tang, C. W.; Albrecht, A. C., Photovoltaic Effects of Metal-Chlorophyll-a-Metal Sandwich Cells. *J. Chem. Phys.* **1975,** *62*, 2139.

24. Tang, C. W., 2-Layer Organic Photovoltaic Cell. *Appl. Phys. Lett.* **1986,** *48*, 183.

25. Peumans, P.; Yakimov, A.; Forrest, S. R., Small Molecular Weight Organic Thin-Film Photodetectors and Solar Cells. *J. Appl. Phys.* **2003,** *93*, 3693.

26. Menke, S. M.; Holmes, R. J., Exciton Diffusion in Organic Photovoltaic Cells. *Energy Environ. Sci.* **2014,** *7*, 499.

27. Peumans, P.; Uchida, S.; Forrest, S. R., Efficient Bulk Heterojunction Photovoltaic Cells Using Small-Molecular-Weight Organic Thin Films. *Nature* **2003,** *425*, 158.

28. Yu, G.; Gao, J.; Hummelen, J. C.; Wudl, F.; Heeger, A. J., Polymer Photovoltaic Cells: Enhanced Efficiencies Via a Network of Internal Donor-Acceptor Heterojunctions. *Science* **1995,** *270*, 1789.

29. Ma, H.; Yip, H. L.; Huang, F.; Jen, A. K. Y., Interface Engineering for Organic Electronics. *Adv. Funct. Mater.* **2010,** *20*, 1371.

30. Harada, K.; Edura, T.; Adachi, C., Nanocrystal Growth and Improved Performance of Small Molecule Bulk Heterojunction Solar Cells Composed of a Blend of Chloroaluminum Phthalocyanine and C-70. *Applied Physics Express* **2010,** *3*, 121602.

31. Heremans, P.; Cheyns, D.; Rand, B. P., Strategies for Increasing the Efficiency of Heterojunction Organic Solar Cells: Material Selection and Device Architecture. *Accounts. Chem. Res.* **2009,** *42*, 1740.

32. Dennler, G.; Sariciftci, N. S., Flexible Conjugated Polymer-Based Plastic Solar Cells: From Basics to Applications. *Proc. Ieee.* **2005,** *93*, 1429.

33. Zhang, Q.; Kan, B.; Liu, F.; Long, G. K.; Wan, X. J.; Chen, X. Q.; Zuo, Y.; Ni, W.; Zhang, H. J.; Li, M. M.; Hu, Z. C.; Huang, F.; Cao, Y.; Liang, Z. Q.; Zhang, M. T.; Russell, T. P.; Chen, Y. S., Small-Molecule Solar Cells with Efficiency over 9%. *Nat. Photonics* **2015,** *9*, 35.

34. Huo, L.; Liu, T.; Sun, X.; Cai, Y.; Heeger, A. J.; Sun, Y., Single-Junction Organic Solar Cells Based on a Novel Wide-Bandgap Polymer with Efficiency of 9.7. *Adv. Mater.* **2015,** *27*, 2938.

35. Chen, J.-D.; Cui, C.; Li, Y.-Q.; Zhou, L.; Ou, Q.-D.; Li, C.; Li, Y.; Tang, J.-X., Single-Junction Polymer Solar Cells Exceeding 10% Power Conversion Efficiency. *Adv. Mater.* **2015,** *27*, 1035.

36. Subbiah, J.; Purushothaman, B.; Chen, M.; Qin, T.; Gao, M.; Vak, D.; Scholes, F. H.; Chen, X.; Watkins, S. E.; Wilson, G. J.; Holmes, A. B.; Wong, W. W.; Jones, D. J., Organic Solar Cells Using a High-Molecular-Weight Benzodithiophene-Benzothiadiazole Copolymer with an Efficiency of 9.4%. *Adv. Mater.* **2015,** *27*, 702.

37. Kan, B.; Zhang, Q.; Li, M.; Wan, X.; Ni, W.; Long, G.; Wang, Y.; Yang, X.; Feng, H.; Chen, Y., Solution-Processed Organic Solar Cells Based on Dialkylthiol-Substituted Benzodithiophene Unit with Efficiency near 10%. *J. Am. Chem. Soc.* **2014,** *136*, 15529.

38. Liu, Y.; Chen, C. C.; Hong, Z.; Gao, J.; Yang, Y.; Zhou, H.; Dou, L.; Li, G., Solution-Processed Small-Molecule Solar Cells: Breaking the 10% Power Conversion Efficiency. *Sci. Rep.* **2013,** *3*.

39. Zhou, H.; Zhang, Y.; Mai, C. K.; Collins, S. D.; Bazan, G. C.; Nguyen, T. Q.; Heeger, A. J., Polymer Homo-Tandem Solar Cells with Best Efficiency of 11.3%. *Adv. Mater.* **2015,** *27*, 1767.

40. Lee, J.; Kang, H.; Kong, J.; Lee, K., A Depletion-Free, Ionic, Self-Assembled Recombination Layer for Tandem Polymer Solar Cells. *Adv. Energy. Mater.* **2014,** *4*.

41. Chen, C. C.; Chang, W. H.; Yoshimura, K.; Ohya, K.; You, J.; Gao, J.; Hong, Z.; Yang, Y., An Efficient Triple-Junction Polymer Solar Cell Having a Power Conversion Efficiency Exceeding 11%. *Adv. Mater.* **2014,** *26*, 5670.

42. Zheng, Z.; Zhang, S.; Zhang, M.; Zhao, K.; Ye, L.; Chen, Y.; Yang, B.; Hou, J., Highly Efficient Tandem Polymer Solar Cells with a Photovoltaic Response in the Visible Light Range. *Adv. Mater.* **2015,** *27*, 1189.

43. Lassiter, B. E.; Renshaw, C. K.; Forrest, S. R., Understanding Tandem Organic Photovoltaic Cell Performance. *J. Appl. Phys.* **2013,** *113*, 214505.

44. Jo, J.; Pouliot, J. R.; Wynands, D.; Collins, S. D.; Kim, J. Y.; Nguyen, T. L.; Woo, H. Y.; Sun, Y.; Leclerc, M.; Heeger, A. J., Enhanced Efficiency of Single and Tandem Organic Solar Cells Incorporating a Diketopyrrolopyrrole-Based Low-Bandgap Polymer by Utilizing Combined Zno/Polyelectrolyte Electron-Transport Layers. *Adv. Mater.* **2013,** *25*, 4783.

45. Chang, C.-Y.; Zuo, L.; Yip, H.-L.; Li, Y.; Li, C.-Z.; Hsu, C.-S.; Cheng, Y.-J.; Chen, H.; Jen, A. K. Y., A Versatile Fluoro-Containing Low-Bandgap Polymer for Efficient Semitransparent and Tandem Polymer Solar Cells. *Adv. Funct. Mater.* **2013,** *23*, 5084.

46. Li, N.; Baran, D.; Forberich, K.; Turbiez, M.; Ameri, T.; Krebs, F. C.; Brabec, C. J., An Efficient Solution-Processed Intermediate Layer for Facilitating Fabrication of Organic Multi-Junction Solar Cells. *Adv. Energy. Mater.* **2013,** *3*, 1597.

47. You, J.; Chen, C. C.; Hong, Z.; Yoshimura, K.; Ohya, K.; Xu, R.; Ye, S.; Gao, J.; Li, G.; Yang, Y., 10.2% Power Conversion Efficiency Polymer Tandem Solar Cells Consisting of Two Identical Sub-Cells. *Adv. Mater.* **2013,** *25*, 3973.

48. Jingbi, Y.; Letian, D.; Ken, Y.; Takehito, K.; Kenichiro, O.; Tom, M.; Keith, E.; Chun-Chao, C.; Jing, G.; Gang, L.; Yang, Y., A Polymer Tandem Solar Cell with 10.6% Power Conversion Efficiency. *Nature Communications* **2013,** *4*, 1446.

49. Li, N.; Baran, D.; Forberich, K.; Machui, F.; Ameri, T.; Turbiez, M.; Carrasco-Orozco, M.; Drees, M.; Facchetti, A.; Krebs, F. C.; Brabec, C. J., Towards 15% Energy Conversion Efficiency: A Systematic Study of the Solution-Processed Organic Tandem Solar Cells Based on Commercially Available Materials. *Energy Environ. Sci.* **2013,** *6*, 3407.

50. Riede, M.; Uhrich, C.; Widmer, J.; Timmreck, R.; Wynands, D.; Schwartz, G.; Gnehr, W. M.; Hildebrandt, D.; Weiss, A.; Hwang, J.; Sundarraj, S.; Erk, P.; Pfeiffer, M.; Leo, K., Efficient Organic Tandem Solar Cells Based on Small Molecules. *Adv. Funct. Mater.* **2011,** *21*, 3019.

51. Che, X. Z.; Xiao, X.; Zimmerman, J. D.; Fan, D. J.; Forrest, S. R., High-Efficiency, Vacuum-Deposited, Small-Molecule Organic Tandem and Triple-Junction Photovoltaic Cells. *Adv. Energy. Mater.* **2014,** *4*.

52. . Press Release.

53. Widmer, J.; Tietze, M.; Leo, K.; Riede, M., Open-Circuit Voltage and Effective Gap of Organic Solar Cells. *Adv. Funct. Mater.* **2013,** *23*, 5814.

54. Garcia-Belmonte, G.; Bisquert, J., Open-Circuit Voltage Limit Caused by Recombination through Tail States in Bulk Heterojunction Polymer-Fullerene Solar Cells. *Appl. Phys. Lett.* **2010,** *96*, 113301.

55. Potscavage, W. J.; Sharma, A.; Kippelen, B., Critical Interfaces in Organic Solar Cells and Their Influence on the Open-Circuit Voltage. *Accounts. Chem. Res.* **2009,** *42*, 1758.

56. Blom, P. W. M.; Mihailetchi, V. D.; Koster, L. J. A.; Markov, D. E., Device Physics of Polymer : Fullerene Bulk Heterojunction Solar Cells. *Adv. Mater.* **2007,** *19*, 1551.

57. Forrest, S.; Burrows, P.; Thompson, M., The Dawn of Organic Electronics. *Spectrum, IEEE* **2000,** *37*, 29.

58. Loo, Y.-L.; McCulloch, I., Progress and Challenges in Commercialization of Organic Electronics. *MRS Bull.* **2008,** *33*, 653.

59. Pope, M.; Swenberg, C. E., *Electronic Processes in Organic Crystals and Polymers*. Oxford University Press: 1999.

60. Turro, N. J., *Modern Molecular Photochemistry*. University Science Books: 1991.

61. Segal, M.; Baldo, M. A.; Holmes, R. J.; Forrest, S. R.; Soos, Z. G., Excitonic Singlet-Triplet Ratios in Molecular and Polymeric Organic Materials. *Phys. Rev. B* **2003,** *68*, 075211.

62. Albani, J. R., *Structure and Dynamics of Macromolecules: Absorption and Fluorescence Studies: Absorption and Fluorescence Studies*. Elsevier Science: 2011.

63. Hill, I. G.; Milliron, D.; Schwartz, J.; Kahn, A., Organic Semiconductor Interfaces: Electronic Structure and Transport Properties. *Appl. Surf. Sci.* **2000,** *166*, 354.

64. Nakayama, Y.; Nguyen, T. L.; Ozawa, Y.; Machida, S.; Sato, T.; Tokairin, H.; Noguchi, Y.; Ishii, H., Complete Demonstration of the Valence Electronic Structure inside a Practical Organic Solar Cell Probed by Low Energy Photoemission. *Adv. Energy. Mater.* **2014,** *4*.

65. Hill, I. G.; Rajagopal, A.; Kahn, A.; Hu, Y., Molecular Level Alignment at Organic Semiconductor-Metal Interfaces. *Appl. Phys. Lett.* **1998,** *73*, 662.

66. Djurovich, P. I.; Mayo, E. I.; Forrest, S. R.; Thompson, M. E., Measurement of the Lowest Unoccupied Molecular Orbital Energies of Molecular Organic Semiconductors. *Org. Electron.* **2009,** *10*, 515.

67. Cho, S. W.; Piper, L. F. J.; DeMasi, A.; Preston, A. R. H.; Smith, K. E.; Chauhan, K. V.; Sullivan, P.; Hatton, R. A.; Jones, T. S., Electronic Structure of C60/Phthalocyanine/Ito Interfaces Studied Using Soft X-Ray Spectroscopies. *J. Phys. Chem. C* **2010,** *114*, 1928.

68. Cho, S. W.; Piper, L. F. J.; DeMasi, A.; Preston, A. R. H.; Smith, K. E.; Chauhan, K. V.; Hatton, R. A.; Jones, T. S., Soft X-Ray Spectroscopy of C60/Copper Phthalocyanine/Moo3 Interfaces: Role of Reduced Moo3 on Energetic Band Alignment and Improved Performance. *J. Phys. Chem. C* **2010,** *114*, 18252.

69. D'Andrade, B. W.; Datta, S.; Forrest, S. R.; Djurovich, P.; Polikarpov, E.; Thompson, M. E., Relationship between the Ionization and Oxidation Potentials of Molecular Organic Semiconductors. *Org. Electron.* **2005,** *6*, 11.

70. Forster, T., 10th Spiers Memorial Lecture. Transfer Mechanisms of Electronic Excitation. *Discussions of the Faraday Society* **1959,** *27*, 7.

71. Fratini, S.; Ciuchi, S., Bandlike Motion and Mobility Saturation in Organic Molecular Semiconductors. *Phys. Rev. Lett.* **2009,** *103*, 266601.

72. Sakanoue, T.; Sirringhaus, H., Band-Like Temperature Dependence of Mobility in A solution-Processed Organic Semiconductor. *Nat. Mater.* **2010,** *9*, 736.

73. Mott, N. F., Conduction in Non-Crystalline Materials. *Philosophical Magazine* **1969,** *19*, 835.

74. Sundar, V. C.; Zaumseil, J.; Podzorov, V.; Menard, E.; Willett, R. L.; Someya, T.; Gershenson, M. E.; Rogers, J. A., Elastomeric Transistor Stamps: Reversible Probing of Charge Transport in Organic Crystals. *Science* **2004,** *303*, 1644.

75. Takeya, J.; Yamagishi, M.; Tominari, Y.; Hirahara, R.; Nakazawa, Y.; Nishikawa, T.; Kawase, T.; Shimoda, T.; Ogawa, S., Very High-Mobility Organic Single-Crystal Transistors with in-Crystal Conduction Channels. *Appl. Phys. Lett.* **2007,** *90*, 102120.

76. Xia, Y.; Kalihari, V.; Frisbie, C. D.; Oh, N. K.; Rogers, J. A., Tetracene Air-Gap Single-Crystal Field-Effect Transistors. *Appl. Phys. Lett.* **2007,** *90*, 162106.

77. Atahan-Evrenk, Ş.; Aspuru-Guzik, A., *Prediction and Calculation of Crystal Structures: Methods and Applications*. Springer International Publishing: 2014.

78. Tessler, N.; Preezant, Y.; Rappaport, N.; Roichman, Y., Charge Transport in Disordered Organic Materials and Its Relevance to Thin-Film Devices: A Tutorial Review. *Adv. Mater.* **2009,** *21*, 2741.

79. Noriega, R.; Rivnay, J.; Vandewal, K.; Koch, F. P. V.; Stingelin, N.; Smith, P.; Toney, M. F.; Salleo, A., A General Relationship between Disorder, Aggregation and Charge Transport in Conjugated Polymers. *Nat. Mater.* **2013,** *12*, 1038.

80. Larson, R.; Rehg, T., Spin Coating. In *Liquid Film Coating*, Kistler, S.; Schweizer, P., Eds. Springer Netherlands: 1997; pp 709.

81. Dhanaraj, G.; Byrappa, K.; Prasad, V.; Dudley, M., *Springer Handbook of Crystal Growth*. Springer: 2010.

82. Ashraf, R. S.; Schroeder, B. C.; Bronstein, H. A.; Huang, Z.; Thomas, S.; Kline, R. J.; Brabec, C. J.; Rannou, P.; Anthopoulos, T. D.; Durrant, J. R.; McCulloch, I., The Influence of Polymer Purification on Photovoltaic Device Performance of a Series of Indacenodithiophene Donor Polymers. *Adv. Mater.* **2013,** *25*, 2029.

83. Roberson, L. B.; Kowalik, J.; Tolbert, L. M.; Kloc, C.; Zeis, R.; Chi, X.; Fleming, R.; Wilkins, C., Pentacene Disproportionation During Sublimation for Field-Effect Transistors. *J. Am. Chem. Soc.* **2005,** *127*, 3069.

84. McGhie, A. R.; Garito, A. F.; Heeger, A. J., A Gradient Sublimer for Purification and Crystal Growth of Organic Donor and Acceptor Molecules. *J. Cryst. Growth* **1974,** *22*, 295.

85. Liu, S.-W.; Su, W.-C.; Lee, C.-C.; Chou, C.-C.; Cheng, C.-W., Efficient Organic Photovoltaic Device Using a Sublimated Subphthalocyanine as an Electron Donor. *ECS Solid State Letters* **2012,** *1*, P70.

86. Peumans, P.; Forrest, S. R., Separation of Geminate Charge-Pairs at Donor–Acceptor Interfaces in Disordered Solids. *Chem. Phys. Lett.* **2004,** *398*, 27.

87. Sharma, A.; Hotchkiss, P. J.; Marder, S. R.; Kippelen, B., Tailoring the Work Function of Indium Tin Oxide Electrodes in Electrophosphorescent Organic Light-Emitting Diodes. *J. Appl. Phys.* **2009,** *105*, 084507.

88. Gordon, R. G., Criteria for Choosing Transparent Conductors. *MRS Bull.* **2000,** *25*, 52.

89. Guo, F.; Kubis, P.; Li, N.; Przybilla, T.; Matt, G.; Stubhan, T.; Ameri, T.; Butz, B.; Spiecker, E.; Forberich, K.; Brabec, C. J., Solution-Processed Parallel Tandem Polymer Solar Cells Using Silver Nanowires as Intermediate Electrode. *ACS Nano* **2014,** *8*, 12632.

90. Mihailetchi, V. D.; Blom, P. W. M.; Hummelen, J. C.; Rispens, M. T., Cathode Dependence of the Open-Circuit Voltage of Polymer:Fullerene Bulk Heterojunction Solar Cells. *J. Appl. Phys.* **2003,** *94*, 6849.

91. Gommans, H.; Verreet, B.; Rand, B. P.; Muller, R.; Poortmans, J.; Heremans, P.; Genoe, J., On the Role of Bathocuproine in Organic Photovoltaic Cells. *Adv. Funct. Mater.* **2008,** *18*, 3686.

92. Hiramoto, M.; Fujiwara, H.; Yokoyama, M., Three-Layered Organic Solar Cell with a Photoactive Interlayer of Codeposited Pigments. *Appl. Phys. Lett.* **1991,** *58*, 1062.

93. Li, G.; Shrotriya, V.; Huang, J. S.; Yao, Y.; Moriarty, T.; Emery, K.; Yang, Y., High-Efficiency Solution Processable Polymer Photovoltaic Cells by Self-Organization of Polymer Blends. *Nature Mater.* **2005,** *4*, 864.

94. Park, S. H.; Roy, A.; Beaupre, S.; Cho, S.; Coates, N.; Moon, J. S.; Moses, D.; Leclerc, M.; Lee, K.; Heeger, A. J., Bulk Heterojunction Solar Cells with Internal Quantum Efficiency Approaching 100%. *Nat. Photonics* **2009,** *3*, 297.

95. Ma, W. L.; Yang, C. Y.; Gong, X.; Lee, K.; Heeger, A. J., Thermally Stable, Efficient Polymer Solar Cells with Nanoscale Control of the Interpenetrating Network Morphology. *Adv. Funct. Mater.* **2005,** *15*, 1617.

96. Peet, J.; Senatore, M. L.; Heeger, A. J.; Bazan, G. C., The Role of Processing in the Fabrication and Optimization of Plastic Solar Cells. *Adv. Mater.* **2009,** *21*, 1521.

97. Chen, Y. H.; Lin, L. Y.; Lu, C. W.; Lin, F.; Huang, Z. Y.; Lin, H. W.; Wang, P. H.; Liu, Y. H.; Wong, K. T.; Wen, J.; Miller, D. J.; Darling, S. B., Vacuum-Deposited Small-Molecule Organic Solar Cells with High Power Conversion Efficiencies by Judicious Molecular Design and Device Optimization. *J. Am. Chem. Soc.* **2012,** *134*, 13616.

98. Yang, F.; Shtein, M.; Forrest, S. R., Controlled Growth of a Molecular Bulk Heterojunction Photovoltaic Cell. *Nat. Mater.* **2005,** *4*, 37.

99. Xi, H.; Wei, Z.; Duan, Z.; Xu, W.; Zhu, D., Facile Method for Fabrication of Nanostructured Cupc Thin Films to Enhance Photocurrent Generation. *J. Phys. Chem. C* **2008,** *112*, 19934.

100. Boudouris, B. W.; Frisbie, C. D.; Hillmyer, M. A., Nanoporous Poly(3-Alkylthiophene) Thin Films Generated from Block Copolymer Templates.

Macromolecules **2008,** *41*, 67.

101. Etxebarria, I.; Furlan, A.; Ajuria, J.; Fecher, F. W.; Voigt, M.; Brabec, C. J.; Wienk, M. M.; Slooff, L.; Veenstra, S.; Gilot, J.; Pacios, R., Series Vs Parallel Connected Organic Tandem Solar Cells: Cell Performance and Impact on the Design and Operation of Functional Modules. *Sol. Energ. Mater. Sol. C.* **2014,** *130*, 495.

102. Zuo, L.; Chueh, C. C.; Xu, Y. X.; Chen, K. S.; Zang, Y.; Li, C. Z.; Chen, H.; Jen, A. K., Microcavity-Enhanced Light-Trapping for Highly Efficient Organic Parallel Tandem Solar Cells. *Adv. Mater.* **2014,** *26*, 6778.

103. Pandey, R.; Holmes, R. J., Characterizing the Charge Collection Efficiency in Bulk Heterojunction Organic Photovoltaic Cells. *Appl. Phys. Lett.* **2012,** *100*, 083303.

104. Zou, Y.; Holst, J.; Zhang, Y.; Holmes, R. J., 7.9% Efficient Vapor-Deposited Organic Photovoltaic Cells Based on a Simple Bulk Heterojunction. *J. Mater. Chem. A* **2014,** *2*, 12397.

105. Credgington, D.; Jamieson, F. C.; Walker, B.; Nguyen, T. Q.; Durrant, J. R., Quantification of Geminate and Non-Geminate Recombination Losses within a Solution-Processed Small-Molecule Bulk Heterojunction Solar Cell. *Adv. Mater.* **2012,** *24*, 2135.

106. Basham, J. I.; Jackson, T. N.; Gundlach, D. J., Predicting Thej-Vcurve in Organic Photovoltaics Using Impedance Spectroscopy. *Adv. Energy. Mater.* **2014,** *4*.

107. Mullenbach, T. K.; Zou, Y.; Holst, J.; Holmes, R. J., Interpreting Impedance Spectra of Organic Photovoltaic Cells—Extracting Charge Transit and Recombination Rates. *J. Appl. Phys.* **2014,** *116*, 124513.

108. Casalini, R.; Tsang, S. W.; Deininger, J. J.; Arroyave, F. A.; Reynolds, J. R.; So, F., Investigation of the Role of the Acceptor Molecule in Bulk Heterojunction Photovoltaic Cells Using Impedance Spectroscopy. *J. Phys. Chem. C* **2013,** *117*, 13798.

109. Garcia-Belmonte, G.; Munar, A.; Barea, E. M.; Bisquert, J.; Ugarte, I.; Pacios, R., Charge Carrier Mobility and Lifetime of Organic Bulk Heterojunctions Analyzed by Impedance Spectroscopy. *Org. Electron.* **2008,** *9*, 847.

110. Kirchartz, T.; Gong, W.; Hawks, S. A.; Agostinelli, T.; MacKenzie, R. C. I.; Yang, Y.; Nelson, J., Sensitivity of the Mott–Schottky Analysis in Organic Solar Cells. *J. Phys. Chem. C* **2012,** *116*, 7672.

111. Mingebach, M.; Deibel, C.; Dyakonov, V., Built-in Potential and Validity of the Mott-Schottky Analysis in Organic Bulk Heterojunction Solar Cells. *Phys. Rev. B* **2011,** *84*.

112. Pettersson, L. A. A.; Roman, L. S.; Inganas, O., Modeling Photocurrent Action Spectra of Photovoltaic Devices Based on Organic Thin Films. *J. Appl. Phys.* **1999,** *86*, 487.

113. Bube, R. H.; Fahrenbruch, A. L.; Aranovich, J., *Advances in Electronics and Electron Physics*. Academic: New York, 1981; p p. 163.

114. A. L. Fahrenbruch, J. A., *Solar Energy Conversion: Solid-State Physics Aspects*. Springer-Verlag: New York, 1979; p p. 270.

115. Vandewal, K.; Tvingstedt, K.; Gadisa, A.; Inganäs, O.; Manca, J. V., Relating the Open-Circuit Voltage to Interface Molecular Properties of Donor:Acceptor Bulk Heterojunction Solar Cells. *Phys. Rev. B* **2010,** *81*, 125204.

116. Vandewal, K.; Tvingstedt, K.; Gadisa, A.; Inganas, O.; Manca, J. V., On the Origin of the Open-Circuit Voltage of Polymer-Fullerene Solar Cells. *Nat. Mater.* **2009,** *8*, 904.

117. Rand, B.; Burk, D.; Forrest, S., Offset Energies at Organic Semiconductor Heterojunctions and Their Influence on the Open-Circuit Voltage of Thin-Film Solar Cells. *Phys. Rev. B* **2007,** *75*, 115327.

118. Foertig, A.; Kniepert, J.; Gluecker, M.; Brenner, T.; Dyakonov, V.; Neher, D.; Deibel, C., Nongeminate and Geminate Recombination in Ptb7:Pcbm Solar Cells. *Adv. Funct. Mater.* **2014,** *24*, 1306.

119. Groves, C., Developing Understanding of Organic Photovoltaic Devices: Kinetic Monte Carlo Models of Geminate and Non-Geminate Recombination, Charge Transport and Charge Extraction. *Energy Environ. Sci.* **2013,** *6*, 3202.

120. Proctor, C. M.; Albrecht, S.; Kuik, M.; Neher, D.; Nguyen, T. Q., Overcoming Geminate Recombination and Enhancing Extraction in Solution-Processed Small Molecule Solar Cells. *Adv. Energy. Mater.* **2014,** *4*.

121. Groves, C., Suppression of Geminate Charge Recombination in Organic Photovoltaic Devices with a Cascaded Energy Heterojunction. *Energy Environ. Sci.* **2013,** *6*, 1546.

122. De, S.; Pascher, T.; Maiti, M.; Jespersen, K. G.; Kesti, T.; Zhang, F.; Inganäs, O.; Yartsev, A.; Sundström, V., Geminate Charge Recombination in Alternating Polyfluorene Copolymer/Fullerene Blends. *J. Am. Chem. Soc.* **2007,** *129*, 8466.

123. Braun, C. L., Electric Field Assisted Dissociation of Charge Transfer States as a Mechanism of Photocarrier Production. *J. Chem. Phys.* **1984,** *80*, 4157.

124. Vithanage, D. A.; Wang, E. G.; Wang, Z. Q.; Ma, F.; Inganas, O.; Andersson, M.

R.; Yartsev, A.; Sundstrom, V.; Pascher, T., Charge Carrier Dynamics of Polymer: Fullerene Blends: From Geminate to Non-Geminate Recombination. *Adv. Energy. Mater.* **2014,** *4*.

125. Gorenflot, J.; Heiber, M. C.; Baumann, A.; Lorrmann, J.; Gunz, M.; Kampgen, A.; Dyakonov, V.; Deibel, C., Nongeminate Recombination in Neat P3ht and P3ht:Pcbm Blend Films. *J. Appl. Phys.* **2014,** *115*.

126. Proctor, C. M.; Kim, C.; Neher, D.; Nguyen, T.-Q., Nongeminate Recombination and Charge Transport Limitations in Diketopyrrolopyrrole-Based Solution-Processed Small Molecule Solar Cells. *Adv. Funct. Mater.* **2013,** *23*, 3584.

127. Credgington, D.; Hamilton, R.; Atienzar, P.; Nelson, J.; Durrant, J. R., Non-Geminate Recombination as the Primary Determinant of Open-Circuit Voltage in Polythiophene:Fullerene Blend Solar Cells: An Analysis of the Influence of Device Processing Conditions. *Adv. Funct. Mater.* **2011,** *21*, 2744.

128. Burke, T. M.; Sweetnam, S.; Vandewal, K.; McGehee, M. D., Beyond Langevin Recombination: How Equilibrium between Free Carriers and Charge Transfer States Determines the Open-Circuit Voltage of Organic Solar Cells. *Adv. Energy. Mater.* **2015**.

129. Di Nuzzo, D.; Wetzelaer, G.-J. A. H.; Bouwer, R. K. M.; Gevaerts, V. S.; Meskers, S. C. J.; Hummelen, J. C.; Blom, P. W. M.; Janssen, R. A. J., Simultaneous Open-Circuit Voltage Enhancement and Short-Circuit Current Loss in Polymer: Fullerene Solar Cells Correlated by Reduced Quantum Efficiency for Photoinduced Electron Transfer. *Adv. Energy. Mater.* **2013,** *3*, 85.

130. Dimitrov, S. D.; Huang, Z.; Deledalle, F.; Nielsen, C. B.; Schroeder, B. C.; Ashraf, R. S.; Shoaee, S.; McCulloch, I.; Durrant, J. R., Towards Optimisation of Photocurrent from Fullerene Excitons in Organic Solar Cells. *Energy Environ. Sci.* **2014,** *7*, 1037.

131. Vandewal, K.; Widmer, J.; Heumueller, T.; Brabec, C. J.; McGehee, M. D.; Leo, K.; Riede, M.; Salleo, A., Increased Open-Circuit Voltage of Organic Solar Cells by Reduced Donor-Acceptor Interface Area. *Adv. Mater.* **2014,** *26*, 3839.

132. Chen, K. S.; Yip, H. L.; Salinas, J. F.; Xu, Y. X.; Chueh, C. C.; Jen, A. K. Y., Strong Photocurrent Enhancements in Highly Efficient Flexible Organic Solar Cells by Adopting a Microcavity Configuration. *Adv. Mater.* **2014,** *26*, 3349.

133. Marcus, R. A.; Sutin, N., Electron Transfers in Chemistry and Biology. *Biochimica et Biophysica Acta (BBA) - Reviews on Bioenergetics* **1985,** *811*, 265.

134. Zhang, M.; Irfan; Ding, H.; Gao, Y.; Tang, C. W., Organic Schottky Barrier Photovoltaic Cells Based on MoO_x/C_{60}. *Appl. Phys. Lett.* **2010,** *96*, 183301.

135. Lo, M. F.; Ng, T. W.; Liu, T. Z.; Roy, V. A. L.; Lai, S. L.; Fung, M. K.; Lee, C. S.; Lee, S. T., Limits of Open Circuit Voltage in Organic Photovoltaic Devices. *Appl. Phys. Lett.* **2010,** *96*, 113303.

136. Yang, B.; Guo, F.; Yuan, Y.; Xiao, Z.; Lu, Y.; Dong, Q.; Huang, J., Solution-Processed Fullerene-Based Organic Schottky Junction Devices for Large-Open-Circuit-Voltage Organic Solar Cells. *Adv. Mater.* **2013,** *25*, 572.

137. Zou, Y.; Holmes, R. J., Influence of a Moox Interlayer on the Open-Circuit Voltage in Organic Photovoltaic Cells. *Appl. Phys. Lett.* **2013,** *103*, 053302.

138. Zou, Y.; Holmes, R. J., The Role of Exciton Ionization Processes in Bulk Heterojunction Organic Photovoltaic Cells. *Adv. Energy. Mater.* **2015,** *5*, 1500019.

139. Chen, S.; Tsang, S. W.; Lai, T. H.; Reynolds, J. R.; So, F., Dielectric Effect on the Photovoltage Loss in Organic Photovoltaic Cells. *Adv. Mater.* **2014,** *26*, 6125.

140. Barker, A. J.; Chen, K.; Hodgkiss, J. M., Distance Distributions of Photogenerated Charge Pairs in Organic Photovoltaic Cells. *J. Am. Chem. Soc.* **2014,** *136*, 12018.

141. Koster, L. J. A.; Mihailetchi, V. D.; Ramaker, R.; Blom, P. W. M., Light Intensity Dependence of Open-Circuit Voltage of Polymer:Fullerene Solar Cells. *Appl. Phys. Lett.* **2005,** *86*, 123509.

142. Cowan, S. R.; Roy, A.; Heeger, A. J., Recombination in Polymer-Fullerene Bulk Heterojunction Solar Cells. *Phys. Rev. B* **2010,** *82*, 245207.

143. Pandey, R.; Holmes, R. J., Graded Donor-Acceptor Heterojunctions for Efficient Organic Photovoltaic Cells. *Adv. Mater.* **2010,** *22*, 5301.

144. Jeong, W. I.; Lee, Y. E.; Shim, H. S.; Kim, T. M.; Kim, S. Y.; Kim, J. J., Photoconductivity of C60 as an Origin of Bias-Dependent Photocurrent in Organic Photovoltaics. *Adv. Funct. Mater.* **2012,** *22*, 3089.

145. Kim, H.; Kim, J. Y.; Park, S. H.; Lee, K.; Jin, Y.; Kim, J.; Suh, H., Electroluminescence in Polymer-Fullerene Photovoltaic Cells. *Appl. Phys. Lett.* **2005,** *86*, 183502.

146. Westenhoff, S.; Howard, I. A.; Hodgkiss, J. M.; Kirov, K. R.; Bronstein, H. A.; Williams, C. K.; Greenham, N. C.; Friend, R. H., Charge Recombination in Organic Photovoltaic Devices with High Open-Circuit Voltages. *J. Am. Chem. Soc.* **2008,** *130*, 13653.

147. Tvingstedt, K.; Vandewal, K.; Gadisa, A.; Zhang, F.; Manca, J.; Inganäs, O.,

Electroluminescence from Charge Transfer States in Polymer Solar Cells. *J. Am. Chem. Soc.* **2009,** *131*, 11819.

148. Faist, M. A.; Kirchartz, T.; Gong, W.; Ashraf, R. S.; McCulloch, I.; de Mello, J. C.; Ekins-Daukes, N. J.; Bradley, D. D. C.; Nelson, J., Competition between the Charge Transfer State and the Singlet States of Donor or Acceptor Limiting the Efficiency in Polymer:Fullerene Solar Cells. *J. Am. Chem. Soc.* **2011,** *134*, 685.

149. Deibel, C.; Strobel, T.; Dyakonov, V., Role of the Charge Transfer State in Organic Donor–Acceptor Solar Cells. *Adv. Mater.* **2010,** *22*, 4097.

150. Campbell, I. H.; Crone, B. K., Improving an Organic Photodiode by Incorporating a Tunnel Barrier between the Donor and Acceptor Layers. *Appl. Phys. Lett.* **2012,** *101*, 023301.

151. Liu, F.; Crone, B. K.; Paul Ruden, P.; Smith, D. L., Control of Interface Microscopic Processes in Organic Bilayer Structures and Their Effect on Photovoltaic Device Performance. *J. Appl. Phys.* **2013,** *113*, 044516.

152. Fukagawa, H.; Watanabe, K.; Tsuzuki, T.; Tokito, S., Highly Efficient, Deep-Blue Phosphorescent Organic Light Emitting Diodes with a Double-Emitting Layer Structure. *Appl. Phys. Lett.* **2008,** *93*, 133312.

153. Bernardo, B.; Cheyns, D.; Verreet, B.; Schaller, R. D.; Rand, B. P.; Giebink, N. C., Delocalization and Dielectric Screening of Charge Transfer States in Organic Photovoltaic Cells. *Nat. Commun.* **2014,** *5*.

154. Lee, B. H.; Jung, I. H.; Woo, H. Y.; Shim, H.-K.; Kim, G.; Lee, K., Multi-Charged Conjugated Polyelectrolytes as a Versatile Work Function Modifier for Organic Electronic Devices. *Adv. Funct. Mater.* **2014,** *24*, 1100.

155. Yip, H. L.; Hau, S. K.; Baek, N. S.; Ma, H.; Jen, A. K. Y., Polymer Solar Cells That Use Self-Assembled-Monolayer-Modified Zno/Metals as Cathodes. *Adv. Mater.* **2008,** *20*, 2376.

156. Zhicai, H.; Chengmei, Z.; Shijian, S.; Miao, X.; Hongbin, W.; Yong, C., Enhanced Power-Conversion Efficiency in Polymer Solar Cells Using an Inverted Device Structure. *Nat. Photonics* **2012,** *6*, 593.

157. Beaumont, N.; Hancox, I.; Sullivan, P.; Hatton, R. A.; Jones, T. S., Increased Efficiency in Small Molecule Organic Photovoltaic Cells through Electrode Modification with Self-Assembled Monolayers. *Energy Environ. Sci.* **2011,** *4*, 1708.

158. Hoven, C. V.; Garcia, A.; Bazan, G. C.; Nguyen, T. Q., Recent Applications of

Conjugated Polyelectrolytes in Optoelectronic Devices. *Adv. Mater.* **2008,** *20*, 3793.

159. Hau, S. K.; Yip, H.-L.; Ma, H.; Jen, A. K. Y., High Performance Ambient Processed Inverted Polymer Solar Cells through Interfacial Modification with a Fullerene Self-Assembled Monolayer. *Appl. Phys. Lett.* **2008,** *93*, 233304.

160. Destruel, P.; Bock, H.; Séguy, I.; Jolinat, P.; Oukachmih, M.; Bedel-Pereira, E., Influence of Indium Tin Oxide Treatment Using Uv–Ozone and Argon Plasma on the Photovoltaic Parameters of Devices Based on Organic Discotic Materials. *Polym. Int.* **2006,** *55*, 601.

161. Zhang, M.; Wang, H.; Tian, H.; Geng, Y.; Tang, C. W., Bulk Heterojunction Photovoltaic Cells with Low Donor Concentration. *Adv. Mater.* **2011,** *23*, 4960.

162. Kinoshita, Y.; Takenaka, R.; Murata, H., Independent Control of Open-Circuit Voltage of Organic Solar Cells by Changing Film Thickness of Moo[Sub 3] Buffer Layer. *Appl. Phys. Lett.* **2008,** *92*, 243309.

163. Sun, Y.; Takacs, C. J.; Cowan, S. R.; Seo, J. H.; Gong, X.; Roy, A.; Heeger, A. J., Efficient, Air-Stable Bulk Heterojunction Polymer Solar Cells Using Moox as the Anode Interfacial Layer. *Adv. Mater.* **2011,** *23*, 2226.

164. Kim, D. Y.; Subbiah, J.; Sarasqueta, G.; So, F.; Ding, H.; Irfan; Gao, Y., The Effect of Molybdenum Oxide Interlayer on Organic Photovoltaic Cells. *Appl. Phys. Lett.* **2009,** *95*, 093304.

165. Hancox, I.; Sullivan, P.; Chauhan, K. V.; Beaumont, N.; Rochford, L. A.; Hatton, R. A.; Jones, T. S., The Effect of a Moox Hole-Extracting Layer on the Performance of Organic Photovoltaic Cells Based on Small Molecule Planar Heterojunctions. *Org. Electron.* **2010,** *11*, 2019.

166. Shrotriya, V.; Li, G.; Yao, Y.; Chu, C. W.; Yang, Y., Transition Metal Oxides as the Buffer Layer for Polymer Photovoltaic Cells. *Appl. Phys. Lett.* **2006,** *88*, 073508.

167. Giebink, N. C.; Wiederrecht, G. P.; Wasielewski, M. R.; Forrest, S. R., Ideal Diode Equation for Organic Heterojunctions. I. Derivation and Application. *Phys. Rev. B* **2010,** *82*, 155305.

168. Shrotriya, V.; Li, G.; Yao, Y.; Chu, C.-W.; Yang, Y., Transition Metal Oxides as the Buffer Layer for Polymer Photovoltaic Cells. *Appl. Phys. Lett.* **2006,** *88*, 073508.

169. Greiner, M. T.; Chai, L.; Helander, M. G.; Tang, W. M.; Lu, Z. H., Metal/Metal-Oxide Interfaces: How Metal Contacts Affect the Work Function and Band Structure of Moo3. *Adv. Funct. Mater.* **2013,** *23*, 215.

170. Dasgupta, B.; Goh, W. P.; Ooi, Z. E.; Wong, L. M.; Jiang, C. Y.; Ren, Y.; Tok, E. S.; Pan, J.; Zhang, J.; Chiam, S. Y., Enhanced Extraction Rates through Gap States of Molybdenum Oxide Anode Buffer. *J. Phys. Chem. C* **2013,** *117*, 9206.

171. Girotto, C.; Voroshazi, E.; Cheyns, D.; Heremans, P.; Rand, B. P., Solution-Processed Moo3 Thin Films as a Hole-Injection Layer for Organic Solar Cells. *ACS Appl. Mater. Interfaces* **2011,** *3*, 3244.

172. Battaglia, C.; Yin, X.; Zheng, M.; Sharp, I. D.; Chen, T.; McDonnell, S.; Azcatl, A.; Carraro, C.; Ma, B.; Maboudian, R.; Wallace, R. M.; Javey, A., Hole Selective Moox Contact for Silicon Solar Cells. *Nano Lett.* **2014,** *14*, 967.

173. Kim, D. Y.; Sarasqueta, G.; So, F., Snpc:C60 Bulk Heterojunction Organic Photovoltaic Cells with Moo3 Interlayer. *Sol. Energ. Mater. Sol. C.* **2009,** *93*, 1452.

174. Hancox, I.; Chauhan, K. V.; Sullivan, P.; Hatton, R. A.; Moshar, A.; Mulcahy, C. P. A.; Jones, T. S., Increased Efficiency of Small Molecule Photovoltaic Cells by Insertion of a Moo3 Hole-Extracting Layer. *Energy Environ. Sci.* **2010,** *3*, 107.

175. Kröger, M.; Hamwi, S.; Meyer, J.; Riedl, T.; Kowalsky, W.; Kahn, A., Role of the Deep-Lying Electronic States of Moo[Sub 3] in the Enhancement of Hole-Injection in Organic Thin Films. *Appl. Phys. Lett.* **2009,** *95*, 123301.

176. Kröger, M.; Hamwi, S.; Meyer, J.; Riedl, T.; Kowalsky, W.; Kahn, A., P-Type Doping of Organic Wide Band Gap Materials by Transition Metal Oxides: A Case-Study on Molybdenum Trioxide. *Org. Electron.* **2009,** *10*, 932.

177. Meyer, J.; Hamwi, S.; Kröger, M.; Kowalsky, W.; Riedl, T.; Kahn, A., Transition Metal Oxides for Organic Electronics: Energetics, Device Physics and Applications. *Adv. Mater.* **2012,** *24*, 5408.

178. Greiner, M. T.; Helander, M. G.; Tang, W. M.; Wang, Z. B.; Qiu, J.; Lu, Z. H., Universal Energy-Level Alignment of Molecules on Metal Oxides. *Nat. Mater.* **2012,** *11*, 76.

179. Kumar, P.; Jain, S. C.; Kumar, V.; Chand, S.; Tandon, R. P., A Model for the J-V Characteristics of P3ht:Pcbm Solar Cells. *J. Appl. Phys.* **2009,** *105*, 104507.

180. Boix, P. P.; Ajuria, J.; Etxebarria, I.; Pacios, R.; Garcia-Belmonte, G.; Bisquert, J., Role of Zno Electron-Selective Layers in Regular and Inverted Bulk Heterojunction Solar Cells. *J. Phys. Chem. Lett.* **2011,** *2*, 407.

181. Woo, S.; Kim, W. H.; Kim, H.; Yi, Y.; Lyu, H. K.; Kim, Y., 8.9% Single-Stack Inverted Polymer Solar Cells with Electron-Rich Polymer Nanolayer-Modified Inorganic

Electron-Collecting Buffer Layers. *Adv. Energy. Mater.* **2014,** *4*.

182. Xiao, X.; Bergemann, K. J.; Zimmerman, J. D.; Lee, K.; Forrest, S. R., Small-Molecule Planar-Mixed Heterojunction Photovoltaic Cells with Fullerene-Based Electron Filtering Buffers. *Adv. Energy. Mater.* **2014,** *4*.

183. Li, C. Z.; Chang, C. Y.; Zang, Y.; Ju, H. X.; Chueh, C. C.; Liang, P. W.; Cho, N.; Ginger, D. S.; Jen, A. K., Suppressed Charge Recombination in Inverted Organic Photovoltaics Via Enhanced Charge Extraction by Using a Conductive Fullerene Electron Transport Layer. *Adv. Mater.* **2014,** *26*, 6262.

184. Zhang, W. J.; Wu, Y. L.; Bao, Q. Y.; Gao, F.; Fang, J. F., Morphological Control for Highly Efficient Inverted Polymer Solar Cells Via the Backbone Design of Cathode Interlayer Materials. *Adv. Energy. Mater.* **2014,** *4*.

185. Guo, X.; Zhang, M.; Ma, W.; Ye, L.; Zhang, S.; Liu, S.; Ade, H.; Huang, F.; Hou, J., Enhanced Photovoltaic Performance by Modulating Surface Composition in Bulk Heterojunction Polymer Solar Cells Based on Pbdttt-C-T/Pc71 Bm. *Adv. Mater.* **2014,** *26*, 4043.

186. Zheng, Y.; Potscavage, J. W. J.; Komino, T.; Hirade, M.; Adachi, J.; Adachi, C., Highly Efficient Bulk Heterojunction Photovoltaic Cells Based on C[Sub 70] and Tetraphenyldibenzoperiflanthene. *Appl. Phys. Lett.* **2013,** *102*, 143304.

187. Zheng, Y.; Potscavage, J. W. J.; Komino, T.; Adachi, C., Highly Efficient Bulk Heterojunction Photovoltaic Cell Based on Tris[4-(5-Phenylthiophen-2-Yl)Phenyl]Amine and C[Sub 70] Combined with Optimized Electron Transport Layer. *Appl. Phys. Lett.* **2013,** *102*, 153302.

188. Zhong, Y.; Tada, A.; Izawa, S.; Hashimoto, K.; Tajima, K., Enhancement of Voc without Loss of Jsc in Organic Solar Cells by Modification of Donor/Acceptor Interfaces. *Adv. Energy. Mater.* **2014,** *4*.

189. Graham, K. R.; Erwin, P.; Nordlund, D.; Vandewal, K.; Li, R.; Ngongang Ndjawa, G. O.; Hoke, E. T.; Salleo, A.; Thompson, M. E.; McGehee, M. D.; Amassian, A., Re-Evaluating the Role of Sterics and Electronic Coupling in Determining the Open-Circuit Voltage of Organic Solar Cells. *Adv. Mater.* **2013,** *25*, 6076.

190. Tietze, M. L.; Tress, W.; Pfützner, S.; Schünemann, C.; Burtone, L.; Riede, M.; Leo, K.; Vandewal, K.; Olthof, S.; Schulz, P.; Kahn, A., Correlation of Open-Circuit Voltage and Energy Levels in Zinc-Phthalocyanine: C_{60} Bulk Heterojunction Solar Cells with Varied Mixing Ratio. *Phys. Rev. B* **2013,** *88*, 085119.

191. Vandewal, K.; Gadisa, A.; Oosterbaan, W. D.; Bertho, S.; Banishoeib, F.; Van

Severen, I.; Lutsen, L.; Cleij, T. J.; Vanderzande, D.; Manca, J. V., The Relation between Open-Circuit Voltage and the Onset of Photocurrent Generation by Charge-Transfer Absorption in Polymer : Fullerene Bulk Heterojunction Solar Cells. *Adv. Funct. Mater.* **2008,** *18*, 2064.

192. Hoke, E. T.; Vandewal, K.; Bartelt, J. A.; Mateker, W. R.; Douglas, J. D.; Noriega, R.; Graham, K. R.; Fréchet, J. M. J.; Salleo, A.; McGehee, M. D., Recombination in Polymer:Fullerene Solar Cells with Open-Circuit Voltages Approaching and Exceeding 1.0 V. *Adv. Energy. Mater.* **2013,** *3*, 220.

193. Reinhard, S.; Regina, L.; Gotthard, S.; Till, J.-H.; Christian, K.; Karl, L.; Mathias, R., Quantifying Charge Transfer Energies At donor–Acceptor Interfaces in Small-Molecule Solar Cells with Constrained Dftb and Spectroscopic Methods. *J. Phys.: Condens. Mater.* **2013,** *25*, 473201.

194. Wetzelaer, G. J. A. H.; Kuik, M.; Blom, P. W. M., Identifying the Nature of Charge Recombination in Organic Solar Cells from Charge-Transfer State Electroluminescence. *Adv. Energy. Mater.* **2012,** *2*, 1232.

195. Kazaoui, S.; Ross, R.; Minami, N., Intermolecular Charge-Transfer Excitation in C_{60} Films: Evidence from Luminescence and Photoconductivity. *Phys. Rev. B* **1995,** *52*, R11665.

196. Kazaoui, S.; Minami, N.; Tanabe, Y.; Byrne, H. J.; Eilmes, A.; Petelenz, P., Comprehensive Analysis of Intermolecular Charge-Transfer Excited States in C_{60} and C_{70} Films. *Phys. Rev. B* **1998,** *58*, 7689.

197. Cook, S.; Ohkita, H.; Kim, Y.; Benson-Smith, J. J.; Bradley, D. D. C.; Durrant, J. R., A Photophysical Study of Pcbm Thin Films. *Chem. Phys. Lett.* **2007,** *445*, 276.

198. Pandey, R.; Gunawan, A. A.; Mkhoyan, K. A.; Holmes, R. J., Efficient Organic Photovoltaic Cells Based on Nanocrystalline Mixtures of Boron Subphthalocyanine Chloride and C60. *Adv. Funct. Mater.* **2012,** *22*, 617.

199. Reber, C.; Yee, L.; McKiernan, J.; Zink, J. I.; Williams, R. S.; Tong, W. M.; Ohlberg, D. A. A.; Whetten, R. L.; Diederich, F., Luminescence and Absorption Spectra of Carbon (C60) Films. *J. Phys. Chem.* **1991,** *95*, 2127.

200. Capozzi, V.; Casamassima, G.; Lorusso, G. F.; Minafra, A.; Piccolo, R.; Trovato, T.; Valentini, A., Optical Spectra and Photoluminescence of C60 Thin Films. *Solid State Commun.* **1996,** *98*, 853.

201. Li, G. Z.; Peng, J.; Minami, N., Electroluminescence of Fullerene C60-Doped Poly(Methyl Methacrylate). *J. Lumin.* **2001,** *93*, 173.

202. Bisquert, J.; Garcia-Belmonte, G., On Voltage, Photovoltage, and Photocurrent in Bulk Heterojunction Organic Solar Cells. *J. Phys. Chem. Lett.* **2011,** *2*, 1950.

203. Hains, A. W.; Marks, T. J., High-Efficiency Hole Extraction/Electron-Blocking Layer to Replace Poly(3,4-Ethylenedioxythiophene):Poly(Styrene Sulfonate) in Bulk-Heterojunction Polymer Solar Cells. *Appl. Phys. Lett.* **2008,** *92*, 023504.

204. Liao, H. H.; Chen, L. M.; Xu, Z.; Li, G.; Yang, Y., Highly Efficient Inverted Polymer Solar Cell by Low Temperature Annealing of Cs2co3 Interlayer. *Appl. Phys. Lett.* **2008,** *92*, 173303.

205. Chen, L. M.; Hong, Z.; Li, G.; Yang, Y., Recent Progress in Polymer Solar Cells: Manipulation of Polymer:Fullerene Morphology and the Formation of Efficient Inverted Polymer Solar Cells. *Adv. Mater.* **2009,** *21*, 1434.

206. Wynands, D.; Levichkova, M.; Leo, K.; Uhrich, C.; Schwartz, G.; Hildebrandt, D.; Pfeiffer, M.; Riede, M., Increase in Internal Quantum Efficiency in Small Molecular Oligothiophene: C60 Mixed Heterojunction Solar Cells by Substrate Heating. *Appl. Phys. Lett.* **2010,** *97*, 073503.

207. Wang, Z.; Yokoyama, D.; Wang, X. F.; Hong, Z.; Yang, Y.; Kido, J., Highly Efficient Organic P-I-N Photovoltaic Cells Based on Tetraphenyldibenzoperiflanthene and Fullerene C70. *Energy Environ. Sci.* **2013,** *6*, 249.

208. Chiu, S. W.; Lin, L. Y.; Lin, H. W.; Chen, Y. H.; Huang, Z. Y.; Lin, Y. T.; Lin, F.; Liu, Y. H.; Wong, K. T., A Donor-Acceptor-Acceptor Molecule for Vacuum-Processed Organic Solar Cells with a Power Conversion Efficiency of 6.4%. *Chem. Commun.* **2012,** *48*, 1857.

209. Kim, D. Y.; So, F.; Gao, Y., Aluminum Phthalocyanine Chloride/C60 Organic Photovoltaic Cells with High Open-Circuit Voltages. *Sol. Energ. Mater. Sol. C.* **2009,** *93*, 1688.

210. Cnops, K.; Rand, B. P.; Cheyns, D.; Verreet, B.; Empl, M. A.; Heremans, P., 8.4% Efficient Fullerene-Free Organic Solar Cells Exploiting Long-Range Exciton Energy Transfer. *Nat. Commun.* **2014,** *5*, 3406.

211.Li, N.; Lassiter, B. E.; Lunt, R. R.; Wei, G.; Forrest, S. R., Open Circuit Voltage Enhancement Due to Reduced Dark Current in Small Molecule Photovoltaic Cells. *Appl. Phys. Lett.* **2009,** *94*, 023307.

212. Wynands, D.; Mannig, B.; Riede, M.; Leo, K.; Brier, E.; Reinold, E.; Bauerle, P., Organic Thin Film Photovoltaic Cells Based on Planar and Mixed Heterojunctions between Fullerene and a Low Bandgap Oligothiophene. *J. Appl. Phys.* **2009,** *106*, 054509.

213. Xiao, X.; Zimmerman, J. D.; Lassiter, B. E.; Bergemann, K. J.; Forrest, S. R., A Hybrid Planar-Mixed Tetraphenyldibenzoperiflanthene/C[Sub 70] Photovoltaic Cell. *Appl. Phys. Lett.* **2013,** *102*, 073302.

214. Tseng, Y. C.; Mane, A. U.; Elam, J. W.; Darling, S. B., Ultrathin Molybdenum Oxide Anode Buffer Layer for Organic Photovoltaic Cells Formed Using Atomic Layer Deposition. *Sol. Energ. Mater. Sol. C.* **2012,** *99*, 235.

215. Tress, W.; Petrich, A.; Hummert, M.; Hein, M.; Leo, K.; Riede, M., Imbalanced Mobilities Causing S-Shaped Iv Curves in Planar Heterojunction Organic Solar Cells. *Appl. Phys. Lett.* **2011,** *98*, 063301.

216. Wagenpfahl, A.; Rauh, D.; Binder, M.; Deibel, C.; Dyakonov, V., S-Shaped Current-Voltage Characteristics of Organic Solar Devices. *Phys. Rev. B* **2010,** *82*, 115306.

217. Tress, W.; Corvers, S.; Leo, K.; Riede, M., Investigation of Driving Forces for Charge Extraction in Organic Solar Cells: Transient Photocurrent Measurements on Solar Cells Showing S-Shaped Current–Voltage Characteristics. *Adv. Energy. Mater.* **2013,** *3*, 873.

218. Tress, W.; Leo, K.; Riede, M., Influence of Hole-Transport Layers and Donor Materials on Open-Circuit Voltage and Shape of I–V Curves of Organic Solar Cells. *Adv. Funct. Mater.* **2011,** *21*, 2140.

219. Luhman, W. A.; Holmes, R. J., Investigation of Energy Transfer in Organic Photovoltaic Cells and Impact on Exciton Diffusion Length Measurements. *Adv. Funct. Mater.* **2011,** *21*, 764.

220. Lunt, R. R.; Giebink, N. C.; Belak, A. A.; Benziger, J. B.; Forrest, S. R., Exciton Diffusion Lengths of Organic Semiconductor Thin Films Measured by Spectrally Resolved Photoluminescence Quenching. *J. Appl. Phys.* **2009,** *105*, 053711.

221. Seaman, C. H., Calibration of Solar Cells by the Reference Cell Method—the Spectral Mismatch Problem. *Sol. Energy* **1982,** *29*, 291.

222. Shrotriya, V.; Li, G.; Yao, Y.; Moriarty, T.; Emery, K.; Yang, Y., Accurate Measurement and Characterization of Organic Solar Cells. *Adv. Funct. Mater.* **2006,** *16*, 2016.

223. Wang, D. H.; Kyaw, A. K. K.; Gupta, V.; Bazan, G. C.; Heeger, A. J., Enhanced Efficiency Parameters of Solution-Processable Small-Molecule Solar Cells Depending on Ito Sheet Resistance. *Adv. Energy. Mater.* **2013,** *3*, 1161.

224. Snaith, H. J., How Should You Measure Your Excitonic Solar Cells? *Energy Environ. Sci.* **2012,** *5*, 6513.

225. van der Poll, T. S.; Love, J. A.; Nguyen, T. Q.; Bazan, G. C., Non-Basic High-Performance Molecules for Solution-Processed Organic Solar Cells. *Adv. Mater.* **2012,** *24*, 3646.

226. Beaujuge, P. M.; Amb, C. M.; Reynolds, J. R., Spectral Engineering in Π-Conjugated Polymers with Intramolecular Donor−Acceptor Interactions. *Accounts. Chem. Res.* **2010,** *43*, 1396.

227. Ajayaghosh, A., Donor-Acceptor Type Low Band Gap Polymers: Polysquaraines and Related Systems. *Chem. Soc. Rev.* **2003,** *32*, 181.

228. Lin, L.-Y.; Tsai, C.-H.; Lin, F.; Huang, T.-W.; Chou, S.-H.; Wu, C.-C.; Wong, K.-T., 2,1,3-Benzothiadiazole-Containing Donor–Acceptor–Acceptor Dyes for Dye-Sensitized Solar Cells. *Tetrahedron* **2012,** *68*, 7509.

229. Zhang, X.-H.; Cui, Y.; Katoh, R.; Koumura, N.; Hara, K., Organic Dyes Containing Thieno[3,2-B]Indole Donor for Efficient Dye-Sensitized Solar Cells. *J. Phys. Chem. C* **2010,** *114*, 18283.

230. Irgashev, R. A.; Karmatsky, A. A.; Kozyukhin, S. A.; Ivanov, V. K.; Sadovnikov, A.; Kozik, V. V.; Grinberg, V. A.; Emets, V. V.; Rusinov, G. L.; Charushin, V. N., A Facile and Convenient Synthesis and Photovoltaic Characterization of Novel Thieno[2,3-B]Indole Dyes for Dye-Sensitized Solar Cells. *Synthetic. Met.* **2015,** *199*, 152.

231. Sum, T. C.; Mathews, N., Advancements in Perovskite Solar Cells: Photophysics Behind the Photovoltaics. *Energy Environ. Sci.* **2014,** *7*, 2518.

232. Gao, P.; Grätzel, M.; Nazeeruddin, M. K., Organohalide Lead Perovskites for Photovoltaic Applications. *Energy Environ. Sci.* **2014,** *7*, 2448.

233. Green, M. A.; Ho-Baillie, A.; Snaith, H. J., The Emergence of Perovskite Solar Cells. *Nat. Photonics* **2014,** *8*, 506.

234. Salau, A. M., Fundamental Absorption Edge in Pbi2:Ki Alloys. *Solar Energy Materials* **1980,** *2*, 327.

235. Mitzi, D. B.; Wang, S.; Feild, C. A.; Chess, C. A.; Guloy, A. M., Conducting Layered Organic-Inorganic Halides Containing <110>-Oriented Perovskite Sheets. *Science* **1995,** *267*, 1473.

236. Mitzi, D. B.; Chondroudis, K.; Kagan, C. R., Organic-Inorganic Electronics. *Ibm. J. Res. Dev.* **2001,** *45*, 29.

237. Kojima, A.; Teshima, K.; Shirai, Y.; Miyasaka, T., Organometal Halide

Perovskites as Visible-Light Sensitizers for Photovoltaic Cells. *J. Am. Chem. Soc.* **2009,** *131*, 6050.

238. Im, J.-H.; Lee, C.-R.; Lee, J.-W.; Park, S.-W.; Park, N.-G., 6.5% Efficient Perovskite Quantum-Dot-Sensitized Solar Cell. *Nanoscale* **2011,** *3*, 4088.

239. Kim, H. S.; Lee, C. R.; Im, J. H.; Lee, K. B.; Moehl, T.; Marchioro, A.; Moon, S. J.; Humphry-Baker, R.; Yum, J. H.; Moser, J. E.; Gratzel, M.; Park, N. G., Lead Iodide Perovskite Sensitized All-Solid-State Submicron Thin Film Mesoscopic Solar Cell with Efficiency Exceeding 9%. *Sci Rep* **2012,** *2*, 591.

240. Lee, M. M.; Teuscher, J.; Miyasaka, T.; Murakami, T. N.; Snaith, H. J., Efficient Hybrid Solar Cells Based on Meso-Superstructured Organometal Halide Perovskites. *Science* **2012,** *338*, 643.

241. Stranks, S. D.; Eperon, G. E.; Grancini, G.; Menelaou, C.; Alcocer, M. J. P.; Leijtens, T.; Herz, L. M.; Petrozza, A.; Snaith, H. J., Electron-Hole Diffusion Lengths Exceeding 1 Micrometer in an Organometal Trihalide Perovskite Absorber. *Science* **2013,** *342*, 341.

242. Heo, J. H.; Im, S. H.; Noh, J. H.; Mandal, T. N.; Lim, C. S.; Chang, J. A.; Lee, Y. H.; Kim, H. J.; Sarkar, A.; Nazeeruddin, M. K.; Gratzel, M.; Seok, S. I., Efficient Inorganic-Organic Hybrid Heterojunction Solar Cells Containing Perovskite Compound and Polymeric Hole Conductors. *Nat. Photonics* **2013,** *7*, 487.

243. Jeon, N. J.; Noh, J. H.; Yang, W. S.; Kim, Y. C.; Ryu, S.; Seo, J.; Seok, S. I., Compositional Engineering of Perovskite Materials for High-Performance Solar Cells. *Nature* **2015,** *517*, 476.

244. Marchioro, A.; Teuscher, J.; Friedrich, D.; Kunst, M.; van de Krol, R.; Moehl, T.; Gratzel, M.; Moser, J. E., Unravelling the Mechanism of Photoinduced Charge Transfer Processes in Lead Iodide Perovskite Solar Cells. *Nat. Photonics* **2014,** *8*, 250.

245. Yin, W. J.; Shi, T.; Yan, Y., Unique Properties of Halide Perovskites as Possible Origins of the Superior Solar Cell Performance. *Adv. Mater.* **2014,** *26*, 4653.

246. Xing, G.; Mathews, N.; Sun, S.; Lim, S. S.; Lam, Y. M.; Grätzel, M.; Mhaisalkar, S.; Sum, T. C., Long-Range Balanced Electron- and Hole-Transport Lengths in Organic-Inorganic Ch3nh3pbi3. *Science* **2013,** *342*, 344.

247. Even, J.; Pedesseau, L.; Jancu, J.-M.; Katan, C., Importance of Spin–Orbit Coupling in Hybrid Organic/Inorganic Perovskites for Photovoltaic Applications. *J. Phys. Chem. Lett.* **2013,** *4*, 2999.

248. Sun, S.; Salim, T.; Mathews, N.; Duchamp, M.; Boothroyd, C.; Xing, G.; Sum, T. C.; Lam, Y. M., The Origin of High Efficiency in Low-Temperature Solution-Processable Bilayer Organometal Halide Hybrid Solar Cells. *Energy Environ. Sci.* **2014,** *7*, 399.

249. Snaith, H. J., Perovskites: The Emergence of a New Era for Low-Cost, High-Efficiency Solar Cells. *J. Phys. Chem. Lett.* **2013,** *4*, 3623.

250. Yin, W. J.; Shi, T.; Yan, Y., Unusual Defect Physics in Ch3nh3pbi3 Perovskite Solar Cell Absorber. *Appl. Phys. Lett.* **2014,** *104*, 063903.

251. Kim, J.; Lee, S. H.; Lee, J. H.; Hong, K. H., The Role of Intrinsic Defects in Methylammonium Lead Iodide Perovskite. *J. Phys. Chem. Lett.* **2014,** *5*, 1312.

252. Liu, M.; Johnston, M. B.; Snaith, H. J., Efficient Planar Heterojunction Perovskite Solar Cells by Vapour Deposition. *Nature* **2013,** *501*, 395.

253. Chen, Q.; Zhou, H.; Hong, Z.; Luo, S.; Duan, H.-S.; Wang, H.-H.; Liu, Y.; Li, G.; Yang, Y., Planar Heterojunction Perovskite Solar Cells Via Vapor-Assisted Solution Process. *J. Am. Chem. Soc.* **2013,** *136*, 622.

254. Burschka, J.; Pellet, N.; Moon, S.-J.; Humphry-Baker, R.; Gao, P.; Nazeeruddin, M. K.; Gratzel, M., Sequential Deposition as a Route to High-Performance Perovskite-Sensitized Solar Cells. *Nature* **2013,** *499*, 316.

255. Xiao, Z. G.; Bi, C.; Shao, Y. C.; Dong, Q. F.; Wang, Q.; Yuan, Y. B.; Wang, C. G.; Gao, Y. L.; Huang, J. S., Efficient, High Yield Perovskite Photovoltaic Devices Grown by Interdiffusion of Solution-Processed Precursor Stacking Layers. *Energy Environ. Sci.* **2014,** *7*, 2619.

256. Frost, J. M.; Butler, K. T.; Brivio, F.; Hendon, C. H.; van Schilfgaarde, M.; Walsh, A., Atomistic Origins of High-Performance in Hybrid Halide Perovskite Solar Cells. *Nano Lett.* **2014,** *14*, 2584.

257. Tress, W.; Marinova, N.; Moehl, T.; Zakeeruddin, S. M.; Nazeeruddin, M. K.; Gratzel, M., Understanding the Rate-Dependent J-V Hysteresis, Slow Time Component, and Aging in Ch3nh3pbi3 Perovskite Solar Cells: The Role of a Compensated Electric Field. *Energy Environ. Sci.* **2015,** *8*, 995.

258. Kim, H. S.; Park, N. G., Parameters Affecting I–V Hysteresis of Ch3nh3pbi3 Perovskite Solar Cells: Effects of Perovskite Crystal Size and Mesoporous Tio2 Layer. *J. Phys. Chem. Lett.* **2014**, 2927.

259. Unger, E. L.; Hoke, E. T.; Bailie, C. D.; Nguyen, W. H.; Bowring, A. R.; Heumuller, T.; Christoforo, M. G.; McGehee, M. D., Hysteresis and Transient Behavior in

Current-Voltage Measurements of Hybrid-Perovskite Absorber Solar Cells. *Energy Environ. Sci.* **2014,** *7*, 3690.

260. Snaith, H. J.; Abate, A.; Ball, J. M.; Eperon, G. E.; Leijtens, T.; Noel, N. K.; Stranks, S. D.; Wang, J. T. W.; Wojciechowski, K.; Zhang, W., Anomalous Hysteresis in Perovskite Solar Cells. *J. Phys. Chem. Lett.* **2014,** *5*, 1511.

261. Shao, Y.; Xiao, Z.; Bi, C.; Yuan, Y.; Huang, J., Origin and Elimination of Photocurrent Hysteresis by Fullerene Passivation in Ch3nh3pbi3 Planar Heterojunction Solar Cells. *Nat. Commun.* **2014,** *5*, 5784.

262. Chen, H. W.; Sakai, N.; Ikegami, M.; Miyasaka, T., Emergence of Hysteresis and Transient Ferroelectric Response in Organo-Lead Halide Perovskite Solar Cells. *J. Phys. Chem. Lett.* **2014**, 164.

263. Jeon, N. J.; Noh, J. H.; Kim, Y. C.; Yang, W. S.; Ryu, S.; Seok, S. I., Solvent Engineering for High-Performance Inorganic–Organic Hybrid Perovskite Solar Cells. *Nat. Mater.* **2014,** *advance online publication*.

264. Kim, H. S.; Mora-Sero, I.; Gonzalez-Pedro, V.; Fabregat-Santiago, F.; Juarez-Perez, E. J.; Park, N. G.; Bisquert, J., Mechanism of Carrier Accumulation in Perovskite Thin-Absorber Solar Cells. *Nat. Commun.* **2013,** *4*, 2242.

265. Stoumpos, C. C.; Malliakas, C. D.; Kanatzidis, M. G., Semiconducting Tin and Lead Iodide Perovskites with Organic Cations: Phase Transitions, High Mobilities, and near-Infrared Photoluminescent Properties. *Inorg. Chem.* **2013,** *52*, 9019.

266. Bertoluzzi, L.; Sanchez, R. S.; Liu, L.; Lee, J. W.; Mas-Marza, E.; Han, H.; Park, N. G.; Mora-Sero, I.; Bisquert, J., Cooperative Kinetics of Depolarization in Ch3nh3pbi3 Perovskite Solar Cells. *Energy Environ. Sci.* **2015,** *8*, 910.

267. Xiao, Z.; Yuan, Y.; Shao, Y.; Wang, Q.; Dong, Q.; Bi, C.; Sharma, P.; Gruverman, A.; Huang, J., Giant Switchable Photovoltaic Effect in Organometal Trihalide Perovskite Devices. *Nat. Mater.* **2015,** *14*, 193.

268. Wu, Y.; Islam, A.; Yang, X.; Qin, C.; Liu, J.; Zhang, K.; Peng, W.; Han, L., Retarding the Crystallization of Pbi2 for Highly Reproducible Planar-Structured Perovskite Solar Cells Via Sequential Deposition. *Energy Environ. Sci.* **2014,** *7*, 2934.

269. Ono, L. K.; Raga, S. R.; Wang, S.; Kato, Y.; Qi, Y., Temperature-Dependent Hysteresis Effects in Perovskite-Based Solar Cells. *J. Mater. Chem. A* **2015,** *3*, 9074.

270. Savenije, T. J.; Ponseca, C. S.; Kunneman, L.; Abdellah, M.; Zheng, K.; Tian, Y.; Zhu, Q.; Canton, S. E.; Scheblykin, I. G.; Pullerits, T.; Yartsev, A.; Sundström, V.,

Thermally Activated Exciton Dissociation and Recombination Control the Carrier Dynamics in Organometal Halide Perovskite. *J. Phys. Chem. Lett.* **2014,** *5*, 2189.

271. D'Innocenzo, V.; Grancini, G.; Alcocer, M. J.; Kandada, A. R.; Stranks, S. D.; Lee, M. M.; Lanzani, G.; Snaith, H. J.; Petrozza, A., Excitons Versus Free Charges in Organo-Lead Tri-Halide Perovskites. *Nat. Commun.* **2014,** *5*, 3586.

272. Roiati, V.; Mosconi, E.; Listorti, A.; Colella, S.; Gigli, G.; De Angelis, F., Stark Effect in Perovskite/Tio2 Solar Cells: Evidence of Local Interfacial Order. *Nano Lett.* **2014,** *14*, 2168.

273. O'Regan, B. C.; Barnes, P. R. F.; Li, X.; Law, C.; Palomares, E.; Marin-Beloqui, J. M., Optoelectronic Studies of Methylammonium Lead Iodide Perovskite Solar Cells with Mesoporous Tio2: Separation of Electronic and Chemical Charge Storage, Understanding Two Recombination Lifetimes, and the Evolution of Band Offsets During J–V Hysteresis. *J. Am. Chem. Soc.* **2015,** *137*, 5087.

274. Wang, Q.; Shao, Y.; Xie, H.; Lyu, L.; Liu, X.; Gao, Y.; Huang, J., Qualifying Composition Dependent P and N Self-Doping in Ch3nh3pbi3. *Appl. Phys. Lett.* **2014,** *105*, 163508.

275. Jeon, N. J.; Noh, J. H.; Kim, Y. C.; Yang, W. S.; Ryu, S.; Seok, S. I., Solvent Engineering for High-Performance Inorganic-Organic Hybrid Perovskite Solar Cells. *Nat. Mater.* **2014,** *13*, 897.

276. Wang, Q.; Shao, Y.; Dong, Q.; Xiao, Z.; Yuan, Y.; Huang, J., Large Fill-Factor Bilayer Iodine Perovskite Solar Cells Fabricated by a Low-Temperature Solution-Process. *Energy Environ. Sci.* **2014,** *7*, 2359.

277. Bryant, D.; Wheeler, S.; O'Regan, B. C.; Watson, T.; Barnes, P. R. F.; Worsley, D.; Durrant, J., Observable Hysteresis at Low Temperature in "Hysteresis Free" Organic–Inorganic Lead Halide Perovskite Solar Cells. *J. Phys. Chem. Lett.* **2015,** *6*, 3190.

278. Yang, B.; Yuan, Y.; Huang, J., Reduced Bimolecular Charge Recombination Loss in Thermally Annealed Bilayer Heterojunction Photovoltaic Devices with Large External Quantum Efficiency and Fill Factor. *J. Phys. Chem. C* **2014,** *118*, 5196.

279. Verreet, B.; Heremans, P.; Stesmans, A.; Rand, B. P., Microcrystalline Organic Thin-Film Solar Cells. *Adv. Mater.* **2013,** *25*, 5504.

280. Hinsch, A.; Kroon, J. M.; Kern, R.; Uhlendorf, I.; Holzbock, J.; Meyer, A.; Ferber, J., Long-Term Stability of Dye-Sensitised Solar Cells. *Progress in Photovoltaics: Research and Applications* **2001,** *9*, 425.

281. Mateker, W. R.; Douglas, J. D.; Cabanetos, C.; Sachs-Quintana, I. T.; Bartelt, J. A.; Hoke, E. T.; El Labban, A.; Beaujuge, P. M.; Frechet, J. M. J.; McGehee, M. D., Improving the Long-Term Stability of Pbdttpd Polymer Solar Cells through Material Purification Aimed at Removing Organic Impurities. *Energy Environ. Sci.* **2013,** *6*, 2529.

282. Zhang, H.; Borgschulte, A.; Castro, F. A.; Crockett, R.; Gerecke, A. C.; Deniz, O.; Heier, J.; Jenatsch, S.; Nüesch, F.; Sanchez-Sanchez, C.; Zoladek-Lemanczyk, A.; Hany, R., Photochemical Transformations in Fullerene and Molybdenum Oxide Affect the Stability of Bilayer Organic Solar Cells. *Adv. Energy. Mater.* **2015,** *5*.

Appendix

A: List of Publications and Presentations

PUBLICATIONS

1. **Zou, Y.**; Holmes, R. J., Temperature-dependent Bias-poling and Hysteresis in Planar Organo-metal Halide Perovskite Photovoltaic Cells. *Adv. Energy Mater.* **2015**, *in press*.

2. **Zou, Y.**; Holmes, R. J., Correlation Between the Theoretical Maximum Achievable Open-circuit Voltage and Charge Transfer State Energy in Organic Photovoltaic Cells. *ACS Appl. Mater. Interfaces,* **2015**, *7*, 18306.

3. **Zou, Y.**; Holmes, R. J., The Role of Exciton Ionization Processes in Bulk Heterojunction Organic Photovoltaic Cells. *Adv. Energy Mater.* **2015**, *5*, 1500019.

4. Mullenbach, T.K.; **Zou, Y.**; Holmes, R. J., Interpreting Impedance Spectra of Organic Photovoltaic Cells—Extracting Charge Transit and Recombination Rates. *J. Appl. Phys.* **2014**, *116*, 124513.

5. **Zou, Y.**; Holst, J.; Zhang, Y.; Holmes, R. J., 7.9% Efficient Vapor-Deposited Organic Photovoltaic Cells Based on a Simple Bulk Heterojunction. *J. Mater. Chem. A* **2014**, *2*, 12397.

6. **Zou, Y.**; Holmes, R. J., Influence of a MoO_x Interlayer on the Open-Circuit Voltage in Organic Photovoltaic Cells. *Appl. Phys. Lett.* **2013,** *103*, 053302.

7. Pandey, R.; **Zou, Y.**; Holmes, R. J., Efficient, Bulk Heterojunction Organic Photovoltaic Cells Based on Boron Subphthalocyanine Chloride-C_{70}. *Appl. Phys. Lett.* **2012,** *101*, 033308.

PRESENTATIONS

1. **Zou, Y.**; Holmes, R. J., Realizing Efficienct Energy Harvesting from Thin Film Photovoltaic Cells. **2015**, Industrial Partnership for Research in Interfacial and Materials Engineering (IPrime) Annual Meeting, Minneapolis MN.

2. **Zou, Y.**; Holmes, R. J., The Role of Exciton Ionization Process in Bulk Heterojunction Organic Photovoltaic Cells. **2015**, American Physical Society (APS) March Meeting, San Antonio TX.
3. **Zou, Y.**; Holst, J.; Zhang, Y.; Holmes, R. J., 7.9% Efficient Vapor-deposited Organic

Photovoltaic Cells Based on a Simple Bulk Heterojunction. **2014**, Industrial Partnership for Research in Interfacial and Materials Engineering (IPrime) Annual Meeting, Minneapolis MN.

4. **Zou, Y.**; Holst, J.; Zhang, Y.; Holmes, R. J. Highly Efficient Vapor-deposited Organic Photovoltaic Cells Based on a Simple Mixed Heterojunction, **2014**, Materials Research Society (MRS) Spring Meeting, San Francisco CA.

5. **Zou, Y.**; Holmes, R. J. Influence of MoO_x Interlayer on the Open-circuit Voltage in Organic Photovoltaic Cells, **2013**, Industrial Partnership for Research in Interfacial and Materials Engineering (IPrime) Annual Meeting, Minneapolis MN.

6. **Zou, Y.**; Holmes, R. J. Influence of MoO_x Interlayer on the Open-circuit Voltage in Organic Photovoltaic Cells, **2013**,American Physical Society (APS) March Meeting, Baltimore MD

B. Matlab Codes

Code for fitting dark current

This code is a combination of two programs to extract the ideality factor, series resistance, shunt resistance and reverse saturation current from the dark current. The main program provides an interface to input initial guess and boundaries for the fitting parameters using the 'lsqnonlin' function. The solving program takes advantage of the 'fzero' function to solve the Shockley equation with the input parameters and return the error between simulated results and experimental data to the main program.

```
clc;
clear;
global expJV simJ err T initial;
expJV = load('expJV.txt');

simJ = expJV(:,2);
err=zeros(length(expJV),1);
T=300;
options = optimset('Display','iter','Tolfun',1e-20,'MaxIter',800);

data = lsqnonlin('SolveShockley',initial,[0.039 0 0 0 0],[1 200000000000 1000000000 196
1000000000],options)
initial = data;

figure(1)
simJ(:,2) = abs(simJ(:,1));
semilogy(expJV(:,1),abs(simJ(:,1)),'-');

hold on
semilogy(expJV(:,1),abs(expJV(:,2)),'+');

Solving function
function [err] = SolveShockley(data)

global expJV simJ T;

Rs = data(1)/10;
nD = data(2)/100;
JsD = data(3)/100000;
nA = data(4)/100;
JsA = data(5)/100000;
```

```
 for i=1:length(expJV)
simJ(i,1)=fzero(@(y)y-JsD*(exp((expJV(i)-y*Rs)/nD/(T/300*0.0259))-1)-
JsA*(exp((expJV(i)-y*Rs)/nA/(T/300*0.0259))-1),1);

 if (abs(expJV(i,2)/simJ(i,1))>1)
 err(i)=abs(expJV(i,2)/simJ(i,1))-1;
 else
        err(i)=abs(simJ(i,1)/expJV(i,2))-1;
 end

 end

end
```

Optical simulation for tandem cells

This code is a combination of two programs to predict the photocurrent output from a tandem photovoltaic cell by varying the thickness of each sub-cell. The main program provides an interface to input the device architecture and load optical constants.

The transfer matrix program takes the input device architecture and returns the photocurrent output of each sub-cell to the main program. A 2D map of the photocurrent is generated by iterating the thickness of each sub-cell.

Main Program:

```
clc;
clear;
global n layers lambda stepsize activeLayer1 activeLayer2 Jsc;
i=1;
Photocurrent=zeros(10,3);
thickX=60;
thickY=60;
Jsc = [0 0];

lambda=300:5:900; % Wavelengths over which field patterns are calculated
stepsize = 1;      % The electric field is calculated at a lattice of points (nm)
                        % in the device cross section separated by this distance

layers = {'SiO2' 'ITO' 'MoO3' 'FoC70' 'Bphen' 'MoO3' 'CTB11' 'Bphen' 'Ag'};
activeLayer1 = 4;
activeLayer2 = 7;
n = zeros(size(layers,2),size(lambda,2));

for index = 1:size(layers,2)
      n(index,:) = LoadRef(layers{index},lambda);
end

for    thickX = 20:20:120
      for thickY = 20:20:120
            Photocurrent(i,1) = thickX;
            Photocurrent(i,2) = thickY;
            Photocurrent(i,3:4) = tandem(thickX ,thickY);
            Photocurrent(i,5) = min(Photocurrent(i,3),Photocurrent(i,4));
            i=i+1;
      end
end
%plot
```

```
tri = delaunay(Photocurrent(:,1),Photocurrent(:,2));
[r,c] = size(tri);
h = trisurf(tri, Photocurrent(:,1), Photocurrent(:,2), Photocurrent(:,5));
axis vis3d
%l = light('Position',[-50 -15 29]);
%lighting phong
shading interp
colorbar EastOutside
```

Transfer Matrix Program:

```
function Jsc = tandem(thickX,thickY)
global n lambda stepsize activeLayer1 activeLayer2 Jsc;

thicknesses = [0 150 10 thickY 5 5 thickX 7 100];   % thickness of each corresponding layer in nm (thickness of the first layer is irrelivant)

% Load in index of refraction for each material

t = thicknesses;

% Constants
h=6.626e-34; % Js Planck's constant
c=2.998e8; %m/s speed of light
q=1.602e-19; %C electric charge

% Calculate Incoherent power transmission through substrate
T_glass=abs(4*1*n(1,:)./(1+n(1,:)).^2);
R_glass=abs((1-n(1,:))./(1+n(1,:))).^2;

% Calculate transfer matrices, and field at each wavelength and position
t(1)=0;
t_cumsum=cumsum(t);
x_pos=(stepsize/2):stepsize:sum(t); %positions to evaluate field
%x_mat specifies what layer number the corresponding point in x_pos is in:
x_mat= sum(repmat(x_pos,length(t),1)>repmat(t_cumsum',1,length(x_pos)),1)+1;
R=lambda*0;
E=zeros(length(x_pos),length(lambda));
for l = 1:length(lambda)
    % Calculate transfer matrices for incoherent reflection and transmission at the first interface
    S=I_mat(n(1,l),n(2,l));
    for matindex=2:(length(t)-1)
```

```
S=S*L_mat(n(matindex,l),t(matindex),lambda(l))*I_mat(n(matindex,l),n(matindex+1,l));
    end
    R(l)=abs(S(2,1)/S(1,1))^2; %JAP Vol 86 p.487 Eq 9 Power Reflection from layers other than substrate
    T(l)=abs(2/(1+n(1,l)))/sqrt(1-R_glass(l)*R(l)); %Transmission of field through glass substrate Griffiths 9.85 + multiple reflection geometric series

    % Calculate all other transfer matrices
    for material = 2:length(t)
        xi=2*pi*n(material,l)/lambda(l);
        dj=t(material);
        x_indices=find(x_mat == material); %indices of points which are in the material layer considered
        x=x_pos(x_indices)-t_cumsum(material-1); %distance from interface with previous layer
        % Calculate S matrices (JAP Vol 86 p.487 Eq 12 and 13)
        S_prime=I_mat(n(1,l),n(2,l));
        for matindex=3:material
            S_prime=S_prime*L_mat(n(matindex-1,l),t(matindex-1),lambda(l))*I_mat(n(matindex-1,l),n(matindex,l));
        end
        S_doubleprime=eye(2);
        for matindex=material:(length(t)-1)

S_doubleprime=S_doubleprime*I_mat(n(matindex,l),n(matindex+1,l))*L_mat(n(matindex+1,l),t(matindex+1),lambda(l));
        end
        % Normalized Field profile (JAP Vol 86 p.487 Eq 22)
        E(x_indices,l)=T(l)*(S_doubleprime(1,1)*exp(-1i*xi*(dj-x))+S_doubleprime(2,1)*exp(1i*xi*(dj-x)))    ./(S_prime(1,1)*S_doubleprime(1,1)*exp(-1i*xi*dj)+S_prime(1,2)*S_doubleprime(2,1)*exp(1i*xi*dj));
    end
end

% Overall Reflection from device with incoherent reflections at first
% interface (typically air-glass)
Reflection=R_glass+T_glass.^2.*R./(1-R_glass.*R);

% Plots electric field intensity |E|^2 vs position in device for
% wavelengths specified in the initial array, plotWavelengths.

a=zeros(length(t),length(lambda));
```

```
for matindex=2:length(t)
        a(matindex,:)=4*pi*imag(n(matindex,:))./(lambda*1e-7);
end


      % Load in 1sun AM 1.5 solar spectrum in mW/cm2nm
      AM15_data=xlsread('AM15.xls');
      AM15=interp1(AM15_data(:,1), AM15_data(:,2), lambda, 'linear', 'extrap');

      ActivePos=find(x_mat == activeLayer1);

Q=repmat(a(activeLayer1,:).*real(n(activeLayer1,:)).*AM15,length(ActivePos),1).*(abs(
E(ActivePos,:)).^2);

      % Exciton generation rate per second-cm3-nm at each position and wavelength
      Gxl=(Q*1e-3).*repmat(lambda*1e-9,length(ActivePos),1)/(h*c);

      if length(lambda)==1
            lambdastep= 1;
      else
            lambdastep=(max(lambda)-min(lambda))/(length(lambda)-1);
      end
      Gx=sum(Gxl,2)*lambdastep; % Exciton generation rate as a function of position/(sec-
cm^3)

      % outputs predicted Jsc under AM1.5 illumination assuming 100% internal
      % quantum efficiency at all wavelengths
      Jsc(1,1)=sum(Gx)*stepsize*1e-7*q*1e3; %in mA/cm^2

      ActivePos=find(x_mat == activeLayer2);

Q=repmat(a(activeLayer2,:).*real(n(activeLayer2,:)).*AM15,length(ActivePos),1).*(abs(
E(ActivePos,:)).^2);

      % Exciton generation rate per second-cm3-nm at each position and wavelength
      Gxl=(Q*1e-3).*repmat(lambda*1e-9,length(ActivePos),1)/(h*c);

      if length(lambda)==1
            lambdastep= 1;
      else
            lambdastep=(max(lambda)-min(lambda))/(length(lambda)-1);
      end
```

```
Gx=sum(Gxl,2)*lambdastep; % Exciton generation rate as a function of position/(sec-cm^3)

Jsc(1,2) = sum(Gx)*stepsize*1e-7*q*1e3 %in mA/cm^2



function I = I_mat(n1,n2)
r=(n1-n2)/(n1+n2);
t=2*n1/(n1+n2);
I=[1 r; r 1]/t;

% complex dielectric constant n and thickness d for the wavelength lambda.
function L = L_mat(n,d,lambda)
xi=2*pi*n/lambda;
L=[exp(-1i*xi*d) 0; 0 exp(1i*xi*d)];
```

Solving charge carrier drift-diffusion equation

This code is a combination of several programs to solve the charge carrier drift-diffusion problem in a homogeneous semiconductor with given boundary conditions and initial guess. The main program provides an interface for inputting parameters and calls for solving functions to numerically solve the drift-diffusion equation. By solving the drift-diffusion equation at various bias, the current density-voltage characteristics can be simulated.

Main Program

```
T = 300; % Set temperature

global beta gamma alpha V_bi V_factor V e_Density h_Density;
options = bvpset('Nmax',2000);
V = 1; % Bias Voltage (V)
V_factor = (V_bi-V)/V;
beta = V/(0.0259*T/300);
gamma = 0.01; % hole/electron Mobility ratio
alpha = 0.5; % Recombination factor
V_bi = 0; % Built-in Voltage (V)
e_Density = 1e21;
h_Density = 1e21;
epsilon = 8.85e-12;
L = 50e-9;
q = 1.6e-19;
R_epsilon = 3;
u_hole = 1e-4;
D = 0.0259*T/300*u_hole;


solinit = bvpinit(linspace(0,1,40),@init_guess);

  %solinit.x = sol.x;
  %solinit.y = sol.y;

sol = bvp5c(@DriftODE,@BC,solinit);
%plot the results
figure
plot(sol.x,sol.y(1,:)/1.50659e-23*V);
hold on
plot(sol.x,sol.y(2,:)/1.50659e-23*V,':') ;
legend('N','P');ylabel('N,P');xlabel('d')
figure
```

```
plot(sol.x,sol.y(5,:),'-.');
legend('E');ylabel('E');xlabel('d')
figure
plot(sol.x,sol.y(6,:),'-.');
legend('Potential');ylabel('Potential');xlabel('d')

Current_Left    = V/L*sol.y(5,1)*(u_hole*sol.y(2,1)       -u_hole/gamma*sol.y(1,1))
*q*D*epsilon*R_epsilon*V/L/L    +    (sol.y(3,1)    /gamma - sol.y(4,1))
*q*D*epsilon*R_epsilon*V/L/L/L/q    %A/m_2
Current_Right = V/L*sol.y(5,end)*(u_hole*sol.y(2,end)-
u_hole/gamma*sol.y(1,end))*q*D*epsilon*R_epsilon*V/L/L    +    (sol.y(3,end)/gamma
- sol.y(4,end))*q*D*epsilon*R_epsilon*V/L/L/L/q      %A/m_2
```

Solving Drift-Diffusion Equation

```
function    dydx = DriftODE( x,y )
global beta gamma alpha;

dydx = [ y(3)
              y(4)
              beta*( alpha*(1+gamma)*y(1)*y(2)-y(3)*y(5)-(y(2)-y(1))*y(1))
             -beta*(-alpha*((1+gamma)/gamma)*y(1)*y(2)-y(4)*y(5)-(y(2)-y(1))*y(2))
              y(2)-y(1)
              -y(5)
              ];
end
%    y1 = N electron density
%    y2 = P hole density
%    y3 = N' slope of electron density
%    y4 = P' slope of hole density
%    y5 = E electric field
%    y6 = V bias voltage
```

Initial Guess

```
function yinit = init_guess( x )
global V_factor e_Density h_Density;
yinit = [ x %1.50659e-23/V_factor*e_Density*x
              (1-x) %1.50659e-23/V_factor*h_Density*(1-x)
              1 %1.50659e-23/V_factor*e_Density
              -1 %-1.50659e-23/V_factor*h_Density
              -V_factor
              x*V_factor
```

```
                ];
 end
%    y1 = N
%    y2 = P
%    y3 = N'
%    y4 = P'
%    y5 = E
%    y6 = V
```

Calculate Current Density

```
function [ Current ] = DriftDiffusion( data )
T = 300;
global beta gamma alpha V_bi V_factor V i sol;
V = data(1); % Bias Voltage (V)
V_factor = (V_bi-V)/V;
beta = V/(0.0259*T/300);
gamma = 1; % hole/electron Mobility ratio
alpha = 0; % Recombination factor
V_bi = 0; % Built-in Voltage (V)
%e_Density = 1e21;
%h_Density = 1e21;
epsilon = 8.85e-12;
L = 50e-9;
q = 1.6e-19;
R_epsilon = 3;
u_hole = 1e-4;
D = 0.0259*T/300*u_hole;
if (i == 1)
solinit = bvpinit(linspace(0,1,40),@init_guess);
else
  solinit.x = sol.x;
  solinit.y = sol.y;
end
sol = bvp4c(@DriftODE,@BC,solinit);

Current_Left    = V/L*sol.y(5,1)*(u_hole*sol.y(2,1)       -u_hole/gamma*sol.y(1,1))
*q*D*epsilon*R_epsilon*V/L/L+    (sol.y(3,1)    /gamma - sol.y(4,1))
*q*D*epsilon*R_epsilon*V/L/L/L/q    %A/m_2
Current_Right = V/L*sol.y(5,end)*(u_hole*sol.y(2,end)-
u_hole/gamma*sol.y(1,end))*q*D*epsilon*R_epsilon*V/L/L+    (sol.y(3,end)/gamma -
sol.y(4,end))*q*D*epsilon*R_epsilon*V/L/L/L/q      %A/m_2
```

```
Current = Current_Left;
 end
```

Plot Current Density-Voltage Characteristics

```
global i sol;
i = 1;
EndVoltage = 2;
Datapoints = 20;
JV = zeros(Datapoints+1,2);

for i=1:Datapoints
JV(i,1) = i/Datapoints*EndVoltage;
        JV(i,2) = DriftDiffusion(JV(i,1));
end
figure (1)
semilogy(JV(:,1),JV(:,2),'-.');
hold on;
```

Code for fitting impedance spectroscopy data

This code is a combination of two programs to extract the capacitance, series resistance and shunt resistance from the frequency dependence of complex impedance. The main program provides an interface to input initial guess and boundaries for the fitting parameters using the 'lsqnonlin' function. The solving program solves for the complex impedance at each frequency with the input parameters and return the error between simulated results and experimental data to the main program.

Main Program:

```
clc;
clear;

global A fitCF initial data ;

h=1;

[fileName,pathName] = uigetfile('.TXT');

cd(pathName);
files = dir('*.TXT');

while h<=length(files)

    A = importdata(files(h).name);
    fitCF = zeros(length(A.data),2);

options = optimset('Display','iter','Tolfun',1e-12,'MaxIter',800,'MaxFunEvals',10000);

data(h,:) = lsqnonlin('SolveCF',initial,[0 0 0 0],[8000 100000000 20000000 10],options)
  figure(h)
plot(A.data(:,4),A.data(:,5),'*');
hold on
plot(fitCF(:,1),fitCF(:,2),'o');
initial(1,:) = data(h,:);

button = questdlg('qstring');
G = strcmp(button,'No');

if (G)
    h=h-1;
    clf;
end
```

```
h=h+1;

end
```

Solving Function:

```
function [err] = SolveCF(data)

global A fitCF;
Rs = data(1);
Rp = data(2);
C = data(3)/100000000;
n = 1;


 for i=1:length(A.data)

      fitCF(i,1) = abs(Rs+Rp/(1+Rp^2*(A.data(i,1)*2*pi)^(2*n)*C^2));
      fitCF(i,2) = -(A.data(i,1)*2*pi)^n*C*Rp^2/(1+Rp^2*(A.data(i,1)*2*pi)^(2*n)*C^2);



 end

      err = abs(A.data(:,4)-fitCF(:,1))+ abs(A.data(:,5)-fitCF(:,2));

end
```

Solving function for complicated equivalent circuit:

```
function [err] = SolveDoubleARC2(data)

global expCF fitCF;

R_s = data(1);
Rp_1 = data(2);
C_1 = data(3)/1e9;
Rp_2 = data(4);
C_2 = data(5)/1e9;
temp = 0;
temp2 = 0;
 for i=1:length(expCF)
temp=Rp_2/(1j*Rp_2*C_2*expCF(i,1)*2*pi()+1)+Rp_1;
```

```
temp2=1/(1j*C_1*2*pi()*expCF(i,1));
        fitCF(i,1) = real(R_s+temp*temp2/(temp+temp2));
    fitCF(i,2) = imag(R_s+temp*temp2/(temp+temp2));

 end

      err = abs(expCF(:,2)-fitCF(:,1))+ abs(expCF(:,3)-fitCF(:,2));

end
```

Fitting code for bulk-ionization

This code is a combination of two programs to extract the built-in electric field, charge transfer state binding energy, effective mobility, recombination rate constant and fraction of bulk-ionization from the temperature dependence of charge collection efficiency. The main program provides an interface to input initial guess and boundaries for the fitting parameters using the 'lsqnonlin' function. The solving program solves for the charge collection efficiency with the input parameters and return the error between simulated results and experimental data to the main program.

Main Program:

```
clc;
clear;
global expJT simJ err T    K_d initial;
expJT = load('DATA_T.txt');
K_d = zeros(length(expJT),1);
simJ = expJT(:,2);
err=zeros(length(expJT),1);
options = optimset('Display','iter','Tolfun',1e-20,'MaxIter',2000,'MaxFunEvals',50000);

data = lsqnonlin('OB_T',initial,[0 0 0 0 0],[3 10 1 100 1],options)

initial = data;

figure(1)

plot(expJT(:,1),abs(simJ(:,1)),'-');
hold on
plot(expJT(:,1),abs(expJT(:,2)),'o');
axis([0 300 0 1]);
```

Solving function:

```
function [ err ] = OB_T( data )
global expJT simJ;
epsilon = 8.85e-12;
q = 1.6e-19;
R_epsilon = 3;
k = 1.38e-23;
V = data(1);
u = data(4)*1e-8; % Mobility
datapoints = length(expJT);
K_d = zeros(datapoints,1);
```

```
K_R = q*u/R_epsilon/epsilon;
a=q^2/4/3.14/R_epsilon/epsilon/(data(3)*1.6e-19);
A = K_R*3/4/3.14/a^3;
K_f = data(2)*1e8;
delta_E = data(3); % Binding energy eV
d = 60e-9; % thickness

for i=1:length(expJT)

    b = q^3*V/d/(8*pi*R_epsilon*epsilon*k^2*expJT(i,1)^2);
    K_d(i,1) = A * exp(-delta_E/(0.0259*expJT(i,1)/300)) *
real(besselj(1,2*sqrt(2)*sqrt(-b))/sqrt(2)/sqrt(-b));

    simJ(i,1) = K_d(i,1)/(K_d(i,1)+K_f)+data(5);


end
err = simJ-expJT(:,2);

end
```

Code for Exciton diffusion:

This code is used to numerically solve the drift-diffusion equation of exciton in an isotropic medium with given generation profile. The boundary condition can be set as reflective or perfectively quenching by changing the matrix elements. The flux at each boundary is calculated to estimate the photocurrent density.

```
G = load('Generation.txt');
G=G*1e-21;

    thickness = 10;
    LD = 20;
    Diff = 2e11;
    n = length(G);          %   No. of unknowns = no. of interior grid points.
    h = thickness/(n+1)             %   Grid spacing.
    x = [0:h:thickness]';           %   Grid points, including boundary.
    J_interior = zeros(n+1,1);

    Ah_diag = -2 * ones(n+2,1)-h^2/LD^2;
    Ah_sub = 1 * ones(n+1,1);
    A_h = spdiags([[Ah_sub;0],Ah_diag,[0;Ah_sub]],[-1 0 1],n+2,n+2);
    A_h(1,1) = -1;
    A_h(1,2) = 1;
    A_h(n+2,n+1) = 0;
    A_h(n+2,n+2) = 1;


G=[0;G;0];
uh = -A_h\G*h^2/Diff;
    %uh = [uh_interior(1,1);uh_interior;0]

%   Calculating Flux Density
for k=2:n+2
J_interior(k-1) =   (uh(k)-uh(k-1))/h*1e14*Diff;
end
J = -[J_interior;2*J_interior(n+1)-J_interior(n)];   % linear interpolation of Flux at end
point


 figure(1)
      plot(x,uh*1e21,'-')
      xlabel('x axis')
      ylabel('Exciton Density')
      legend('Exciton Density','Location','South')
```

```
set(gcf,'Position',[0 0 400 300]);
set(gca,'Position',[.13 .17 .80 .74]);
figure_FontSize=8;
set(get(gca,'XLabel'),'FontSize',figure_FontSize,'Vertical','top');
set(get(gca,'YLabel'),'FontSize',figure_FontSize,'Vertical','middle');
set(findobj('FontSize',10),'FontSize',figure_FontSize);
set(findobj(get(gca,'Children'),'LineWidth',0.5),'LineWidth',2);


figure(2)
        plot(x,J,'-')
        xlabel('x axis')
        ylabel('Exciton Flux')
        legend('Exciton Flux','Location','South')

        Jsc_left = J(1)*1.6e-19*1e3
        Jsc_right = J(n+2)*1.6e-19*1e3

  set(gcf,'Position',[0 0 400 300]);
set(gca,'Position',[.13 .17 .80 .74]);
figure_FontSize=8;
set(get(gca,'XLabel'),'FontSize',figure_FontSize,'Vertical','top');
set(get(gca,'YLabel'),'FontSize',figure_FontSize,'Vertical','middle');
set(findobj('FontSize',10),'FontSize',figure_FontSize);
set(findobj(get(gca,'Children'),'LineWidth',0.5),'LineWidth',2);
```

C. Device Optimization for DTDCPB-DF_o, DTDCPB-DF_m and DTDCPB-F_oF_m[‡]

Chapter 8 discussed device optimization based on the D-A pairing of mono-fluorinated DTDCPB and C_{70}. To improve the V_{OC} even further, di-fluorinated DTDCPB were synthesized by Prof. Wong's research group at National Taiwan University. Three possible configurations of the bi-fluorinated DTDCPB are shown in Figure C.1. The di-fluorinated DTDCPB showed a blue shift in both absorption spectra and photoluminescence spectra

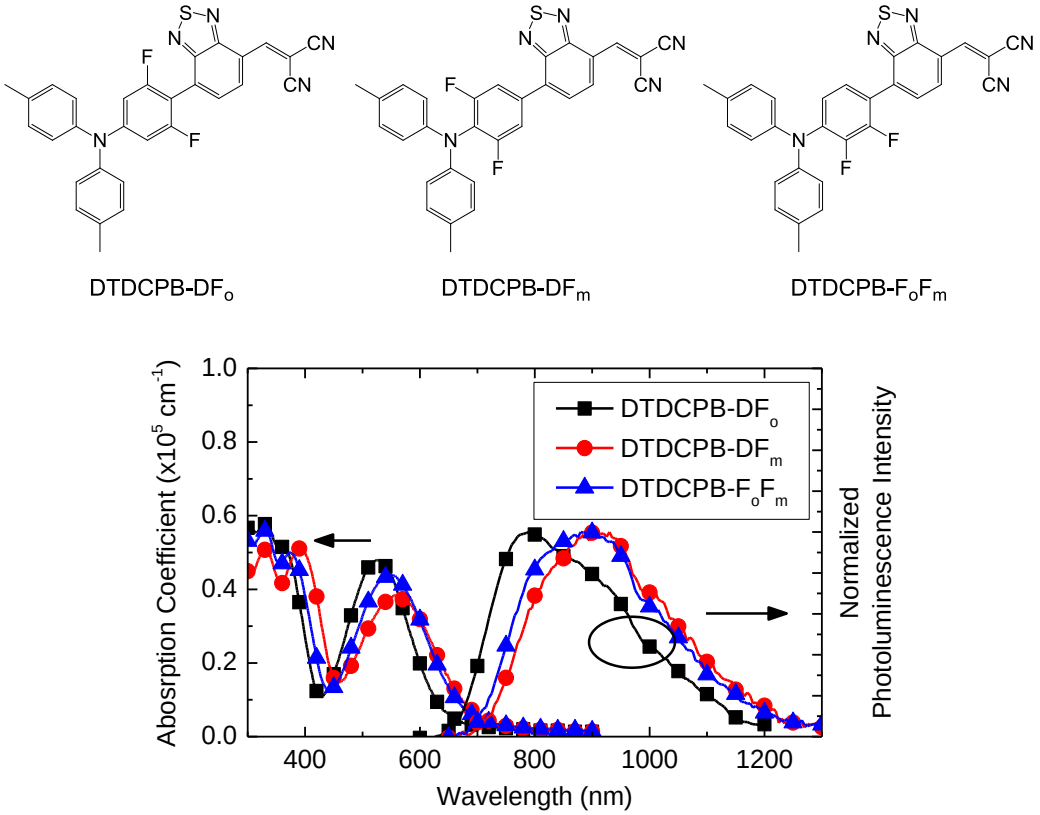

Figure C.1 Molecular structures and optical properties of DTDCPB-DF_o, DTDCPB-DF_m and DTDCPB-F_oF_m.

[‡] The di-fluorinated DTDCPB compounds were synthesized by Prof. Ken-Tsung Wong's research group in the Department of Chemistry at National Taiwan University.

compared to mono-fluorinated DTDCPB materials as also shown in Figure C.1.

BHJ OPVs with the device architecture of ITO/MoO_x 10nm/donor:C_{70} ~55 nm/BCP 10 nm/Al 100 nm are fabricated by co-depositing di-fluorinated DTDCPB and C_{70} at a total rate of 0.2 nm/s. The dependence of device operating parameters on donor concentration is plotted in Figure C.2. All di-fluorinated DTDCPB compounds showed improved V_{OC} together with reduced J_{SC} as predicted. However, the FF of devices fabricated with di-fluorinated DTDCPB is significantly lower than regular DTDCPB at all donor concentrations. This suggests that the charge transport property and the morphology of the DTDCPB:C_{70} film is affected after the di-fluorination process.

Figure C.3 contains the result of an active layer thickness optimization for the champion devices in Figure C.2. Neither V_{OC} nor J_{SC} showed much improvement when increasing the active layer thickness from 55 nm to 80 nm. The FF increased with increasing active layer thickness for DTDCPB-DF_m and DTDCPB-F_oF_m. The overall η_P stays roughly the same through a wide range of active layer thickness. As a result, fully optimized OPVs based on di-fluorinated DTDCPB and C_{70} can only achieve η_P of 3~4%.

Figure C.4 shows the η_{EQE} spectra for optimized BHJ OPVs containing di-fluorinated DTDCPB compounds. Most of the photocurrent is contributed by the acceptor (C_{70}) rather than the donor, due to the low absorption coefficient of di-fluorinated DTDCPBs. In summary, the di-fluorinated DTDCPBs are not the ideal candidates for photovoltaic application.

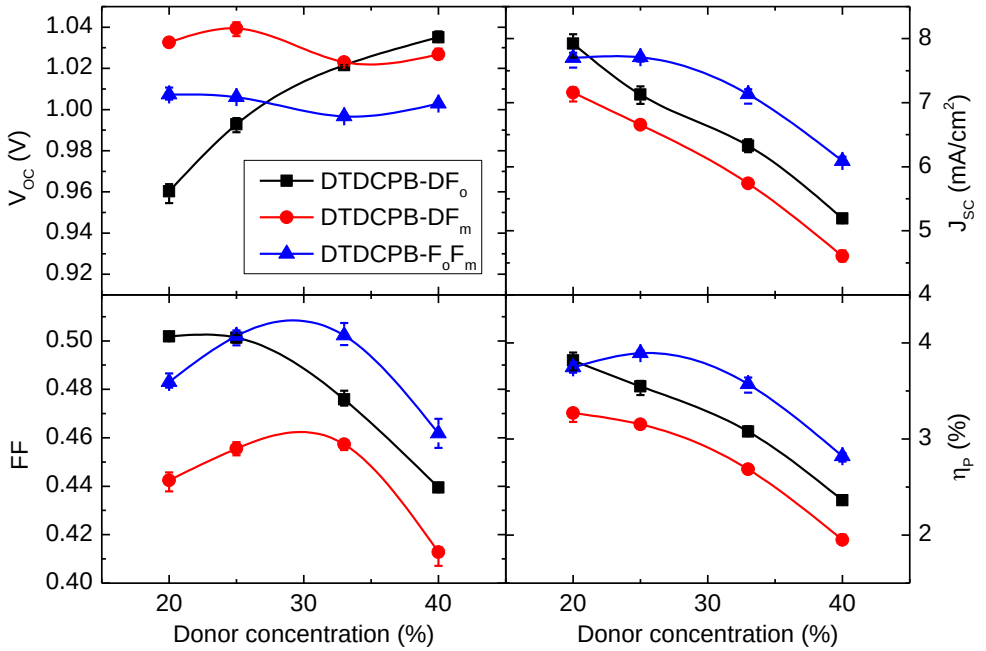

Figure C.2 Device operating parameters for BHJ OPVs (ITO/MoO_x 10nm/donor: C_{70} ~55 nm/BCP 10 nm/Al 100 nm) fabricated with di-fluorinated DTDCPB at various donor concentrations.

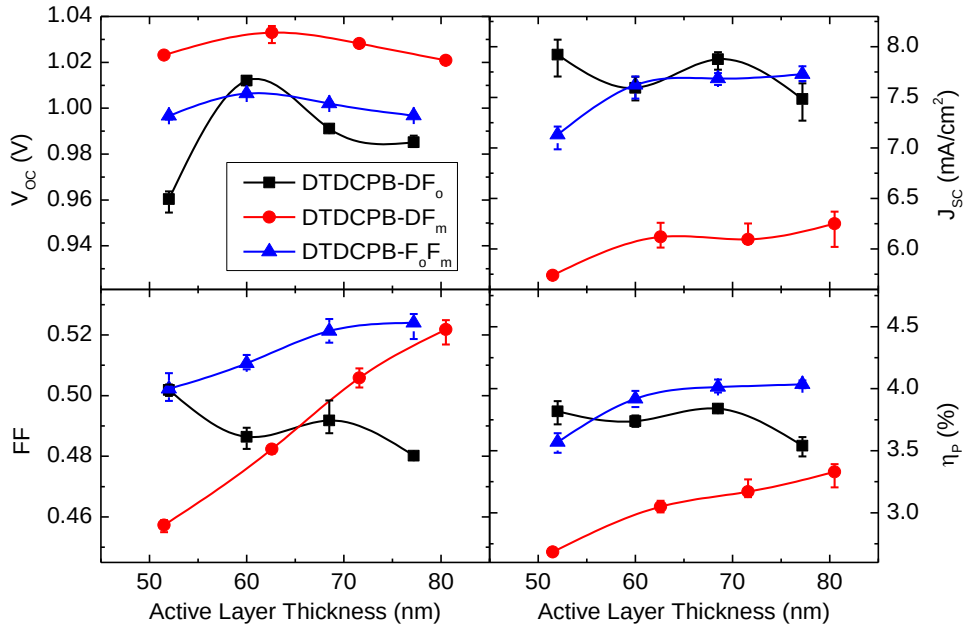

Figure C.3 Device operating parameters for BHJ OPVs (ITO/MoO_x 10nm/donor: C_{70} ~x nm/BCP 10 nm/Al 100 nm) fabricated with di-fluorinated DTDCPB at various active layer thicknesses.

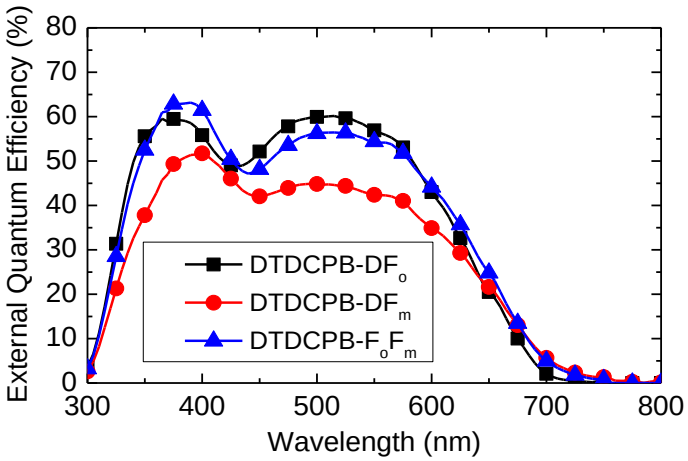

Figure C.4 The external quantum efficiency spectra for the optimized BHJ OPVs in Figure C.3.

D. Copy Right Information

Figures in Chapter 4 are reprinted with permission from Zou, Y.; Holmes, R. J., Correlation Between the Theoretical Maximum Achievable Open-circuit Voltage and Charge Transfer State Energy in Organic Photovoltaic Cells. *ACS Appl. Mater. Interfaces*, **2015**, *7*, 18306. Copyright 2015 American Chemical Society.

JOHN WILEY AND SONS LICENSE
TERMS AND CONDITIONS
May 27, 2015
This Agreement between Yunlong Zou ("You") and John Wiley and Sons ("John Wiley and Sons") consists of your license details and the terms and conditions provided by John Wiley and Sons and Copyright Clearance Center.
License Number: 3637271270834
License date: May 27, 2015
Licensed Content Publisher: John Wiley and Sons
Licensed Content Publication: Advanced Energy Materials
Licensed Content Title: The Role of Exciton Ionization Processes in Bulk Heterojunction Organic Photovoltaic Cells
Licensed Content Author: Yunlong Zou,Russell J. Holmes
Licensed Content Date: Apr 20, 2015
Pages: 1
Type of use: Dissertation/Thesis
Requestor type: Author of this Wiley article
Format: Print and electronic
Portion: Full article
Will you be translating?: No
Title of your thesis / dissertation: Realizing Efficient Energy Harvesting from Organic Photovoltaic Cells
Expected completion date: Jul 2015
Expected size (number of pages): 200
Total: 0.00 USD
TERMS AND CONDITIONS
This copyrighted material is owned by or exclusively licensed to John Wiley & Sons, Inc. or one of its group companies (each a"Wiley Company") or handled on behalf of a society with which a Wiley Company has exclusive publishing rights in relation to a particular work (collectively "WILEY"). By clicking accept in connection with completing this licensing transaction, you agree that the following terms and conditions apply to this transaction (along with the billing and payment terms and conditions established by the Copyright Clearance Center Inc., ("CCC's Billing and Payment terms and conditions"), at the time that you opened your Rightslink account (these are available at any time at http://myaccount.copyright.com).

AIP PUBLISHING LLC LICENSE
TERMS AND CONDITIONS
May 27, 2015
All payments must be made in full to CCC. For payment instructions, please see information listed at the bottom of this form.
License Number: 3637280122045
Order Date: May 27, 2015
Publisher: AIP Publishing LLC
Publication: Applied Physics Letters
Article Title: Influence of a MoOx interlayer on the open-circuit voltage in organic photovoltaic cells
Author: Yunlong Zou, Russell J. Holmes
Online Publication Date: Jul 31, 2013
Volume number: 103
Issue number: 5
Type of Use: Thesis/Dissertation
Requestor type: Author (original article)
Format: Print and electronic
Portion: Excerpt (> 800 words)
Will you be translating?: No
Title of your thesis / dissertation: Realizing Efficient Energy Harvesting from Organic Photovoltaic Cells
Expected completion date: Jul 2015
Estimated size (number of pages): 200
Total: 0.00 USD
Terms and Conditions
AIP Publishing LLC -- Terms and Conditions: Permissions Uses
AIP Publishing LLC ("AIPP"") hereby grants to you the non-exclusive right and license to use and/or distribute the Material according to the use specified in your order, on a one-time basis, for the specified term, with a maximum distribution equal to the number that you have ordered. Any links or other content accompanying the Material are not the subject of this license.
You agree to include the following copyright and permission notice with the reproduction of the Material:"Reprinted with permission from [FULL CITATION]. Copyright [PUBLICATION YEAR], AIP Publishing LLC." For an article, the copyright and permission notice must be printed on the first page of the article or book chapter. For photographs, covers, or tables, the copyright and permission notice may appear with the Material, in a footnote, or in the reference list.
If you have licensed reuse of a figure, photograph, cover, or table, it is your responsibility to ensure that the material is original to AIPP and does not contain the copyright of another entity, and that the copyright notice of the figure, photograph, cover, or table does not indicate that it was reprinted by AIPP, with permission, from another source. Under no

circumstances does AIPP, purport or intend to grant permission to reuse material to which it does not hold copyright.

You may not alter or modify the Material in any manner. You may translate the Material into another language only if you have licensed translation rights. You may not use the Material for promotional purposes. AIPP reserves all rights not specifically granted herein.

The foregoing license shall not take effect unless and until AIPP or its agent, Copyright Clearance Center, receives the Payment in accordance with Copyright Clearance Center Billing and Payment Terms and Conditions, which are incorporated herein by reference.

AIPP or the Copyright Clearance Center may, within two business days of granting this license, revoke the license for any reason whatsoever, with a full refund payable to you. Should you violate the terms of this license at any time, AIPP, AIP Publishing LLC, or Copyright Clearance Center may revoke the license with no refund to you. Notice of such revocation will be made using the contact information provided by you. Failure to receive such notice will not nullify the revocation.

AIPP makes no representations or warranties with respect to the Material. You agree to indemnify and hold harmless AIPP, AIP Publishing LLC, and their officers, directors, employees or agents from and against any and all claims arising out of your use of the Material other than as specifically authorized herein.

The permission granted herein is personal to you and is not transferable or assignable without the prior written permission of AIPP. This license may not be amended except in a writing signed by the party to be charged.

If purchase orders, acknowledgments or check endorsements are issued on any forms containing terms and conditions which are inconsistent with these provisions, such inconsistent terms and conditions shall be of no force and effect. This document, including the CCC Billing and Payment Terms and Conditions, shall be the entire agreement between the parties relating to the subject matter hereof.

This Agreement shall be governed by and construed in accordance with the laws of the State of New York. Both parties hereby submit to the jurisdiction of the courts of New York County for purposes of resolving any disputes that may arise hereunder.